

## **Université Paris Nanterre**

Ecole doctorale Connaissance, langage et modélisation (Nanterre)

Laboratoire Energétique Mécanique Electromagnétisme

Thèse Présentée par :

Ruijie LI

pour obtenir le grade

de

Docteur de l'Université Paris Nanterre

Spécialité: Energétique

---

### **Applications of Stirling engine in sustainable development context-experimental and numerical study**

---

Soutenance prévue le 6 Juillet 2017 devant le jury composé de:

F. Aloui	Professeur	Université de Valenciennes	Rapporteur
M. Costea	Professeur	Polytechnic University of Bucharest	Examineur
M. Feidt	Professeur Emérite	Université de Lorraine	Examineur
L. Grosu	MCF HDR	Université Paris Nanterre	Directeur de thèse
L. Luo	DR CNRS	Université de Nantes	Rapporteur
D. Queiros-Condé	Professeur	Université Paris Nanterre	Co-Directeur de thèse



## Acknowledgement

Time flies, I have studied in France for three years. The study experience, the familiar professors, colleagues, and friends in LEME laboratory is a treasure which will accompany me in my life.

The study presented here is realized in LEME laboratory of Paris Nanterre University.

My first and foremost words of appreciation go to my esteemed research advisor, Professor Lavinia Grosu. Since the first day I shook hands with her in the 3<sup>rd</sup> floor of building A, I have continuously benefited from her terrific disposition, enormous source of knowledge, outstanding expertise in both theoretical and practical matters, unmatched availability, unsurmountable patience, and assiduous encouragement throughout the past three years. I am blessed with such an opportunity to observe and learn her unique approach to analyzing problems, to think out of viable solutions, and to put them into practice. I sincerely hope that she could enjoy our collaboration as much as I did.

I am highly honored, also to appreciate my esteemed thesis co-advisor, Professor Diogo Queiros Conde. I was impressed with his profound knowledge in academics, enormous enthusiasm for research, sustaining optimism for life, incomparable curiosity for matters, and infinite patience. Those characters have been affecting me for those years. I remember that one day he talked with me an interesting experiment which had Water-Electricity-Separation function, which impresses so much that how much he fuses the research interest into the daily life. His endless curiosity inspires me to advance in the road of research. It's my fortunate to have the chance to collaborate with him.

I'm highly honored, also, for having Professor Michel Feidt, Monica Costea, Lingai Luo, and Fethi Aloui in my dissertation committee. I would like to express my sincere gratitude to them for their patiently reviewing this thesis and their detailed and constructive remarks.

Throughout the past three years, I have enjoyed the friendship and support of Dr. Mengxiong Zhao, Dr. Patrick Ribeiro, Dr. Xingkai Wang, Dr. Xiaoxue Pu, Dr. Ye Zhi, Dr. Haoming Wang, Dr. Romain Pawelko, Dr. Tanguy Davin, Dr. Julien-Pierre Offret, Dr. Lorris Navello, Dr. Mohand Ouarabi, Dr. Fanhong Meng, Dr. Zhaoyi Jiang, Dr. Jeremy Lebedinsky, Dr. Yonghao Chen, Dr. Menghua Zhao, Dr. Wenjing Du, Dr. Chao He, Mrs. Saerom Kang, Ms. Shaimma Moustafa, Mengting Tang, Jingyi Sun, and Ms. Mariana Martinez. We have discussed about the research, the study, and the trivial matters in daily life. Their accompanying bring me the color and happiness during the research life which will go on in my memory.

I'd also acknowledge the technicians of LEME in for their contribution in tests. Mr. Maurice helps me a lot during the experiment testing.

I would like to thank my grandmother, my parents and my brother for their efforts in cultivating my personality, their comprehension, and support in my studying period. Last but not least, I should thank my wife, Xiaoyun Zhu, for her accompanying and continuous supporting in daily life and my research field, and her family's support for our daily life study abroad.

## Résumé

Dans ce travail, un moteur Stirling de type Gamma alimenté par énergie solaire avec une faible différence de température a été étudié numériquement et expérimentalement. Un nouveau modèle appelé Polytropic Stirling Model with Losses (PSML) a été proposé et appliqué au moteur GPU-3 Stirling. Un cryoréfrigérateur basé sur un moteur Stirling intégral de type Alpha a été étudié numériquement, après avoir mesuré ses dimensions géométriques au laboratoire.

Pour le moteur Stirling de type gamma du laboratoire, le modèle ait thermodynamique à vitesse finie et le modèle isotherme a été développé, incluant les bilans de masse et d'énergie à travers les différents volumes (compression, régénération et expansion) dans le moteur. Différents types de pertes thermiques et mécaniques ont été considérés dans le modèle afin d'analyser les processus thermodynamiques et les pertes dans le moteur Stirling. En outre, des études paramétriques sur les performances du moteur Stirling alimenté à l'énergie solaire ont également été étudiées expérimentalement et numériquement.

La comparaison entre les résultats expérimentaux et les résultats de simulation à différents déphasages entre le déplaceur et le piston, et à différentes course de piston montre que le modèle est convaincant dans la prédiction des performances du moteur Stirling.

Basé sur la méthode thermodynamique en dimension physique finie, une méthode d'algorithme génétique multi-objectives, objectifs étant la puissance fournie, le rendement énergétique et le taux de génération d'entropie a été utilisé pour optimiser la fonction et la géométrie du moteur du type Gamma. En comparant avec la méthode d'optimisation écologique, la méthode multi-objectif permet de mieux équilibrer les trois objectifs.

Le nouveau modèle (PSML) proposé pour prédire les performances du moteur de type Bêta ou Gamma du moteur Stirling, il divise l'espace de travail en 5 parties (volume de compression, refroidisseur, régénérateur, chauffage et volume d'extension).

Une liaison entre volume de compression et volume d'extension a été ajoutée dans le modèle adiabatique classique du moteur Stirling. Ainsi, des processus polytropiques ont été considérés dans les volumes de compression et d'expansion du moteur Stirling. Le moteur Stirling GPU-3 a été utilisé pour valider le nouveau modèle. Il a été démontré que le nouveau modèle (PSML) prédit correctement la puissance de sortie et le rendement du moteur.

Dans la dernière partie de la thèse, un Cryorefroidisseur Stirling de type Alpha, a été étudié en utilisant un modèle isotherme prenant en considération différentes pertes. Les volumes de compression et d'expansion sont considérés isothermes, et la variation de la température du régénérateur est considéré linéaire. Les bilans d'énergie et d'exergie du Cryorefroidisseur ont été réalisés, et l'effet de divers paramètres sur la performance (puissance de refroidissement et puissance mécanique consommée) est étudié. Les résultats de la simulation pour PPG-102 Stirling cryocooler ont été comparés avec deux autres résultats de simulation de la littérature et des résultats expérimentaux indiquant que ce modèle est convaincant pour prédire la performance du Cryorefroidisseur.

**Mots-clés:** Moteur Stirling; Réfrigérateur cryogénique Stirling; Isotherme; Polytropique; Multi-objectifs; optimisation; exergie

## Abstract:

In this work a solar powered low temperature difference Gamma type Stirling engine has been studied experimentally and numerically using an isothermal model coupled with various losses and using an objective optimization. A new model named Polytropic Stirling Model with Losses (*PSML*) has been proposed which was applied to the Beta type GPU-3 Stirling engine. An Alpha type integral Stirling cryocooler has been studied numerically using an isothermal model with losses.

To study a Gamma type Stirling engine of our laboratory, an isothermal model coupled with finite speed method has been developed, including mass and energy balances through different spaces of the engine. The engine is divided into 3 volumes: compression volume, regeneration volume, and expansion volume. Different kind of thermal and mechanical losses have been considered in the model, in order to analyze thermodynamic processes and losses in the Stirling Engine. In addition, parameter effects on the performance of the solar powered gamma type Stirling engine have also been studied experimentally and numerically. The comparison between the experimental results and the simulation results at different phase shift between the displacer and the piston, and at different piston stroke shows that the model is convincing to predict the Stirling engine performance. Based on the Finite Physical Dimensional Thermodynamic method, a multi-objective genetic method considering output power, thermal efficiency and entropy generating rate as objective functions simultaneously, has been used to multi-objective optimize the Gamma type Stirling engine. Comparing with the ecological optimization method, the multi-objective method can better balance the three objective goals.

The new model (*PSML*) proposed in the thesis for predicting performance of Beta or Gamma type of Stirling engine divides the working space into 5 parts (compression volume, cooler, regenerator, heater, and expansion volume). A bypass linking compression volume and expansion volume has been added in the classic adiabatic model of Stirling engine. Thus, polytropic processes have been considered in the compression and expansion volumes of the Stirling engine. The GPU-3 Stirling engine has been used to validate the new model. It was shown that the new model (*PSML*) predict well the output power and the thermal efficiency of the engine well.

An isothermal model considering various losses was developed and presented in the last part of this thesis to study an Alpha type Stirling cryocooler, whose geometrical dimensions were measured in our laboratory. The compression and expansion volumes are supposed to be isothermal, the variation of the regenerator temperature is supposed to be linear. Energy and exergy balances of the cryocooler were developed. The effect of various parameters on the cryocooler performance (cooling power and input power) are investigated. The simulation results for PPG-102 Stirling cryocooler were compared with two other simulation results of the literature and with experimental results which indicated that this model is convincing to predict the performance of the Stirling cryocooler.

**Keywords:** Stirling engine; Stirling cryocooler; isothermal; polytropic; multi-objective; optimization; exergy

## Nomenclature

$A$	cross section area, $m^2$
$c$	average molecular speed, $m/s$
$C$	specific heat capacity, $J/(kg.K)$
$D$	diameter, $m$
$E$	internal energy, $J$
$Ex$	exergy, $J$
$f$	friction factor, -
$F$	objective function value/frequency, $Hz$
$\bar{F}$	dimensionless value of $F$
$g$	gravitational acceleration, $m/s^2/gap$ , $m$
$h$	heat transfer coefficient, $W/K$
$H$	enthalpy, $J$
$k$	swept volume ratio, -
$K$	heat conductivity, $W/(m.K)$
$L$	length, $m$
$m$	mass, $kg$
$\dot{m}$	mass flow rate, $kg/s$
$n$	rotation speed, $rotation/s$
$Nu$	Nusselt number, -
$NTU$	number of transfer unit, -
$p$	pressure, $Pa$
$P$	output power, $W$
$Pe$	Peclet number, -
$Pr$	Prandtl Number, -
$Q$	heat, $J$
$\dot{Q}$	heat flow, $W$
$r$	gas constant, $J/(kg.K)$
$R$	radius, $m$
$Re$	Reynolds Number, -
$S$	entropy, $J/K$
$\dot{S}$	entropy flow, $W/K$
$\dot{S}_g$	entropy generation rate, $W/K$
$St$	Stanton Number, -
$t$	time, $s$
$T$	temperature, $K$
$u$	velocity, $m/s$
$V$	volume, $m^3$
$W$	work, $J$
$\dot{W}$	mechanical power, $W$

$x_0$	displacer stroke, mm
$y_0$	piston stroke, mm
$z$	height, m
$Z$	stroke, m

### Greek symbols

$\alpha$	thermal diffusivity, $\text{m}^2\cdot\text{s}^{-1}$
$\omega$	angular speed, rad/s
$\varphi$	crank angle, rad
$\Phi_0$	out of phase, rad
$\Phi$	shape factor, $\text{m}^{-1}$
$\rho$	density, $\text{kg}/\text{m}^3$
$\mu$	dynamic viscosity, $\text{N}\cdot\text{s}/\text{m}^2$
$\nu$	kinetic viscosity, $\text{m}^2/\text{s}$
$\Pi$	porosity, -
$\chi$	dead volume ratio, -
$\lambda$	thermal conductance ratio, -
$\lambda_D$	diameter ratio piston/displacer, -
$\lambda_S$	stroke ratio piston/displacer, -
$\gamma$	specific capacity ratio, -
$\varepsilon$	heat exchanger efficiency, -
$\eta$	thermal efficiency, -
$\tau$	compression ratio, -

### Subscripts

$a$	amplitude
$ave$	average
$c$	compression
$ck$	interface of compression space-cooler
$cond$	conduction
$c0$	compression swept
$cr$	compression-regenerator interface
$d$	displacer
$dc$	compression dead
$de$	expansion dead
$dh$	dead (volume) in high temperature space
$dl$	dead (volume) in low temperature space
$e$	expansion
$e0$	expansion swept
$ext$	exterior
$f$	friction
$fin spe$	finite speed
$g$	gas
$h$	hot temperature/heater

<i>he</i>	interface of heater-expansion space
<i>hys</i>	hysteresis
<i>i</i>	indicated
<i>in</i>	inlet
<i>initial</i>	initial state
<i>k</i>	cooler
<i>kr</i>	interface of cooler-regenerator
<i>l</i>	low temperature
<i>leak</i>	leakage
<i>m</i>	mean
<i>mech fri</i>	mechanical friction
<i>o</i>	phase shift
<i>out</i>	outlet
<i>p</i>	piston
<i>passage</i>	passage between compression and expansion volumes
<i>poly</i>	polytropic
<i>r</i>	regenerator
<i>re</i>	regenerator-expansion interface
<i>rh</i>	interface of regenerator-heater
<i>t</i>	total
<i>u</i>	velocity
<i>w</i>	wall

### **Superscripts**

<i>irr</i>	irreversibility
<i>n-1</i>	previous time step
<i>n</i>	current time step

## Table of Contents

Chapter 1 Introduction .....	1
1.1 World energy requirement .....	1
1.2 Research focus.....	4
1.3 Thesis overview.....	6
References:.....	6
Chapter 2 Stirling engine presentation and literature review of simulation model and experimental studies.	9
2.1 Stirling engine .....	9
2.1.1 Background .....	9
2.1.2 Ideal Stirling cycle.....	11
2.1.3 Real Stirling engine cycle.....	12
2.1.4 Stirling engine configurations .....	13
2.1.5 Stirling engine applications .....	17
2.2 Model and experimental studies of Stirling engine .....	22
2.2.1 Second order.....	24
2.2.2 Third order.....	26
2.2.3 Multi-objective optimization .....	28
2.2.4 Combined heat and power generation .....	28
2.2.5 Low temperature difference Stirling engine.....	29
2.2.6 Free piston Stirling engine.....	30
2.2.7 Experimental study and other innovation in Stirling engine .....	32
2.3 Summary .....	34
References:.....	34
Chapter 3 New isothermal model coupled with various losses .....	43
3.1 Geometry of the studied Stirling engine.....	43
3.2 Thermodynamic model.....	44
3.2.1 Study of different losses in the engine.....	46
3.2.2 Study case of the Gamma type Stirling engine.....	52
3.3 Summary .....	60
Reference.....	61
Chapter 4 Experimental study of the Gamma type Stirling engine .....	63
4.1 Presentation of experimental device.....	63
4.2 Comparison between experimental and simulation results .....	64
4.3 Parameter effect on the Gamma type Stirling engine .....	66
4.4 Summary .....	75
Chapter 5 New Polytropic Stirling Model with Losses (PSML).....	77
5.1 Mathematic model .....	77
5.1.1 Basic adiabatic model.....	77
5.1.2 New Polytropic Stirling Model based on the adiabatic model (PSML) .....	79
5.2 Study case of the new model for Beta type GPU-3 Stirling engine .....	87
5.3 Summary .....	106
References .....	106
Chapter 6 Multi-objective optimization of the experimental Gamma Stirling engine .....	109
6.1 Method for multi-objective optimization .....	109

6.2 Non-dimensionalization method .....	111
6.3 Decision-making method .....	112
6.4 Case study: Gamma type Stirling engine .....	113
6.5 Results and analysis.....	119
6.6 Summary .....	127
References .....	128
Chapter 7 Isothermal model with losses applied to an Alpha type Stirling cryocooler.....	131
7.1. Introduction .....	131
7.2. Presentation of the studied cryocooler .....	135
7.3 Case study .....	142
7.4 Model validation .....	148
7.5 Summary .....	150
References:.....	151
Chapter 8 Summary of thesis work and future research.....	155
8.1 Summary of thesis work.....	155
8.2 Future research .....	157
Appendix .....	159

## Chapter 1 Introduction

### 1.1 World energy requirement

Nowadays, the global rising populations and human's thirst for development has been consistently increasing the demand for energy and power [1]. Figure 1.1 shows the world energy consumption studied and predicted by the U.S. Energy Information Administration [2]. It can be seen that the energy consumption in 2040 can nearly be twice times of that of 2016.

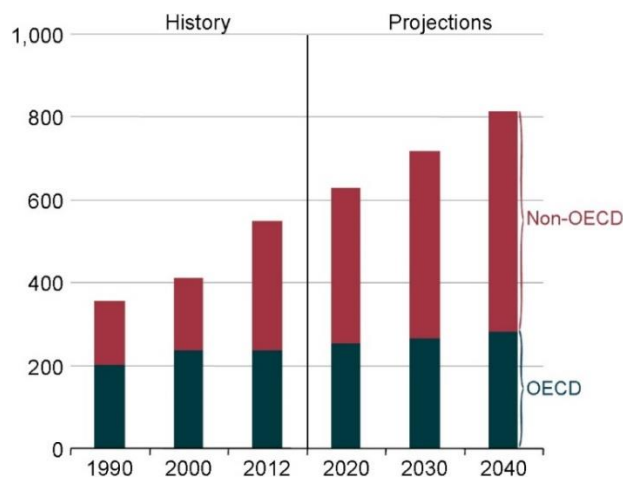


Figure 1.1 World energy consumption, 1990–2040 (quadrillion Btu)

Sources: U.S. Energy Information Administration; International Energy Outlook 2016 [2]

OECD: Organization for Economic Co-operation and Development

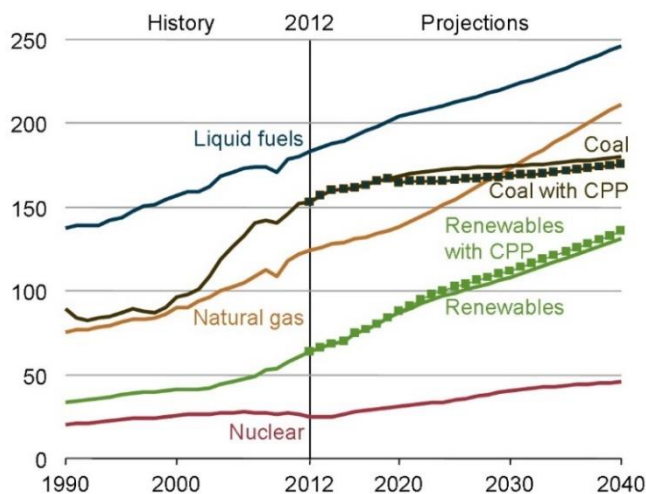


Figure 1.2 Total world energy consumption by energy source, 1990–2040 (quadrillion Btu)

Note: Dotted lines for coal and renewables show projected effects of the U.S. Clean Power Plan. (CPP)

Sources: U.S. Energy Information Administration; International Energy Outlook 2016 [2]

Figure 1.2 shows the total world energy consumption by energy source, studied by the U.S. Energy Information Administration. It can be seen that the demand of natural gas, liquid fuels, coal, and renewable energy resource will increase very quickly in the future.

Figure 1.3 shows the world net electricity generation by energy source. It can be seen that the electricity consumed in 2040 can be 60% higher than that of 2012.

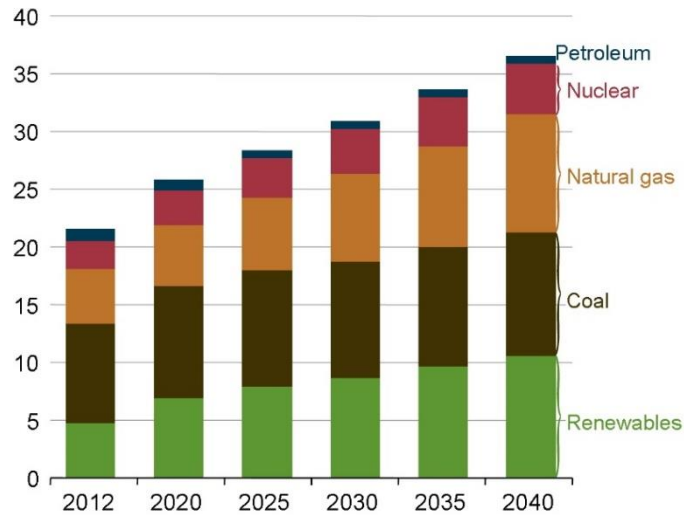


Figure 1.3 World net electricity generation by energy source, 2012–40 (trillion kilowatthours) [2]

The energy source consumed by the transportation will also increase very quickly in the future, as it is seen in Figure 1.4 published by the U.S. Energy Information Administration (EIA).

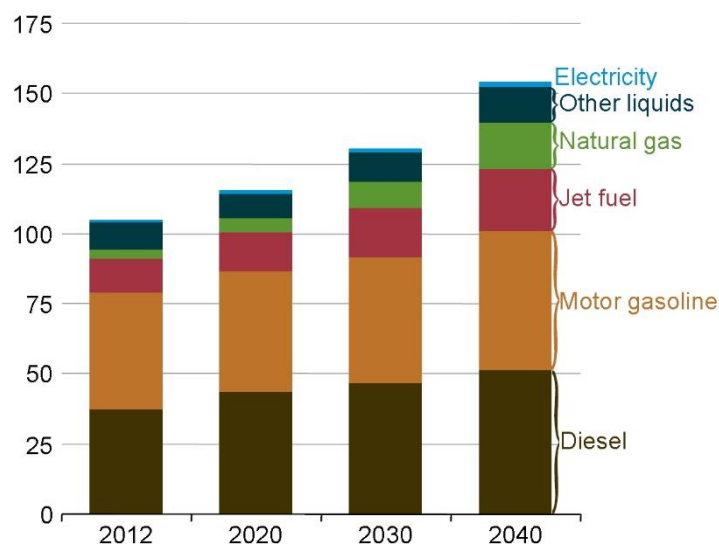


Figure 1.4 World transportation sector delivered energy consumption by energy source, 2012–40 (quadrillion Btu) [2]

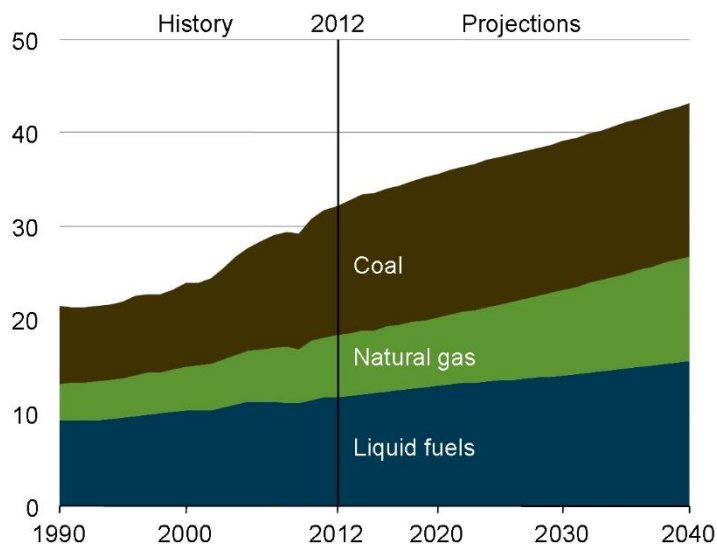
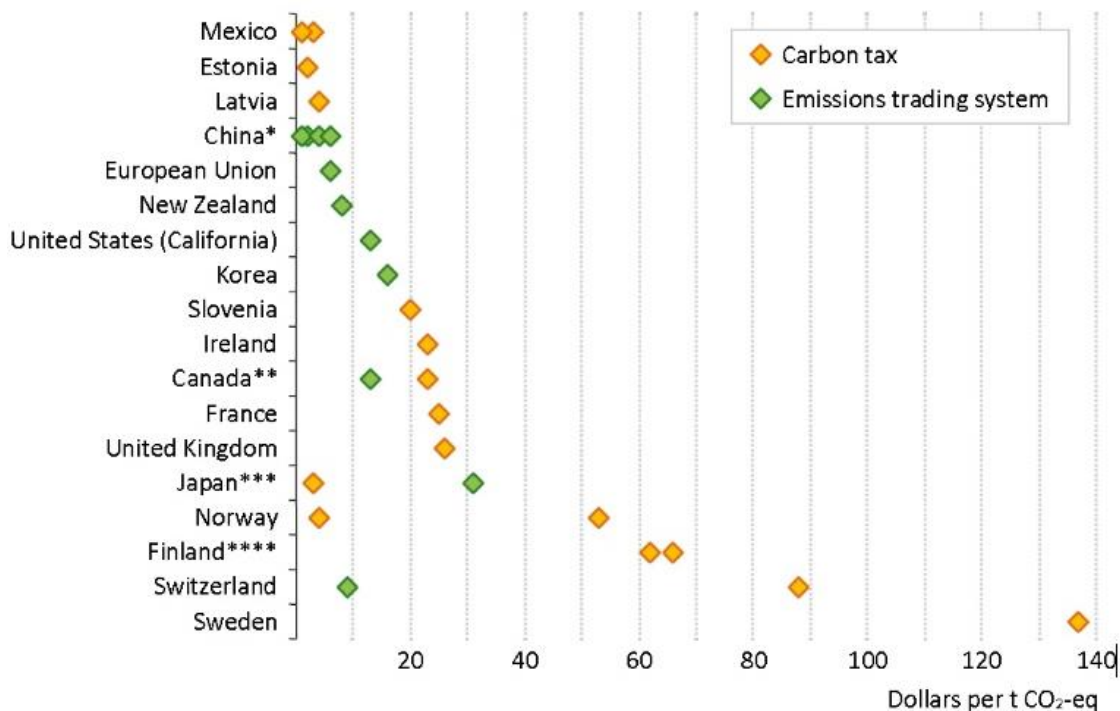


Figure 1.5 World energy-related carbon dioxide emissions by fuel type, 1990–2040 (billion metric tons) [2]



*Countries put a wide range of prices on carbon in different parts of the energy sector*

Figure 1.6 Selected carbon pricing schemes in place as of mid-2016 [3]

Notes: All prices as of 1 July 2016. \$/tCO<sub>2</sub>-eq = US dollars per tonne of carbon-dioxide equivalent. The coverage of the various schemes varies widely, with many limited to specific sub-sectors and/or fuels. Values for Norway cover lower and upper values of carbon tax. \* China includes pilot schemes introduced in Shanghai, Guangdong and Chongqing (\$1-2/tCO<sub>2</sub>-eq), Hubei and Tianjin (\$4/tCO<sub>2</sub>-eq), Beijing and Shenzhen (\$6/tCO<sub>2</sub>-eq). \*\* Canada includes initiatives introduced by Québec (\$13/tCO<sub>2</sub>-eq), Alberta (\$15/tCO<sub>2</sub>-eq) and British Columbia (\$23/tCO<sub>2</sub>-eq). \*\*\* Japan includes national carbon tax (\$3/tCO<sub>2</sub>-eq) and Tokyo emissions trading (\$31/tCO<sub>2</sub>-eq) \*\*\*\* Finland includes initiatives covering heating fuels (\$62/tCO<sub>2</sub>-eq) and the transport sector (\$66/tCO<sub>2</sub>-eq).

Sources: World Bank Group; Ecofys; Carbon Pricing Watch 2016.

With the continuously increasing worldwide consumption of energy resource, the carbon dioxide emissions increases quickly also which leads to the global warming and then destroying the ecological environment in the earth. Figure 1.5 shows the world energy-related carbon dioxide emissions by fuel type, 1990–2040 studied by EIA [2]. It shows that the carbon dioxide emissions will be about 50% higher than that of the 2012, which will causes a serious global warming.

To alleviate the global warming process, governments and non-governmental organizations have tried many measures to reduce the carbon dioxide emission. The *Paris Climate Change Conference (COP21/CMP11)* has been held in 2015, and all the members of *United Nations Framework Convention on Climate Change* have signed documents to control the carbon dioxide emission and the global warming. Some countries have tax for the Carbon emission, and Figure 1.6 shows the different countries which put a wide range of prices on carbon.

## 1.2 Research focus

To reduce the air pollution and greenhouse gases caused by the fossil fuels, solar energy, which is safer, represents an excellent energy resource to replace some parts of the fossil fuels [4]. According to U.S. Energy Information Administration [5], the world total electricity net consumption in 2012 is 19710 Billion kWh, while the earth absorbs  $10700 \times 10^5$  Billion kWh in one year from the sun. Therefore, it is important to highlight that the total electricity consumed in one year is much less than the solar energy received from the sun in an hour. Even if we consider conversion efficiency from thermal energy to electricity, solar energy represents a huge potential to be explored.

Stirling Engine (SE) is an excellent mechanism for using solar sources [6-8]. Compared with Photovoltaic cells, during the fabrication process of which there are pollution emissions, SE is more environmentally friendly, having no emissions and a long life span. One quality that distinguishes the Stirling engine is that it can operate at Low Temperature Difference (LTD) which is especially attractive for low level heat recovery and for solar energy [9-11]. Although the efficiency of a LTD Stirling engine is low compared with those of high temperature SE, its exergy efficiency may be important, which is the accurate parameters to be taken into account to study if a conversion from thermal energy into work is efficient or not; in addition, it is suitable to use solar energy which is safe and with low operation costs [12].

Table 1.1 shows a comparison between solar powered Stirling systems and other competing renewable energy technologies [1], which illustrates the advantages and disadvantages of those technologies. It can be seen that the Stirling systems is very promising.

An effective model is essential for predicting the engine performance and optimization of its parameters. Due to the complexity of the Stirling engine geometry and operation condition, the performance of the engine is difficult to predict. In this work, three types of Stirling engine have been modeled in order to predict its performance and for further optimization.

Table 1.1 Comparing Stirling systems and competing renewable energy technologies [1]

No.	Wind power	Solar PV	Solar CSP	Stirling system
<b>Advantages:</b>				
1	Little Pollution	Pollution free during use	Pollution free during use	High working efficiency and flexible input heat source
2	Long term potential	Grid connected solar electricity reduces transmission/distribution losses	Grid connected solar electricity reduces transmission/distribution losses	Huge long term potential
3	Low capital and operating Cost	Low operating costs and little maintenance needed after initial set up	Low operating costs and little maintenance needed after initial set up	Low capital cost and operating costs
4	Clearing of woods often unnecessary	The amount of solar energy intercepted by the Earth every minute is greater than the amount of fossil fuel the world uses every year	The amount of solar energy intercepted by the Earth every minute is greater than the amount of fossil fuel the world uses every year	Hybrid nature of the device allows for use of plentiful solar energy and biomass which is abundant and cheap
5	Scalable in size	Scalable in size	Scalable in size	Compact size and scalable to any size based on requirement
<b>Disadvantages:</b>				
1	Highly taxed	Large capital costs	Large capital costs	Policy dependent
2	Hazard to birds and ecosystem	Intermittency	Intermittency	CO <sub>2</sub> emission
3	Noisy	Low energy output in high altitudes & cloudy region	Low energy output in high altitudes & cloudy region	/
4	Depreciation of property value	AC to DC conversion	AC to DC conversion	Conversion losses
5	Variable efficiency	Limited power density	Limited power density	Material constraints

6	Land intensive	Land intensive	Land intensive	Depends on input heat source
---	----------------	----------------	----------------	------------------------------

### 1.3 Thesis overview

In this work, the chapter 1 introduced the world energy requirement currently and in the future, and the advantage of Stirling engine for energy conversion using the renewable energy. The chapter 2 will introduce the history of Stirling engine development, the ideal and real thermodynamic Stirling cycle, Stirling engine configurations and division including the engine and cooler, and the different applications of Stirling engine. Then the previous models and experimental research in Stirling engine and its subpart will be reviewed. Chapter 3 will propose an modified isothermal model coupled with finite speed method, in order to study various losses effect including hysteresis loss, piston finite speed loss, regenerator viscous flow loss, heat transfer loss of the imperfect regenerator, displacer shuttle loss, heat conduction loss and leakage loss on the performance of the engine. In chapter 4 experimental results will be done to verify the isothermal model; parameters' effects on the Gamma type Stirling engine performance will be also investigated. Chapter 5 develop a new polytropic Stirling model with losses which considers a polytropic process in the compression and expansion spaces. Polytropic number evolution in compression and expansion volume and effects of rotation speed, pressure and clearance size have also been studied. In chapter 6, the experimental Gamma type Stirling engine will be multi-objective optimized using genetic algorithm with the output power, thermal efficiency, and entropy generation rate as objective functions simultaneously. Chapter 7 will study the parameter effect on the performance of an Alpha type Stirling cryocooler using an isothermal model considering various losses. A cryocooler was examined and measured in our laboratory in order to supply the thermodynamic analysis with the accurate geometrical dimensions. Finally, chapter 8 will summarize the thesis work and propose the prospect of future research.

### References:

- [1] Nayak A.O., Holistic Modeling, Design & Analysis of Integrated Stirling and Auxiliary Clean Energy Systems for Combined Heat and Power Applications. 2015.
- [2] 'International Energy Outlook 2016'. U.S. Energy Information Administration, 2016.
- [3] 'World Energy Outlook 2016'. International Energy Agency, 2016.
- [4] Aksoy F., et al., Thermal performance of a Stirling engine powered by a solar simulator. Applied Thermal Engineering, 2015. **86**(0): p. 161-167.
- [5] <http://www.eia.gov/cfapps/ipdbproject/IEDIndex3.cfm?tid=44&pid=44&aid=2>
- [6] Ahmadi M.H., et al., Multi-objective thermodynamic-based optimization of output power of Solar Dish-Stirling engine by implementing an evolutionary algorithm. Energy Conversion and Management, 2013. **75**: p. 438-445.
- [7] Ahmadi M.H., Mohammadi A.H., and Dehghani S., Evaluation of the maximized power of a regenerative endoreversible Stirling cycle using the thermodynamic analysis.

- Energy Conversion and Management, 2013. **76**: p. 561-570.
- [8] Ahmadi M.H., et al., Thermodynamic optimization of Stirling heat pump based on multiple criteria. Energy Conversion and Management, 2014. **80**: p. 319-328.
- [9] Kongtragool B. and Wongwises S., Performance of low-temperature differential Stirling engines. Renewable Energy, 2007. **32**(4): p. 547-566.
- [10] Martaj N., Grosu L., and Rochelle P., Exergetical analysis and design optimisation of the Stirling engine. International Journal of Exergy, 2005. **3**(1): p. 45-67.
- [11] Martaj N., Grosu L., and Rochelle P., Thermodynamic study of a low temperature difference Stirling engine at steady state operation. International Journal of Thermodynamics, 2007. **10**(4): p. 165.
- [12] Tavakolpour A.R., Zomorodian A., and Akbar Golneshan A., Simulation, construction and testing of a two-cylinder solar Stirling engine powered by a flat-plate solar collector without regenerator. Renewable Energy, 2008. **33**(1): p. 77-87.



## Chapter 2 Stirling engine presentation and literature review of simulation model and experimental studies

### 2.1 Stirling engine

#### 2.1.1 Background

The Stirling engine was invented and patented by Robert Stirling in 1816. As Stirling engine is a close-cycle engine, one part of the engine is heated while another part is cooled simultaneously. However, the invention of the Stirling engine was so much in advance of scientific knowledge at the time that at least 30 years passed before anyone was in a position to understand what made the engine work at all [1]. The first invented Stirling engine is presented in Figure 2.1.

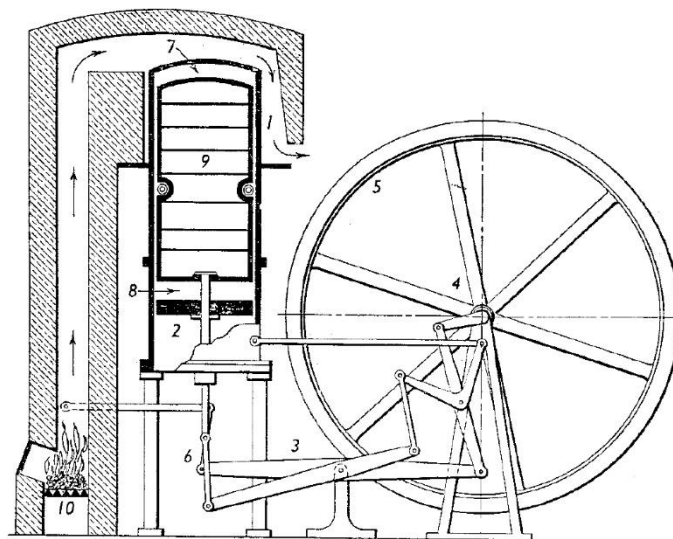


Figure 2.1 Reproduction of drawing showing the first Stirling engine [1]

Although Robert Stirling and other engineers have tried to improve the Stirling engine at that time, the output power and thermal efficiency of the most Stirling engine was very low, because of the limited condition and scientific knowledge[2]. Therefore, Stirling engine was replaced by internal combustion engine gradually, and was produced for toys and a few small ventilating fans, during the early part of the twentieth century [1]. The development of Stirling engine went into a dark period until 1930s when the Philips Company started to explore the modern Stirling engine. In 1938, the rural area of Holland lacked electricity, and required a kind of electricity supplier which had long time span, quiet, and could use multitudinous heat sources. After a systematic comparison of various prime movers, the Philips team decided to go with the Stirling engine [3].

And then different experimental models were built, some using the Rider construction with two

loaded pistons, others the Stirling single-cylinder principle with one piston and one displacer. A number of successful small prototypes had been produced. In 1946, Philips produced 2.h.p (about 1471W) Stirling engine which can be seen in Figure 2.2. This small engine has an output of about 2 h.p. and runs at a speed of up to 2000 RPM with a pressure range of 20-50 atm. In 1947, the Philips company had invented the Stirling engine with 1.2 kW, whose weight and volume were 50% and 60% less than the former engine [2]. By 1951, the 180/200W generator set designated MP1002CA was ready for production by Philips company, which can be seen in Figure 2.3 [3].



Figure 2.2 Single-cylinder Philips 2 h.p. Stirling engine

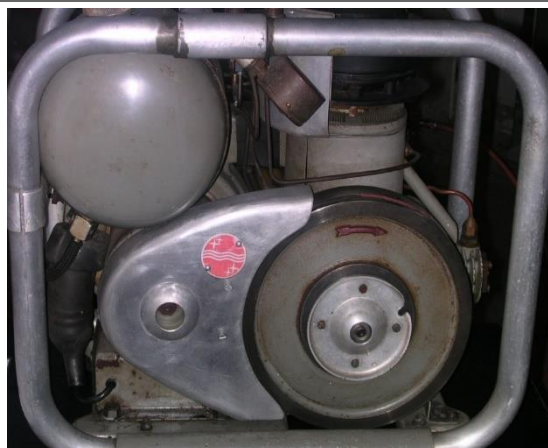


Figure 2.3 Philips MP1002CA Stirling generator of 1951 [3]

In 1957, Philips company had produced the two-cylinder, double-acting Stirling cryocooler attaining the cold end temperature around  $-80\sim-180^{\circ}\text{C}$ , which can be seen in Figure 2.4. The Stirling cooler achieved commercial success with the cryocooler.

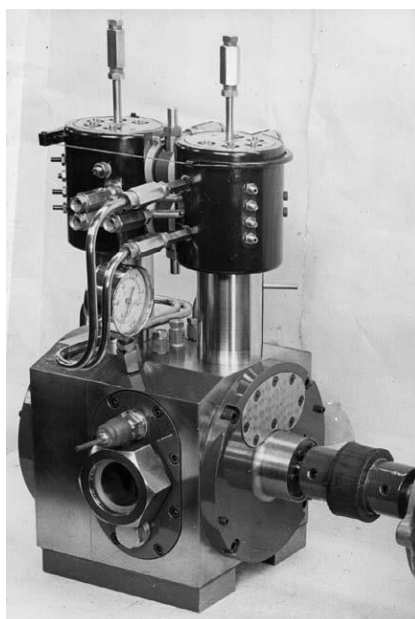
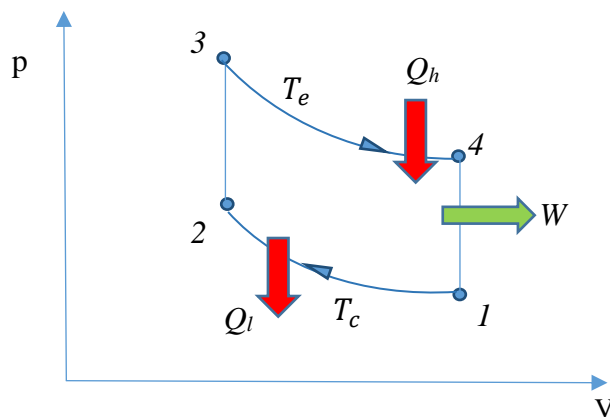


Figure 2.4 Two-cylinder, double-acting Stirling engine for domestic refrigeration

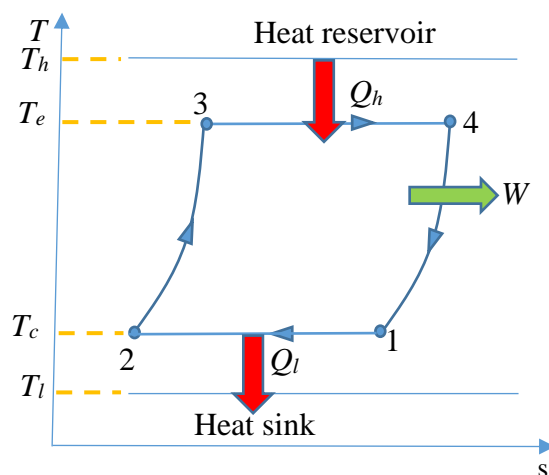
W.T. Beale, professor of mechanical engineering at Ohio University in Athens, invented a free piston version of Stirling engine in the early 1964 [4]. In 1972 the American Ford Motor Company have developed Stirling engine for propulsion in cooperation with Philips Company [2]. In 1996, the Swedish shipbuilder Kockums developed a Stirling-driven generator to recharge batteries and provide electrical power for propulsion in Gotland-class submarines commissioned by Swedish navy. In the 21<sup>st</sup> century, the study of Stirling engine has been more prevalent in many companies and research institutes including Sunpower Inc., Infinia Inc., Qnergy Inc., Cleanergy Inc., Ricor Cryogenic and Vacuum Systems, and Stirling Technology Company etc.

### 2.1.2 Ideal Stirling cycle

The ideal Stirling cycle can be seen in Figure 2.5 ((a)  $PV$  diagram, and (b)  $T-s$  diagram). There are 4 processes: 1-2 is an isothermal compression process corresponding to the temperature  $T_c$ , the working fluid is compressed and releases heat  $Q_l$  to the heat sink; 2-3 is an isochoric process, the working fluid absorbs heat from regenerator material; 3-4 is an isothermal expansion process corresponding to the temperature  $T_e$ , the working fluid expands and absorbs heat  $Q_h$  from the heat source; 4-1 is an isochoric process, the working fluid releases heat to the regenerator material. Because the expansion temperature  $T_e$  is higher than the compression temperature  $T_c$ , the working fluid can output positive work to the environment.



(a)  $PV$  diagram



(b)  $T$ - $s$  diagram

Figure 2.5 Ideal Stirling cycle

Figure 2.6 shows the reversed Stirling cycle. There are also 4 processes: 1-2 is an isochoric process, the working fluid absorbs heat from regenerator material; 2-3 is an isothermal process, the working fluid is compressed and releases heat to the heat sink (hot end); 3-4 is an isochoric process, the working fluid releases heat to the regenerator material; 4-1 is an isothermal process, the working fluid expands and absorbs heat from the cold end. As the working fluid is compressed at high temperature, and expands at low temperature heat is transferred from a low temperature level to a high temperature level and the cycle needs to absorb mechanical work from the environment.

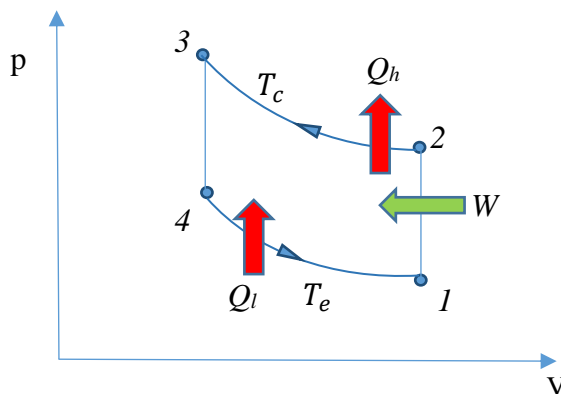
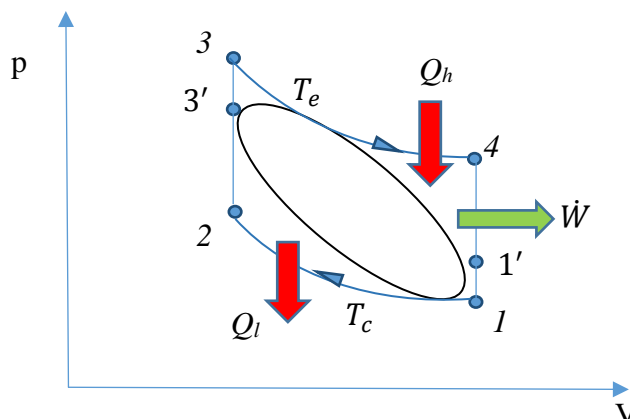


Figure 2.6 Reversed Stirling cycle

### 2.1.3 Real Stirling engine cycle

In reality, the piston and the displacer of the Stirling engine move continuously, in a sinusoidal movement. The real Stirling cycle is elliptical like the inner ellipse in the Figure 2.7(a). In addition, due to the finite time heat transfer and finite heat transfer area of the regenerator, the regenerative processes in Figure 2.7 (process 2-3 and 4-1) are not perfect. In process 2-3, the working fluid cannot arrive at state 3, and it can only arrive at state 3' ( $T_{e'}$ ), therefore the working fluid needs to absorb supplementary heat from the heater during 3'-3 process; similarly, in process 4-1, the working fluid cannot arrive at state 1, and it can only arrive at point 1' ( $T_{c'}$ ), therefore the working fluid releases heat to the cooler during 1'-1 process too.



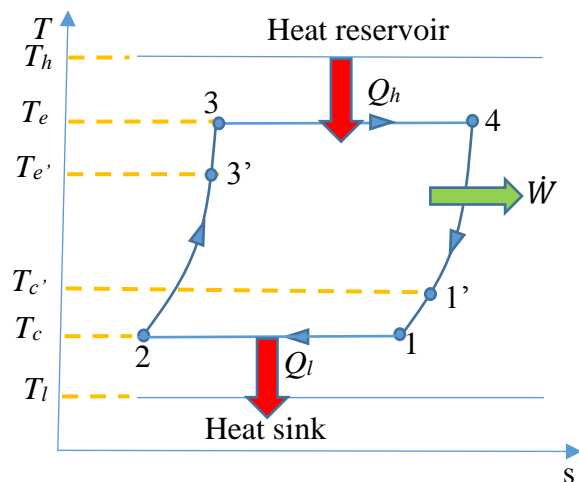
(a) *PV* diagram(b) *T-s* diagram

Figure 2.7 Real Stirling cycle

### 2.1.4 Stirling engine configurations

The Stirling engine can be divided into 3 types based on the arrangement: Alpha type, Beta type, and Gamma type, which can be seen in Figure 2.8. In Alpha type Stirling engine, there are two working pistons; in the Beta type Stirling engine, the piston and the displacer are in the same cylinder; in the Gamma type Stirling engine, the piston and displacer are in the separate cylinder.

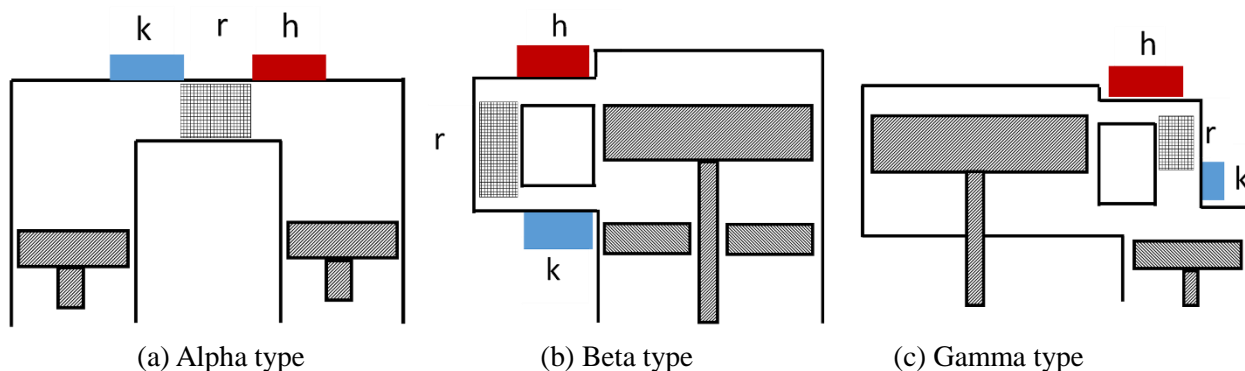


Figure 2.8 Three type of Stirling engine

The Stirling engine can be divided also into crank-connecting-link Stirling engine and free piston Stirling engine, based on the mode of crank-connecting. Figure 2.9 shows a typical Beta type crank-connecting-link Stirling engine. It consists of piston, displacer, heater, cooler,

regenerator, rhombic drive mechanism, compression and expansion space. The advantage of this crank-connecting-link type Stirling engine is that the phase shift between piston and displacer can be easy to maintain. The disadvantage of this kind of Stirling engine is that the mechanical friction loss is high especially for high frequency. The output power can be delivered by piston's expansion. Figure 2.10 shows a typical Beta type free piston Stirling engine with an linear alternator. It consists of piston, displacer, heater, cooler, regenerator, spring flexures, and linear alternator. In free piston Stirling engine, there is no crank-connecting-link, the displacer and piston are connected with the cylinder by spring flexures. When the engine runs stably, the displacer and piston can form a stable phase shift. The advantage of free piston Stirling engine is that the friction loss is low compared with the crank-connecting-link type one, and can run at very high frequency. The disadvantage of this kind of free piston Stirling engine is that the phase shift between piston and displacer is difficult to maintain at a predicted value.

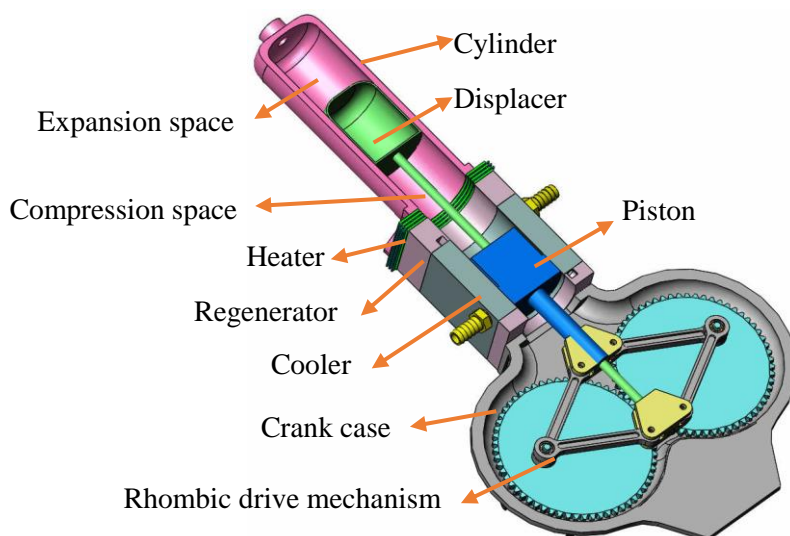


Figure 2.9 Crank-connecting-link Stirling engine [5]

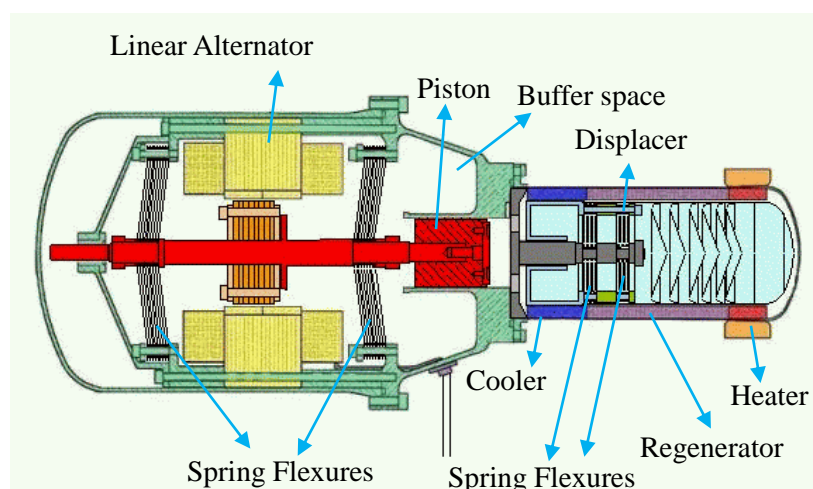


Figure 2.10 Free piston Stirling engine [6]

In some conditions, in order to increase the output power, and save the volume occupied by the engine, double-acting Stirling engine may be used. Figure 2.11 shows the typical double-acting Stirling engine with three cylinders [4]. With three cylinders, the phase angle between piston motion is  $360/3=120^\circ$ . In other systems, the number of cylinders may be three, four, five or six etc. depending on the practical requirement.

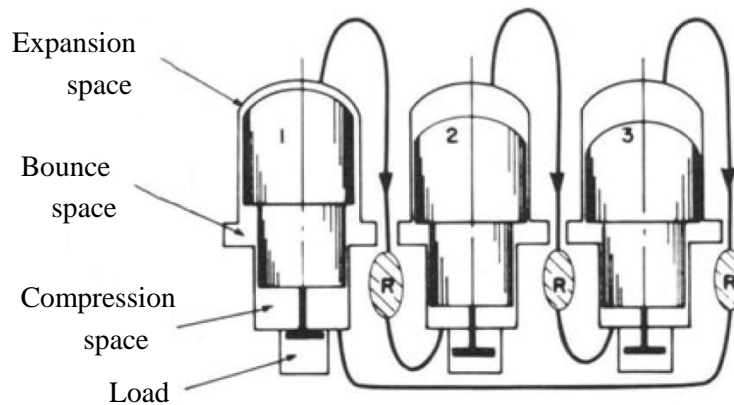


Figure 2.11 Double acting Stirling engine [4]

The Stirling cryocooler can be divided into integral type and split type based on the arrangement. For integral Stirling cryocooler, because that the cold end is connected to the compressor, the vibration of cold end is usually higher than those of a split type, which can limit its application in situations where vibrations are needed to be reduced. Figure 2.12 shows an integral rotary Stirling cryocooler [7]. It consists of piston, displacer (regenerator), crank rod, compression space, expansion space, and dynamic seal. The piston and displacer are connected by the crank rod to maintain a fixed phase shift.

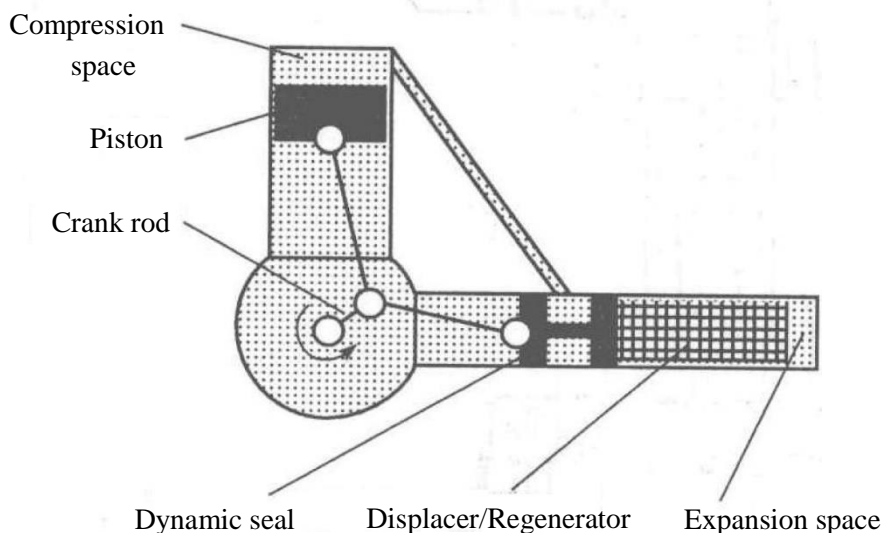


Figure 2.12 Integral rotary Stirling cryocooler [7]

Figure 2.13 shows an integral linear two-stage Stirling cryocooler presented by Wang et. al [8].

It consists of linear compressor, passive oscillator, ambient heat exchanger, displacer spring, 1<sup>st</sup> regenerator, 2<sup>nd</sup> regenerator, 2<sup>nd</sup> cold heat exchanger, compression space, 1<sup>st</sup> expansion space, and 2<sup>nd</sup> expansion space. It can work at 40Hz, and can supply 65W at 30K.

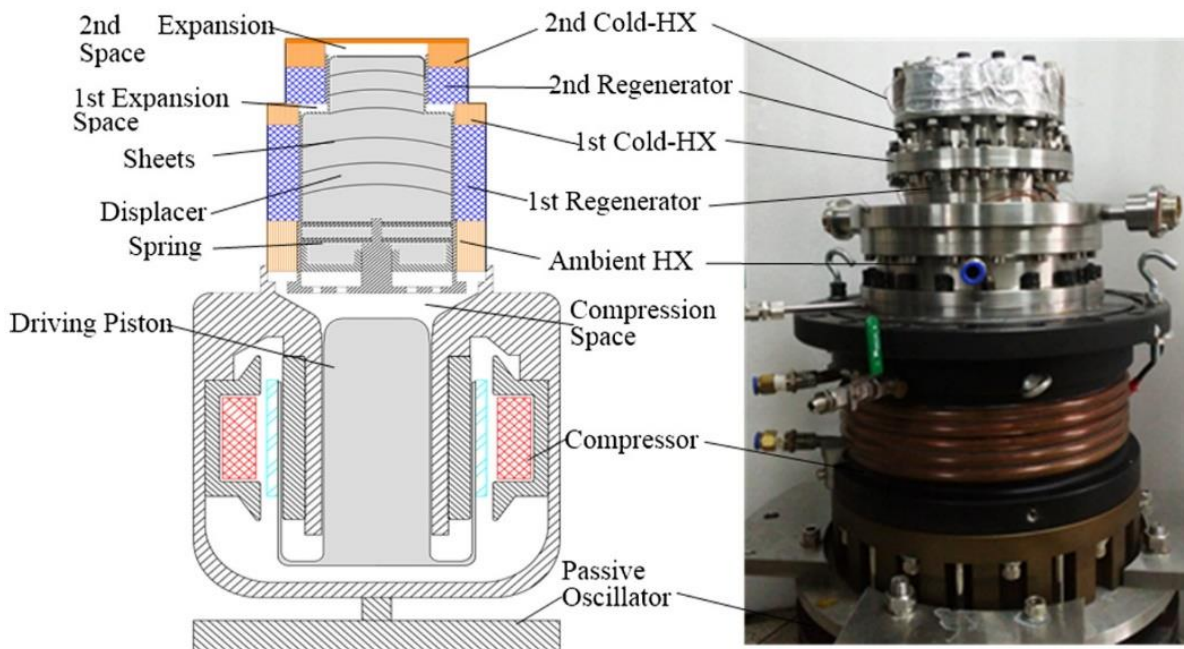


Figure 2.13 Integral linear two-stage Stirling cryocooler [8]

Figure 2.14 shows the split type rotary Stirling cryocooler [7]. The left part represents the compressor and the right part is the expander. It consists of a connecting pipe which connects the compressor and the expander, a compressor piston heat sink, regenerator which is inserted in the displacer, bounce space, and cold end.

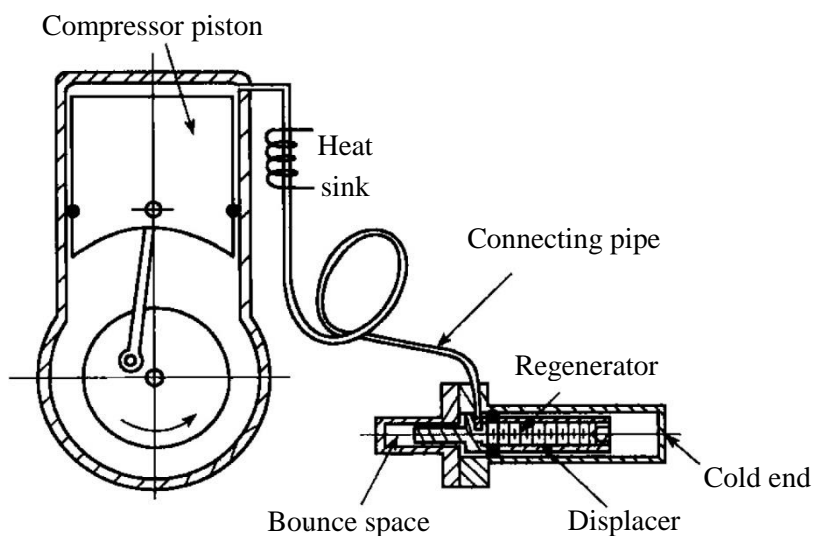


Figure 2.14 Split rotary Stirling cryocooler [7]

Figure 2.15 shows a split linear Stirling cryocooler, which consists of a linear compressor

(piston, coil, magnet, and compression space) and an expander (displacer/regenerator, expansion space, and cold end) [7]. As in split type Stirling cryocooler the expander and compressor are separated and only connected by the flexible connecting pipe, the cold end of the expander is far away from the vibration source (compressor). As a result, we can avoid or reduce effect of compressor vibration on the cold end. The disadvantage of this type of Stirling cryocooler is the added connecting pipe which brings added dead volume and fluid viscosity loss.

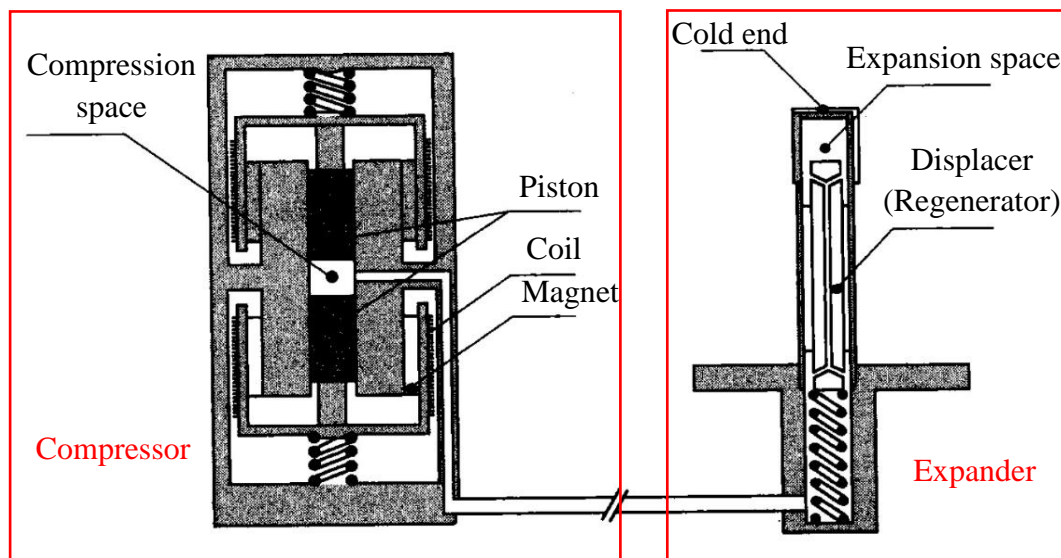


Figure 2.15 Split linear Stirling cryocooler [7]

### 2.1.5 Stirling engine applications

As an external combustion engine, Stirling engine can use multitudinous energy sources, from low quality level energy to high quality level energy, therefore it can use the solar energy, waste heat etc. Figure 2.16 shows the solar powered dish Stirling engine. The concave mirror concentrates the sunlight onto the hot end of the Stirling engine, and thus the Stirling engine can output power or electricity.



Figure 2.16 Solar powered dish Stirling engine

Figure 2.17 shows the Stirling engine used in the Air Independent Propulsion (AIP) system of submarine. The Stirling engine powered AIP system has advantages such as: low mechanical noise, low vibration, and convenience to discharge the exhaust gas. It has been used by countries including Sweden, Denmark, Japan, and Singapore etc.

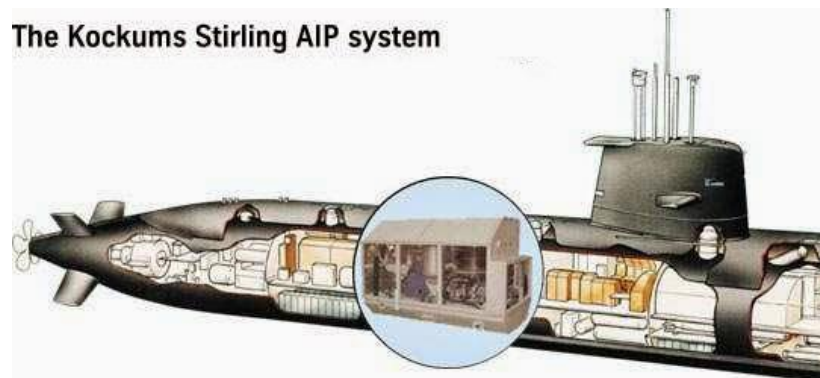


Figure 2.17 Stirling engine used in a submarine

Fig 2.18 shows the Advanced Stirling Radioisotope Generator with two dual-opposed Stirling Convertors, used in the space area [9]. The Advanced Stirling Radioisotope Generator has very high power conversion efficiency making it attractive for future Radioisotope Power Systems (RPS) in order to make best use of the low plutonium-238 fuel.

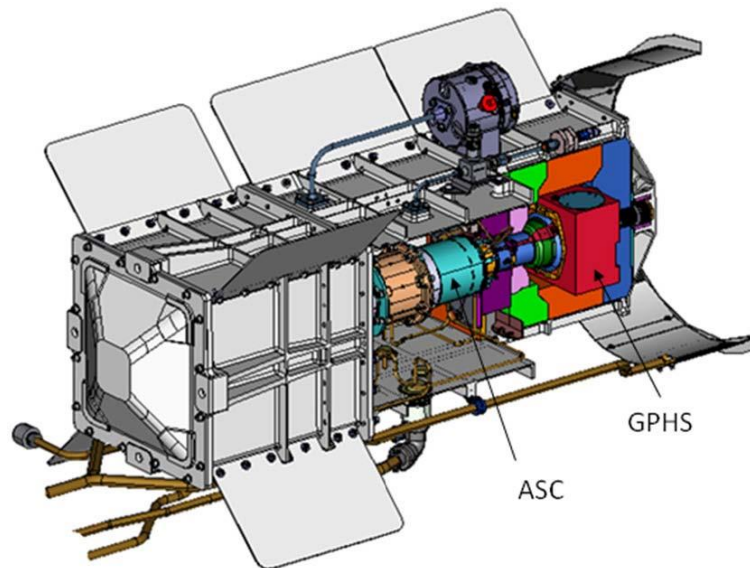


Figure 2.18 Advanced Stirling Radioisotope Generator (ASRG) with two dual-opposed Advanced Stirling Convertors (ASCs) [9]

In addition, the Stirling engine can be used for biomass fuel and Combined Cooling Heating and Power (CCHP) system. Figure 2.19 shows the Stirling engine using biomass produced by Okofen company, which can convert the raw wood into electricity [10]. Figure 2.20 shows a schematic diagram of the CCHP system with utilization of exhausted heat from Stirling engine [11]. It consists of a Stirling engine with natural gas as the primary energy demand, and of a generator for power production with an absorption refrigeration system that works also as a water chilling and heating unit.



Figure 2.19 Stirling engine using biomass [10]

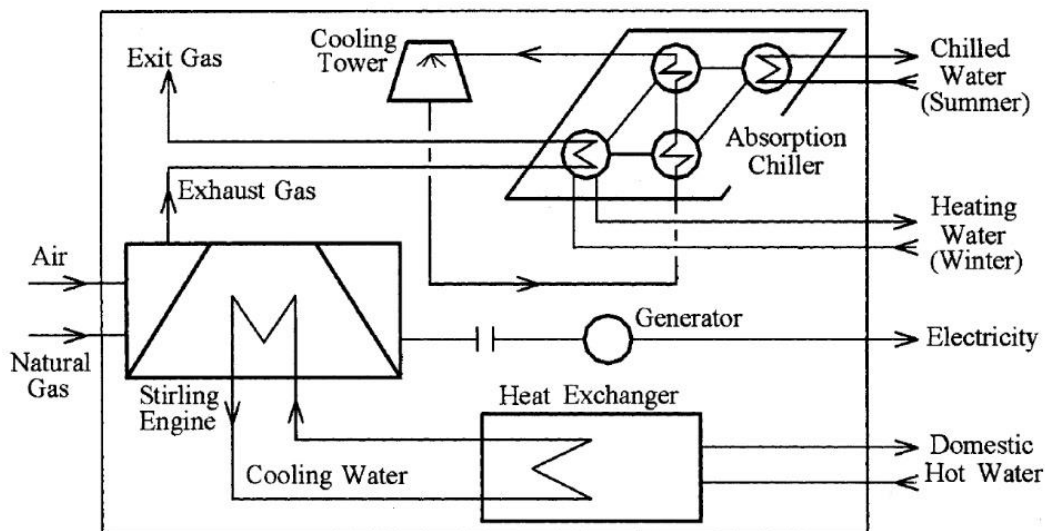


Figure 2.20 Schematic diagram of the CCHP system with utilization of exhausted heat from Stirling engine [11]

In military field, Stirling cryocooler can be used for infrared detector cooling in the night vision, guiding system of missiles, and space detector. The Figure 2.21 shows the seeker in the missile, where Stirling cryocooler can be used to cool the infrared detector.

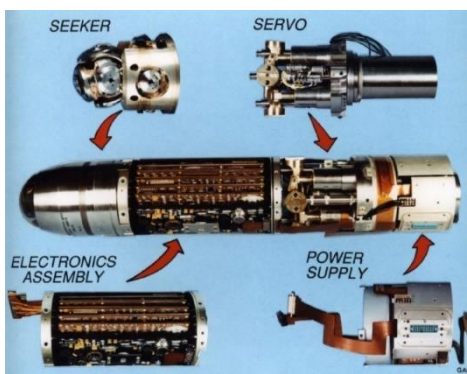


Figure 2.21 The seeker in the missile

In civil field, it also can be used to cool electronic components, to increase the sensitivity of sensors, reduce their parasitic current and the required electrical power. In medical field, with the development of Nuclear Magnetic Resonance Imaging (NMRI) technology which can be seen in Figure 2.22, it's more and more widely used in imaging of the internal tissue of human and improves the process in medical science, neurophysiology, and cognitive neuroscience. In the NMRI there is a superconducting coil, which need to be maintained at about 10K level and can use the Stirling cryocooler to deal with it.



Figure 2.22 NMRI system

In industry field, the Stirling cryocooler can be used for the cryocondensation pump, which can be seen in Figure 2.23. With the development of electronic technique, semiconductor industry, and spatial simulation technique, the requirement for ultra clean operating environment is more and more urgent. Electronic industry, vacuum coating technology, especially semiconductor microelectronics technique and integrated circuit technique require the vacuum environment without oil. The traditional vacuum with lubricating oil pump cannot meet the non-oil and ultra clean demand. The cryocondensation pump can concentrate and absorb the gas on the low temperature surface in the vacuum system, as a result the vacuum system can attain a very high vacuum degree.



Figure 2.23 Cryocondensation pump

In scientific research field, such as the Large Hadron Collider in Figure 2.24 used in the high-energy physics, the high-intensity magnetic field needs the superconducting coil to supply it. Due to that the superconducting coil reveal superconducting characteristics in cryogenic environment, Stirling cryocooler can be used widely.

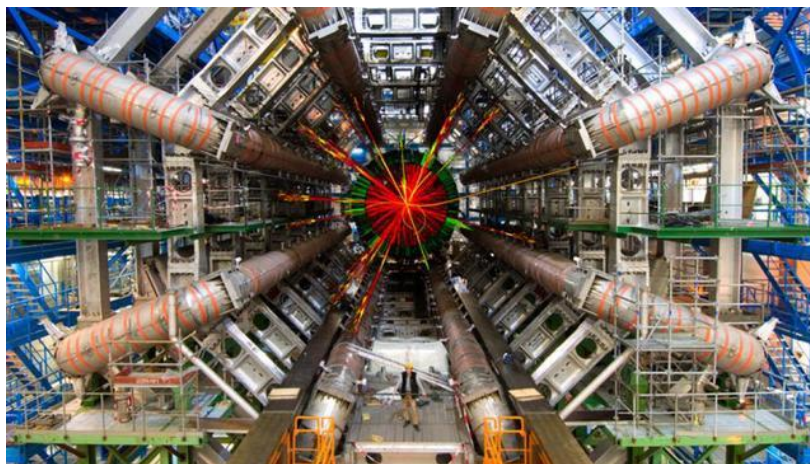


Figure 2.24 Large hadron collider

The performance of Stirling engine is strongly dependent on geometrical and physical parameters such as dimensions, heat transfer coefficients, heat source temperatures and regenerator characteristics. Predicting the performance of an SE is important for the design of the engine. The ideal Stirling cycle has been already studied by several researchers; however the mechanical work provided by a real SE is far from the ideal Stirling cycle. In the past decades years, many researchers and scientists have studied the Stirling engine numerically or experimentally.

Among theoretical and numerical studies of Stirling engine presented in the literature, simulation models have different complexity levels: first order, second order and third order analysis. First order analysis, such as for example [12-14], is a 0-D model to predict the performance using experimental coefficients. The second order analysis leads to mechanical power calculation considering an engine divided into several volumes and taking into account piston motion [1, 15, 16]. Several researchers have modified the basic isothermal and adiabatic models, in order to better simulate the engine performance [17-19]. The third order method is the most accurate analysis, as all losses are coupled and performance is simulated using Computational Fluid Dynamics (CFD) codes. Among these methods, the CFD method is the most complex one, consuming intensive computing resource and calculating time [20]. Results of a 0-D adiabatic analysis [21], built on Matlab/Simulink, were compared with those of several 1-D models which take several energy losses into account. It was shown that 0-D model overestimates the power but keeps its interest because of its simplicity, easy adaptability into a global model of a more complex system, and reduced computing time. Nevertheless, the 0-D model was suggested to add empirical correlations, which contain coefficients according to experimental results, to estimate the total power losses.

## 2.2 Model and experimental studies of Stirling engine

First order analysis predict the performance using experimental coefficients or by doing experimental test.

Senft. has studied the low temperature difference Stirling engine [22, 23], and optimized the

geometrical parameter of Stirling engine for shaft work. He presents a solution to finding the piston-to-displacer swept volume ratio and phase angle which will give the maximum brake output for a given total swept volume, given temperature extremes, a given mean operating pressure, and a given engine mechanism effectiveness [24].

Finkelstein T. has investigated the gas particle trajectories in Stirling engine [25]. Costea et al. have studied the effect of irreversibilities on solar Stirling engine cycle performance [26]. Chang et al. have studied the effect of gap flow on shuttle heat transfer between displacer and cylinder [27], and found that the gap flow does affect the shuttle phenomena when the inertial force in the oscillating flow is relatively significant over the viscous force. Thomas and Pittman evaluated different correlations for the flow friction factor and heat transfer of Stirling engine regenerators [28] including the Oscillating-Flow Regenerator Test Rig data collected by Gedeon and Wood [29]. Kaushik and Kumar have used finite time thermodynamic method to optimize the power output and the corresponding thermal efficiency of irreversible Ericsson and Stirling heat engine, including the finite heat capacitance rates of external fluids in the heat source and heat sink reservoirs, regenerative heat losses, direct heat leak losses, finite regeneration processes time and real hot and cold side heat exchangers [30]. Petrescu et al. have used Direct Method to evaluate the irreversible Stirling engine cycles with finite speed, and the results predicted by this analysis are in good agreement with the actual engine performance data of 12 different Stirling engines over a range of output from economy to maximum power [12]. Martaj and Grosu have exegerically analyzed and optimized the Stirling engine [31] using exergy approach. 1<sup>st</sup> order model was developed and completed with exergy analysis [32]. Esposito et al. have studied the efficiency at maximum power of low-dissipation Carnot engines, performing finite time Carnot cycles between a hot and a cold reservoir at temperatures  $T_h$ , and  $T_c$ , respectively [33]. For engines reaching Carnot efficiency  $\eta_c = 1 - \frac{T_c}{T_h}$  in the reversible limit (long cycle time, zero dissipation), it's found that in the limit of low dissipation that  $\eta^*$  is bounded from above by  $\frac{\eta_c}{2-\eta_c}$  and from below by  $\frac{\eta_c}{2}$ . Formosa and Despesse have provided an analytical model for Stirling cycle machine preliminary design, which takes into account the heat losses and mechanical effectiveness [34].

Hu et al. have evaluated the thermal efficiency and energy conversion of thermos-acoustic Stirling engine [35]. Costane M. Invernizzi has studied the Stirling engine using working fluids including helium (He), hydrogen (H<sub>2</sub>), nitrogen (N<sub>2</sub>), argon (Ar), carbon dioxide (CO<sub>2</sub>), trifluoromethane (HFC-23, CHF<sub>3</sub>), ethane (CH<sub>6</sub>), sulfur hexafluoride (SF<sub>6</sub>), pentafluoroethane(HFC-125,CF<sub>3</sub>- CHF<sub>2</sub>), and difluoromethane(CHF<sub>2</sub>), with strong real gas effects [36]. Petrescu et al. have developed a methodology of computation, design and optimization of solar Stirling engine power plant using hydrogen/oxygen fuel cell [37]. Iskander Tlili has evaluated endoreversible Stirling heat engine at maximum power conditions with finite time thermodynamics method [38]. Formosa et al. presented a network model to simulate the periodic behavior of a double acting free piston type Stirling engine and compared with the experimental results of three-phase low temperature differential double acting free membrane Stirling engine [39].

Ahmadi et al have employed a new generation of intelligent models named “least square support

vector machine (*LSSVM*)” to predict the output power and shaft torque of Stirling engines which had the merit of low degree of uncertainty and high precision [40]. Ding et al. analyzed the power and efficiency performance of a Stirling engine and optimized the engine with heat resistance, heat leakage, regeneration loss and mechanical losses by using the combination of Senft’s mechanical efficiency model with finite time thermodynamics analysis method, where the analytical formulae for indicated power, shaft power, thermal efficiency and brake thermal efficiency for the Stirling engine were derived by assuming that the heat transfer at finite temperature difference between the heat reservoirs and the working fluid obeys the linear phenomenological heat transfer law [41].

Hooshang et al. optimized Stirling engine design parameters using Multi-Layer Perceptron (*MLP*) neural networks, with design variables as phase angle, displacer stroke and working frequency of ST500 Stirling engine [42]. Petrescu et al. studied the possibility of unifying the two branches of the irreversible engineering thermodynamics, namely finite physical dimensions thermodynamics (*FPDT*) and finite speed thermodynamics (*FST*), aiming to take into account their benefits and successes and to eliminate as much as possible their disadvantages [14].

## **2.2.1 Second order**

The second order analysis leads to mechanical power calculation considering an engine divided into several volumes and taking into account piston motion. Isothermal mode, adiabatic model, polytropic model, and their combinations are usually used in the second order.

### **2.2.1.1 Isothermal model**

In isothermal model the compression and expansion volumes of the engine is usually assumed to be isothermal during the cycle.

Berrin Erbay and Yavuz have analyzed the Stirling heat engine at maximum power condition, and found the compression ratio at maximum power density [43]. Martaj et al. have used the zero dimensional numerical model for thermodynamic study of a Low Temperature Difference Stirling engine at steady state operation [44, 45]. Puech and Tishkova have thermodynamic analyzed a Stirling engine including regenerator dead volume by isothermal model, and found that engine efficiency with perfect regeneration doesn’t depend on the regenerator dead volume but this dead volume strongly amplifies the imperfect regeneration effect [46]. Rochelle and Grosu have analyzed and optimized the exo-irreversible Schmidt cycle with imperfect regenerator for the 3 classical types of Stirling engine (alpha type, beta type, gamma type) [47]. Li et al. optimized solar powered Stirling heat engine with finite time thermodynamics which considering finite-rate heat transfer, generative heat losses, conductive thermal bridging losses and finite regeneration processes time [48]. Cheng and Yang have optimized geometrical parameters for Stirling engines based on theoretical analysis and shown that gamma type Stirling engine is most capable of operating with low temperature difference [49].

Reséndiz-Antonio and Santillán have introduced a isothermal mathematical model for a beta

type Stirling engine to investigate the thermodynamic performance of the Stirling cycle [50].

### **2.2.1.2 Adiabatic model**

In an adiabatic model the compression and expansion volumes are supposed to be adiabatic during the cycle. Timoumi et al. have optimized the GPU-3 Stirling engine using the second-order model which includes thermal losses [51]. Parlak et al. have performed a thermodynamic analysis of a gamma type Stirling engine by using a quasi-steady flow [52]. Ahmadi et al. have optimized the Stirling engine using genetic algorithm with the process [53-55]. Cheng has theoretically and experimentally studied a 300W beta type Stirling engine [56]. A non-ideal adiabatic model is built and applied to predict the performance of the engine. Engine torque, engine speed and shaft power output are measured under various operating conditions, different working gases (air and helium), various charged pressures and heating temperatures which shows that the shaft power output of the engine is much higher using helium as the working fluid than using air. Araoz et al. have developed a numerical Stirling model that could be integrated into combined heat and power schemes for the overall techno-economic analysis of these systems, considering adiabatic working spaces, isothermal heat exchangers, dead volumes, imperfect regeneration, mechanical pumping losses due to friction, limited heat transfer and thermal losses on the heat exchangers [57]. Babaelahi and Sayyaadi have developed a new numerical thermal model for predicting the thermal performance of Stirling engines which considered adiabatic expansion and compression spaces, effect of gas leakage from cylinder to buffer space and shuttle effect of displacer, non-ideal thermal operation of the regenerator, and the longitudinal heat conduction between heater and cooler through the regenerator wall [58]. Mabrouk et al. have developed an analytical model which took into account the pressure gradient in the gap, the gas compressibility and real gas effect to evaluate the displacer gap losses of the clearance between the displacer and cylinder in beta and gamma type Stirling engines [59]. They have shown, taking the GPU-3 Stirling engine for example, that there is an optimum clearance thickness for the total appendix gap losses which include enthalpy pumping and shuttle heat transfer; and there is an optimum frequency for the total appendix gap losses.

Araoz et al. developed and validated a numerical model that represents the performance of a gamma Stirling engine prototype which considered ideal adiabatic working spaces, limited internal and external heat transfer through the heat exchangers, mechanical and thermal losses during the cycle, the crank mechanism effectiveness, and the forced work during the cycle, and showed an acceptable degree of accuracy comparing with the experimental data [60]. Later Araoz et al. have simulated the kinematic Stirling engines using for Combined Heating and Power system based on the developed model [61].

Hosseinzade and Sayyaadi developed a novel thermal model based on the combination of adiabatic analysis and finite speed thermodynamics called *CAFS* (Combined Adiabatic-Finite Speed) which considered the effect of finite speed of piston, pressure throttling in heat exchangers and regenerator and piston's mechanical friction in the basic Simple model and used a new correlation to calculate the regenerator's effectiveness [62]. J. Paul and Engeda developed an ideal adiabatic plus simple heat exchanger model which included the external components such

as the fan, combustor, and preheater and the external heat transfer to the engine heater was modeled using a log-mean-temperature difference for a constant tube surface temperature, and suggested that second order models of Stirling engines need to account for the gradient of the divergence of velocity term in the compressible momentum equation if the mean engine pressure is low enough (less than 3.0 MPa) and the engine speed is high enough (above 30 Hz) [63].

### 2.2.1.3 Polytropic model

In polytropic model, the work gas in expansion and compression volumes evolve a polytropic process during the cycle.

Babaelahi and Sayyaadi have developed a new thermal model (*PSVL*) based on polytropic numerical simulation for Stirling engines which gives a methodology for determining the average polytropic indexes and considers various power and heat losses during the calculation process [64]. Then Babaelahi and Sayyaadi developed a second order model for thermal simulation of Stirling engines based on convective-polytropic heat transfer of working spaces by modifying the *PSVL* model, which assumed an exponential temperature distribution in regenerator and considered various loss mechanisms [65], and get a better accuracy than the *PSVL* model comparing with experimental results of the GPU-3 Stirling engine.

Hosseinzade et al. presented a new closed-form thermal model which called *PFST* (polytropic-finite speed thermodynamics) for the thermal simulation of Stirling engines based on the combination of polytropic analysis of expansion/compression processes and the concept of finite speed thermodynamics (*FST*); therefore compression/expansion works of compression/expansion processes and transferred heat into the heater of Stirling engines were determined based on polytropic analysis, instead of isothermal processes of the ideal Stirling cycle [66]. The calculated work of polytropic processes was corrected to include the effects of internal irreversibilities including pressure throttling in heat exchangers, mechanical friction, and finite motion of the pistons. Output power and thermal efficiency of Stirling engines were calculated as functions of various engine parameters.

### 2.2.2 Third order

The third order method is the most accurate analysis, as all losses are coupled and performance is simulated using Computational Fluid Dynamics (CFD) codes.

Andersen et al. have done numerical study (one-dimension) on optimal Stirling engine regenerator matrix designs taking into account the effects of matrix temperature oscillations [67]. They found that the regenerator matrix temperatures oscillates in two modes: the first mode was oscillation of a nearly linear axial matrix temperature profile while the second mode bended the ends of the axial matrix temperature profile when gas flowed into the regenerator with a temperature significantly different from the matrix temperature. The first mode of oscillation improved the efficiency of the engine but the second mode reduced both the work output and efficiency of the engine. Karabulut et al. have done nodal analysis of a Stirling

engine with concentric piston and displacer, where the inner volume of the engine is divided into 103 cells, which indicated that the heats received from and delivered to the regenerator are not equal to each other and therefore, the ends of the regenerator should be coupled with a heater and a cooler [68]. Dyson et al. have presented a fully converged axisymmetric and three-dimensional simulation of an actual free-piston Stirling engine without considering the thermal non-equilibrium regenerator model [69]. Cheng and Yu developed a numerical model for a beta type Stirling engine with rhombic drive mechanism by taking into account the non-isothermal effects, the effectiveness of the regenerative channel, and the thermal resistance of the heating head, and researched the dependence of the power output and thermal efficiency on the geometrical and physical parameters, involving regenerative gap, distance between two gears, offset distance from the crank to the center of gear, and the heat source temperature [17]. Aksoy and Cinar have analyzed a beta type Stirling engine with rhombic drive mechanism using nodal analysis which used different displacer cylinders (one displacer has smooth inner surface and another has axial slots grooved into the cylinder) [70]. Costa et al. have numerically studied (CFD) the pressure drop phenomena in wound woven wire matrix of a Stirling regenerator over a specified range of Reynolds number, diameter and porosity using a finite volume method (FVM) and developed new correlations applied for the regenerator [71]. Mabrouk et al. proposed an unsteady analytical model to calculate the gas leakage mass flow rate by considering an oscillating flow in the annular clearance and to evaluate the power lost in both locations (clearance between piston and cylinder wall and clearance between displacer and cylinder wall) [72].

Della Torre et al. have applied CFD to the simulation of a Beta-type Stirling machine involving different parameters: regenerator properties, working fluid, mean cycle operating pressure and amount of heat introduced in the machine [73].

Leon Salazar and Chen have developed a compressible CFD code to study the heat transfer characteristics of a beta type Stirling engine with a very simple design and geometry and found that impingement is the major heat transfer mechanism in the expansion and compression chamber, and the temperature distribution is highly non-uniform across the engine at any given moment [74]. In addition, the results, especially the rates of heat transfer, are quite different from those obtained by a second-order model and the variations of heat transfer rates are much more complicated than the simple variations returned by the second-order model.

Solmaz and Karabulut have devised a beta type lever driven Stirling engine mechanism and its thermodynamic performance using nodal method was compared with the rhombic drive engine's performance, which showed that the work generation of the lever driven engine was higher than the rhombic drive engine on the same working conditions, the thermal efficiency of the lever driven engine was lower than that of the rhombic drive engine under the equal charge pressure, and the efficiency of lever driven engine is equal or higher than that of rhombic drive engine under the equal mass of working fluid [75].

Chen et al. numerically studied the effects of moving regenerator to the performance of a beta type Stirling engine using CFD code, which found that the moving regenerator acts as an effective thermal barrier between the expansion and compression chambers, resulting in significant reduction in rates of heat input and output and promotion on engine's indicated power; however, the porous medium in the moving regenerator also increases pressure loss, and

hence slightly reducing the net engine power; and overall engine performance, in terms of net output power and efficiency, is largely improved by the introduction of the moving regenerator [76].

Aksoy et al analyzed the effect of rhombic drive and crank drive mechanisms on the performance of a beta type Stirling engine with nodal Fortran code and showed that the specific power and thermal efficiency of the rhombic-driven engine was greater than the crank-driven engine at optimum charge pressure values [77]. Hooshang et al. presented a dynamic model using a third order thermodynamic analysis code of a gamma-type Stirling engine and validated by experimental results which can be used for design process of a proper close-loop load controller [78].

Pfeiffer and Kuehl presented a new optimization procedure for the design of the appendix gap in Stirling engines considering unsteady flow velocity and temperature profiles, whose variables included the gap width, a conical design with an expansion towards the open end, and a modification of the seal design, reducing the volumetric displacement and the almost isothermal buffer volume at the bottom end of the gap etc. [79]. Sauer and Kuehl introduced a one-dimensional differential models for Stirling cycle machines including a differential simulation of the appendix gap [80].

Scott et al. have used the CFD to predict the heat exchange in heat head of a Stirling engine powered by radioisotope heat source [81], and to analyze the pressure drop by the porous-media model of the commercial CFD code [82]. Terry et al. has analyzed the heat loss in heat head of the Stirling engine by the CFD code [83].

### **2.2.3 Multi-objective optimization**

In some conditions, researchers want to get the maximum output power, thermal efficiency, and minimum entropy generation which needs multi-objective optimization method. Duan et al. proposed a mathematical model based on thermodynamic analysis of Stirling engine considering regenerative losses and internal irreversibilities [84]. Power output, thermal efficiency and the cycle irreversibility parameter of Stirling engine are optimized simultaneously using Particle Swarm Optimization (PSO) algorithm, which is more effective than traditional genetic algorithms. Temperatures of the working fluid both in the high temperature isothermal process and in the low temperature isothermal process, dead volume ratios of each heat exchanger, volumes of each working spaces, effectiveness of the regenerator, and the system charge pressure have been defined as the decision variables.

Toghyani et al. multi-objective optimized the GPU3 Stirling engine using third order analysis with four decision variables including the temperature of heat source, stroke, mean effective pressure, and the engine frequency, and with three objectives including maximum efficiency, maximum output power and minimum pressure drop, and used three decision-making technique including *TOPSIS*, *LINMAP*, and *Fuzzy* method to get the optimum parameters [85].

### **2.2.4 Combined heat and power generation**

Dorer and Weber simulated the energy and CO<sub>2</sub> emissions performance assessment of

residential micro-cogeneration systems with dynamic whole-building and different cogeneration technologies including natural gas-fueled solid oxide and polymer electrolyte membrane fuel cells, Stirling and internal combustion engines [86]. Rogdakis et al. have analyzed numerical and experimentally the thermal performance of the Combined Heating and Power (CHP) Solo Stirling engine V161 unit and found that the Stirling unit is very promising and quite adequate for CHP systems [87]. Ulloa et al. analyzed the behavior of a Stirling engine micro-cogeneration system that supplies a sailing boat and the corresponding weather conditions and sea surface temperatures (SST) along fifteen European ports [88]. Cacabelos et al. developed a dynamic model of a commercial micro-combined heat and power (mCHP) unit and analyzed its dynamic behavior when the engine was running at different mass flow inputs [89].

L. Grosu et al have studied the geometry of Stirling engine used for domestic micro cogeneration (The three thermodynamic model were developed: Direct Method from Finite Speed Thermodynamics, isothermal model, and adiabatic model) and the results were compared with experimental results [19]. Damirchi et al. designed, fabricated and evaluated a gamma type Stirling engine to produce electricity from biomass for the micro-CHP system, and confirmed the fact that Stirling engines driven by temperature of biomass gases are able to achieve a valuable output power [90, 91].

## **2.2.5 Low temperature difference Stirling engine**

In the renewable energy application field, the low temperature difference Stirling engine is usually used.

Kongtragool and Wongwises have reviewed the solar-powered Stirling engine and low temperature differential Stirling engine and showed that Stirling engines working with relatively low temperature air are potentially attractive engines of the future, especially solar-powered low temperature differential Stirling engines with vertical, double-acting, gamma-configuration [92] and have provided a theoretical investigation on the optimum absorber temperature of a once-reflecting full conical concentrator for maximizing overall efficiency of a solar-powered low temperature difference Stirling engine [93]. Later they have provided an experimental investigation on the performance of a twin power piston, low temperature differential, and gamma-configuration, Stirling engine powered by a solar simulator [94, 95]. Variation of engine torque, shaft power, and brake thermal efficiency with engine speed and engine performance at various heat inputs are presented. Rochell and Grosu designed a LDT Gamma Stirling engine and tested it using a new engineer approach taking into account engineer constraints as maximum volume, maximum pressure and rotation speed [13, 47, 96]. Tavakolpour et al. have simulated, constructed, and tested a two-cylinder low-temperature difference solar Stirling engine powered by a flat-plate solar collector without regenerator, and obtained the optimum parameters such as compression ratio, piston stroke, piston diameter, displacer stroke, and displacer diameter [97]. Tlili et al. presented a technical innovation, with study of solar power system based on the Stirling dish technology and design considerations to be taken in designing of a mean temperature differential Stirling engine for solar application [98]. Kraitong and Mahkamov have optimized a low temperature difference solar Stirling

engine using genetic algorithm taking into account hydraulic and mechanical losses in the engine's working process with the strokes of displacer and piston, displacer diameter, thickness of the regenerator as variables [99].

Yoshitaka Kato studied a low temperature differential Stirling engine experimentally using flat plates as heat exchangers, and get the polytropic exponents variation with crank angle [100].

### **2.2.6 Free piston Stirling engine**

For free piston Stirling engine, due to its compactness and high running frequency, there are also a number of researchers studied it experimentally and analytically. F. de Monte and G. Benvenuto have studied the stable operation and optimization of free piston Stirling engine [101, 102]. Rogdakis et al. have studied thermodynamically the optimization of stable operation of free piston Stirling engines using the isothermal model [103]. Boucher et al. presented the theoretical study of the dynamic behavior of a single-acting free piston Stirling engine coupled with an asynchronous linear alternator in order to determine the operating frequency and electrical power output [104]. Later Boucher et al. optimized a dual free piston Stirling engine integrating one piston and two displacers placed in a symmetrical way compared to the piston to improve the stability of the machine coupled with an asynchronous linear alternator, which takes into account the non-linear dissipative effects of the fluid and the electromagnetic forces [105]. F. Formosa developed a semi-analytical dynamic model of free piston Stirling engine to define the thermal variables that are used in the dynamic model for evaluating the kinematic results which used a coupled iterative strategy [106]. Halit Karabulut has developed the dynamic model of a free piston Stirling engine working with closed and open thermodynamic cycles derived and numerically solved for an optional pair of the piston and displacer masses, and optimized the stiffness of the displacer spring and static positions of the piston and displacer [107].

Bégot et al. presented a stability analysis of a free piston Stirling engine of which the stability of the machine was studied by the observation of the eigenvalues of the model matrix [108]. The results showed that most parameters that are beneficial for machine power seem to induce irregular mechanical characteristics with load, suggesting that self-sustained oscillations could be difficult to maintain and control. Formosa and Fréchette explores the scaling effects for free piston Stirling engines which are known for their simple architecture and potentially high thermodynamic performances and proposed a simple model which allows the design of the geometrical parameters of the heat exchangers, the regenerator and the masses of the pistons [109]. Johannes Matthias Strauss studied the direct piston displacement control of free piston Stirling engines to control the engine according to preferred criteria, e.g. maximum power conversion or efficiency which independently controls both the displacement of the displacer and the power piston in real time [110].

Ivan Niell Deetlefs has designed and manufactured an experimentally testable free-piston Stirling engine, including a linear electric generator; developed and validated a theoretical simulation model; identified problem areas pertaining to its manufacture; and finally assessed the work undertaken, to lay out the groundwork for the future development of a 3 kW FPSE

suitable for incorporation in a solar Stirling dish power generator [111]. Kwankaomeng et al. presented stability and performance investigation of free-piston Stirling engine considering isothermal model in the simulation, obtained dynamic motion of engine pistons such as the displacer and the power piston, and gave the optimum parameters such as engine specifications, engine characteristics and working conditions to yield the maximum efficiency and reliability [112]. Ghozzi and Boukhanouf proposed a new design of free piston Stirling engine prototype for small-scale power generator, such as solar dish Stirling engine using a special bellows with high reliability and long life mechanical springs displacer and power piston and analyzed by Ideal Adiabatic and Simple analysis [113]. Maxwell briggs studied the method to improve the free piston Stirling engine power density, by designing an engine for sinusoidal motion being forced to operate with both second and third harmonics, resulting in a maximum piston power increase of 14% [114]. Louis Hoogenhout Joubert designed and optimized a linear oscillatory electric generator for application in free piston Stirling engines [115]. Loktionov et al. proposed and tested a solar-powered free-piston stirling module concept for a moon base [116]. Park et al. describes the continuing effort to analysis and design on dynamic and electrical behavior of gamma-type free piston Stirling engine/generator with dual-opposed linear generator for domestic micro-CHP (Combined Heat and Power) system, and with one displacer and two power piston which are supported by flexure springs [117].

Sim and Kim presented the performance-prediction methodology using a linear and nonlinear dynamic analytical model considering the external load of free piston Stirling engine where linear analyses was used to predict the operating point of the engine using the root locus technique and nonlinear analysis was used to predict the amplitude of pistons by performing numerical integration considering both the linear and nonlinear damping terms of the external load [118]. Salem Ghozzi and Rabah Boukhanouf presented design and preliminary testing results of a free piston Stirling Engine prototype operating at low temperature heat sources with the displacer using flexure bellows as a mechanical supporting spring and as a working fluid seal and with the power piston, on the other hand, being made of a planar elastomer material in the shape of a disk with a suitable mechanical elasticity, rigidity, and thermal properties to support the range of operating temperatures [119]. Hassan et al. proposed a vibration control system of free piston Stirling engine with an electromagnetic active tuned mass damper which features a zero-placement technique that utilizes both relative or absolute position and velocity feedback from the system response as well as a feedthrough measurement of the disturbance frequency that is used to determine the position gain online [120]. Jang et al. introduced a design method for selecting the physical parameters of a free piston Stirling engine where the dynamics of the engine were described in the form of a transfer function including the inherent feedback mechanism [121].

Dmitriy A. Dobrodomov presented methodological approaches used in development of free-piston Stirling engines, which was based on Integrated Design Methodology (*IDM*), which included several interrelated stages arranged in a fixed sequence to achieve a satisfactory result [122]. Tavakolpour-Saleh et al. described a novel design approach of the free piston Stirling engines based on multiple-scale perturbation method [123]. And a simulation study was carried out to investigate how much the engine frequency, strokes of pistons, and phase angle of the FPSE are sensitive to the variation of gas temperature. Besides, the effect of changes in the

engine design parameters such as mass and stiffness of the pistons on the output power of the FPSE was also studied using simulation. Zare and Tavakolpour-Saleh introduced frequency-based design of a free piston Stirling engine using genetic algorithm including mass and stiffness of power and displacer pistons and cross-sectional area of the displacer rod are considered as unknown variables [124].

Dobbs et al. presented the maturing technologies for Stirling space power generation which used free piston Stirling engine [125]. Wilson et al. have presented a breadboard active vibration reduction systems, or “balancers”, implemented on the Advanced Stirling Converter, which can reduce the dynamic disturbance forces created by the power piston and displacer internal moving components of a single operating converter to meet spacecraft requirements for induced disturbance force [126]. The active vibration reduction systems included a linear motor, a motor mount, and a closed-loop controller able to balance out the transmitted peak dynamic disturbance using acceleration feedback, and showed excellent result (the transmitted force was reduced to 2 percent of the total unbalanced force by actively balancing).

Berchowitz and Kwon presented a small demonstrator inline four cylinder alpha type free piston Stirling engine and studied it theoretically and experimentally [127]. Wilson et al. investigated experimental and computational analysis of unidirectional flow through the free piston Stirling engine heater head [82]. Hoshino et al. have designed and manufactured a prototype of free piston Stirling converter for household use [128]. Qiu et al. have designed and tested the spring flexure for free piston Stirling converters, and provided some general design criteria when designing a new flexure including axial stiffness, radial stiffness, subassembly rocking modes, and flexure arm modes [129].

## **2.2.7 Experimental study and other innovation in Stirling engine**

Koester et al. have used experimental method to study the oscillating flow loss in Stirling engine heat exchanger [130]. Tanaka et al. have studied the flow and heat transfer characteristics of the Stirling engine regenerator in an oscillating flow [131]. They have obtained a new relationship between regenerator reheat loss and regenerator size including the mesh diameter and the length of the regenerator from the analysis of the experimental data.

Gedeon D. and Wood J.G. have researched the oscillating flow including friction factor, Nusselt number, axial conduction ratio, and overall heat flux ratio, in the regenerator in Stirling engine [29] using experimental method with a number of wire mesh and metal felt and a range of porosities. Zhao and Cheng have investigated the oscillating pressure drop through a woven-screen packed column subjected to a cyclic flow [132]. Isshiki et al. have studied the flow resistance and heat transfer of regenerator wire meshes of Stirling engine in oscillatory flow experimentally [133]. They have found that the friction factor in a decelerating period is higher than that in an accelerating period under the condition that both Valensi number and maximum Reynolds number exceed certain values. Aksoy and Karabulut have tested a Fresnel/Stirling micro solar energy conversion system, with different displacer cylinder cavities materials: aluminum, cooper and stainless steel [134]. Costa et al. presented both preliminary experimental and numerical studies (finite volume method based on CFD) of pressure drop and

heat transfer characteristics of Stirling engine regenerators [135]. Gheith et al. have studied a new phenomenon (different temperature between both regenerator sides) causing the thermal energy dissipation in a Gamma type Stirling engine, and the factors which influence on this new phenomenon including heating temperature, initial filling pressure, cooling water flow rate and operation time [136]. Kwankaomeng et al. have investigated on stability and performance of a free piston Stirling engine analytically and experimentally, and given the optimum parameters such as engine specifications, engine characteristics and working conditions to yield the maximum efficiency and reliability [112].

Aksoy et al. have studied the performance of a beta type Stirling engine experimentally, which works at relatively lower temperatures using 400 W and 1000 W halogen lamps as a heat source and helium as the working fluid, and compared the experimental results with the thermodynamic nodal analysis [137]. Féliès et al. have modeled, experimented and optimized a three phase free piston type double acting Stirling engine with the modeling strategy based on a combination of two sub-models: a global thermal model of the engine to deal with heat sources coupling and a detailed equivalent electrical network model which accounts for the gas and mechanical dynamic physics of the engine [138]. With the experimentally validated model, the double-acting free piston Stirling engine was optimized considering three critical parameters: (i) dead volume of the chambers, (ii) natural frequency of the mechanical oscillators and (iii) thermal conduction between hot and cold sides.

Gheith and Aloui et al. dealt with an optimization of a gamma type Stirling engine regenerator [139]. Different materials were experimented (Stainless Steel, Copper, aluminum and Monel 400) and the Stainless steel was the material that best satisfies both two conditions: maximum heat transfer and minimum pressure drop. Five regenerators in stainless steel with different porosities (95%, 90%, 85%, 80% and 75%) were experimented, and the regenerator in stainless steel with porosity of 85% was considered as the most suitable matrix maximizing the Stirling engine performances and minimizing heat and friction losses.

Hachem et al. developed a numerical model to optimize a kinematic Gamma Stirling engine, which included thermal and mechanical losses, studied the influences of three operation parameters (filling pressure (3, 5, 10 bar), hot end temperature (300, 400, 500 °C) and rotation speed (160, 360, 600 rpm)) as well as heat exchangers efficiencies on the Stirling engine performances, and found that for high initial filling pressure, the brake power became more sensitive to the rotation speed and the hot end temperature [140]. Song et al. Studied the heat transfer enhancement in tubular heater of Stirling engine for waste heat recovery from flue gas using steel wool experimentally and showed that the steel wool effectively enhanced the combined heat transfer coefficient on the outer surface of heater tubes; as the porosity of the steel wool was decreased, the combined heat transfer coefficient continued to increase but at a successively slower rate [141]. Glushenkov et al. have proposed the concept of a kind of single-piston Stirling engine [142]. Yang et al. introduced an integrated two-cylinder liquid piston Stirling engine [143].

## 2.3 Summary

In this chapter, the background and history of Stirling engine has been stated. Ideal thermodynamic Stirling cycle and real Stirling engine cycle has been presented. Different types of Stirling engine including Alpha type, Beta type, Gamma type, crank-connecting-link type, free piston type, single-acting type, and double-acting type have been presented and compared. Different Stirling cryocooler including integral type, split type, rotary type, and linear type have been introduced and compared to state their advantages and disadvantages. Then, applications of Stirling engine and Stirling cryocooler in solar energy, submarine, spatial detection, biomass, CCHP system, seeker of missile, NMRI system, cryocondensation pump, and Large Hadron Collider have been introduced.

The previous research on the Stirling engine has been reviewed. Different previous model study including first order, second order, and third order has been summarized. The study of different kind of Stirling engine has been introduced which consists of the low-temperature-difference type, free-piston type, single piston type, double acting type, solar dish type, and the micro combined heat and power system (Micro CHP) type. Previous studies of the different part of the engine such as clearance between piston/displacer and cylinder wall, regenerator, and heater has also been proposed. The model study in this work will be presented in the following chapters.

## References:

- [1] Finkelstein T., Air engines: the history, science, and reality of the perfect engine/Theodor Finkelstein, Allan J. Organ, 2001.
- [2] Qian G., Zhou Z., and Yan S., Principle and design of the Stirling engine. 1987.
- [3] Hargreaves C.M., The Phillips stirling engine. 1991.
- [4] Walker G. and Senft J.R., Free-piston Stirling engines. 1985: Springer.
- [5] Stirling engine. Available from:  
<https://zh.wikipedia.org/wiki/%E6%96%AF%E7%89%B9%E6%9E%97%E5%8F%91%E5%8A%A8%E6%9C%BA>.
- [6] Schifer N.A. and Oriti S.M., Summary of Stirling Convertor Testing at NASA Glenn Research Center in Support of Stirling Radioisotope Power System Development. 2013.
- [7] Chen G. and Tang K., Principle of miniature cryocooler 2010: Science press.
- [8] Wang X., et al., Study on a high capacity two-stage free piston Stirling cryocooler working around 30 K. Cryogenics, 2016.
- [9] Wong W.A., Wilson S.D., and Collins J., Advanced Stirling Convertor Development for NASA Radioisotope Power Systems. 2015.
- [10] Simet A. Packing a Punch. 2015; Available from:  
<http://biomassmagazine.com/articles/12404/packing-a-punch>.
- [11] Kong X.Q., Wang R.Z., and Huang X.H., Energy efficiency and economic feasibility of CCHP driven by Stirling engine. Energy Conversion and Management, 2004. **45**(9–10): p. 1433-1442.

- [12] Petrescu S., et al., Application of the Direct Method to irreversible Stirling cycles with finite speed. *International Journal of Energy Research*, 2002. **26**(7): p. 589-609.
- [13] Grosu L., Rochelle P., and Martaj N., An engineer-oriented optimisation of Stirling engine cycle with finite-size finite-speed of revolution thermodynamics. *International Journal of Exergy*, 2012. **11**(2): p. 191-204.
- [14] Petrescu S., et al., Unification perspective of finite physical dimensions thermodynamics and finite speed thermodynamics. *International Journal of Energy and Environmental Engineering*, 2015. **6**(3): p. 245-254.
- [15] Walker G., *Stirling engines*. 1980.
- [16] Urieli I. and Berchowitz D.M., *Stirling cycle engine analysis*. 1984: Taylor & Francis.
- [17] Cheng C.-H. and Yu Y.-J., Numerical model for predicting thermodynamic cycle and thermal efficiency of a beta-type Stirling engine with rhombic-drive mechanism. *Renewable Energy*, 2010. **35**(11): p. 2590-2601.
- [18] Grosu L., et al., Stirling refrigerating machine: confrontation of direct and finite physical dimensions thermodynamics methods to experiments. *International Journal of Energy, Environment and Economics*, 2012. **20**(3): p. 195.
- [19] Grosu L., Dobre C., and Petrescu S., Study of a Stirling engine used for domestic micro - cogeneration. Thermodynamic analysis and experiment. *International Journal of Energy Research*, 2015.
- [20] Dyson R.W., Wilson S.D., and Tew R.C. Review of computational stirling analysis methods. 2004.
- [21] Martaj N., et al., Simulation of a Stirling engine used for a micro solar power plant : 0-D modelling, comparison with 1-D modelling. *Environmental Engineering and Management Journal*, 2016. **15**(8): p. 1889-1895.
- [22] Senft J. A low temperature difference Ringbom Stirling demonstration engine. in *Proc., Intersoc. Energy Convers. Eng. Conf.;*(United States). 1984. University of Wisconsin at River Falls.
- [23] Senft J. An ultra low temperature differential Stirling engine. in *Proceeding of the 5th international Stirling engine Conference*, paper ISEC. 1991.
- [24] Senft J.R., Optimum Stirling engine geometry. *International Journal of Energy Research*, 2002. **26**(12): p. 1087-1101.
- [25] Finkelstein T. Gas particle trajectories in Stirling machines. in *7th Int. Conf. on Stirling Cycle Machines*, ICSC. 1995.
- [26] Costea M., Petrescu S., and Harman C., The effect of irreversibilities on solar Stirling engine cycle performance. *Energy conversion and management*, 1999. **40**(15): p. 1723-1731.
- [27] Chang H.-M., Park D.-J., and Jeong S., Effect of gap flow on shuttle heat transfer. *Cryogenics*, 2000. **40**(3): p. 159-166.
- [28] Thomas B. and Pittman D. Update on the evaluation of different correlations for the flow friction factor and heat transfer of Stirling engine regenerators. in *Energy Conversion Engineering Conference and Exhibit*, 2000.(IECEC) 35th Intersociety. 2000. IEEE.
- [29] Gedeon D. and Wood J., Oscillating-flow regenerator test rig: hardware and theory with derived correlations for screens and felts. 1996.

- [30] Kaushik S.C. and Kumar S., Finite time thermodynamic evaluation of irreversible Ericsson and Stirling heat engines. *Energy Conversion and Management*, 2001. **42**(3): p. 295-312.
- [31] Martaj N., Grosu L., and Rochelle P., Exergetical analysis and design optimisation of the Stirling engine. *International Journal of Exergy*, 2005. **3**(1): p. 45-67.
- [32] Grosu L., *Exergie et systèmes énergétiques: Transition vers l'EXERGETIQUE*. 2014: Presses Académiques Francophones.
- [33] Esposito M., et al., Efficiency at maximum power of low-dissipation Carnot engines. *Physical review letters*, 2010. **105**(15): p. 150603.
- [34] Formosa F. and Despesse G., Analytical model for Stirling cycle machine design. *Energy Conversion and Management*, 2010. **51**(10): p. 1855-1863.
- [35] Hu Z.J., et al., Evaluation of thermal efficiency and energy conversion of thermoacoustic Stirling engines. *Energy Conversion and Management*, 2010. **51**(4): p. 802-812.
- [36] Invernizzi C.M., Stirling engines using working fluids with strong real gas effects. *Applied Thermal Engineering*, 2010. **30**(13): p. 1703-1710.
- [37] Petrescu S., et al., A methodology of computation, design and optimization of solar Stirling power plant using hydrogen/oxygen fuel cells. *Energy*, 2010. **35**(2): p. 729-739.
- [38] Tlili I., Finite time thermodynamic evaluation of endoreversible Stirling heat engine at maximum power conditions. *Renewable and Sustainable Energy Reviews*, 2012. **16**(4): p. 2234-2241.
- [39] Formosa F., Badel A., and Lottin J., Equivalent electrical network model approach applied to a double acting low temperature differential Stirling engine. *Energy Conversion and Management*, 2014. **78**: p. 753-764.
- [40] Ahmadi M.H., et al., Connectionist intelligent model estimates output power and torque of stirling engine. *Renewable and Sustainable Energy Reviews*, 2015. **50**(0): p. 871-883.
- [41] Ding Z.M., Chen L.G., and Sun F.R., Performance optimization of a linear phenomenological law system Stirling engine. *Journal of the Energy Institute*, 2015. **88**(1): p. 36-42.
- [42] Hooshang M., et al., Optimization of Stirling engine design parameters using neural networks. *Renewable Energy*, 2015. **74**: p. 855-866.
- [43] Erbay L.B. and Yavuz H., Analysis of the stirling heat engine at maximum power conditions. *Energy*, 1997. **22**(7): p. 645-650.
- [44] MARTAJ N., et al., Time-dependent simulation of a Gamma-type LTD Stirling engine. *Mechanics & Industry*, 2010. **11**(1): p. 5.
- [45] Martaj N., Grosu L., and Rochelle P., Thermodynamic study of a low temperature difference Stirling engine at steady state operation. *International Journal of Thermodynamics*, 2007. **10**(4): p. 165.
- [46] Puech P. and Tishkova V., Thermodynamic analysis of a Stirling engine including regenerator dead volume. *Renewable Energy*, 2011. **36**(2): p. 872-878.
- [47] Rochelle P. and Grosu L., Analytical Solutions and Optimization of the Exo-Irreversible Schmidt Cycle with Imperfect Regeneration for the 3 Classical Types of Stirling Engine. *Oil & Gas Science and Technology—Revue d'IFP Energies nouvelles*, 2011. **66**(5): p. 747-758.

- [48] Yaqi L., Yaling H., and Weiwei W., Optimization of solar-powered Stirling heat engine with finite-time thermodynamics. *Renewable energy*, 2011. **36**(1): p. 421-427.
- [49] Cheng C.-H. and Yang H.-S., Optimization of geometrical parameters for Stirling engines based on theoretical analysis. *Applied Energy*, 2012. **92**: p. 395-405.
- [50] Reséndiz-Antonio M. and Santillán M., On the dynamical vs. thermodynamical performance of a  $\beta$ -type Stirling engine. *Physica A: Statistical Mechanics and its Applications*, 2014. **409**: p. 162-174.
- [51] Timoumi Y., Tlili I., and Ben Nasrallah S., Design and performance optimization of GPU-3 Stirling engines. *Energy*, 2008. **33**(7): p. 1100-1114.
- [52] Parlak N., et al., Thermodynamic analysis of a gamma type Stirling engine in non-ideal adiabatic conditions. *Renewable Energy*, 2009. **34**(1): p. 266-273.
- [53] Ahmadi M.H., et al., Multi-objective thermodynamic-based optimization of output power of Solar Dish-Stirling engine by implementing an evolutionary algorithm. *Energy Conversion and Management*, 2013. **75**: p. 438-445.
- [54] Ahmadi M.H., Mohammadi A.H., and Dehghani S., Evaluation of the maximized power of a regenerative endoreversible Stirling cycle using the thermodynamic analysis. *Energy Conversion and Management*, 2013. **76**: p. 561-570.
- [55] Ahmadi M.H., et al., Designing a solar powered Stirling heat engine based on multiple criteria: Maximized thermal efficiency and power. *Energy Conversion and Management*, 2013. **75**: p. 282-291.
- [56] Cheng C.-H., Yang H.-S., and Keong L., Theoretical and experimental study of a 300-W beta-type Stirling engine. *Energy*, 2013. **59**: p. 590-599.
- [57] Araoz J.A., et al., Non-ideal Stirling engine thermodynamic model suitable for the integration into overall energy systems. *Applied Thermal Engineering*, 2014. **73**(1): p. 205-221.
- [58] Babaelahi M. and Sayyaadi H., Simple-II: A new numerical thermal model for predicting thermal performance of Stirling engines. *Energy*, 2014. **69**: p. 873-890.
- [59] Mabrouk M.T., Kheiri A., and Feidt M., Displacer gap losses in beta and gamma Stirling engines. *Energy*, 2014. **72**: p. 135-144.
- [60] Araoz J.A., et al., Development and validation of a thermodynamic model for the performance analysis of a gamma Stirling engine prototype. *Applied Thermal Engineering*, 2015. **83**: p. 16-30.
- [61] Araoz J.A., et al., Numerical simulation for the design analysis of kinematic Stirling engines. *Applied Energy*, 2015. **159**: p. 633-650.
- [62] Hosseinzade H. and Sayyaadi H., CAFS: The Combined Adiabatic-Finite Speed thermal model for simulation and optimization of Stirling engines. *Energy Conversion and Management*, 2015. **91**: p. 32-53.
- [63] Paul C.J. and Engeda A., Modeling a complete Stirling engine. *Energy*, 2015. **80**: p. 85-97.
- [64] Babaelahi M. and Sayyaadi H., A new thermal model based on polytropic numerical simulation of Stirling engines. *Applied Energy*, 2015. **141**: p. 143-159.
- [65] Babaelahi M. and Sayyaadi H., Modified PSVL: A second order model for thermal simulation of Stirling engines based on convective-polytropic heat transfer of working spaces. *Applied Thermal Engineering*, 2015. **85**: p. 340-355.

- [66] Hosseinzade H., Sayyaadi H., and Babaelahi M., A new closed-form analytical thermal model for simulating Stirling engines based on polytropic-finite speed thermodynamics. *Energy Conversion and Management*, 2015. **90**: p. 395-408.
- [67] Andersen S.K., Carlsen H., and Thomsen P.G., Numerical study on optimal Stirling engine regenerator matrix designs taking into account the effects of matrix temperature oscillations. *Energy Conversion and Management*, 2006. **47**(7-8): p. 894-908.
- [68] Karabulut H., Yücesu H.S., and Çınar C., Nodal analysis of a Stirling engine with concentric piston and displacer. *Renewable Energy*, 2006. **31**(13): p. 2188-2197.
- [69] Dyson R.W., et al., Towards fully three-dimensional virtual Stirling convertors for multi-physics analysis and optimization. *Engineering Applications of Computational Fluid Mechanics*, 2008. **2**(1): p. 95-118.
- [70] Aksoy F. and Cinar C., Thermodynamic analysis of a beta-type Stirling engine with rhombic drive mechanism. *Energy Conversion and Management*, 2013. **75**: p. 319-324.
- [71] Costa S.C., et al., Numerical study of the pressure drop phenomena in wound woven wire matrix of a Stirling regenerator. *Energy Conversion and Management*, 2013. **67**: p. 57-65.
- [72] Mabrouk M.T., Kheiri A., and Feidt M., Effect of leakage losses on the performance of a  $\beta$  type Stirling engine. *Energy*, 2015. **88**: p. 111-117.
- [73] Della Torre A., et al. CFD modelling of a beta-type Stirling machine. in 5th European Conference on Computational Mechanics (ECCM V), Barcelona. 2014.
- [74] Salazar J.L. and Chen W.-L., A computational fluid dynamics study on the heat transfer characteristics of the working cycle of a  $\beta$ -type Stirling engine. *Energy Conversion and Management*, 2014. **88**: p. 177-188.
- [75] Solmaz H. and Karabulut H., Performance comparison of a novel configuration of beta-type Stirling engines with rhombic drive engine. *Energy Conversion and Management*, 2014. **78**: p. 627-633.
- [76] Chen W.-L., Wong K.-L., and Chang Y.-F., A numerical study on the effects of moving regenerator to the performance of a  $\beta$ -type Stirling engine. *International Journal of Heat and Mass Transfer*, 2015. **83**: p. 499-508.
- [77] Aksoy F., et al., A thermodynamic approach to compare the performance of rhombic-drive and crank-drive mechanisms for a beta-type Stirling engine. *Applied Thermal Engineering*, 2016. **93**: p. 359-367.
- [78] Hooshang M., Askari Moghadam R., and AlizadehNia S., Dynamic response simulation and experiment for gamma-type Stirling engine. *Renewable Energy*, 2016. **86**: p. 192-205.
- [79] Pfeiffer J. and Kuehl H.-D., Optimization of the Appendix Gap Design in Stirling Engines. *Journal of Thermophysics and Heat Transfer*, 2016. **30**(4): p. 831-842.
- [80] Sauer J. and Kuehl H.-D., Numerical model for Stirling cycle machines including a differential simulation of the appendix gap. *Applied Thermal Engineering*, 2017. **111**: p. 819-833.
- [81] Wilson S. Overview of Heat Addition and Efficiency Predictions for an Advanced Stirling Convertor. in 9th Annual International Energy Conversion Engineering Conference. 2012.
- [82] Wilson S.D., et al. Experimental and computational analysis of unidirectional flow

- through stirling engine heater head. in 3rd International Energy Conversion Engineering Conference. 2006.
- [83] Reid T., Wilson S., and Schifer N. A Computational Methodology for Simulating Thermal Loss Testing of the Advanced Stirling Converter. in 9th Annual International Energy Conversion Engineering Conference. 2012.
- [84] Duan C., et al., Thermodynamic design of Stirling engine using multi-objective particle swarm optimization algorithm. *Energy Conversion and Management*, 2014. **84**: p. 88-96.
- [85] Toghyani S., et al., Multi-objective optimization of GPU3 Stirling engine using third order analysis. *Energy Conversion and Management*, 2014. **87**: p. 521-529.
- [86] Dorer V. and Weber A., Energy and CO<sub>2</sub> emissions performance assessment of residential micro-cogeneration systems with dynamic whole-building simulation programs. *Energy Conversion and Management*, 2009. **50**(3): p. 648-657.
- [87] Rogdakis E.D., Antonakos G.D., and Koronaki I.P., Thermodynamic analysis and experimental investigation of a Solo V161 Stirling cogeneration unit. *Energy*, 2012. **45**(1): p. 503-511.
- [88] Ulloa C., et al., Feasibility of using a Stirling engine-based micro-CHP to provide heat and electricity to a recreational sailing boat in different European ports. *Applied Thermal Engineering*, 2013. **59**(1-2): p. 414-424.
- [89] Cacabelos A., et al., Development of an improved dynamic model of a Stirling engine and a performance analysis of a cogeneration plant. *Applied Thermal Engineering*, 2014. **73**(1): p. 608-621.
- [90] Yan J., et al., Clean, Efficient and Affordable Energy for a Sustainable Future: The 7th International Conference on Applied Energy (ICAE2015) Design, Fabrication and Evaluation of Gamma-Type Stirling Engine to Produce Electricity from Biomass for the Micro-CHP System. *Energy Procedia*, 2015. **75**: p. 137-143.
- [91] Damirchi H., et al., Micro Combined Heat and Power to provide heat and electrical power using biomass and Gamma-type Stirling engine. *Applied Thermal Engineering*, 2016. **103**: p. 1460-1469.
- [92] Kongtragool B. and Wongwises S., A review of solar-powered Stirling engines and low temperature differential Stirling engines. *Renewable and Sustainable Energy Reviews*, 2003. **7**(2): p. 131-154.
- [93] Kongtragool B. and Wongwises S., Optimum absorber temperature of a once-reflecting full conical concentrator of a low temperature differential Stirling engine. *Renewable Energy*, 2005. **30**(11): p. 1671-1687.
- [94] Kongtragool B. and Wongwises S., Performance of a twin power piston low temperature differential Stirling engine powered by a solar simulator. *Solar Energy*, 2007. **81**(7): p. 884-895.
- [95] Kongtragool B. and Wongwises S., Performance of low-temperature differential Stirling engines. *Renewable Energy*, 2007. **32**(4): p. 547-566.
- [96] Grosu L., et al., Etude expérimentale d'un moteur STIRLING LTD de type gamma, influence des paramètres physiques et géométriques sur le fonctionnement du moteur. Comparaison avec des modèles de simulation. Colloque francophone COFRET 2010. IASI, Roumanie. , 2010. **LVI, Fasc.3a.** : p. 13.

- [97] Tavakolpour A.R., Zomorodian A., and Akbar Golneshan A., Simulation, construction and testing of a two-cylinder solar Stirling engine powered by a flat-plate solar collector without regenerator. *Renewable Energy*, 2008. **33**(1): p. 77-87.
- [98] Tlili I., Timoumi Y., and Nasrallah S.B., Analysis and design consideration of mean temperature differential Stirling engine for solar application. *Renewable Energy*, 2008. **33**(8): p. 1911-1921.
- [99] Kraitong K. and Mahkamov K. Optimisation of Low Temperature Difference Solar Stirling Engines using Genetic Algorithm. in *World Renewable Energy Congress-Sweden*; 8-13 May; 2011; Linköping; Sweden. 2011. Linköping University Electronic Press.
- [100] Kato Y., Indicated diagrams of a low temperature differential Stirling engine using flat plates as heat exchangers. *Renewable Energy*, 2016. **85**: p. 973-980.
- [101] De Monte F. and Benvenuto G., Reflections on free-piston Stirling engines, part 1: cyclic steady operation. *Journal of propulsion and power*, 1998. **14**(4): p. 499-508.
- [102] Monte F.d. and Benvenuto G., Reflections on free-piston Stirling engines, part 2: Stable operation. *Journal of Propulsion and Power*, 1998. **14**(4): p. 509-518.
- [103] Rogdakis E.D., Bormpilas N.A., and Koniakos I.K., A thermodynamic study for the optimization of stable operation of free piston Stirling engines. *Energy Conversion and Management*, 2004. **45**(4): p. 575-593.
- [104] Boucher J., Nika P., and Lanzetta F. Modélisation Thermomécanique d'un moteur Stirling apistons libres. in *VIIeme Colloque Interuniversitaire Franco-Québécois, sur la Thermique des Systemes*. 2005.
- [105] Boucher J., Lanzetta F., and Nika P., Optimization of a dual free piston Stirling engine. *Applied Thermal Engineering*, 2007. **27**(4): p. 802-811.
- [106] Formosa F., Coupled thermodynamic–dynamic semi-analytical model of free piston Stirling engines. *Energy Conversion and Management*, 2011. **52**(5): p. 2098-2109.
- [107] Karabulut H., Dynamic analysis of a free piston Stirling engine working with closed and open thermodynamic cycles. *Renewable Energy*, 2011. **36**(6): p. 1704-1709.
- [108] Bégot S., et al., Stability analysis of free piston Stirling engines. *The European Physical Journal Applied Physics*, 2013. **61**(03): p. 30901.
- [109] Formosa F. and Fréchette L.G., Scaling laws for free piston Stirling engine design: Benefits and challenges of miniaturization. *Energy*, 2013. **57**: p. 796-808.
- [110] Strauss J.M., Direct piston displacement control of free-piston Stirling engines. 2013, Stellenbosch: Stellenbosch University.
- [111] Deetlefs I.N., Design, simulation, manufacture and testing of a free-piston Stirling engine. 2014, Stellenbosch: Stellenbosch University.
- [112] Kwankaomeng S., Silpsakoolsook B., and Savangvong P., Investigation on Stability and Performance of a Free-piston Stirling Engine. *Energy Procedia*, 2014. **52**: p. 598-609.
- [113] Ghazzi S. and Boukhanouf R., Computer Modeling of a Novel Mechanical Arrangement of a Free-Piston Stirling Engine. *Journal of Clean Energy Technologies*, 2015. **3**(2): p. 140-144.
- [114] Briggs M., Improving Free-Piston Stirling Engine Power Density. 2015.
- [115] Joubert L.H., Design optimisation of a transverse flux linear oscillating generator for resonant free-piston Stirling applications. 2015, Stellenbosch: Stellenbosch University.

- [116] Martirosyan A.A. and Shcherbina M.D., Solar-powered free-piston tirling – linear generator module concept for a moon base. IAC-15-C3.1.6, 2015.
- [117] PARK S., et al., A Study on Design of the Linear Generator in the Double Acting Stirling Engine. Transactions of the Korean hydrogen and new energy society, 2015. **26**(6): p. 638-644.
- [118] Sim K. and Kim D.-J., Dynamic Model Prediction and Validation for Free-Piston Stirling Engines Considering Nonlinear Load Damping. Transactions of the Korean Society of Mechanical Engineers A, 2015. **39**(10): p. 985-993.
- [119] Ghozzi S. and Boukhanouf R., Preliminary testing results of a diaphragm FPSE. 2016.
- [120] Hassan A., et al., Vibration control of a Stirling engine with an electromagnetic active tuned mass damper. Control Engineering Practice, 2016. **51**: p. 108-120.
- [121] Jang S.-J., et al., A design method for selecting the physical parameters of a free piston Stirling engine. Proceedings of the Institution of Mechanical Engineers, Part C: Journal of Mechanical Engineering Science, 2016: p. 0954406216634120.
- [122] Lezhnev L.Y., et al., Integrated design methodology for development of a free-piston Stirling engine. International Journal of Applied Engineering Research, 2016. **11**(13): p. 8067-8074.
- [123] Tavakolpour-Saleh A.R., Zare S., and Omidvar A., Applying perturbation technique to analysis of a free piston Stirling engine possessing nonlinear springs. Applied Energy, 2016. **183**: p. 526-541.
- [124] Zare S. and Tavakolpour-Saleh A.R., Frequency-based design of a free piston Stirling engine using genetic algorithm. Energy, 2016. **109**: p. 466-480.
- [125] Wilson S.D., et al. Maturing Technologies for Stirling Space Power Generation. in 14th International Energy Conversion Engineering Conference. 2016.
- [126] Wilson S.D., Metscher J., and Schifer N.A. Active Vibration Reduction of the Advanced Stirling Converter. in 14th International Energy Conversion Engineering Conference. 2016.
- [127] Berchowitz D.M. and Yong-Rak K., Multiple cylinder free-piston Stirling machinery. Journal of Power and Energy Systems, 2008. **2**(5): p. 1209-1220.
- [128] Hoshino T., et al., Prototype of Free Piston Stirling Converter for Household Use. Journal of Power and Energy Systems, 2008. **2**(5): p. 1232-1240.
- [129] Qiu S., Peterson A., and Augenblick J. Flexure design and testing for STC Stirling converters. in 1st International Energy Conversion Engineering Conference (IECEC). 2003.
- [130] Koester G., et al., Oscillating flow loss test results in Stirling engine heat exchangers. Final Report. 1990, Sunpower, Inc., Athens, OH (United States).
- [131] Tanaka M., Yamashita I., and Chisaka F., Flow and heat transfer characteristics of the Stirling engine regenerator in an oscillating flow. JSME international journal. Ser. 2, Fluids engineering, heat transfer, power, combustion, thermophysical properties, 1990. **33**(2): p. 283-289.
- [132] Zhao T. and Cheng P., Oscillatory pressure drops through a woven-screen packed column subjected to a cyclic flow. Cryogenics, 1996. **36**(5): p. 333-341.
- [133] Isshiki S., et al., Studies on Flow Resistance and Heat Transfer of Regenerator Wire Meshes of Stirling Engine in Oscillatory Flow. JSME International Journal Series B,

1997. **40**(2): p. 281-289.
- [134] Aksoy F. and Karabulut H., Performance testing of a Fresnel/Stirling micro solar energy conversion system. *Energy Conversion and Management*, 2013. **75**: p. 629-634.
- [135] Costa S.-C., et al., Experimental and numerical flow investigation of Stirling engine regenerator. *Energy*, 2014. **72**: p. 800-812.
- [136] Gheith R., Aloui F., and Ben Nasrallah S., Study of temperature distribution in a Stirling engine regenerator. *Energy Conversion and Management*, 2014. **88**: p. 962-972.
- [137] Aksoy F., et al., Thermal performance of a Stirling engine powered by a solar simulator. *Applied Thermal Engineering*, 2015. **86**(0): p. 161-167.
- [138] Féliès G., et al., Double acting Stirling engine: Modeling, experiments and optimization. *Applied Energy*, 2015. **159**: p. 350-361.
- [139] Gheith R., Aloui F., and Ben Nasrallah S., Determination of adequate regenerator for a Gamma-type Stirling engine. *Applied Energy*, 2015. **139**: p. 272-280.
- [140] Hachem H., et al., Numerical characterization of a  $\gamma$ -Stirling engine considering losses and interaction between functioning parameters. *Energy Conversion and Management*, 2015. **96**: p. 532-543.
- [141] Song Z., Chen J., and Yang L., Heat transfer enhancement in tubular heater of Stirling engine for waste heat recovery from flue gas using steel wool. *Applied Thermal Engineering*, 2015. **87**(0): p. 499-504.
- [142] Glushenkov M., et al., Single-piston alternative to Stirling engines. *Applied Energy*, 2012. **97**: p. 743-748.
- [143] Yang N., et al., Integrated two-cylinder liquid piston Stirling engine. *Applied Physics Letters*, 2014. **105**(14): p. 143903.

## Chapter 3 New isothermal model coupled with various losses

### --Case study for a Gamma type Stirling engine

In this chapter, a 0-D isothermal analysis is coupled with finite speed model to predict the performance of a solar powered Gamma type SE. The model includes mass and energy balances through the different spaces of the engine and takes several losses into consideration such as: viscous friction, regenerator imperfection, hysteresis loss, clearance seal leakage, shuttle heat loss by displacer, finite speed piston loss and heat conduction loss. As a 0-D isothermal analysis over-estimates the mechanical power provided by the engine, different losses are considered at each step time of the model.

### 3.1 Geometry of the studied Stirling engine

A gamma type Low Temperature Difference Stirling engine (SE) has been designed and built in our laboratory, powered by the artificial solar energy. The geometry and operation conditions of this engine were used as central parameter of the model presented in this part.

A section of the Gamma SE can be seen in Figure 3.1. The working piston and the displacer are connected on the same crankshaft with a specific out of phases. There is no regenerator material in this engine. The air flows between the hot and cold sides of the engine through the gap between the cylinder and the displacer. Consequently, this gap is supposed to be a very imperfect regenerator. The interface between cold space and regenerator is the interface 2 (Figure 3.1) and the interface between hot space and regenerator is the interface 4. Hot and cold volumes temperatures are supposed to be constant. This assumption was already validated in previous work [1].

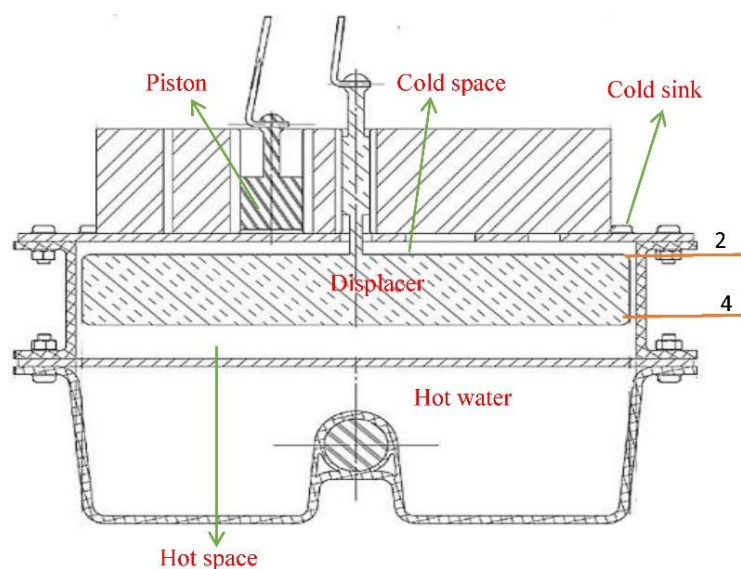


Figure 3.1 Configuration of Gamma Stirling engine of our laboratory

### 3.2 Thermodynamic model

Several previous works have already studied the Stirling cycle, starting from an ideal cycle containing two isothermal processes **a-b** and **c-d**, and two isochoric processes **b-c** and **d-a**, and considering imperfect regeneration (Figure 3.2). From **b** to **c**, working gas absorbs heat from the regenerator materials; while from **d** to **a** it discharges heat to regenerator materials. Due to the imperfection of the regenerator, the working gas can only be heated by the regenerator from **b** to **c'**, and cooled from **d** to **a'**. Internal and external irreversibilities have been considered in the past, starting from this cycle using for example Direct Methods [2], Finite Time Thermodynamics [3, 4] or Finite Physical Dimensions Thermodynamics [5]. The main assumption of these methods is that total mass follows the four evolutions of the cycle.

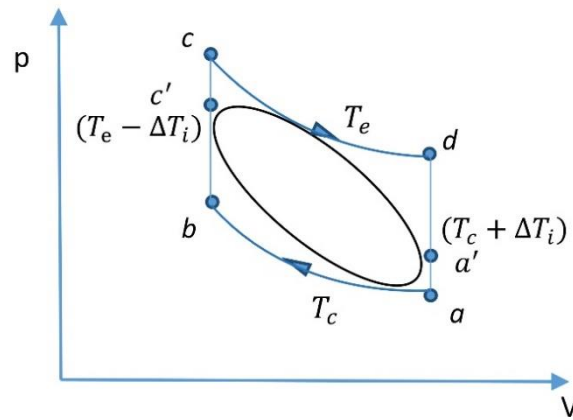


Figure 3.2 Stirling cycle

The isothermal model [6] and adiabatic model [7] take, in addition to this, the kinematic movement of the pistons into account to complete the thermodynamic model. The engine is divided into three or five volumes for which mass variation is taken into account. Thus, Stirling cycle represented by the inside curve on Figure 3.2, is closer to the real one than ideal representation. The hot and cold volumes are expressed as follows:

$$V_e = \frac{V_{e0}}{2} [1 - \cos(\omega t + \varphi_{initial})] + V_{dh} \quad (1)$$

$$V_c = \frac{V_{e0}}{2} [1 + \cos(\omega t)] + \frac{V_{c0}}{2} [1 - \cos(\omega t + \varphi_{initial} - \varphi_0)] + V_{dl} \quad (2)$$

where  $V_{e0}$  is the swept volume of the displacer,  $V_{c0}$  is the swept volume of the piston,  $\varphi_{initial}$  is the initial crankshaft angle,  $\varphi_0$  is the phase shift between the piston and the displacer,  $V_{dh}$  is the hot side dead volume,  $V_{dl}$  is the cold side dead volume,  $\omega$  is rotation speed of the crankshaft.

In this model, the isothermal model is coupled with finite speed method in order to take different losses into account due to viscous friction, regenerator imperfections, hysteresis, clearance seal leakage, shuttle heat by displacer, finite speed piston, heat conduction; these losses interact with each other and are calculated at each time step. Supposing a linear distribution of air temperature in the regenerator, a logarithmic average temperature can be calculated as bellow:

$$T_r = \frac{1}{\int_0^{L_r} \rho(x) A_r dx} \int_0^{L_r} \rho(x) A_r T(x) dx = \frac{1}{\int_0^{L_r} \frac{p}{r_g T(x)} dx} \int_0^{L_r} \frac{p}{r_g} dx = \frac{L_r}{\int_0^{L_r} \frac{1}{T_c + \frac{T_e - T_c x}{L_r}} dx} = \frac{T_e - T_c}{\ln\left(\frac{T_e}{T_c}\right)} \quad (3)$$

Assuming the working gas as an ideal gas, the pressure in the engine can be expressed as:

$$p^n = m_t^n r_g / \left( \frac{V_e}{T_e} + \frac{V_c}{T_c} + \frac{V_r}{T_r} \right) \quad (4)$$

where  $p^n$  is the current time step pressure in the engine and  $m_t^{n-1}$  is the total mass in the engine of previous time step. The total mass in engine of current time step can be expressed as follow:

$$m_t^n = m_t^{n-1} - dm_{leak} \quad (5)$$

where  $dm_{leak}$  is the mass leakage in one time step which can be seen in leakage loss section.

The differential of pressure on the current time step condition is:

$$dp^n = - \frac{p^n \left( \frac{dV_e}{T_e} + \frac{dV_c}{T_c} \right)}{\frac{V_e}{T_e} + \frac{V_r}{T_r} + \frac{V_c}{T_c}} \quad (6)$$

To an open system as represented in Figure 3.3, the energy balance can be written as:

$$dE = \delta Q + \delta W + dm_{in} \left( gz_{in} + \frac{u_{in}^2}{2} + h_{in} \right) - dm_{out} \left( gz_{out} + \frac{u_{out}^2}{2} + h_{out} \right) \quad (7)$$

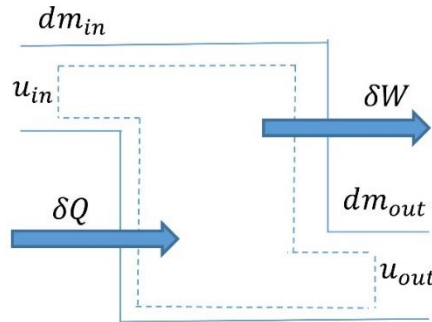


Figure 3.3 Open system sketch

Kinematic and potential energy variation can be neglected considering the small dimensions of the engine. Thus, the energy balance applied on cold and hot volume can be expressed as (without leakage):

$$\delta Q_c = \frac{c_v}{r_g} V_c dp + \frac{c_p}{r_g} p dV_c + c_p T_2 dm_2 \quad (8)$$

$$\delta Q_e = \frac{c_v}{r_g} V_e dp + \frac{c_p}{r_g} p dV_e - c_p T_4 dm_4 \quad (9)$$

where,  $Q_c$  and  $Q_e$  are heat exchanged in cold and hot volume. Indicated output work  $W_i$  can be expressed as:

$$\delta W_i = -(pdV_e + pdV_c) \quad (10)$$

Considering work losses due to viscous friction, hysteresis losses etc., the shaft work can be

calculated as:

$$|W_{shaft}| = |W_i| - W_{total\ loss} \quad (11)$$

In addition, a total heat loss should be added to the actual hot space and cold space heat exchanged, taking phenomenon into account such as conduction, displacer shuttle loss, etc.

### 3.2.1 Study of different losses in the engine

The working gas of the investigated engine is heated and cooled through the plate surface of the expansion and the compression volumes, which are in contact with the two heat sources (solar water flow and ambient air). In addition to this, the hot volume also acts as expansion volume and the cold volume also acts as compression volume. Consequently, this engine can be divided into three main volumes and the simulation model can start with the isothermal approach. However, this model is inaccurate without considering irreversibilities in the engine. In this model, power losses (including piston finite speed loss, hysteresis loss, mass leakage loss, regenerator flow dissipation), and heat losses (regenerator imperfections, heat conduction and displacer shuttle loss) are considered, using the finite speed thermodynamics approach. Usually, those losses can have interaction between each other, so they are calculated at the same time step to take their interactions into consideration.

#### 3.2.1.1 Regenerator loss

In SE, working fluid has an oscillated flow in the regenerator, heater, and cooler. Pressure loss in heater and cooler are neglected here, as the transversal section of the two heat exchangers is much higher than the regenerator section (Figure 3.1). Only regenerator pressure loss is considered in this work. In Artin's previous work [8] this pressure loss due to the working fluid viscosity was expressed as:

$$\Delta p_r(t) = \Delta p_{max} \cos(\omega t + \varphi_{initial}) \quad (12)$$

where  $\varphi_{initial}$  is the initial phase angle for the displacer velocity and  $\omega$  is the angular speed of the SE.

Tanaka et al. [9] proposed the following expression to air SE, using experimental results:

$$\Delta p_{max} = \frac{\rho}{2} f_{max} \frac{L_r}{D_r} u_{max}^2 = \frac{\rho}{2A_0^2} f_{max} \frac{L_r}{D_r} \dot{V}_{max}^2 \quad (13)$$

where  $f_{max} = \frac{C_{sf}}{Re_{max}} + C_{fd}$ ,  $Re_{max} = \frac{\rho}{\mu} D_r u_{max} = \frac{1}{\nu} D_r u_{max}$ ,  $\rho$  is the average density of the working fluid in the engine,  $L_r$  is the length of the regenerator,  $f_{max}$  is the maximum friction factor,  $D_r$  is hydraulic diameter in the regenerator,  $A_0$  is the fluid cross section area of the regenerator,  $C_{sf}$  and  $C_{fd}$  are empirical factors (suggested to be  $C_{sf} = 175$  and  $C_{fd} = 1.6$  for stacks of screens),  $\nu$  and  $\mu$  are respectively the kinetic and the dynamic viscosity,  $u_{max}$  is the maximum fluid velocity in the regenerator,  $\dot{V}_{max}$  is the maximum volume flow rate of working fluid in regenerator and  $Re$  is the Reynolds number.

In this work, the equation below has been used, obtained combining Artin and Tanaka's expressions:

$$\Delta p_r(t) = \frac{1}{2} \left( 175\mu \frac{u_{max}}{D_r^2} + 1.6\rho \frac{u_{max}^2}{D_r} \right) L_r \cos(\omega t + \varphi_{initial}) \quad (14)$$

The average fluid friction dissipation in terms of power is calculated as:

$$\overline{\dot{W}}_r = \frac{1}{t_{cycle}} \int_0^{t_{cycle}} \Delta p(t) dV(t) = \frac{\rho L_r}{4D_r} u_{max}^3 A_0 \left( \frac{175\mu}{\rho D_r u_{max}} + 1.6 \right) \quad (15)$$

The regenerator of the engine studied in this paper is far from perfect. It represents the gap between the displacer and the cylinder wall. The working fluid flowing through this space exchanges heat with the edge surface of the displacer and the corresponding inner part of the cylinder. Thus, it is important to consider the regenerator efficiency. Hosseinzade H., Sayyaadi H. [10] used the following expression to calculate the effectiveness of the regenerator:

$$\varepsilon_r = \frac{NTU}{1+NTU} \quad (16)$$

where  $NTU$  is the number of transfer unit in the regenerator,  $NTU = \frac{StL_r}{R_r}$ ,  $St$  and  $R_r$  are respectively Stanton number and hydraulic radius of regenerator, defined as below:

$$St = 0.023Re^{-0.2}Pr^{-0.6}, R_r = \frac{D_r}{4} = \frac{\Pi}{\Phi(1-\Pi)}, \Phi = \frac{A_{wetted}}{V_{mesh}}$$

with  $Pr$  Prandtl number,  $\Pi$  the porosity,  $\Phi$  a shape factor,  $A_{wetted}$  the wet surface of wires in regenerator and  $V_{mesh}$  the regenerator wires volume.

Another researchers as Artin [8] used the expression below to estimate the regenerator efficiency:

$$\varepsilon_r = \frac{NTU}{NTU+2} \quad (17)$$

with  $NTU = \frac{A_{wetted}h}{\dot{m}_{ave}c_p}$ , where  $\dot{m}_{ave}$  is the gas average mass flow rate in the regenerator and  $h$  is the heat transfer coefficient which can be calculated by the following equation proposed by Tanaka [9]:

$$h = \frac{Nu.K_g}{D_r} = \frac{K_g}{D_r} \cdot (C_1 + C_2(Re_{ave}Pr)^{C_3})(1 - C_4(1 - \Pi)) \quad (18)$$

where  $K_g$  is heat conductivity of the working gas,  $C_1$  to  $C_4$  are empirical coefficients ( $C_1 = C_4 = 0, C_2 = 0.42, C_3 = 0.67$ ),  $Re_{ave} = \frac{\rho}{\mu} D_r u_{ave}$ ,  $u_{ave} = \frac{2}{\pi} D_r u_{max}$ ,  $Pr = \frac{\nu}{\alpha}$ .

Starting with these considerations, the following model is considered to define the regenerator's behavior and its efficiency.

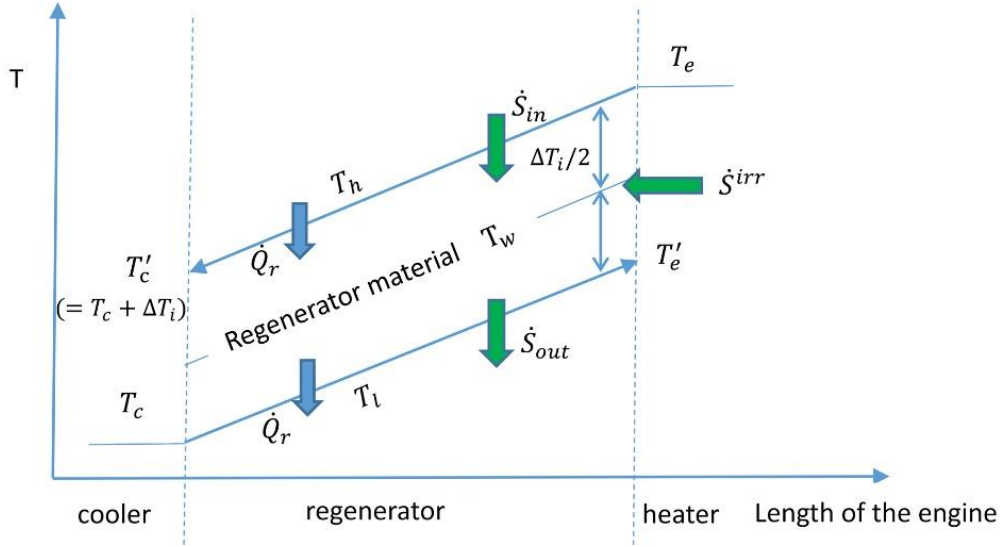


Figure 3.4 Temperature outline in the regenerator

For an imperfect regenerator, Figure 3.4 shows the temperature difference between the working fluid and the regenerator surface, during the alternative transfer between cooled and heated spaces. The same temperature pinch  $\Delta T$  is considered.

According to Newton's law, the heat flow between working fluid and regenerator materials can be calculated as:

$$\dot{Q}_r = (T_h - T_w)A_w h = (T_w - T_l)A_w h = \Delta T_i A_w h / 2 \quad (19)$$

During the cooled or heated process, expression (20) can be stated according to the energy balance:

$$\dot{Q}_r = \dot{m}_g c_p (T_e - T'_c) = \dot{m}_g c_p (T'_e - T_c) \quad (20)$$

Therefore, the regenerator efficiency can be written as (21):

$$\varepsilon_r = \frac{T_e - T'_c}{T_e - T_c} = \frac{T'_e - T_c}{T_e - T_c} = \frac{T_e - T'_c}{T_e - T'_c + \Delta T_i} \quad (21)$$

By combining the above three equations the following equation is obtained:

$$\varepsilon_r = \frac{NTU}{NTU + 2} \quad (22)$$

where  $NTU$  is considered here as  $NTU = \frac{A_w h}{\dot{m} c_p}$ .

The regenerator being imperfect, additional heat  $Q_r$  should be consumed in the heater. Corresponding heat flow  $\dot{Q}_r$  can be calculated as:

$$\dot{Q}_r = \dot{m} c_p (1 - \varepsilon_r) (T_e - T_c) \quad (23)$$

On the other side, due to the temperature pinch, entropy is generated in the regenerator, which is the difference between the outlet and the inlet entropy flows:

$$\dot{S}_{in} = \frac{\dot{Q}_r}{T_{h,ave}} \quad (24)$$

$$\dot{S}_{out} = \frac{\dot{Q}_r}{T_{l,ave}} \quad (25)$$

$$\text{with, } T_{h,ave} = \frac{T_e - T'_c}{\ln(T_e/T'_c)}, \quad T_{l,ave} = \frac{T'_e - T_c}{\ln(T'_e/T_c)}$$

Thus, entropy generation rate  $\dot{S}^{irr}$  can be calculated as:

$$\dot{S}^{irr} = \dot{S}_{out} - \dot{S}_{in} \quad (26)$$

### 3.2.1.2 Loss due to piston finite speed

Due to the piston movement, instantaneous pressure over the piston surface is different from instantaneous internal mean pressure. Costea et al. [11] have demonstrated that, in the expansion process, pressure over the piston is less than the mean pressure of the cylinder, and in the compression process, the pressure over the piston surface is greater than the internal mean pressure. Therefore, during the compression process, the piston should work harder to compress the gas. Thus, the net output work is less than the theoretical one.

The pressure loss due to piston finite speed can be calculated as the following equation referenced in [2, 10, 11]:

$$\Delta p_{fin\ spe} = \frac{1}{2} \left( p_c \frac{a u_{p,c}}{c_c} + p_e \frac{a u_{p,e}}{c_e} \right) \quad (27)$$

where  $p$  represents the instantaneous pressure,  $u_p$  is the piston speed,  $c$  is the average molecular speed  $c = \sqrt{3r_g T}$  and  $a$  is a constant defined as  $a = \sqrt{3\gamma}$ , where  $\gamma$  is the specific heat ratio and  $r_g$  is the gas constant. Supposing that compression speed equals expansion speed, the pressure loss due to finite speed can be expressed by:

$$\Delta p_{fin\ spe} = \frac{p_m a u_p}{c} \quad (28)$$

### 3.2.1.3 Hysteresis loss

The Stirling thermodynamic cycle undergoes both pressure and volume variations in a closed space. Therefore, actually, the working chamber act as a gas spring to the piston for Beta and Gamma type Stirling engine, to the both displacer and piston in Alpha type Stirling engine. As the thermodynamic process occurs in the gas spring is not perfectly reversible, there is a certain amount of  $pV$  work dissipated in each cycle known as hysteresis loss and having function of viscous and temperature gradient in the engine [8].

Usually, the viscous effects can be neglected [12] even if they consume a small part of the mechanical work provided by the working piston. Reference [12] propose a calculation method of gas spring hysteresis loss.

Assuming sinusoidal variations of the total SE volume as:

$$V_{total} = V_o + V_m \sin(\omega t) \quad (29)$$

The average hysteresis loss speed can be expressed as bellow:

$$\overline{\dot{W}_{hys}} = \sqrt{\frac{1}{32} \omega \gamma^3 (\gamma - 1) T_w p_{mean} K_g \left(\frac{V_m}{V_o}\right)^2} A_w \quad (30)$$

where,  $K_g$  is the conductivity of the working gas,  $V_m$  is half of swept volume of the working piston,  $\gamma = \frac{c_p}{c_v}$  is the specific heat capacity ratio,  $T_w$  is the chamber wall temperature,  $p_{mean}$  is the mean pressure in the engine and  $A_w$  is the wetted area which is usually the cross section of the piston.

As is well known, there are strong dependence between the engine work and the mean pressure. So an increase in engine pressure can lead to a decrease in the ratio between the hysteresis loss and the output work. Reduction of hysteresis impact can also be obtained by a diminution of the cross section area of the piston.

#### 3.2.1.4 Clearance leakage loss

One of the ideal SE considerations is no leakage through the clearance between the piston and the cylinder wall. However, in real SE, the leakage is unavoidable. Mass flow rate due to leakage through the gap between the piston and the cylinder wall can be expressed as below equation, according to references [12] and [13]:

$$\dot{m}_{leak} = \pi D \frac{p+p_{ext}}{4r_g T_g} \left( u_p g - \frac{g^3}{6\mu} \frac{p_{ext}-p}{L} \right) \quad (31)$$

where,  $D$  is the mean clearance diameter,  $p$  is the internal pressure,  $p_{ext}$  is the external pressure,  $T_g$  is the gas temperature near the power piston,  $L$  is the length of the gap,  $u_p$  is the speed of the piston,  $g$  is the width of the gap between the power piston and the cylinder,  $\mu$  is the dynamic viscosity.

The mass leakage during one time step is expressed in (32):

$$dm_{leak} = \dot{m}_{leak} \cdot \delta t \quad (32)$$

where  $\delta t$  is the time step. This mass leakage leads to a variation of the total working gas mass,  $m_t$ , which affects the pressure in the engine as seen in equation (4).

Thus, the enthalpy flow wasted due to the leakage can be written as:

$$\dot{H}_{leak} = \dot{m}_{leak} c_p T \quad (33)$$

where the temperature depends on the flow direction.  $T$  is the exterior temperature when the mass leak from outside into the engine, and it is the working gas temperature when mass leak from the engine to outside.

### 3.2.1.5 Heat conduction loss

In Beta type or Gamma type SE, the displacer ensures the temperature gap between the cold volume and the hot volume. Therefore, heat conduction through the displacer and the cylinder wall couldn't be avoided. According to Fourier's conduction law, heat loss by conduction is written as:

$$\dot{Q}_{cond} = K \frac{A}{L} \Delta T \quad (34)$$

where  $K$  is the heat conductivity of the displacer or the cylinder wall,  $A$  is the corresponding cross section area,  $L$  is the length of the displacer piston or the cylinder wall,  $\Delta T$  is the temperature difference between the hot volume and the cold volume.

### 3.2.1.6 Heat loss by displacer shuttle

The displacer is in contact with different temperature layers of the working gas, during its alternative movement, which causes shuttle heat loss expressed as:

$$\dot{Q}_{shuttle} = 0.4 \frac{Z_d^2 K_g D_d}{g_d L_d} (T_e - T_c) \quad (35)$$

where  $Z_d$  is the displacer stroke,  $K_g$  is the working gas thermal conductivity,  $D_d$  is the displacer diameter,  $g_d$  is the width of the gap between the displacer and the cylinder, and  $L_d$  is the length of displacer.

Therefore, shaft work, real heat absorbed and rejected by the engine can be expressed as (36)-(38):

$$|W_{shaft}| = |W_i| - W_r - W_{fin\ spe} - W_{hys} - W_{leak} \quad (36)$$

$$Q_{c\ real} = Q_c + Q_r + Q_{cond} + Q_{leak} + Q_{shuttle} \quad (37)$$

$$Q_{e\ real} = Q_e + Q_r + Q_{cond} + Q_{leak} + Q_{shuttle} \quad (38)$$

where  $W_r$  is the work dissipated in the regenerator due to the pressure drop,  $W_{fin\ spe}$  is the work loss due to finite speed of the piston,  $W_{leak}$  is the work loss due to the leakage.  $Q_r$  is the heat loss due to the imperfection of the regenerator,  $Q_{cond}$  is the heat conduction loss directly from hot volume to cold volume,  $Q_{leak}$  is the heat loss due to the mass leakage and  $Q_{shuttle}$  is the shuttle heat loss due to the reciprocating movement of the displacer.

### 3.2.2 Study case of the Gamma type Stirling engine

In the studied Gamma type Stirling engine a phase shift between the piston and the displacer  $\varphi_0$  can be imposed through the flywheel and the crank. We suppose a reference crank angle at zero degrees when the working piston is at its average position and tends to decrease the cold volume.

The parameters and condition used for the simulation can be seen on Table 3.1.

Table 3.1 Parameter and operation condition of the Gamma type Stirling engine

Working gas	air	Length of the working piston	21.3 mm
Displacer stroke	9 mm	Inner cylinder diameter	176 mm
Working piston stroke	21 mm	Working piston diameter	22 mm
Environmental temperature	299.1 K	Displacer diameter	172 mm
Length of the displacer	24.9 mm	Working piston clearance	0.08 mm
Expansion volume temperature	317.9 K	Phase shift of displacer & piston	90 degree
Compression volume temperature	305.6 K	Initial pressure $p_0$	101325 Pa
Cold sink temperature	303.9K	Frequency	0.4189 Hz

The simulation algorithm is shown in Figure 3.5. Initial parameters are supposed firstly, then the leakage, state parameters and energies exchanged in one time step are calculated. A new mass, pressure and interface regenerator temperatures can be obtained. The absorbed heat, the output mechanical power, and the time are summed up respectively. The simulation repeats until reaching the stop time.

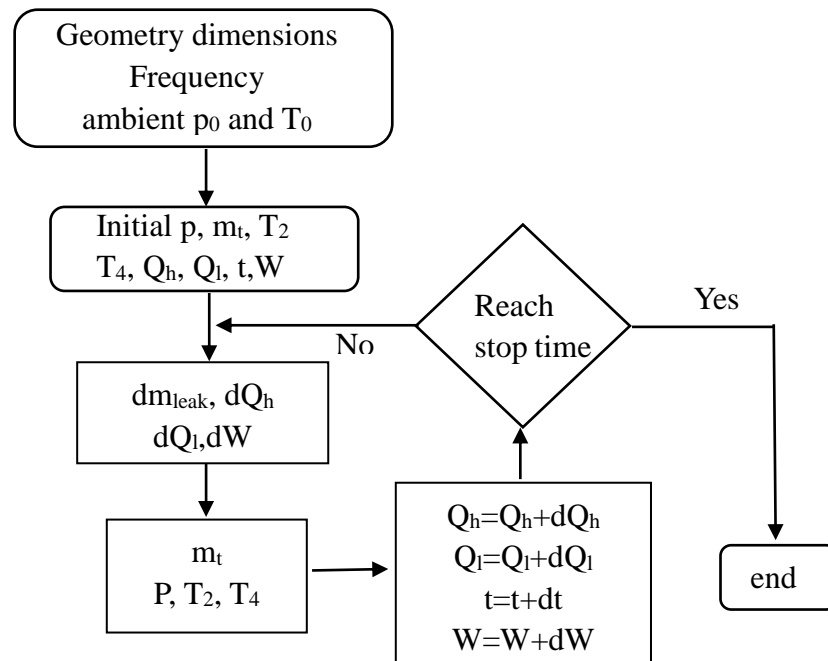


Figure 3.5 Flowchart of the simulation process

Using the parameters and operating condition of Table 3.1, and the thermodynamic model in this section, 15 cycles were calculated for 1000 time steps per cycle, and the last five cycles are considered to get average results. The regenerator efficiency is calculated and obtained about 0.46.

The variation of the total working gas mass with the crank angle is shown on Figure 3.6. The average total mass is estimated at about  $9.163487 \times 10^{-4}$  kg. As this value corresponds to the crank angle about  $-63.36^\circ$ , an initial angle,  $\varphi_i$ , has been set at  $-63.36^\circ$ . The total working gas mass depending on the crank angle, as observed in Figure 3.6, due to the leakage through the clearance between the working piston and the cylinder wall.

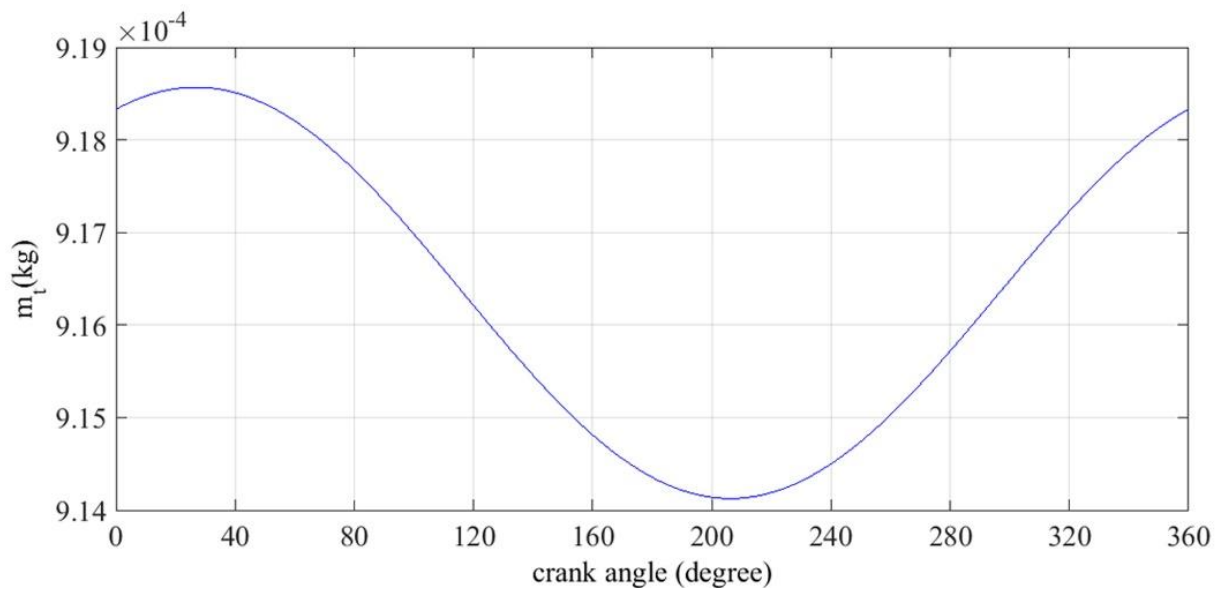


Figure 3.6 Total mass variation versus crank angle

Figure 3.7 shows the pressure variation with the crank angle, caused by this leakage, which leads the pressure to become smaller during the compression process, and bigger during the expansion process. The continuous blue line is the pressure ( $p$ ) without considering pressure losses, the red dash line, is the pressure considering clearance leakage ( $p_{leak}$ ). It can be seen that, the amplitude of the pressure wave is smaller when leakage is considered. In addition, an advanced phase,  $\phi$ , of the pressure wave can be observed due to the leakage. Figure 3.7 also shows that the pressure without leakage (blue line) obtains average value at  $45.72^\circ$  and peak value at  $135.72^\circ$ . However, if leakage is considered, the peak, the average, and the minimum values of the total gas mass in the engine are obtained at the following crankshaft positions:  $21.64^\circ$ ,  $116.64^\circ$  and  $206.64^\circ$  (Figure 3.7). Therefore, we can see in Figure 3.6 that from  $45.72^\circ$  to  $135.72^\circ$ , the total gas mass continuously decreases which leads to a diminution of the pressure. At the same time, between these angles, the working gas is compressed, which leads to the pressure increase. These two effects combined together, will advance the pressure peak location between  $45.72^\circ$  and  $135.72^\circ$ .

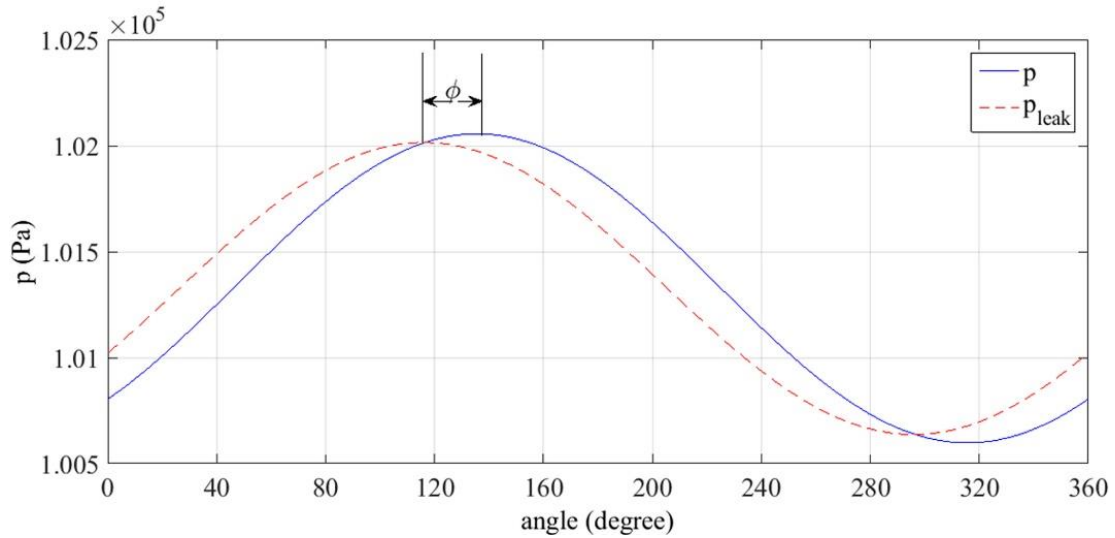


Figure 3.7 Pressure with and without leakage versus crank angle

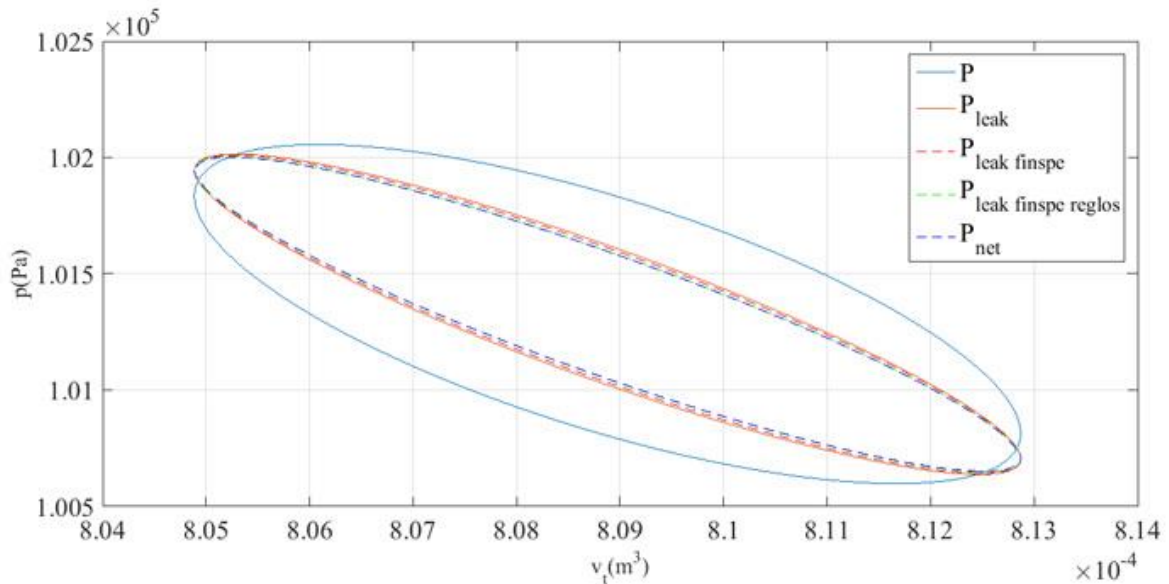


Figure 3.8. Pressure variation versus volume

Figure 3.8 shows the  $pV$  diagram of the cycle,  $p$  is the pressure without pressure losses;  $p_{leak}$  is the pressure considering leakage;  $p_{leak\ finspe}$  is the pressure considering leakage and piston finite speed loss;  $p_{leak\ finspe\ rloss}$  is the pressure considering leakage, piston finite speed loss, and pressure loss in regenerator;  $p_{net}$  is pressure considering all losses (leakage, piston finite speed loss, regenerator pressure loss and hysteresis loss). We can see that, for the considered LDT engine, the leakage loss has the most effect on the mechanical power. However, it must be noticed that the leakage loss is not always the biggest power loss, and it depends on the size and the power scale of the engine. Previous study of GPU-3 Stirling engine with output power about 3kW [14], shows that the leakage loss is about 3% of the total power loss for a clearance about 0.028mm. A decrease in clearance size can actually reduce the leakage loss, as can be seen in Figure 3.9. The engine studied here has a clearance about 0.08mm and provides only about 3mW mechanical power. In these conditions, a very strong impact of the gas leakage on

the mechanical work (about 42%) is noticed. This percentage will be reduced after some improvements of the engine geometry.

Figure 3.9 shows the variation of the total mass of the working gas in the engine for several clearance sizes between the piston and the cylinder wall. It can be seen that the amplitude of the total mass wave increases when the clearance size increases, due to the leakage through the clearance. It must be noticed here that the stability of the cycle from the initial conditions is obtained more quickly for large clearance. This point becomes important to be taken into account for complex models with high simulation time.

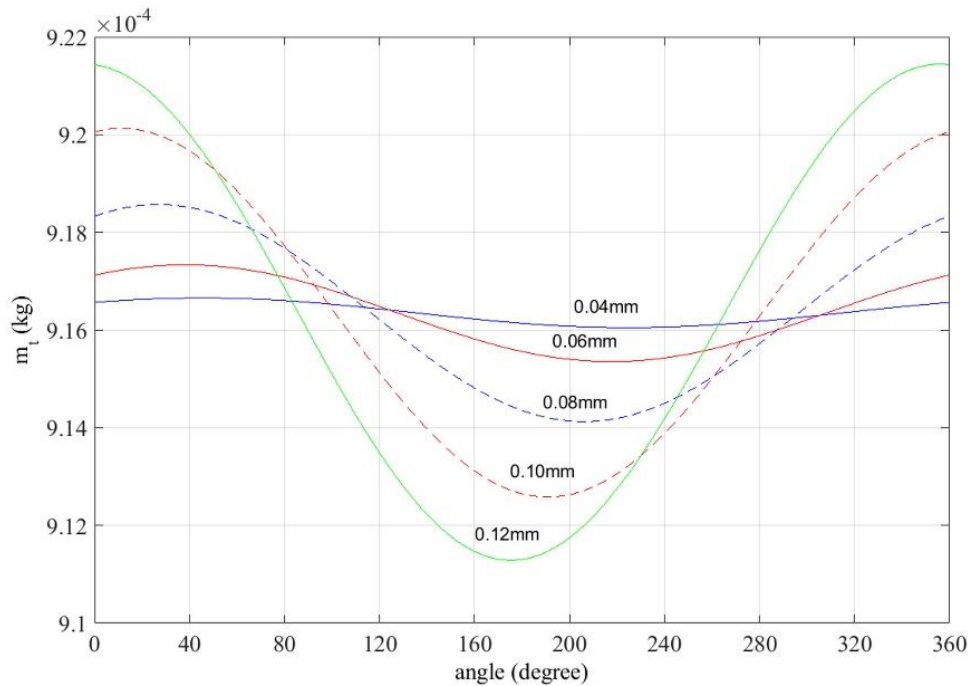


Figure 3.9 Gas mass variation versus crank angle for several clearance sizes

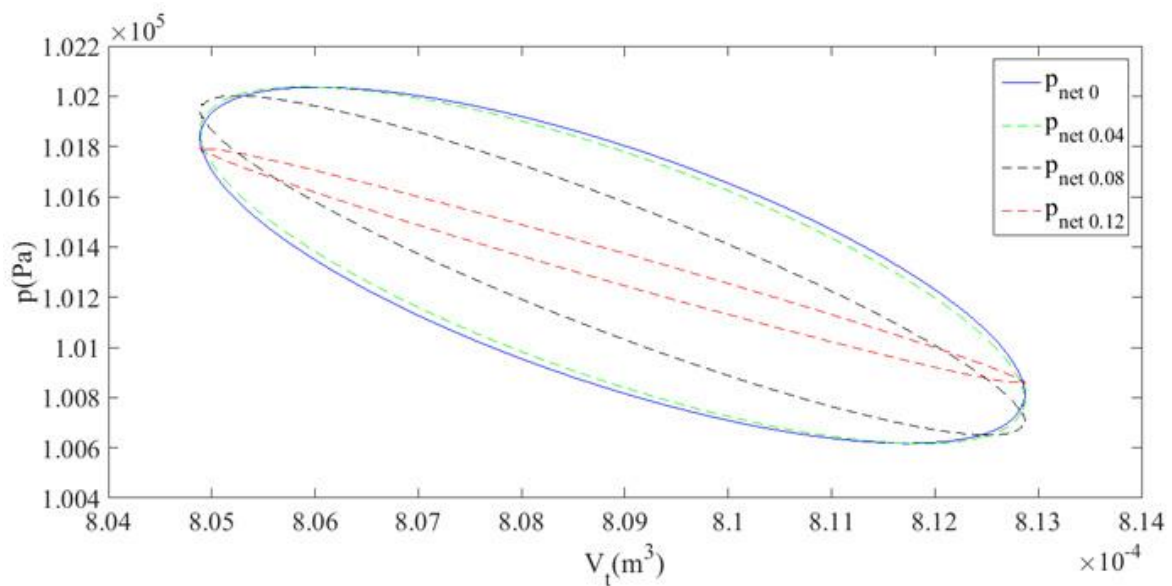
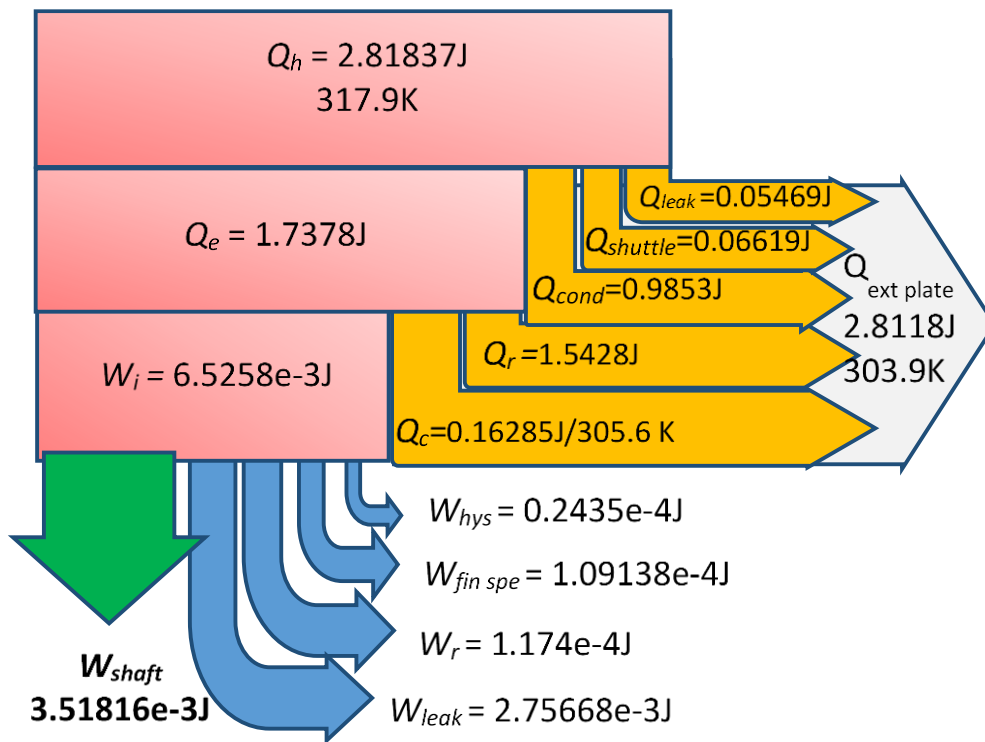


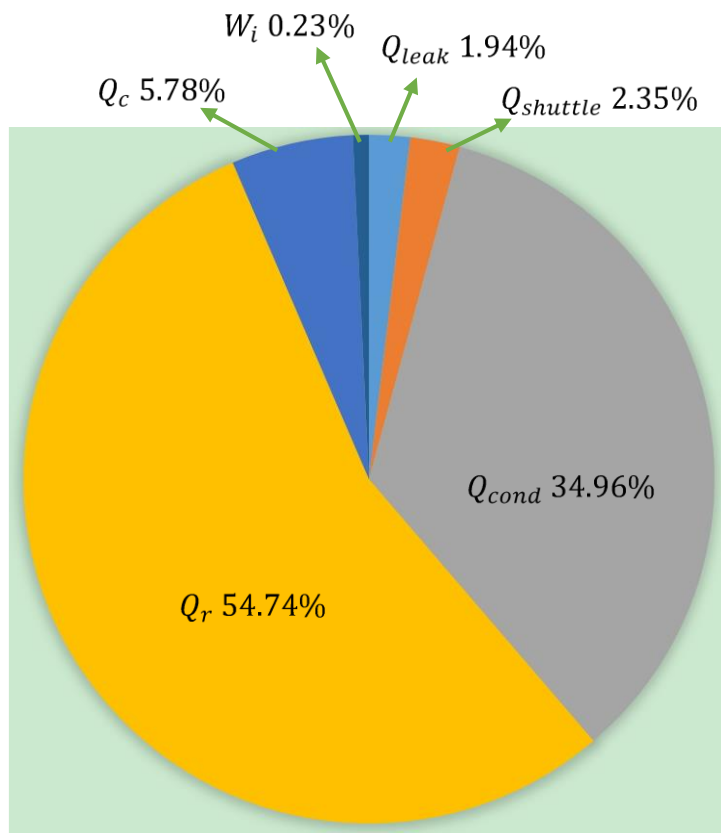
Figure 3.10  $pV$  diagram for several clearance sizes

The leakage leads to a diminution of the indicated work, which can be seen in Figure 3.10, where  $p_{net\ 0}$ ,  $p_{net\ 0.04}$ ,  $p_{net\ 0.08}$ ,  $p_{net\ 0.12}$  are the net gas pressure for clearance size about 0mm, 0.04mm, 0.08mm or 0.12mm. This figure shows that the smaller the clearance is, the less the leakage loss is. However, the clearance size cannot be reduced unlimitedly according to reference [15]. Severe frictions could appear between piston surface and cylinder wall, for very small clearance as the piston is not perfectly coaxial with the cylinder wall. For the engine studied in this paper, the minimum is estimated at about 0.05mm.

In Figure 3.11, the energy balance is represented graphically, where various losses are highlighted:  $Q_{leak}$  - the heat loss due to the mass leakage,  $Q_{shuttle}$  - the shuttle heat loss due to the reciprocating movement of the displacer between hot volume and cold volume,  $Q_{cond}$  - heat conduction loss from hot volume to cold volume,  $Q_r$  - the heat loss due to the imperfection of the regenerator,  $W_{hys}$  - the mechanical loss due to hysteresis,  $W_{fin\ spe}$  - the mechanical loss due to finite speed of the piston,  $W_r$  - the mechanical loss due to fluid friction in the regenerator and  $W_{leak}$  - the mechanical loss due to the gas leakage. Heat exchanged on hot source and cold sink, and mechanical work are also represented:  $Q_c$  - the heat rejected by the cold volume,  $Q_e$  - the heat received by the air in the hot volume,  $Q_{ext\ plate}$  - the heat rejected to the cold sink,  $W_i$  - the indicated work and  $W_{shaft}$  - the shaft work. This diagram shows that, for the investigated case, the loss due to the regenerator imperfection is the biggest one, about 54.74% of the total heat supplied from heat source while it's about 36% (using Helium)/46% (using Hydrogen) in GPU-3 SE as shown in reference [16]. The geometry of our regenerator will be improved and tested in a future work. The displacer will be replaced by a new regenerator, which will be designed based on the constructal theory [17], in order to improve the heat transfer on radial direction and to reduce it on longitudinal direction. Among percentage of the total heat loss, in our case, the regenerator imperfection is the biggest one (58.24%), followed by heat conduction (37.20%), shuttle losses (2.50%), and leakage loss (2.06%), while they are respectively 78.8%, 12.0%, 8.0%, 1.2% in the reference [14]. For this engine, the total power loss is about 46.1% of the total generated power, while it's about only 20.6% in the reference [14]. The main reason could be the small output power scale of our engine (1.4mW for our engine, 3kW for [14]). Among percentage of total power losses, leakage loss is the biggest in our case (91.6%), while in the reference [14] it's heat exchangers pressure drop (76.8%), as our regenerator hasn't filler and the clearance size is 0.08mm against 0.028mm for [14].



(a) Energy distribution



(b) Percentage of energy distribution

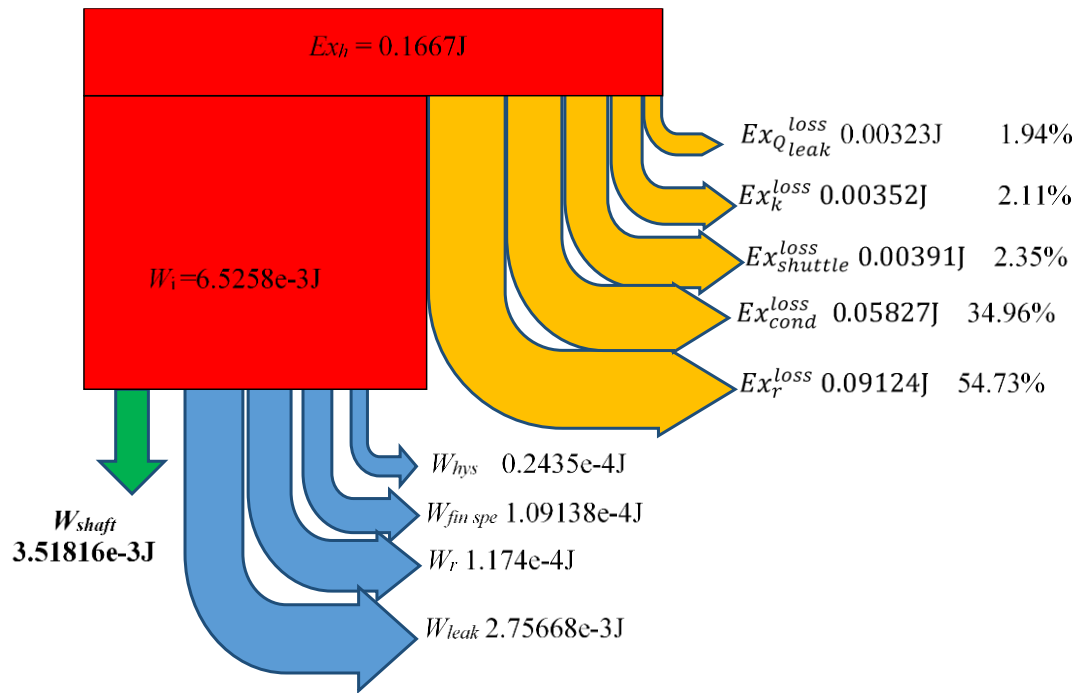
Figure 3.11 Energy balance representation for one cycle

Starting from this diagram, various efficiencies of the engine can be determined, as seen in Table 3.2. It can be confirmed that there are two sensible points of the engine to be improved: regenerator geometry and clearance size.

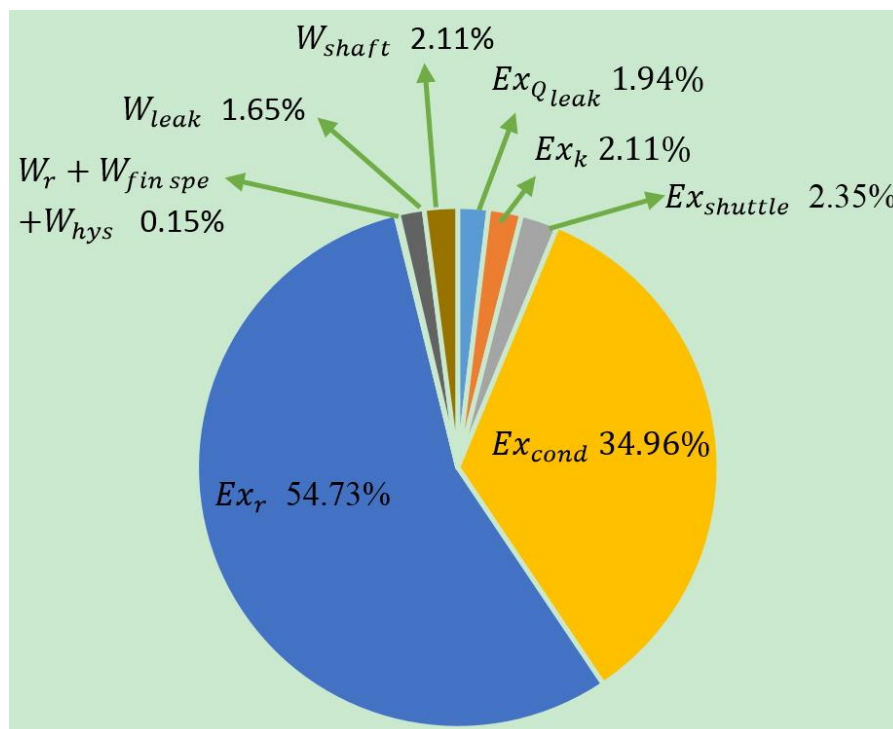
In Table 3.2 and Figure 3.11, engine losses are expressed in terms of heat or work, and then efficiencies are defined as the ratio between the predicted work and the predicted heat. As work and heat are two energies of different quality, the balance of the system must be expressed in terms of exergy which represents the maximum potential work obtained from heat, considering its temperature level. Thus, exergy balance diagram was built in Figure 3.12 and Table 3.3. It can be seen, once again, that regenerator imperfection and heat conduction have the biggest effect and that among exergy dissipations due to pressure loss, the leakage is still the biggest factor as well. These results lead us to propose some improvements to the engine geometry: to improve our regenerator geometry, to reduce conduction loss using isolating material (displacer and cylinder wall) and to decrease clearance leakage in this engine.

Table 3.2 Energy efficiencies of the engine

<b>Engine efficiency</b>	<b>expression</b>	<b>value</b>
$\eta_{Carnot}$	$1 - \frac{T_c}{T_e}$	3.89%
$\eta_{SE\ perfect\ r}$	$\frac{W_i}{Q_e - Q_r}$	3.853%
$\eta_{SE\ imperfect\ r}$	$\frac{W_i}{Q_e}$	0.3755%
$\eta_{SE\ imperfect\ r+hys}$	$\frac{W_i - W_{hys}}{Q_e}$	0.3741%
$\eta_{SE\ imperfect\ r+hys+fin\ spe}$	$\frac{W_i - W_{hys} - W_{fin\ spe}}{Q_e}$	0.3678%
$\eta_{SE\ imperfect\ r+hys+fin\ spe+r}$	$\frac{W_i - W_{hys} - W_{fin\ spe} - W_r}{Q_e}$	0.3611%
$\eta_{SE\ imperfect\ r+hys+fin\ spe+r+leak}$	$\frac{W_{shaft}}{Q_e}$	0.2024%
$\eta_{SE\ imperfect\ r+hys+fin\ spe+r+leak+heat\ los}$	$\frac{W_{shaft}}{Q_h}$	0.1248%



(a) Exergy distribution diagram



(b) Percentage of exergy distribution

Figure 3.12 Exergy analysis of the engine - exergy balance representation

Table 3.3 Various exergy efficiencies of the engine

Engine exergy efficiency	expression	value
$\eta_{ex\_SE\ perfect\ r}$	$\frac{W_i}{Ex_h - Ex_{Q_{leak}}^{loss} - Ex_{shuttle}^{loss} - Ex_{cond}^{loss} - Ex_r^{loss}}$	64.96%
$\eta_{ex\_SE\ imperfect\ r}$	$\frac{W_i}{Ex_h - Ex_{Q_{leak}}^{loss} - Ex_{shuttle}^{loss} - Ex_{cond}^{loss}}$	6.44%
$\eta_{ex\_SE\ imperfect\ r+shuttle}$	$\frac{W_i}{Ex_h - Ex_{Q_{leak}}^{loss} - Ex_{cond}^{loss}}$	6.20%
$\eta_{ex\_SE\ imperfect\ r+shuttle+cond}$	$\frac{W_i}{Ex_h - Ex_{Q_{leak}}^{loss}}$	3.99%
$\eta_{ex\_SE\ imperfect\ r+shuttle+cond+leak}$	$\frac{W_i - W_{leak}}{Ex_h}$	2.26%
$\eta_{ex\_SE\ imperfect\ r+shuttle+cond+leak+hys}$	$\frac{W_i - W_{leak} - W_{hys}}{Ex_h}$	2.25%
$\eta_{ex\_SE\ imperfect\ r+shuttle+cond+leak+hys+fin\ spe}$	$\frac{W_i - W_{leak} - W_{hys} - W_{fin\ spe}}{Ex_h}$	2.18%
$\eta_{ex\_SE\ imperfect\ r+shuttle+cond+leak+hys+fin\ spe+r}$	$\frac{W_{shaft}}{Ex_h}$	2.175%

### 3.3 Summary

In this chapter an isothermal model coupled with finite speed method has been proposed, including mass and energy balances through different spaces of the engine, to model the gamma type low temperature difference Stirling engine of the laboratory. Different kind of thermal and mechanical losses have been considered in the model, in order to analyze thermodynamic processes and losses in the Stirling Engine. The considered losses are the effects of viscous friction, regenerator imperfection, hysteresis, clearance seal leakage, displacer shuttle, finite speed piston and heat conduction.

Simulation results show that heat loss in the regenerator is the most important loss-this component represents the SE particularity which increases engine efficiency by choosing a suitable geometry and material in order to increase its function (to store and discharge heat). Work dissipation due to the leakage through clearance between piston and cylinder wall is very important too. The total working gas mass in the engine is fluctuant considering leakage and the amplitude of the pressure wave is smaller than that without leakage. In addition, it has been remarked that there is an out of phase between the pressure wave with leakage and that without leakage. The oscillation of the total working gas mass in the engine increases with the increase in the clearance size between the piston and the cylinder wall, which leads to a decrease in the

corresponding cycle work.

Energy and exergy analysis has been developed in order to show the impact of different imperfections on the engine performance. They highlighted that regenerator imperfection and leakage lead to the two most important dissipations in the engine. These results lead us to suggest some improvements to the engine geometry: to improve our regenerator geometry, to reduce conduction loss using isolating material (displacer and cylinder wall) and to decrease clearance leakage in this engine. The validation of the model can be seen in the next chapter.

## Reference

- [1] Kongtragool B. and Wongwiset S., Performance of low-temperature differential Stirling engines. *Renewable Energy*, 2007. **32**(4): p. 547-566.
- [2] Petrescu S., et al., Application of the Direct Method to irreversible Stirling cycles with finite speed. *International Journal of Energy Research*, 2002. **26**(7): p. 589-609.
- [3] Philippi I. and Feidt M. Finite time thermodynamics applied to inverse cycle machine. in XVIII Int. Congress on Refrigeration. 1991.
- [4] Ding Z.M., Chen L.G., and Sun F.R., Performance optimization of a linear phenomenological law system Stirling engine. *Journal of the Energy Institute*, 2015. **88**(1): p. 36-42.
- [5] Martaj N., Grosu L., and Rochelle P., Thermodynamic study of a low temperature difference Stirling engine at steady state operation. *International Journal of Thermodynamics*, 2007. **10**(4): p. 165.
- [6] Walker G., *Stirling engines*. 1980.
- [7] Finkelstein T., *Air engines: the history, science, and reality of the perfect engine/Theodor Finkelstein*, Allan J. Organ, 2001.
- [8] Minassians A.D., *Stirling Engines for Low-Temperature Solar-Thermal-Electric Power Generation*, in U Berkeley. 2007, UC Berkeley.
- [9] Tanaka M., Yamashita I., and Chisaka F., Flow and heat transfer characteristics of the Stirling engine regenerator in an oscillating flow. *JSME international journal. Ser. 2, Fluids engineering, heat transfer, power, combustion, thermophysical properties*, 1990. **33**(2): p. 283-289.
- [10] Hosseinzade H. and Sayyaadi H., CAFS: The Combined Adiabatic–Finite Speed thermal model for simulation and optimization of Stirling engines. *Energy Conversion and Management*, 2015. **91**: p. 32-53.
- [11] Costea M., Petrescu S., and Harman C., The effect of irreversibilities on solar Stirling engine cycle performance. *Energy conversion and management*, 1999. **40**(15): p. 1723-1731.
- [12] Urieli I. and Berchowitz D.M., *Stirling cycle engine analysis*. 1984: Taylor & Francis.
- [13] Homutescu V.M., Dumitraşcu G., and Horbaniuc B., Evaluation Of The Work Lost Due To Leaks Through Cylinder-Displacer Gap.
- [14] Babaelahi M. and Sayyaadi H., Simple-II: A new numerical thermal model for predicting thermal performance of Stirling engines. *Energy*, 2014. **69**: p. 873-890.
- [15] Takiguchi M., Kikuchi H., and Furuhashi S., Influence of clearance between piston and

- cylinder on piston friction. 1988, SAE Technical Paper.
- [16] Babaelahi M. and Sayyaadi H., Modified PSVL: A second order model for thermal simulation of Stirling engines based on convective–polytropic heat transfer of working spaces. *Applied Thermal Engineering*, 2015. **85**: p. 340-355.
- [17] Féliès G., et al., Double acting Stirling engine: Modeling, experiments and optimization. *Applied Energy*, 2015. **159**: p. 350-361.

## Chapter 4 Experimental study of the Gamma type Stirling engine

### 4.1 Presentation of experimental device

The studied solar powered Gamma type SE and its bench test (artificial sun and absorber panel) are shown in Figure 4.1. The heat source of the Gamma SE is a hot water flow on the bottom of the engine cylinder which is heated on a panel solar absorber by an artificial sun (9 lamps, 1kW for each lamp). The data of several sensors including pressure sensor (Honey well 40PC 250G), thermocouples (K type), and position sensor have been acquired by the data acquisition unit, and then imported to the computer. The top of the engine is cooled by natural convection. The engine uses air as working gas.

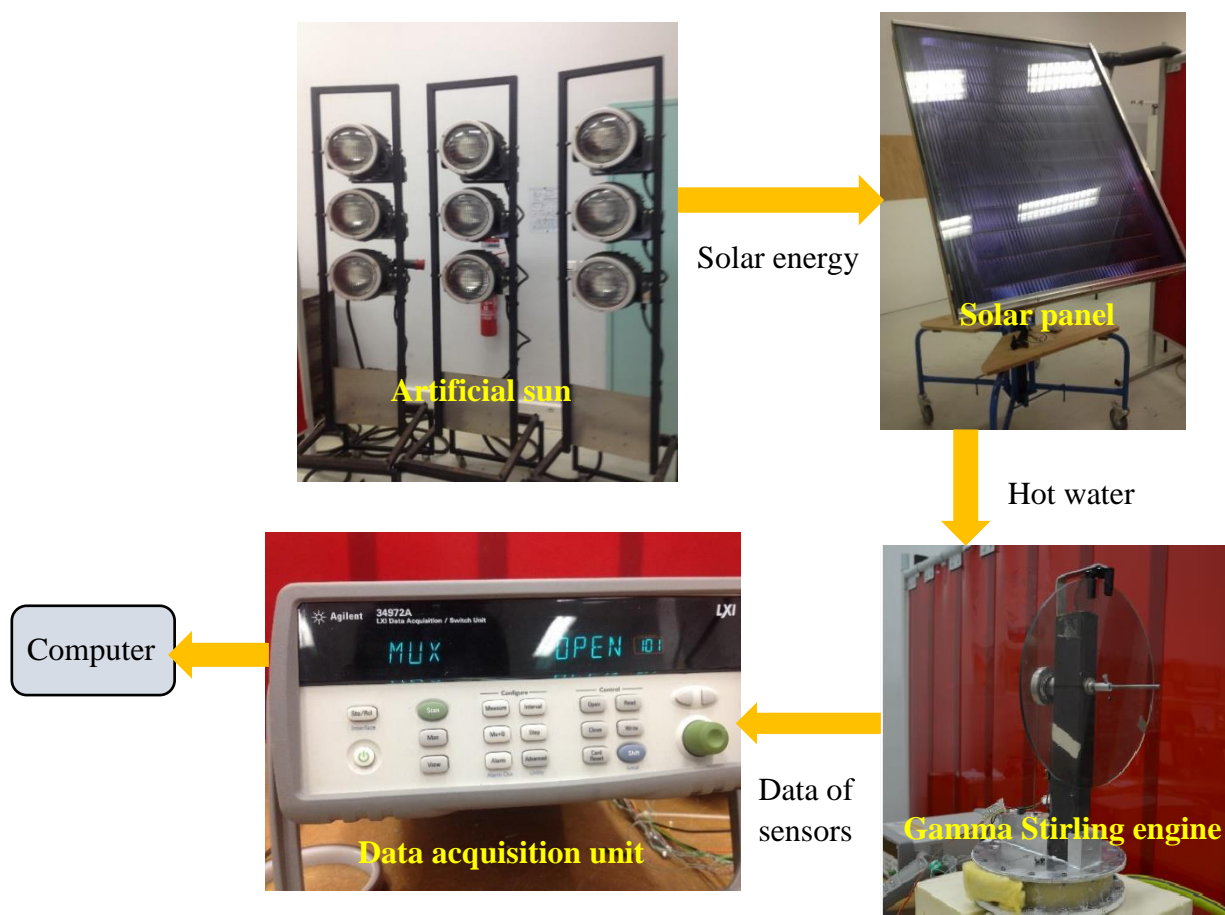


Figure 4.1 Solar powered Gamma type Stirling engine system

Figure 4.2 shows the detailed information of the Gamma type Stirling engine. The displacer and piston are connected to with the same axle which is also connected with the fly wheel.

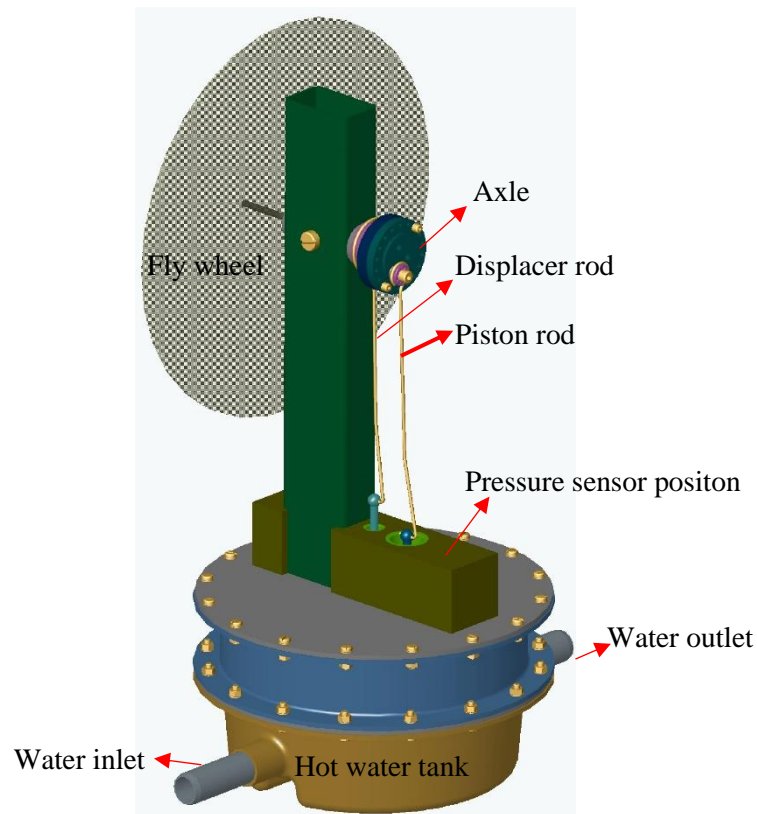


Figure 4.2 Detailed configuration of the solar powered Gamma type Stirling engine

Geometrical dimensions of the engine are presented in table 4.1 which is the same as that in the new isothermal model section.

Table 4.1 Parameters and operating condition of the experimental prototype

Working gas	air	Length of the working piston	21.3 mm
Displacer stroke	9 mm	Inner cylinder diameter	176 mm
Working piston stroke	21 mm	Working piston diameter	22 mm
Environmental temperature	299.1 K	Displacer diameter	172 mm
Length of the displacer	24.9 mm	Working piston clearance	0.08 mm
Expansion volume temperature	317.9 K	Phase shift of displacer & piston	90 degree
Compression volume temperature	305.6 K	Initial pressure $p_0$	101325 Pa
Cold sink temperature	303.9K	Frequency	0.4189

## 4.2 Comparison between experimental and simulation results

Using only three artificial sun lamps in Figure 4.1, experimental  $pV$  diagram is plotted (Figure 4.3) for the configuration presented in Table 4.1. The pressure was measured in the cold space

near the upper cylinder wall. The mechanical work is determined by integrating the  $pV$  diagram. For 149 experimental cycles, the total work is about 0.479J, thus the average for one cycle is calculated at about 0.003213J. The simulated shaft work using the Simulink program which uses the isothermal model is obtained at about 0.003518J/cycle. Therefore, an error can be estimated only about 9.49% which is very small considering the size of the engine.

In Figure 4.3 the experimental pressure range is about 100980~101650Pa, while the range is wider (about 100700~102000Pa) in the simulating section (Figure 3.10). However, the  $pV$  diagram of simulation result is much more oblate than that in Figure 4.3, here below, which gives them a very similar  $pV$  area.

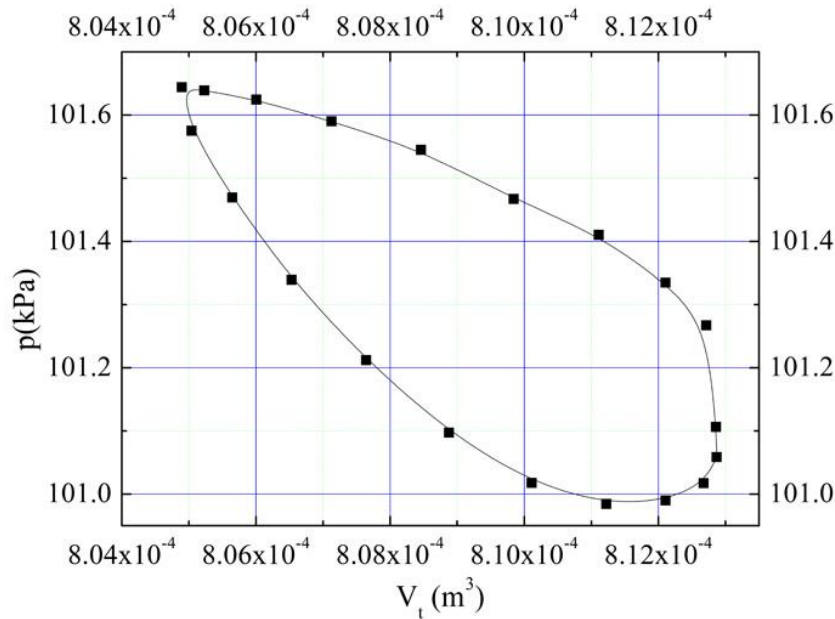


Figure 4.3 Experimental  $pV$  diagram

Actually, in this experiment, the prototype engine does not have any load, so there is no output work. The work provided per cycle is entirely consumed by mechanical friction. According to Hosseinzade H. et al, the mean pressure loss due to mechanical friction in SE can be calculated as:

$$\Delta p_f = \frac{(0.4+0.0045Z_p n) \times 10^5}{3(1-1/(3\tau))} \left(1 - \frac{1}{\tau}\right) \quad (1)$$

where,  $Z_p$  is the piston stroke,  $n$  is the rotational speed of the engine and  $\tau$  is the compression ratio.

Thus, the work loss due to mechanical friction can be calculated as:

$$W_{friction}^{irr} = 2\Delta p_f V_{C0} \quad (2)$$

Using the equation above, the mechanical friction loss is about 0.003123J/cycle. Compared to this value, the Simulation relative error becomes  $(0.003518-0.003123)/0.003123=12.65\%$ , which allows to conclude that the proposed Simulink model can accurately give the engine

behavior for different configurations and parameters of the engine.

### 4.3 Parameter effect on the Gamma type Stirling engine

Different parameters' effect on the Low Temperature Difference Gamma type Stirling engine, has been investigated.

Figure 4.4 shows the average total mass variation in the work space, ambient temperature, and cold space temperature versus the hot space temperature for a piston stroke as 16mm and a phase shift between displacer and piston is about  $96^\circ$ . All other parameters are the same as those in Table 4.1. As there is leakage through the clearance between piston and cylinder, the average density of the working gas in the working space becomes smaller with the hot space temperature increasing. Due to the cold end of the engine being cooled by natural convection, the heat transfer capacity is finite which leads to the cold space temperature increasing with the hot space temperature increasing. In addition, the ambient temperature surrounding the engine increases with the experiment proceeding, as the experiment is done in laboratory.

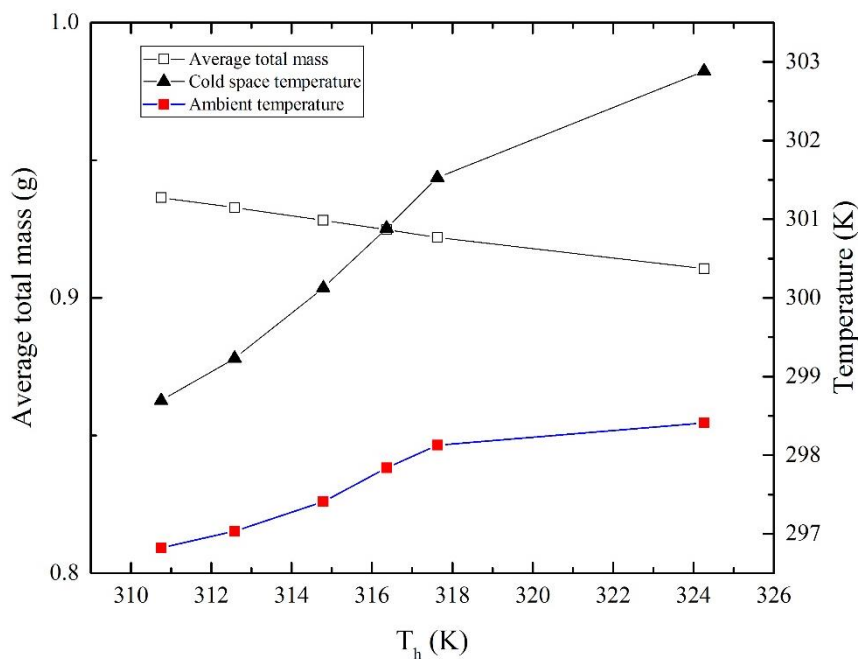


Figure 4.4 Average total mass, ambient temperature, and cold space temperature variation VS hot space temperature for  $96^\circ$  phase shift and about 16mm piston stroke

Figure 4.5 shows the frequency and the experimental and simulation power versus the hot space temperature variation for the piston stroke about 16mm and the phase shift between displacer and piston about  $96^\circ$ . It can be seen that, these parameters increase nearly linearly, with the hot space temperature increasing. The simulation results have similar curve with the experimental one.

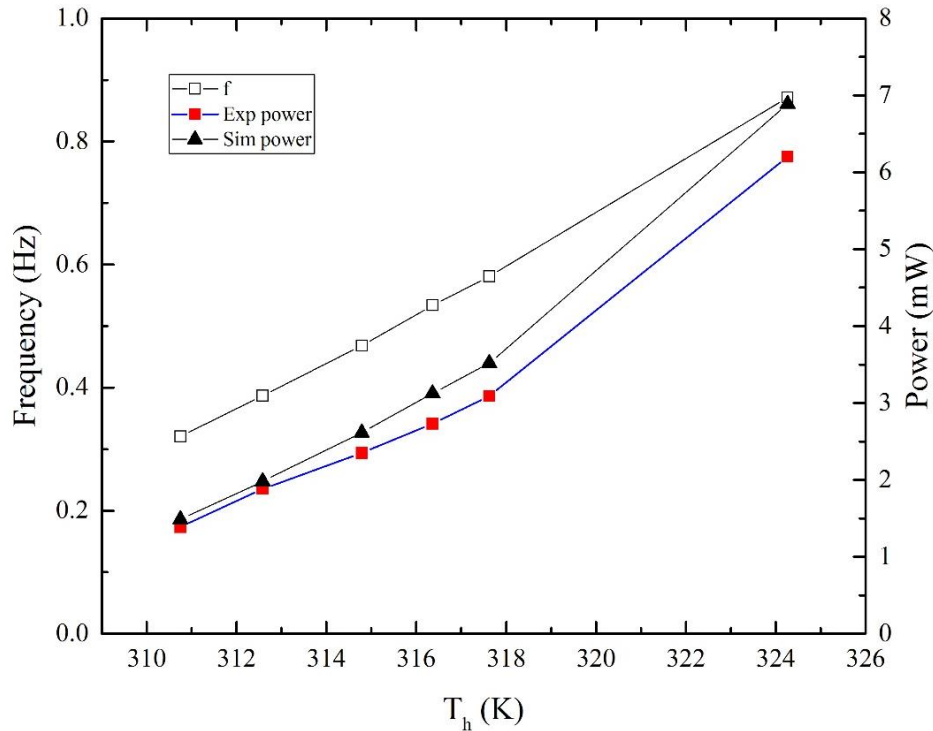


Figure 4.5 Frequency and mechanical power variation VS hot space temperature for a phase shift about  $96^\circ$  and a piston stroke about 16mm

Figure 4.6 shows the power loss variation with the hot space temperature, it can be seen that the regenerator viscous flow loss increases nearly parabolically. The piston finite speed loss increase nearly linearly but the slopes are more and more steeper. The spring hysteresis loss increases also nearly linearly with the hot space temperature increasing, but the increasing range is very small compared with the regenerator viscous flow loss and piston finite speed loss.

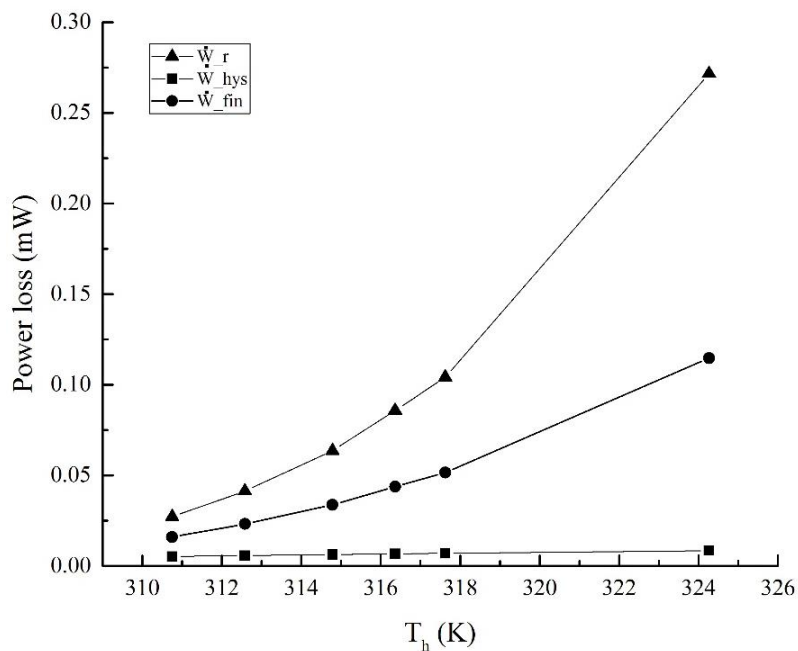


Figure 4.6 Power losses VS hot space temperature with  $96^\circ$  phase shift and 16mm piston stroke

Figure 4.7 shows the heat flow losses variation with the hot space temperature increasing. It can be seen that the heat conduction loss and regeneration imperfect loss increases nearly linearly, as both of them are linear to the temperature difference between hot and cold temperature. On the other side, the seal leakage through the clearance between piston and cylinder and the displacer shuttle loss are nearly constant which implies they are not sensitive to the hot space temperature.

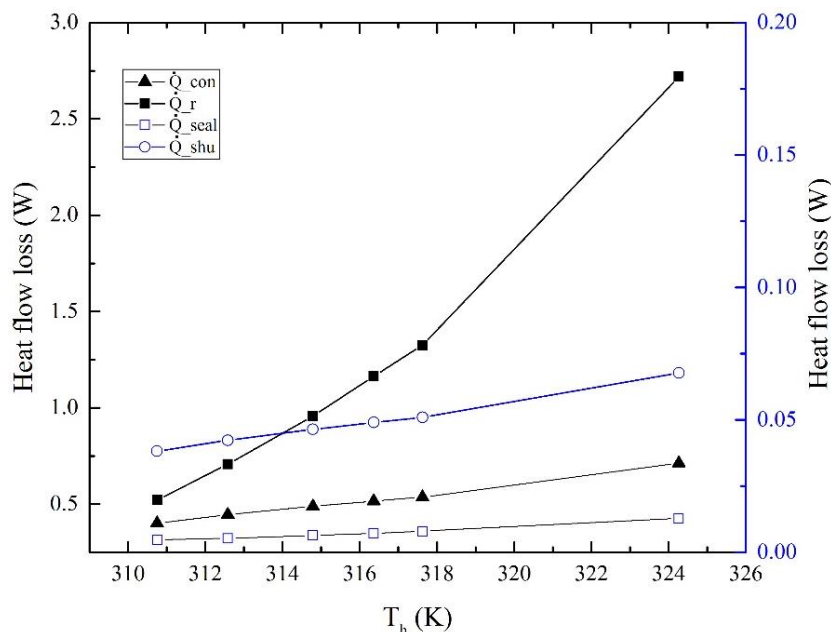


Figure 4.7 Heat flow losses VS hot space temperature with  $96^\circ$  phase shift and 16mm piston stroke

Figure 4.8 shows the experimental and simulation output mechanical power variation with the hot space temperature, at different phase shift between displacer and piston for a piston stroke about 21mm. It can be seen that for a phase shift about  $90^\circ$  the output mechanical power is bigger than others for a given value of the hot space temperature which implies that  $90^\circ$  is the optimal phase shift to get a maximal output power. In addition, the output power is nearly linear to the hot space temperature, and the closer is the phase shift to the optimum value the steeper is the slope. Comparison between experimental and simulation results can lead to seeing that the simulation results are just a little bigger than the experimental results and the gap between them are acceptable.

Figure 4.9 shows the experimental and simulation output power variation with the hot space temperature, at different phase shift between displacer and piston under the condition of 16mm piston stroke. It shows that among those phase shift  $96^\circ$  and  $114^\circ$  can get the biggest output power when the hot space temperature is the same, which implies that the optimal phase shift for maximal output power is between  $96^\circ$  and  $114^\circ$ . Similarly with that in Figure 4.8, the output power is nearly linear to the hot space temperature, and the closer is the phase shift to the optimum value the steeper is the slope. Comparing experimental and simulation results shows that the difference between them are also acceptable and becomes bigger when the hot space temperature is bigger.

Figure 4.10 shows the experimental and simulation output power variation with the hot space temperature, at different phase shift between displacer and piston for 10mm of piston stroke. It can be seen that among those phase shift,  $84^\circ$  is the optimal for the biggest output work. And the difference between simulation and experimental results are also acceptable.

If a line is plotted corresponding to the output power, 3.5mW (as the this output power can interact with as many lines as possible in Figure 5.8~5.10), in Figure 4.8 to Figure 4.10, the intersections of the red dash line and the output work line can reflect the hot space temperature variation with the phase shift under the same output work. Figure 4.11 shows the hot space temperature variation versus the phase shift when the output power is 3.5mW, and the piston stroke is 21mm, 16mm, and 10mm respectively. It can be seen that the hot space temperature decreases initially, and arrives at the bottom in the phase shift range  $85^\circ\sim 115^\circ$ , and then increases after this phase shift range. As those points have the same output power, it can be concluded that the optimal phase shift range is about  $85^\circ\sim 115^\circ$  where a minimum hot space temperature can output the same output power. Another phenomenon seen from Figure 4.11 is that the curves of 21mm, 16mm, and 10mm piston stroke are all nearly symmetrical on the two side of the optimal phase shift. In other words, if the distance between current phase shift and the optimal phase shift is the same, the output power is similar, whether it's higher or lower the optimal phase shift.

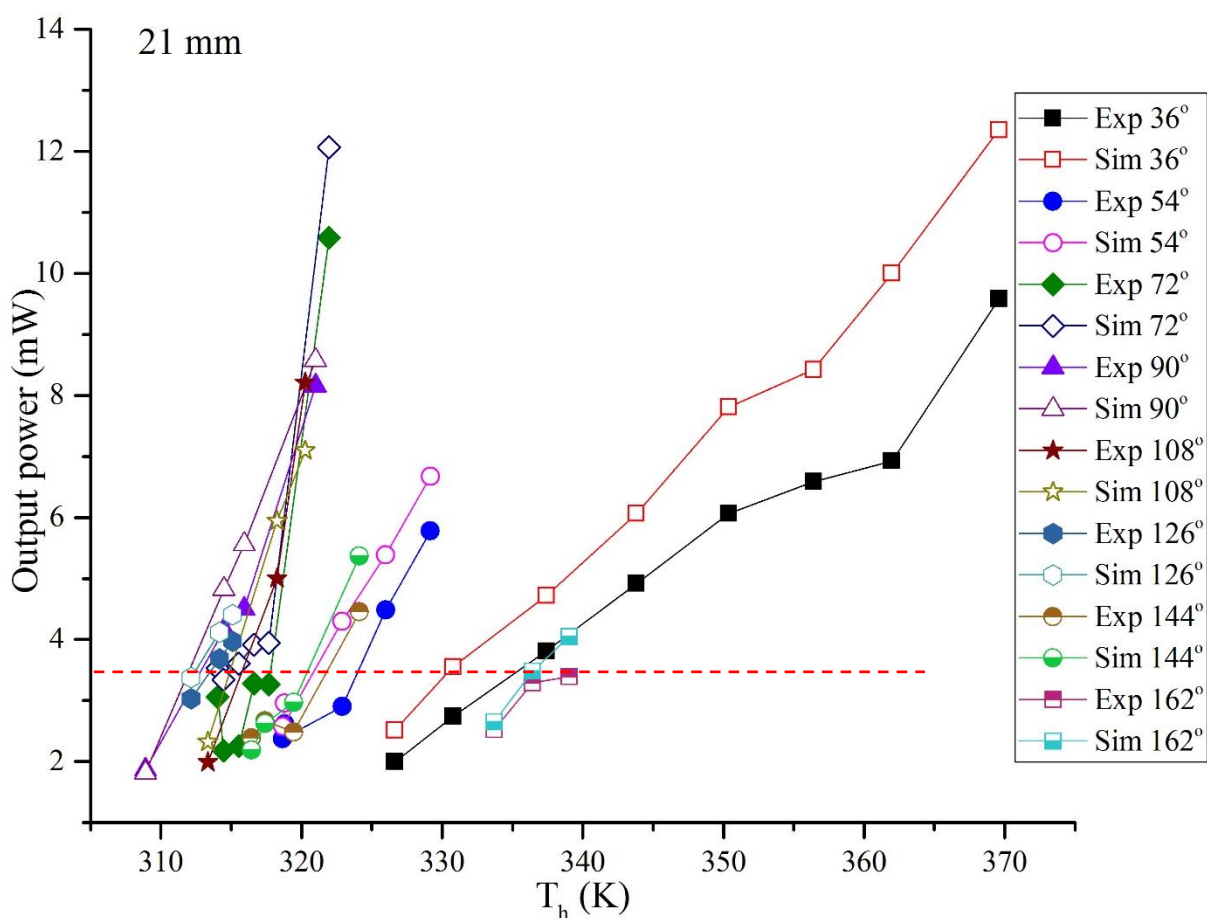


Figure 4.8 Experimental and simulation output power VS hot space temperature with different phase shift under 21mm piston stroke

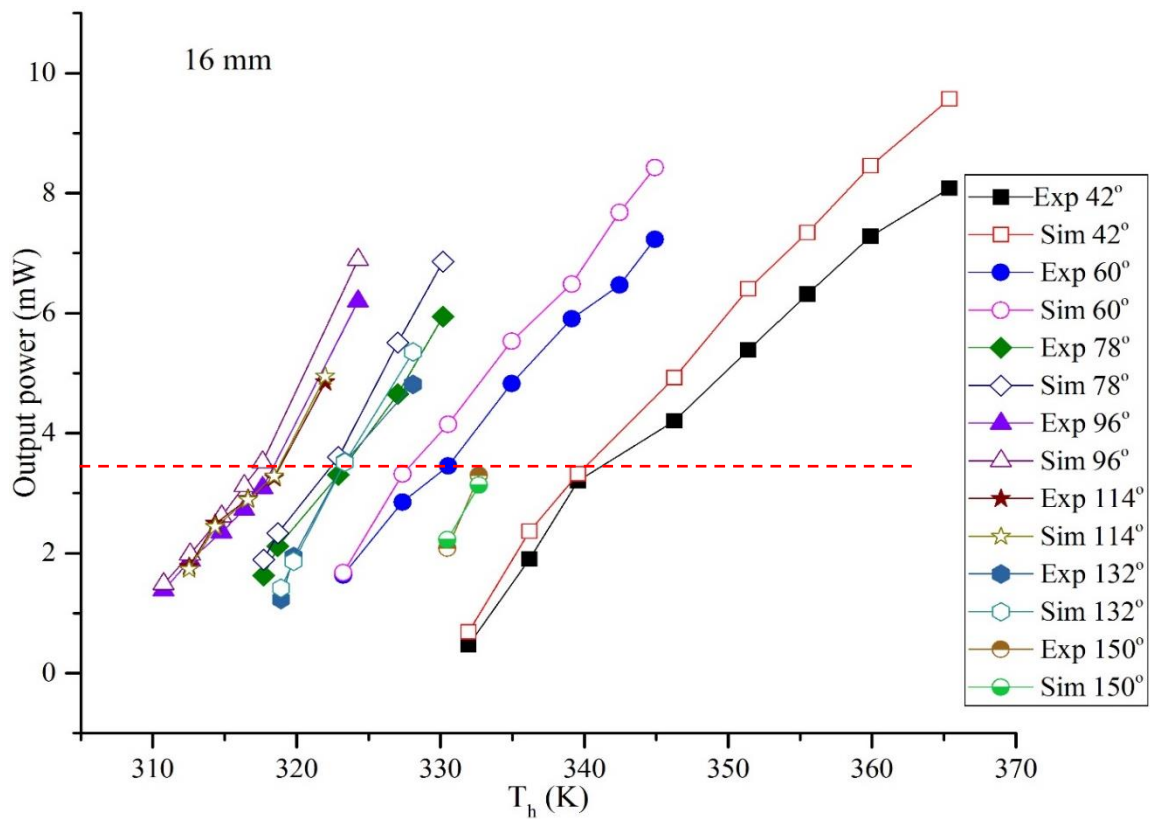


Figure 4.9 Experimental and simulation output power VS hot space temperature with different phase shift for 16mm as piston stroke

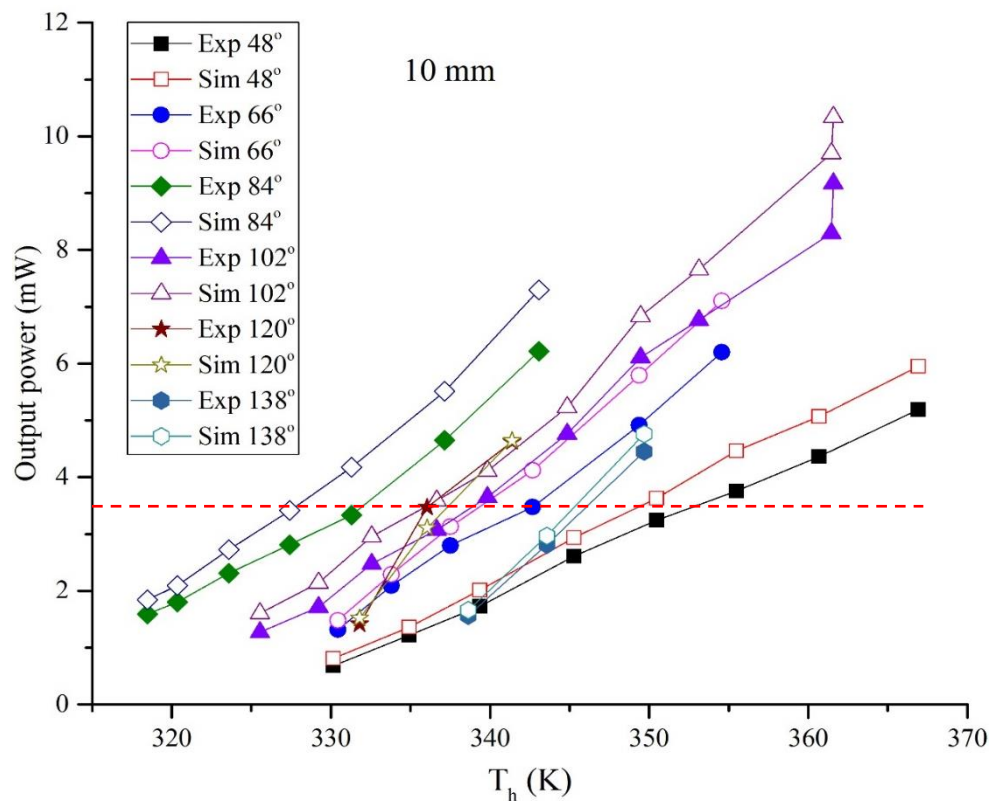


Figure 4.10 Experimental and simulation output power VS hot space temperature with different phase shift for 10mm of piston stroke

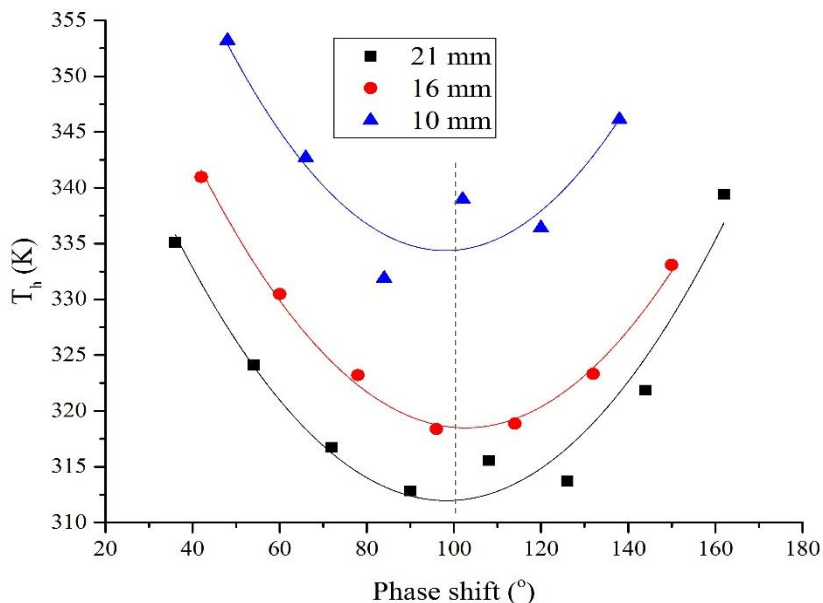


Figure 4.11 Hot space temperature variation versus phase shift for an output power about 3.5mW

Figure 4.12 shows the frequency variation with the hot space temperature at different phase shift when the piston stroke is 21mm. It can be seen that the frequency increases nearly linearly with the hot space temperature increasing, while the slope becomes smaller gradually. In addition, the frequency is smaller when the phase shift is far away from the optimal phase shift under the same hot space temperature.

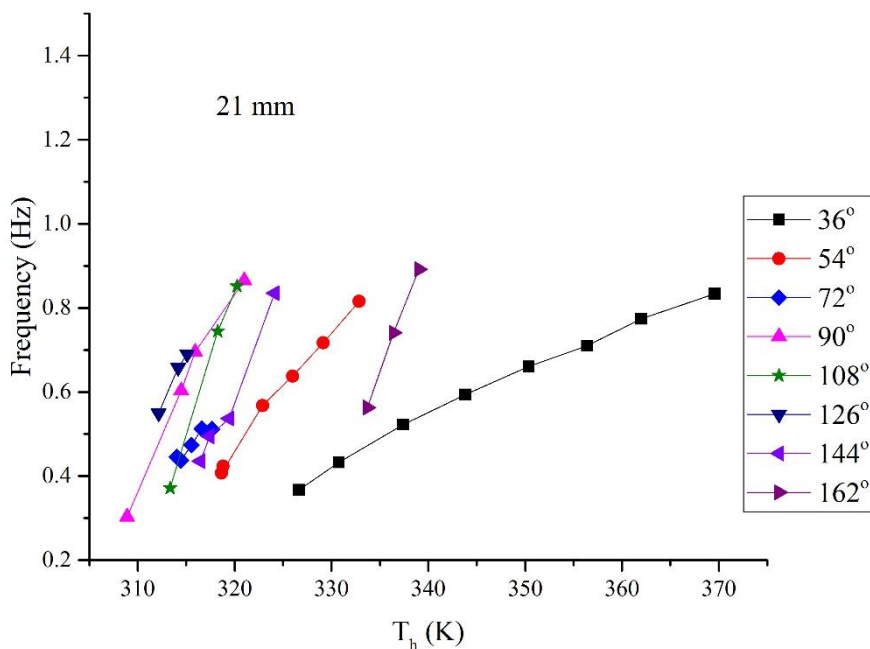


Figure 4.12 Frequency variation VS the hot space temperature with different phase shift for 21mm as piston stroke

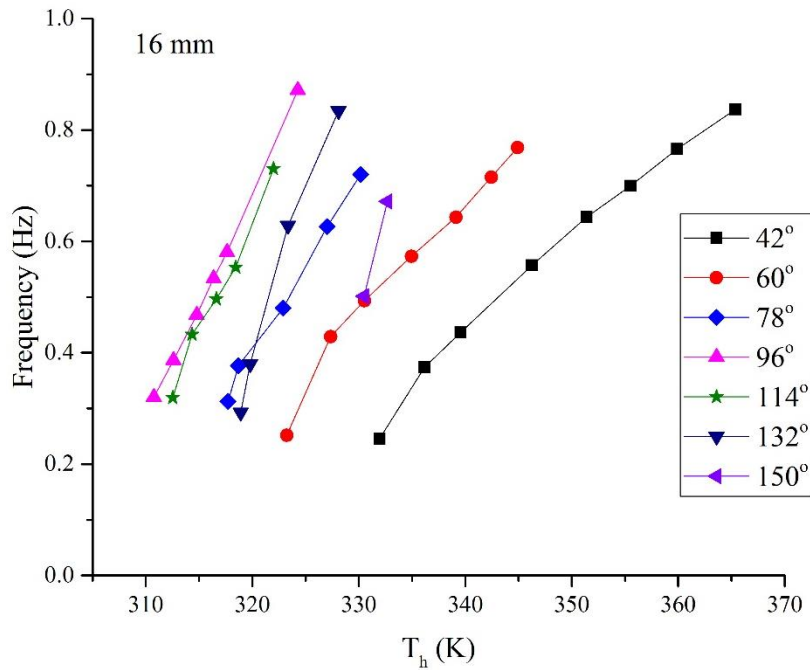


Figure 4.13 Frequency variation VS the hot space temperature with different phase shift for 16mm as piston stroke

Figure 4.13 shows the frequency variation with the hot space temperature at different phase shift when the piston stroke is 16mm. Similarly with that in Figure 4.12, it can be seen that the frequency increases also nearly linearly with the hot space temperature increasing, while the slope becomes smaller gradually. The frequency is the biggest when the phase shift is  $96^\circ$  and then  $114^\circ$  under the same hot space temperature. Which implies also that the frequency is smaller when the phase shift is far away from the optimal phase shift under the same hot space temperature.

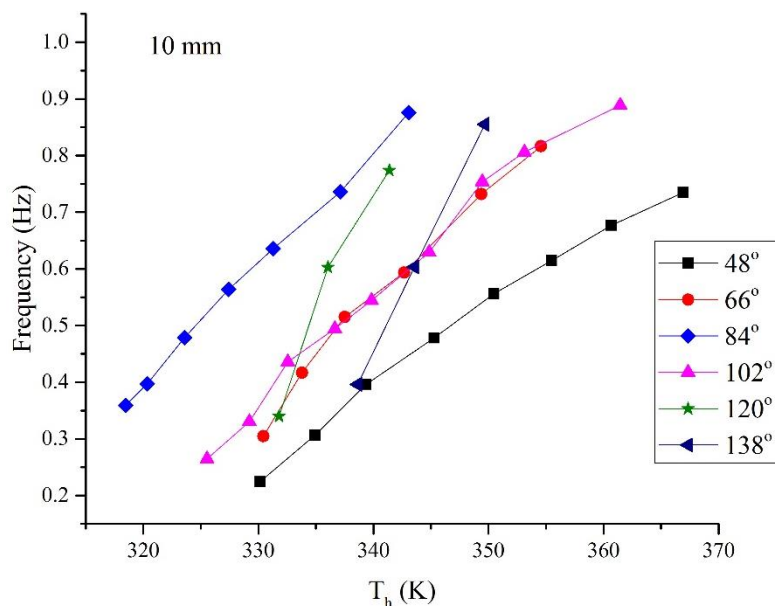


Figure 4.14 Frequency variation VS the hot space temperature with different phase shift for 10mm as piston stroke

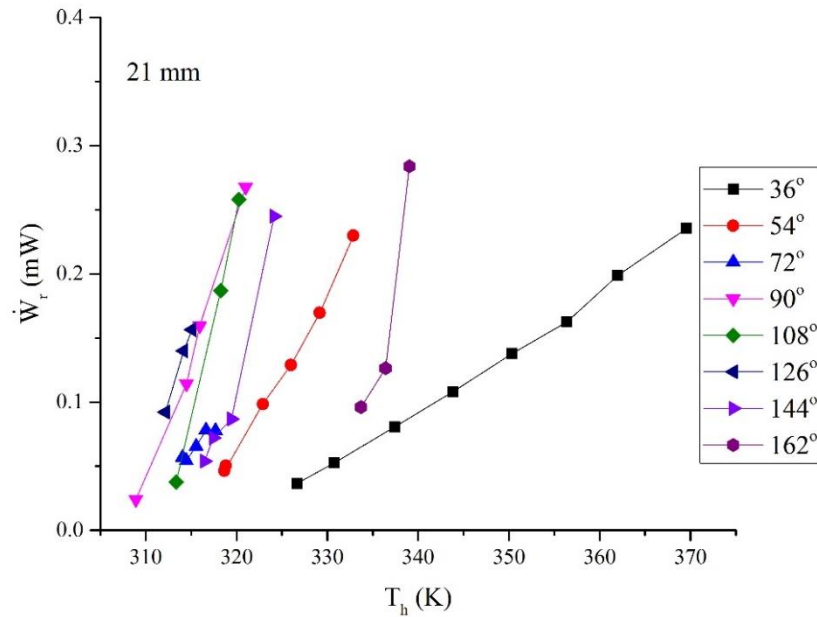


Figure 4.15 Regenerator mechanical power loss versus hot space temperature at different phase shift for 21mm as piston stroke

Figure 4.14 shows the frequency variation with the hot space temperature at different phase shift when the piston stroke is 10mm. The phenomenon is similar with the case above that the frequency increases also nearly linearly with the hot space temperature increasing, while the slope becomes smaller gradually. The frequency is biggest when the phase shift is  $84^\circ$  under the same hot space temperature.

Figure 4.15 shows the regenerator viscous flow loss variation with the hot space temperature at different phase shift when the piston stroke is 21mm. Similar with the output power, the regenerator loss increases nearly linearly, and the more the phase shift closer to the optimal phase shift the steeper are their slopes.

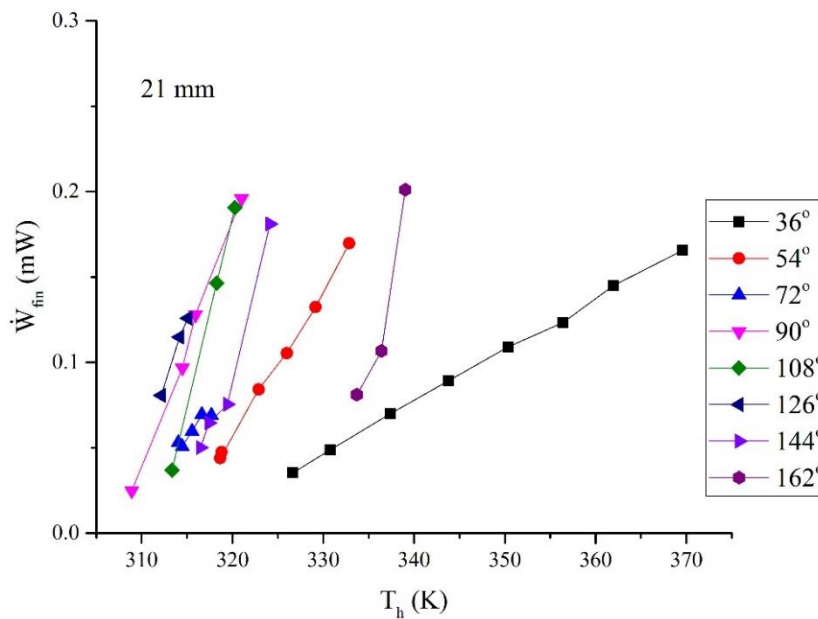


Figure 4.16 Piston finite speed loss versus hot space temperature at different phase shift for 21mm as piston stroke

Figure 4.16 shows the piston finite speed loss variation with the hot space temperature at different phase shift when the piston stroke is 21mm. The profiles of the losses at different phase shift are similar with those of regenerator loss, but the amplitudes are a little smaller than regenerator mechanical loss.

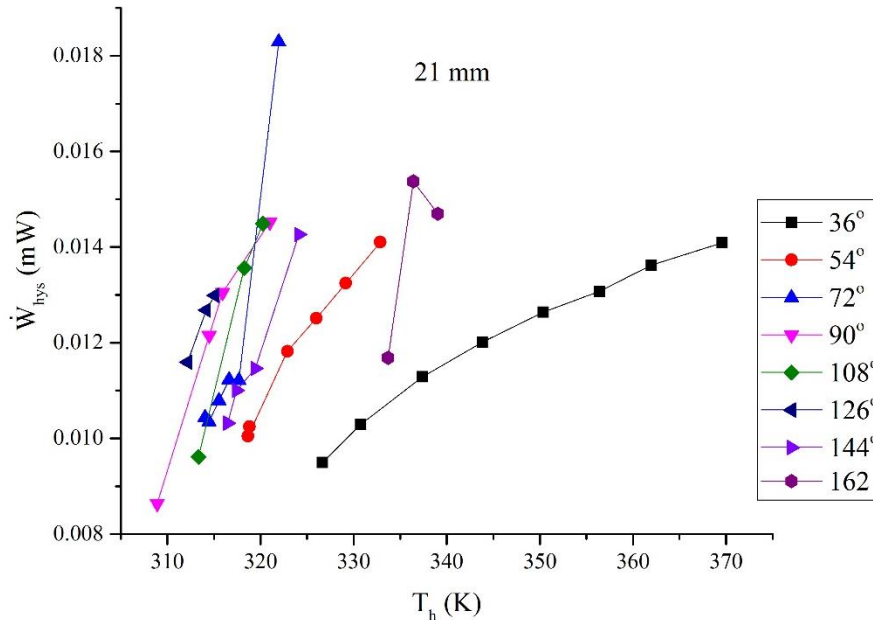


Figure 4.17 Hysteresis loss versus hot space temperature at different phase shift for 21mm as piston stroke

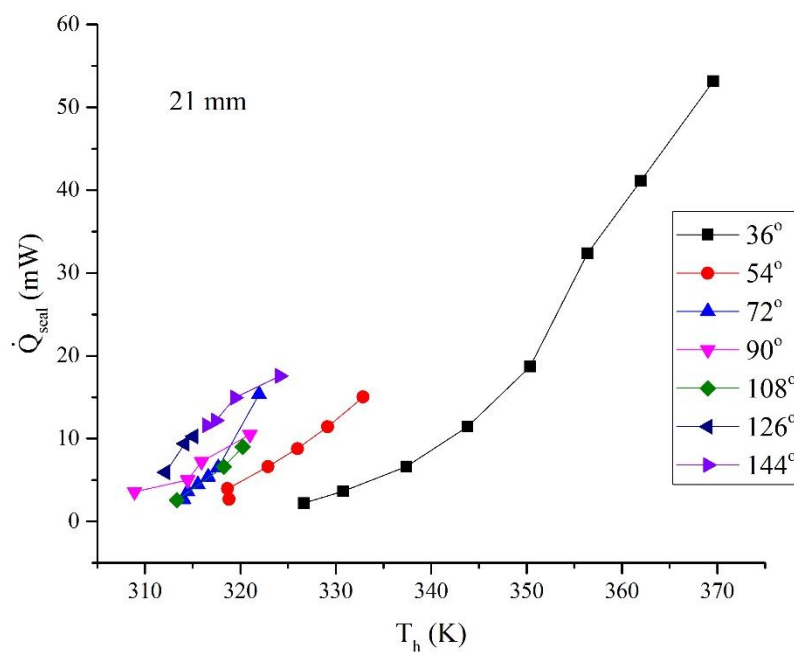


Figure 4.18 Seal leakage loss versus hot space temperature at different phase shift for 21mm as piston stroke

Figure 4.17 shows the spring hysteresis loss variation with hot space temperature at different phase shift, when the piston stroke is 21mm. It can be seen that the profiles are similar with the

regenerator mechanical loss and piston finite speed loss, but the amplitude is much smaller than the two kinds of losses. Under the most conditions, the hysteresis loss can be neglected.

Figure 4.18 shows the seal leakage loss through the clearance between piston and cylinder wall, due to the mass leakage in the clearance at different phase shift for the piston stroke about 21mm. It can be seen that the loss has gentle slope when the phase is  $36^\circ$ , and has relative steep slope when the phase shift is  $126^\circ$  and  $144^\circ$ . Overall, the bigger is the phase shift, the steeper is the slope, which implies that a big phase shift causing a bigger heat loss of leakage.

## 4.4 Summary

In this chapter, experiment has been done to validate the proposed isothermal model. The comparison between the results of the experiment and simulation at different phase shift between displacer and piston, and at different piston stroke shows that the simulation results of the isothermal model is convincing to predict the engine performance.

In addition parameter effect on the performance of the solar powered gamma type Stirling engine have also been studied experimentally and numerically. It shows that the output power, frequency, work loss (including piston finite speed loss, regenerator viscous flow loss and gas spring hysteresis loss), and heat loss (including heat conduction loss, regenerator imperfect heat exchanging loss, displacer shuttle loss, and seal leakage loss through the clearance between piston and cylinder wall) are nearly linearly to the hot space temperature. The optimal phase shift for maximal output power is about  $85^\circ\sim 115^\circ$  and is similar at different piston stroke. If the distance between the current phase shift and optimal phase shift is the same, the output power is similar, whether it's higher or lower than the optimal phase shift. In addition the frequency is smaller when the phase shift is far away from the optimal phase shift value under the same hot space temperature.

In the next chapter, a new polytropic model will be presented for the Beta type Stirling engine.



## Chapter 5 New Polyotropic Stirling Model with Losses (PSML)

### --case study for GPU-3 Stirling engine

In chapter 3 an isothermal model was used with various losses in order to study the low temperature difference Gamma type Stirling engine. The engine was divided into 3 volumes: compression volume, expansion volume, and regenerator volume. In this chapter, a new polytropic Stirling model with various losses has been developed for a beta type Stirling engine which is divided into 5 volumes: cooler, heater, compression volume, expansion volume, and regenerator. This second order model has been developed in order to propose a numerical *Matlab* code with reduced calculation duration, being able to indicate the performance of gamma and beta type Stirling engine for different operation conditions. Most of the researchers who have developed the second order model in the previous work [18-28] used isothermal or adiabatic assumption in the compression and expansion volumes. However, the working gas evolves neither an entire isothermal nor an entire adiabatic process in these two volumes. A polytropic process assumption in the compression and expansion volumes can be more generalized, as the polytropic process can include isothermal, adiabatic, or other processes at the same time.

In this chapter, a modified Polyotropic Stirling engine Model with various Losses (PSML) has been proposed based on the adiabatic model. Several losses are considered, including regenerator imperfection loss, heat conduction loss, fluid viscosity loss in heat exchangers (heater, cooler and regenerator), mass leakage loss from working space to buffer space, shuttle heat exchange and mass leakage in the gap between the displacer and the cylinder, mechanical friction loss, piston finite speed loss, hysteresis spring loss, and temperature difference between the gas and the wall in the heater/cooler. All these losses are calculated in the same time step as they can interact each other. Among them, the mass leakage through clearance between displacer and cylinder wall is the new section compared with the previous studies.

## 5.1 Mathematic model

### 5.1.1 Basic adiabatic model

The basic adiabatic model of Stirling engine [1] is based on the division of the engine into 5 volumes: compression volume, cooler, regenerator, heater and expansion volume.

The main assumptions are:

Uniform pressure in the engine.

Adiabatic process in compression and expansion volume.

Ideal working gas in the engine.

No mass leakage from working space to outside.

Heat losses and pressure losses are ignored.

Main mathematical equations of the model can be seen in table 5.1.

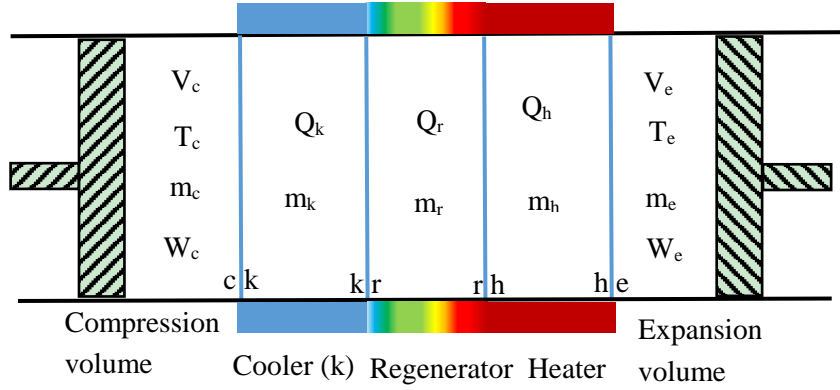


Figure 5.1 Sketch of Stirling engine model

Table 5.1 Main equations of traditional adiabatic model [1]

$p = \frac{m_t r g}{\frac{V_c}{T_c} + \frac{V_k}{T_k} + \frac{V_r}{T_r} + \frac{V_h}{T_h} + \frac{V_e}{T_e}}$	$\frac{dT_c}{T_c} = \frac{dV_c}{V_c} + \frac{dp}{p} - \frac{dm_c}{m_c}$
$m_i = \frac{pV_i}{r_g T_i}, (i = c, k, r, h, e)$	$\frac{dT_e}{T_e} = \frac{dV_e}{V_e} + \frac{dp}{p} - \frac{dm_e}{m_e}$
$dm_i = m_i \frac{dp}{p}, (i = k, r, h)$	$\delta Q_k = \frac{c_v}{r_g} V_k dp - c_p T_{ck} dm_{ck} + c_p T_{kr} dm_{kr}$
$dm_c = -dm_{ck}$	$\delta Q_r = \frac{c_v}{r_g} V_r dp - c_p T_{kr} dm_{kr} + c_p T_{rh} dm_{rh}$
$dm_e = dm_{he}$	$\delta Q_h = \frac{c_v}{r_g} V_h dp - c_p T_{rh} dm_{rh} + c_p T_{he} dm_{he}$
$dm_{kr} = dm_{ck} - dm_k$	$\delta W_e = -pdV_e, \delta W_c = -pdV_c$
$dm_{rh} = dm_{kr} - m_r$	$T_r = \frac{T_e - T_c}{\ln\left(\frac{T_e}{T_c}\right)}$
$dp = -\frac{\gamma p \left( \frac{dV_c}{T_{ck}} + \frac{dV_e}{T_{he}} \right)}{\frac{V_c}{T_{ck}} + \frac{V_e}{T_{he}} + \gamma \left( \frac{V_k}{T_k} + \frac{V_r}{T_r} + \frac{V_h}{T_h} \right)}$	

$dm_c = \frac{pdV_c + \frac{V_c dp}{\gamma}}{T_{ck} r_g}, (T_{ck} = T_c \text{ if } m_{ck} > 0, T_{ck} = T_k \text{ if } m_{ck} < 0)$
$dm_e = \frac{pdV_e + \frac{V_e dp}{\gamma}}{T_{he} r_g}, (T_{he} = T_h \text{ if } m_{he} > 0, T_{he} = T_e \text{ if } m_{ck} < 0)$

### 5.1.2 New Polytropic Stirling Model based on the adiabatic model (PSML)

As there is a clearance between piston/displacer and cylinder wall, there is mass leakage from working space to buffer space and from compression volume to expansion volume for Beta and Gamma type Stirling engine (seen in Figure 5.2), during the reciprocating movement of piston/displacer respectively. In the new model proposed here, mass leakage effect in the displacer clearance has been considered. Therefore, a sketch of the new model is presented in Figure 5.3. A bypass from compression volume to expansion volume has been added to represent the clearance between displacer and cylinder wall.

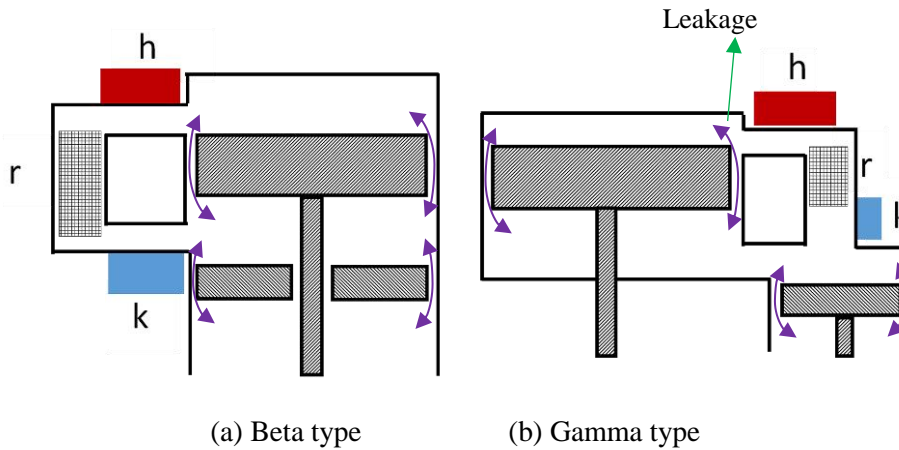


Figure 5.2 Mass leakage through the clearance in Stirling engine

There is a temperature difference between compression and expansion volumes of Stirling engine, which is separated by the displacer. However, the displacer is in contact with different temperature layers of the working gas, during its reciprocating movement, which causes heat loss from expansion volume to compression volume, called shuttle loss. The shuttle loss by displacer reciprocating movement can be expressed as [2, 3]:

$$\dot{Q}_{shuttle} = \frac{\pi Z_d^2 K_g D_d}{8 g_d L_d} (T_e - T_c) \quad (1)$$

The mass leakage through clearance between displacer and cylinder wall,  $dm_{ce}$ , can be calculated according to reference [4] using:

$$\dot{m}_{ce} = \pi D_d \frac{p}{4 r_g T_{ave}} \left( U_d g_d - \frac{g_d^2 \Delta p_{ce}}{6 \mu L_d} \right) \quad (2)$$

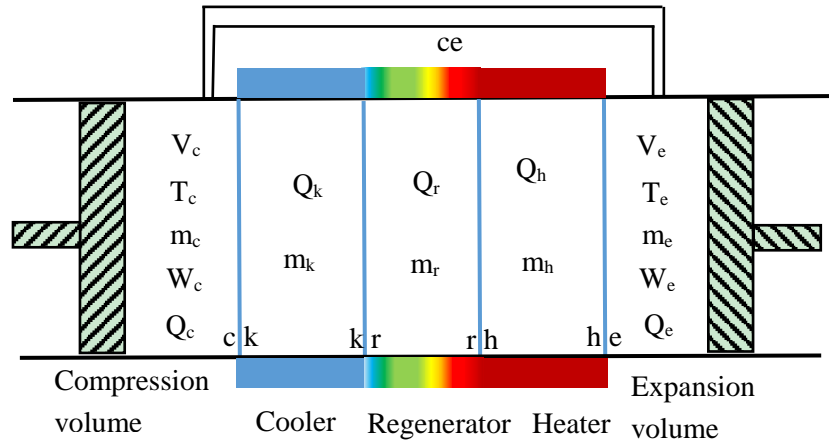


Figure 5.3 New model sketch of the Beta or Gamma type Stirling engine

The pressure of the engine can be expressed based on ideal gas equation:

$$p^n = \frac{m_t^n r_g}{\frac{V_c + V_k + V_r + V_h + V_e}{T_c + T_k + T_r + T_h + T_e}} \quad (3)$$

In this equation, the total mass depends on the time step and the corresponding leakage. Thus, the mass in each volume can be expressed, for each time step, as:

$$m_i^n = \frac{p^n V_i}{r_g T_i}, \quad (i = k, r, h) \quad (4)$$

Each volume is considered as an open system (Figure 5.4) for which the energy and the exergy balance can be written as:

$$dE = \delta Q + \delta p dV - dI + dm_{in} \left( gz_{in} + \frac{u_{in}^2}{2} \right) + dH_{in} - dm_{out} \left( gz_{out} + \frac{u_{out}^2}{2} \right) - dH_{out} \quad (5-a)$$

$$dEx = dEx_Q + \delta W + dm_{in} \left( gz_{in} + \frac{u_{in}^2}{2} \right) + dEx_{H_{in}} - dm_{out} \left( gz_{out} + \frac{u_{out}^2}{2} \right) - dEx_{H_{out}} \quad (5-b)$$

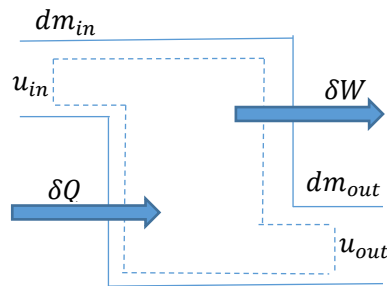


Figure 5.4 Open system sketch

The shuttle heat loss by displacer ( $Q_{shuttle}$ ) and heat exchange by polytropic process ( $Q_{poly}$ ) are taken into account for compression/expansion volume studying [5]. The kinematic and potential energy variation can be neglected due to the small dimension of the engine and the small velocity of the working gas. Therefore, the energy balance can be applied to the compression and expansion volumes as:

$$\delta Q_{shuttle} + \delta Q_{c\ poly} = \delta Q_c = \frac{c_p}{r_g} p dV_c + \frac{c_v}{r_g} V_c dp + c_p T_{ck} dm_{ck} + c_p T_{ce} dm_{ce} \quad (6)$$

$$-\delta Q_{shuttle} + \delta Q_{e\ poly} = \delta Q_e = \frac{c_p}{r_g} p dV_e + \frac{c_v}{r_g} V_e dp - c_p T_{he} dm_{he} - c_p T_{ce} dm_{ce} \quad (7)$$

The polytropic number corresponding to compression and expansion process can be calculated as:

$$n_{i\ poly} = -\frac{v_i dp}{p dv_i} = -\frac{\frac{r_g T_i dp}{p}}{p \left( r_g T_i \frac{-1}{p^2} dp + \frac{r_g}{p} dT_i \right)} = 1 + \frac{p dT_i}{T_i dp - p dT_i} = 1 + \frac{1}{\frac{T_i dp}{p dT_i} - 1}, \quad (i = c, e) \quad (8)$$

According to references [5, 6], the polytropic heat transfer can be calculated as:

$$Q_{i\ poly} = m_i c_{ni} (T_0 - T_i), \quad (i = c, e) \quad (9)$$

$$\delta Q_{i\ poly} = c_{ni} (T_0 - T_i) dm_i - m_i c_{ni} dT_i, \quad (i = c, e) \quad (10)$$

where  $T_0$  is the volume surrounding temperature,  $c_{ni}$  is polytropic specific heat capacity which can be calculated as  $c_{ni} = c_v \frac{n_{i\ poly} - \gamma}{n_{i\ poly} - 1}$ , ( $i = c, e$ ) [5].

Then applying the energy balance equation to the cooler, regenerator, and heater, the heat transfer in the three volumes can be expressed as:

$$\delta Q_k = \frac{c_v}{r_g} V_k dp - c_p T_{ck} dm_{ck} + c_p T_{kr} dm_{kr} \quad (11)$$

$$\delta Q_r = \frac{c_v}{r_g} V_r dp - c_p T_{kr} dm_{kr} + c_p T_{rh} dm_{rh} \quad (12)$$

$$\delta Q_h = \frac{c_v}{r_g} V_h dp - c_p T_{rh} dm_{rh} + c_p T_{he} dm_{he} \quad (13)$$

Due to the polytropic process in the compression and expansion volumes, it's supposed that when the working gas flows from the compression volume to the cooler, the working gas temperature on their interface (between compression volume and cooler) ' $T_{ck}$ ' is the same as that in the compression volume, and it is higher than the cooler gas temperature. When the working gas flows from the cooler to the compression volume, the the working gas temperature on the interface ' $T_{ck}$ ' is equal to the gas temperature in the cooler. The interface temperature between the expansion volume and the heater is defined following the same idea. Due to the imperfection of the regenerator, when the gas flows from the cooler to the regenerator, the working gas temperature on the interface between these volumes is supposed to be the same as that in the cooler; and when the working gas flows from the regenerator to the cooler, the working gas temperature on the interface between them is supposed to be higher than that in cooler. The temperature difference depends on the heat transfer efficiency of the regenerator,  $\varepsilon_r$ .

Therefore, considering the mass flow direction on the interface, the interface temperatures can be expressed as:

$$T_{ck} = T_c, \text{ if } dm_{ck} \geq 0 \quad (14-a)$$

$$T_{ck} = T_k, \text{ if } dm_{ck} < 0 \quad (14-b)$$

$$T_{ce} = T_c, \text{ if } dm_{ce} \geq 0 \quad (14-c)$$

$$T_{ce} = T_e, \text{ if } dm_{ce} < 0 \quad (14-d)$$

$$T_{kr} = T_k, \text{ if } dm_{kr} \geq 0 \quad (14-e)$$

$$T_{kr} = T_k + (1 - \varepsilon_r)(T_h - T_k), \text{ if } dm_{kr} < 0 \quad (14-f)$$

$$T_{rh} = T_h - (1 - \varepsilon_r)(T_h - T_k), \text{ if } dm_{rh} \geq 0 \quad (14-g)$$

$$T_{rh} = T_h, \text{ if } dm_{rh} < 0 \quad (14-h)$$

$$T_{he} = T_h, \text{ if } dm_{he} \geq 0 \quad (14-i)$$

$$T_{he} = T_e, \text{ if } dm_{he} < 0 \quad (14-j)$$

The mass variation in the volumes can be expressed as:

$$-dm_c = dm_{ce} + dm_{ck} \quad (15-a)$$

$$dm_{kr} = dm_{ck} - dm_k \quad (15-b)$$

$$dm_{rh} = dm_{kr} - dm_r \quad (15-c)$$

$$dm_e = dm_{ce} + dm_{he} \quad (15-d)$$

Combining equation (6), (7), (15-a) and (15-d), the mass variation in compression and expansion volume can be expressed as:

$$dm_c = - \frac{\delta Q_{shuttle} + \delta Q_{c poly} - \frac{c_p}{r_g} p dV_c - \frac{c_v}{r_g} V_c dp - c_p T_{ce} dm_{ce}}{c_p T_{ck}} - dm_{ce} \quad (16-a)$$

$$dm_e = \frac{\delta Q_{shuttle} - \delta Q_{e poly} + \frac{c_p}{r_g} p dV_e + \frac{c_v}{r_g} V_e dp - c_p T_{ce} dm_{ce}}{c_p T_{he}} + dm_{ce} \quad (16-b)$$

From the equation (4) the mass variation on the cooler, regenerator and heater can be expressed as:

$$dm_i = m_i \frac{dp}{p}, (i = k, r, h) \quad (17)$$

According to the ideal gas equation,  $pV = mr_g T$ , the temperature in compression and expansion space can be calculated using following differential forms:

$$\frac{dT_c}{T_c} = \frac{dV_c}{V_c} + \frac{dp}{p} - \frac{dm_c}{m_c} \quad (18-a)$$

$$\frac{dT_e}{T_e} = \frac{dV_e}{V_e} + \frac{dp}{p} - \frac{dm_e}{m_e} \quad (18-b)$$

Combining (16-a), (16-b) and (17) we can express the differential of the pressure in the engine as:

$$dp = \frac{\frac{\delta Q_{shuttle} + \delta Q_{cpoly} - \frac{c_p}{r_g} p dV_c - c_p T_{ce} dm_{ce}}{c_p T_{ck}} - \frac{\delta Q_{shuttle} - \delta Q_{cpoly} + \frac{c_p}{r_g} p dV_e - c_p T_{ce} dm_{ce}}{c_p T_{he}}}{\frac{V_k}{T_k} + \frac{V_r}{T_r} + \frac{V_h}{T_h} + \frac{V_e}{\gamma T_{he}} + \frac{V_c}{\gamma T_{ck}}} r_g \quad (19)$$

Due to the leakage in the clearance between piston and cylinder, the total mass in the engine is actually fluctuating, when the working space pressure is higher than the pressure in the buffer space, there is mass leakage from working space to the buffer volume; and when the working space pressure is lower than the buffer space pressure, the mass leakage direction is inverse. Therefore, the total working gas mass in a new time step can be expressed as the difference between the total working gas mass in the previous time step and the mass leakage during the time of one time step:

$$m_t^n = m_t^{n-1} - dm_t \quad (20)$$

where  $dm_t$  is the mass leakage in one time step, as can be seen in leakage loss section.

### 5.1.2.1 Heat exchanger loss

In SE, working fluid has an oscillated flow in the regenerator. Pressure loss due to the working fluid viscosity can be expressed as [7]:

$$\Delta p_r(t) = \Delta p_{max} \cos(\omega t + \varphi_{initial}) \quad (21)$$

where  $\varphi_{initial}$  is the initial phase angle and  $\omega$  is the angular speed of the SE.

where  $\Delta p_{max}$  is calculated according to Tanaka et al [8] who get the following expression to air SE, using experimental results:

$$\Delta p_{max} = \frac{\rho}{2} f_{max} \frac{L_r}{D_r} u_{max}^2 = \frac{\rho}{2A_0^2} f_{max} \frac{L_r}{D_r} \dot{V}_{max}^2 \quad (22)$$

where  $f_{max} = \frac{175}{Re_{max}} + 1.6$ ,  $\rho$  is the average density of working fluid in the engine,  $L_r$  is the length of the regenerator,  $D_r$  is hydraulic diameter in the regenerator,  $A_0$  is the fluid cross section area of the regenerator,  $\dot{V}_{max}$  is the maximum volume rate of the working fluid in the regenerator and  $Re$  is the Reynolds number.

For the heater and cooler, the pressure loss can be expressed as:

$$\Delta p_i = f_i \frac{L_i \rho_i u_i^2}{2D_i}, (i = h, k) \quad (23)$$

where the friction factor,  $f_i$ , can be calculated from reference [9] as:

$$f_i = \frac{64}{Re_i}, \text{ if } Re_i < 2300 \quad (24-a)$$

$$f_i = (0.79 \ln(Re_i) - 1.64)^{-2}, \text{ if } Re_i > 2300 \quad (24-b)$$

The pressure difference between compression and expansion volume,  $\Delta p_{ce}$ , can be calculated as the total pressure loss in cooler, regenerator and heater which can be calculated as:

$$\Delta p_{ce} = \sum_{i=k,r,h} |\Delta p_i| \quad (25)$$

The total power loss due to the flow loss due to viscosity in cooler, regenerator and heater can be calculated as the product of pressure loss and the flow volume of working gas through the cooler, regenerator, and heater:

$$\delta W_{loss\ k,r,h} = \left| \Delta p_k \frac{dV_{ck} + dV_{kr}}{2} \right| + \left| \Delta p_r \frac{dV_{kr} + dV_{rh}}{2} \right| + \left| \Delta p_h \frac{dV_{rh} + dV_{he}}{2} \right|$$

According to the ideal gas equation, the total power loss can be expressed as:

$$\delta W_{loss\ k,r,h} = \left| \Delta p_k \frac{r_g T_{ck} dm_{ck} + r_g T_{kr} dm_{kr}}{2p} \right| + \left| \Delta p_r \frac{r_g T_{kr} dm_{kr} + r_g T_{rh} dm_{rh}}{2p} \right| + \left| \Delta p_h \frac{r_g T_{rh} dm_{rh} + r_g T_{he} dm_{he}}{2p} \right| \quad (26)$$

As finite heat transfer area and finite heat transfer time are considered on the regenerator, the imperfect heat transfer will be defined by the thermal efficiency of the regenerator, expressed according to [7] as:

$$\varepsilon_r = \frac{NTU}{NTU+2} \quad (27)$$

where  $NTU = \frac{A_{wetted} h_r}{\dot{m}_{ave} c_p}$ ,  $\dot{m}_{ave}$  is the gas average mass flow rate in the regenerator and  $h_r$  is the heat transfer coefficient in regenerator which can be calculated by the following equation proposed by Tanaka

$$h_r = \frac{Nu_r K_g}{D_r} = \frac{K_g}{D_r} \cdot (C_1 + C_2 (Re_{ave} Pr)^{C_3}) (1 - C_4 (1 - \Pi)) \quad (28)$$

Where  $K_g$  is heat conductivity of the working gas,  $C_1$  to  $C_4$  are empirical coefficients ( $C_1 = C_4 = 0, C_2 = 0.42, C_3 = 0.67$ ),  $Re_{ave} = \frac{\rho}{\mu} D_r u_{ave}$ ,  $u_{ave} = \frac{2}{\pi} D_r u_{max}$ ,  $Pr = \frac{\nu}{\alpha}$ .

In the heater and cooler of Stirling engine, due to the finite heat transfer time and finite area, there is a temperature difference between the heater or cooler wall and the working gas. The temperature difference depends on the heat flux and the thermal conductance of the heat exchangers. Due to heat losses in the engine, the heat exchanged per cycle in heater and cooler can be expressed as:

$$Q_{h\ real} = Q_h + Q_r + Q_{cond} + Q_{leak} \quad (29-a)$$

$$Q_{k\ real} = Q_k - Q_r - Q_{cond} - Q_{leak} \quad (29-b)$$

where,  $Q_{cond}$  and  $Q_{leak}$  are conduction and leakage loss respectively, which can be calculated as indicated in the conduction loss section and leakage section.

Thus the working gas temperature in heater and cooler can be calculated as [5]:

$$T_h = T_{wh} - \frac{Q_{h\text{ real}F}}{h_h A_{wh}} \quad (30\text{-a})$$

$$T_k = T_{kh} - \frac{Q_{k\text{ real}F}}{h_k A_{wk}} \quad (30\text{-a})$$

where  $h_h$  and  $h_k$  are the heat transfer coefficient in heater and cooler respectively. They can be calculated using the expression as following:

$$h_i = \frac{0.0791\mu c_p Re_i^{0.75}}{2D_i Pr}, (i = h, k) \quad (31)$$

where  $D_i$  is the hydraulic diameter of heater or cooler.

### 5.1.2.2 Loss due to piston finite speed

In Stirling engine, due to the finite piston movement speed, the average pressure in the working space is different from that acting on the piston surface. When the piston compress the working gas, the pressure acting on the piston surface is higher than the average pressure in the engine; when the piston expands, the pressure acting on the piston surface is less than the average pressure in the engine. Supposing the compression speed is equal to expansion one, the pressure loss due to piston finite speed can be calculated as [10]:

$$\Delta p_{fin\ spe} = \frac{p_m \sqrt{3\gamma} u_p}{c} \quad (32)$$

### 5.1.2.3 Loss due to leakage from working space to buffer volume

In Stirling engine, the clearance between piston and cylinder wall, can lead to the mass leakage from working space to buffer space or reverse leakage. The mass leakage can lead to the network decreases slightly. According to [1, 4] the mass leakage can be expressed as:

$$\dot{m}_{leak} = \pi D \frac{p+p_0}{4r_g T_g} (u_p g_p - \frac{g^3}{6\mu} \frac{p_0-p}{L_p}) \quad (33)$$

where  $D$  is the mean clearance diameter in the clearance circular ring,  $T_g$  is the gas temperature near the piston.

The mass leakage in one time step used in equation (21) can be calculated as:

$$dm_t = \dot{m}_{leak} dt \quad (34)$$

The enthalpy flow due to the mass leakage can be expresses as:

$$\dot{H}_{leak} = \dot{m}_{leak} c_p T \quad (35)$$

where the temperature,  $T$ , depends on the flow direction.  $T$  is compression volume temperature, when the mass leaks from the working space volume to the buffer space, and is the buffer volume temperature, when the mass leaks from the buffer space to the working space.

#### 5.1.2.4 Loss due to mechanical friction

In SE, especially those using connecting rod mechanisms, there is mechanical friction in the bearings and other joint connections. The mean pressure loss due to mechanical friction can be expressed according to [11] as:

$$\Delta p_f = \frac{(0.4+0.0045Z_p F) \times 10^5}{3(1-1/(3\tau))} \left(1 - \frac{1}{\tau}\right) \quad (36)$$

where,  $Z_p$  is the piston stroke,  $F$  is the frequency of the engine and  $\tau$  is the compression ratio.

Thus, the work loss because of mechanical friction per cycle can be calculated as:

$$W_{fri}^{irr} = 2\Delta p_f V_{c0} \quad (37)$$

#### 5.1.2.5 Hysteresis loss

During the engine cycle process, the piston undergoes a reciprocating movement which makes the internal gas work as a gas spring. The gas spring has dissipation which is usually called hysteresis loss, and depends on the gas viscosity and temperature gradient effects in engine chamber [7].

Reference [1] provides an accurate calculation to the gas spring hysteresis loss:

$$\overline{W}_{hys} = \sqrt{\frac{1}{32} \omega \gamma^3 (\gamma - 1) T_w p_{mean} K_g \left(\frac{V_{c0}}{2V_{t0}}\right)^2} A_w \quad (38)$$

where,  $K_g$  is the conductivity of the working gas,  $V_{c0}$  is the swept volume of the working piston,  $V_{t0}$  is the average total volume,  $\gamma$  is the specific heat capacity ratio,  $T_w$  is the chamber wall temperature,  $p_{mean}$  is the mean pressure in the engine,  $A_w$  is the wetted area which is usually the cross section of the piston.

#### 5.1.2.6 Conduction loss

In Beta or Gamma type SE, the displacer separates the temperature gap between the compression volume and the expansion volume. Therefore, heat conduction through the displacer and the cylinder wall can't be avoided. According to Fourier conduction law, the heat loss by conduction is written as:

$$\dot{Q}_{cond} = K \frac{A}{L} \Delta T \quad (39)$$

where  $K$  is the heat conductivity of the displacer or the cylinder wall,  $A$  is the corresponding cross section area,  $L$  is the length of the displacer of the cylinder wall,  $\Delta T$  is the temperature difference between the expansion volume and the compression volume.

## 5.2 Study case of the new model for Beta type GPU-3 Stirling engine

In order to verify the above model, the GPU-3 Stirling engine parameters are used as a study case. In support of the Department of Energy's Stirling Engine Highway Vehicle Systems Program, the NASA Lewis Research Center has converted a 7.5kW single-cylinder rhombic-drive Stirling engine to a research configuration in order to obtain data for validating the Stirling cycle computer simulations. The engine was originally built by General Motors Research Laboratories for the U.S. Army in the 1965 as part of a 3kW engine-generator set, designated the GPU-3 (Ground Power Unit) [12]. The GPU-3 Stirling engine is a Beta type engine which can be seen in the Figure 6.5, whose main parameters can be seen in Table 5.2.

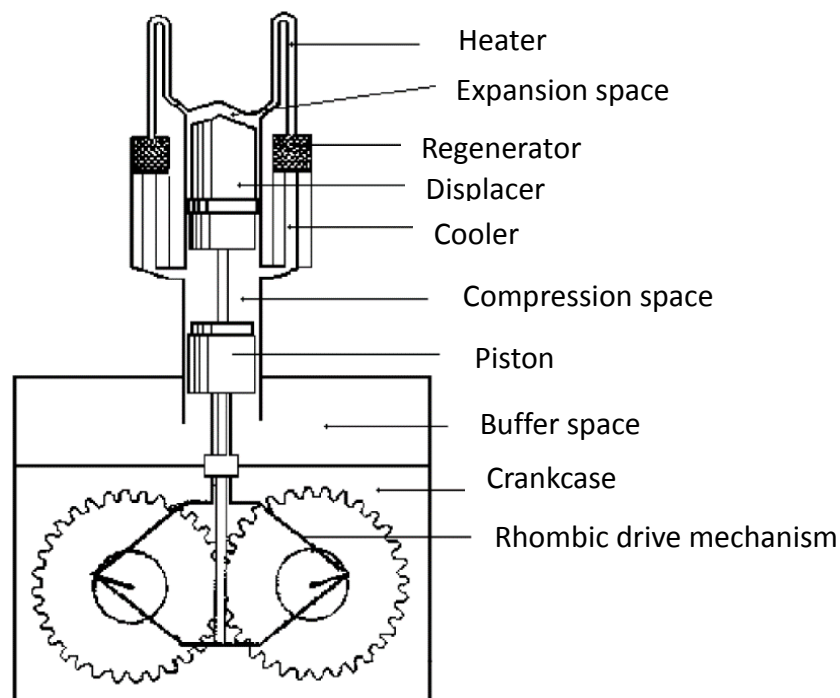


Figure 5.5 Sketch of GPU-3 Stirling engine

Table 5.2 Main Parameters of GPU-3 Stirling engine

Parameters	Values	Parameters	Values
<b>Clearance volumes</b>		<b>Cooler</b>	
Compression space	28.68 cm <sup>3</sup>	Average cooler tube length	46.1 mm
Expansion space	30.52 cm <sup>3</sup>	Cooler tube number	312
<b>Swept volumes</b>		Cooler tube inside diameter	1.08 mm
Compression space	113.14cm <sup>3</sup>	<b>Regenerator</b>	

Expansion space	120.82cm <sup>3</sup>	Regenerator length	226 mm
<b>Dead volumes</b>		Regenerator number	8
Heater	70.88 cm <sup>3</sup>	Regenerator inside diameter	226 mm
Cooler	13.8 cm <sup>3</sup>	Material	Stainless steel wire
Regenerator	50.55 cm <sup>3</sup>	No. of wires, per cm	79×79
<b>Drive</b>		Wire diameter	0.04 mm
Connecting rod length	46 mm	No. of layers	308
Crank radius	13.8 mm	Porosity	69.7%
Eccentricity	20.8 mm	Displacer rod diameter	9.52 mm
<b>Heater</b>		Displacer diameter	69.6 mm
Average heater tube length	245.3 mm	Displacer wall thickness	1.59 mm
Heater tube number	40	Piston rod diameter	22.2 mm
Heater tube inside diameter	3.02 mm	Piston diameter	69.9 mm
Piston clearance	0.028 mm	Displacer clearance	0.15 mm

Figure 5.6 shows the simulation output power, experimental output power and other author's simulations output power using Helium as working gas, with an average compression pressure about 2.76 MPa, heater wall average temperature about 922 K, and cooler wall average temperature of 286 K. The points with legend 'Exp' correspond to experimental results, the curve with legend 'Simple' corresponds to results obtained with the Simple model of the reference [1] and the curves with legend 'CAFS', 'Simple2', 'PSVL' and 'PFST' are plotted using results of the references [13], [14], [5], and [15]. The curve with legend 'PSML' indicates results of this new model presented in this work. In this figure it is shown that the results of the present model are the closest to the experimental results. It can be seen also that when the rotation speed increases, the net output power increases up to an optimal point and then decreases. This is due to the fact that if the rotation speed increases, the working gas flow velocity in the heat exchangers increases too, and the indicated output power increases; however the increasing in the flow velocity causes an increase in the pressure loss in the regenerator (seen in equation (22)) and heater/cooler (seen in equation (23)), in the piston finite speed loss (seen in equation (32)), the leakage loss (seen in equation (33)), in the mechanical friction loss (seen in equation (36)), and in the spring hysteresis loss (seen in equation (38)). For a rotation speed from 1000 rpm to 2500 rpm, the increased indicated power is bigger than the

corresponding increased power losses, which implies an increasing of the net output power. This is reversed over this value of rotation speed (optimum point) as the increased indicated power becomes smaller than the increased losses, which implies a net output power decreasing.

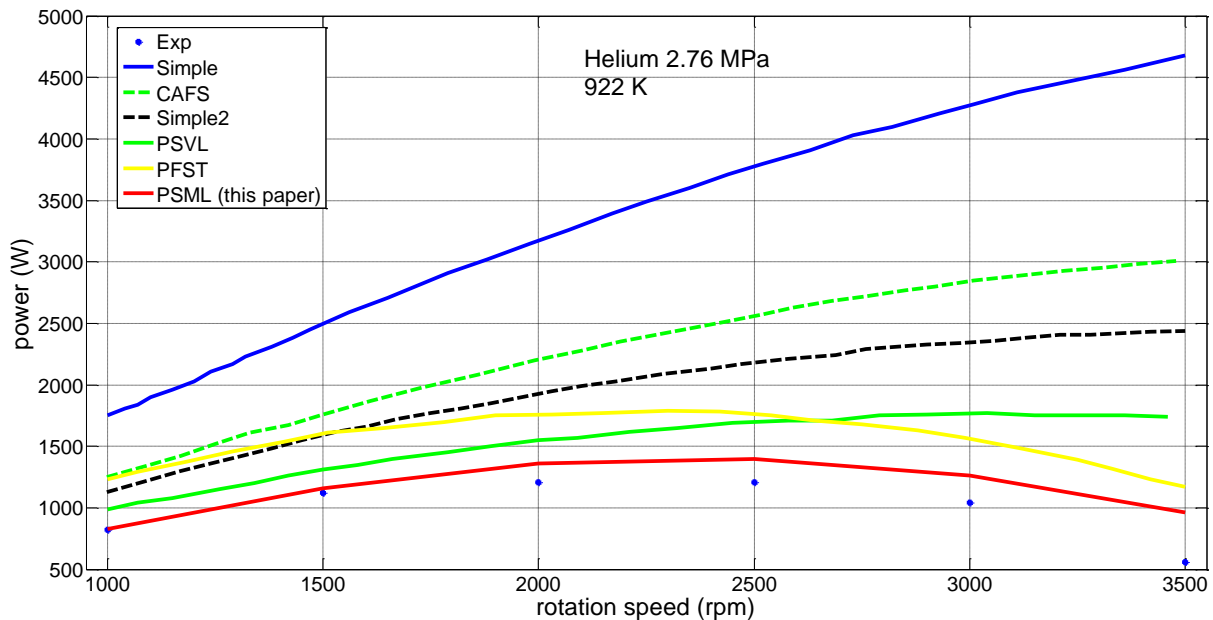


Figure 5.6 Mechanical power variation with the rotation speed for Helium at 2.76 MPa and 922 K

Figure 5.7 shows the variation of the thermal efficiency with the rotation speed in the same conditions as presented above. It shows that among those models, the present model is the closest to the experimental results when the rotation speed is less than 1500 rpm; while it has a slight higher relative error than PFST model when the rotation speed exceeds 1500 rpm. In addition to this, with the rotation speed increasing, the simulation thermal efficiency is progressively closer to the experimental results. Figure 5.8 shows the relative error between the PSML (this paper) model and the experimental results of Figure 5.6 and Figure 5.7. It can be seen that the average relative error of the provided mechanical power and the thermal efficiency are respectively about 20% and 30%.

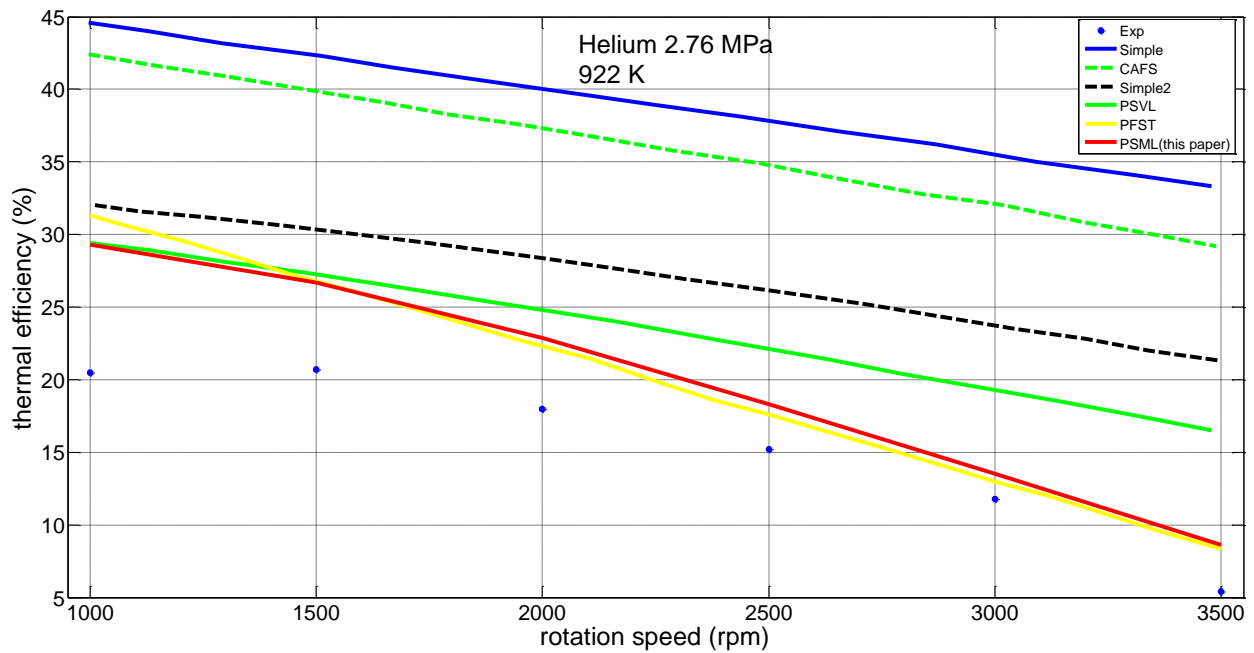


Figure 5.7 Thermal efficiency variation with the rotation speed for Helium at 2.76 MPa and 922 K

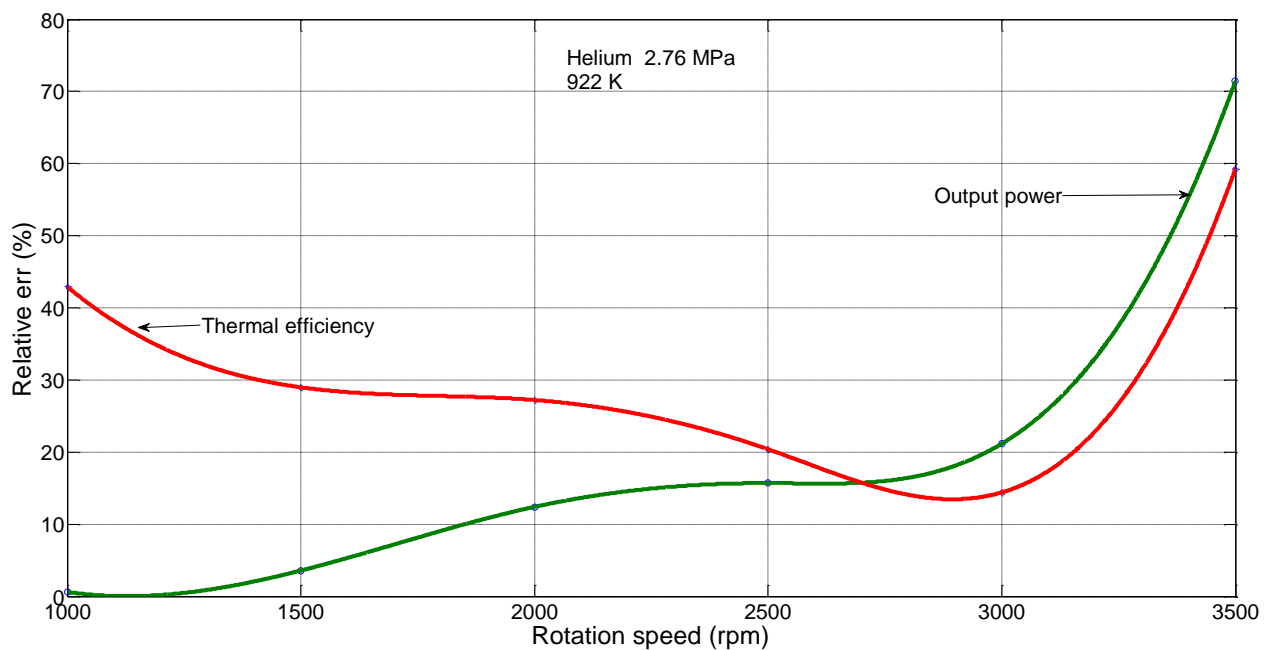
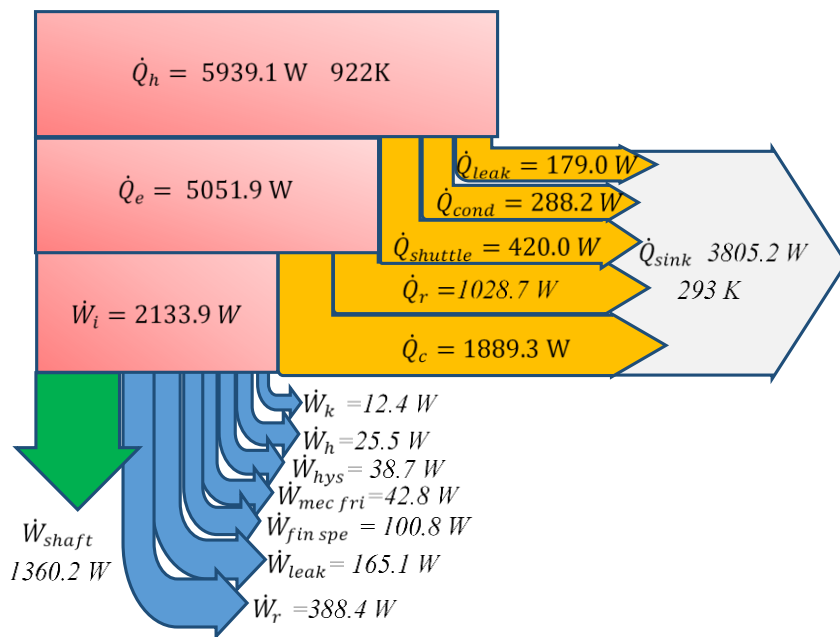
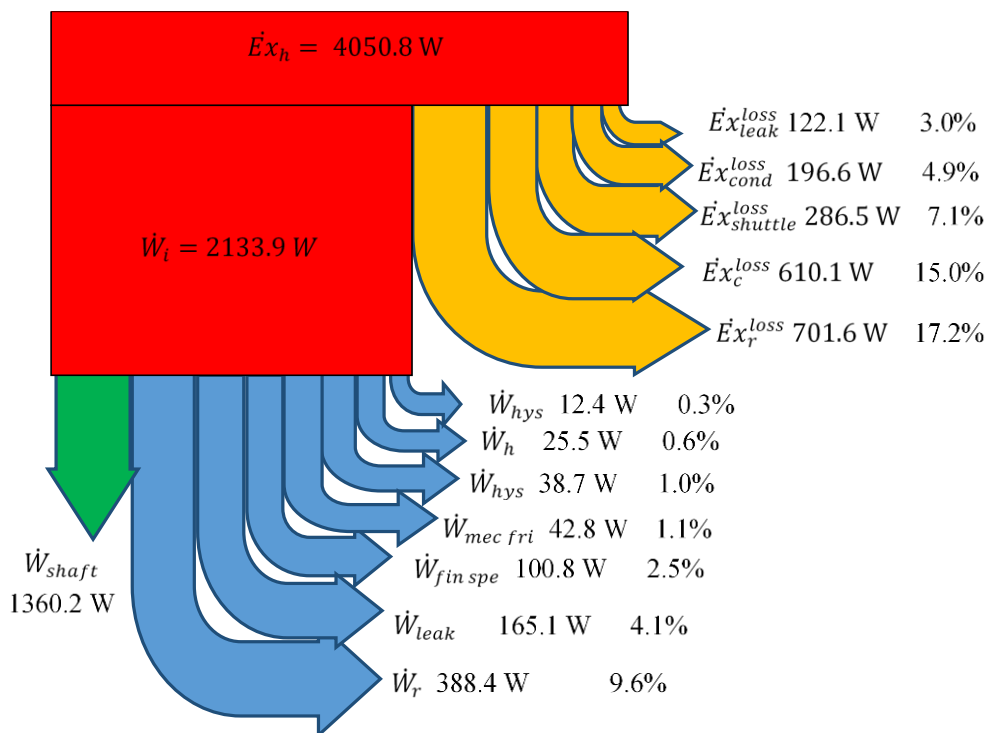


Figure 5.8 Relative error of output power and thermal efficiency versus rotation speed for Helium at 2.76 MPa and 922 K

Figure 5.9 shows the energy and exergy balance of the engine using the Helium as working gas at 2.76 MPa and 922 K and rotation speed at 2000 rpm. It can be seen that the regenerator imperfection loss is the biggest heat loss; and the flow viscosity friction loss in regenerator is the biggest mechanical loss. Displacer's shuttle heat loss is also important which accounts for about 7.1% of the total exergy input.



(a) Energy distribution of the absorbed energy



(b) Exergy distribution of the absorbed exergy

Figure 5.9 Energy and exergy balance of the engine using Helium and for rotation speed of 2000 rpm at 2.76 MPa and 922 K

Figure 5.10 and 5.11 indicate the output power and the efficiency variations with the rotation speed, using Helium as working gas too and the same wall temperature, but for a higher pressure as previously, which is now about 4.14 MPa. In Figure 5.10, the present model results are plotted and the corresponding curve is nearly parallel with the PFST one, and closer to the experimental results. The accuracy of the new polytropic model is similar with that of PSVL model if the rotation speed is less than 3000 rpm, however PSML is more accurate if the rotation speed exceeds 3000 rpm. Concerning the efficiency estimation (Figure 5.11), it can be seen that for a rotation speed less than 2200 rpm, the PSVL model gives the best predictions, while for values exceeding 2200 rpm the new model in this paper and PFST model becomes the most accurate. Figure 5.12 shows the relative error between the PSML (this paper) model and the experimental results of Figure 5.10 and Figure 5.11. It can be seen that at this time, the relative error of the provided mechanical power and the thermal efficiency is about 5% and 10% respectively.

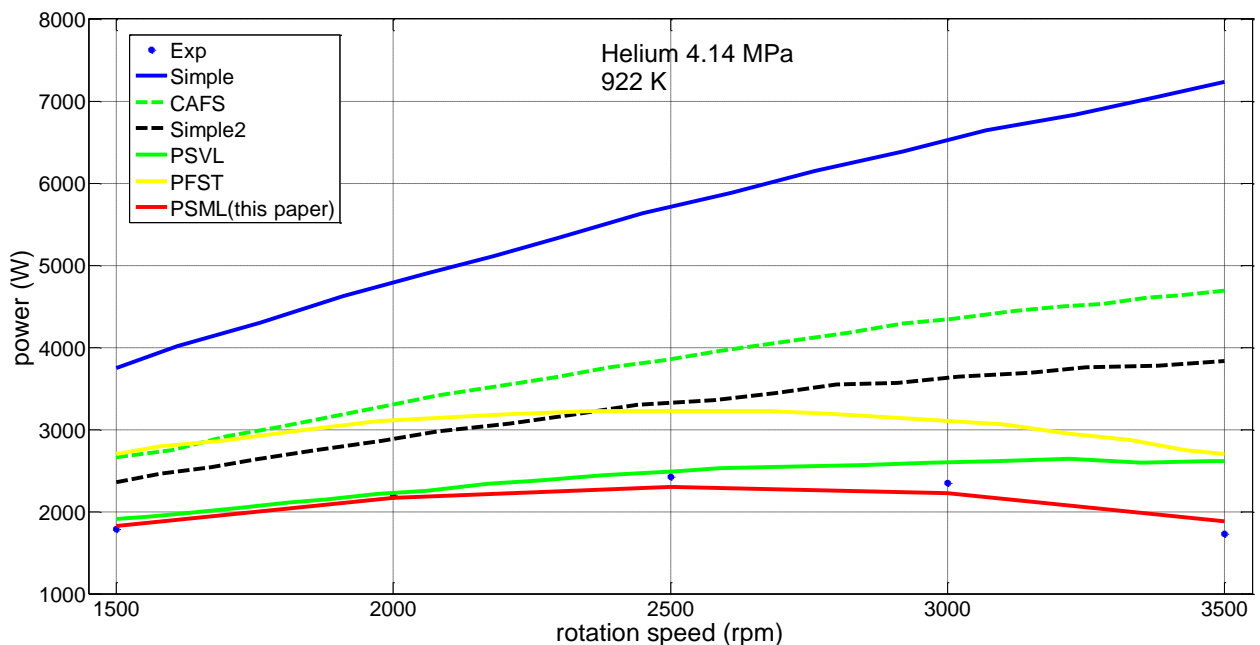


Figure 5.10 Output power variation with rotation speed for Helium at 4.14 MPa 922 K

According to the above comparison, it can be concluded that in order to give a good prediction of the output power, our model (PSML) seems the most accurate model among them; in order to predict the thermal efficiency, PSVL model is more accurate for low rotation speed, but for high rotation speed PSML model (this paper) becomes better as it takes the mass leakage in the clearance between displacer and cylinder wall into account, which increases with the rotation speed increasing. For high rotation speed, PFST is the most accurate model, but our model (PSML) is very close to it.

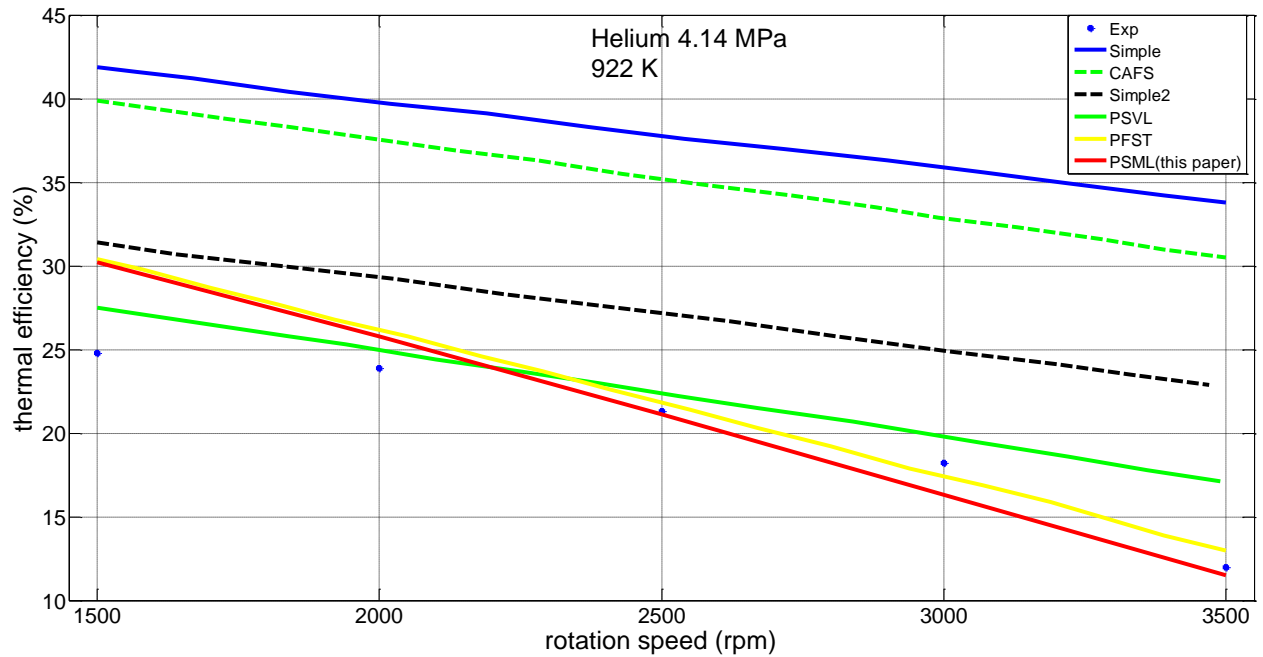


Figure 5.11 Thermal efficiency variation with rotation speed for Helium at 4.14 MPa 922 K

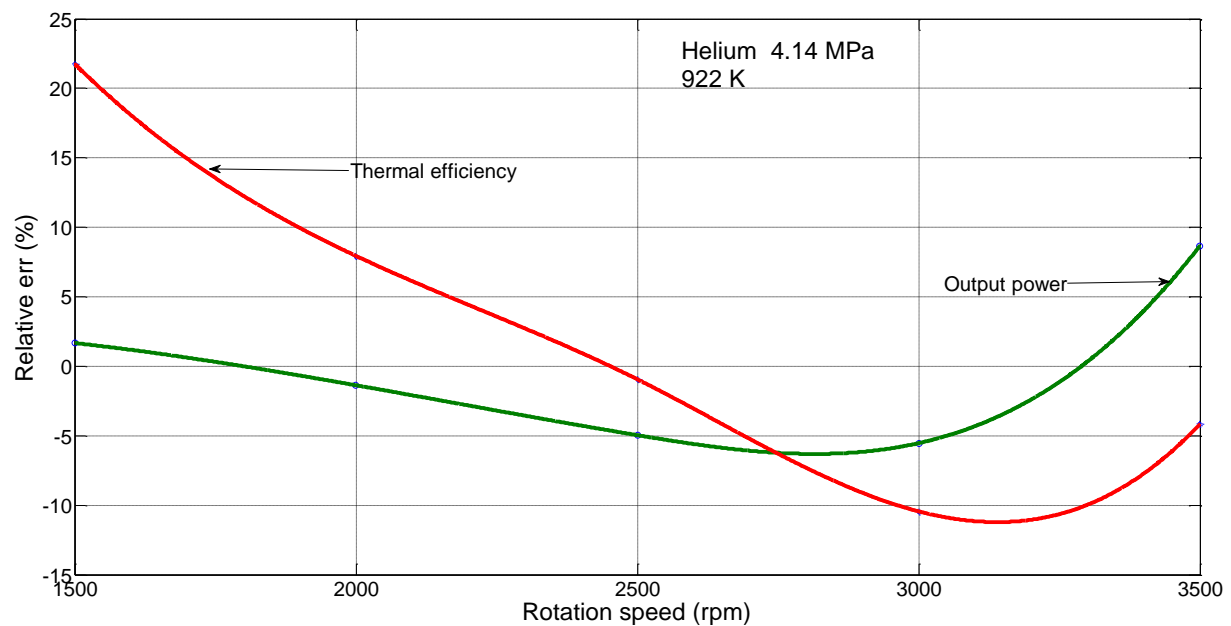


Figure 5.12 Relative err of output power and thermal efficiency versus rotation speed for Helium at 4.14 MPa and 922 K

Figure 5.13 shows output power variation with rotation speed for Helium working gas, with an average compression pressure at 5.52 MPa, heater wall average temperature at 922 K, and cooler wall average temperature at 286 K. It can be seen that when the rotation speed increase, the relative error of the simulation result increase also. And the optimum rotation speed is about 3000 rpm corresponding these operating conditions.

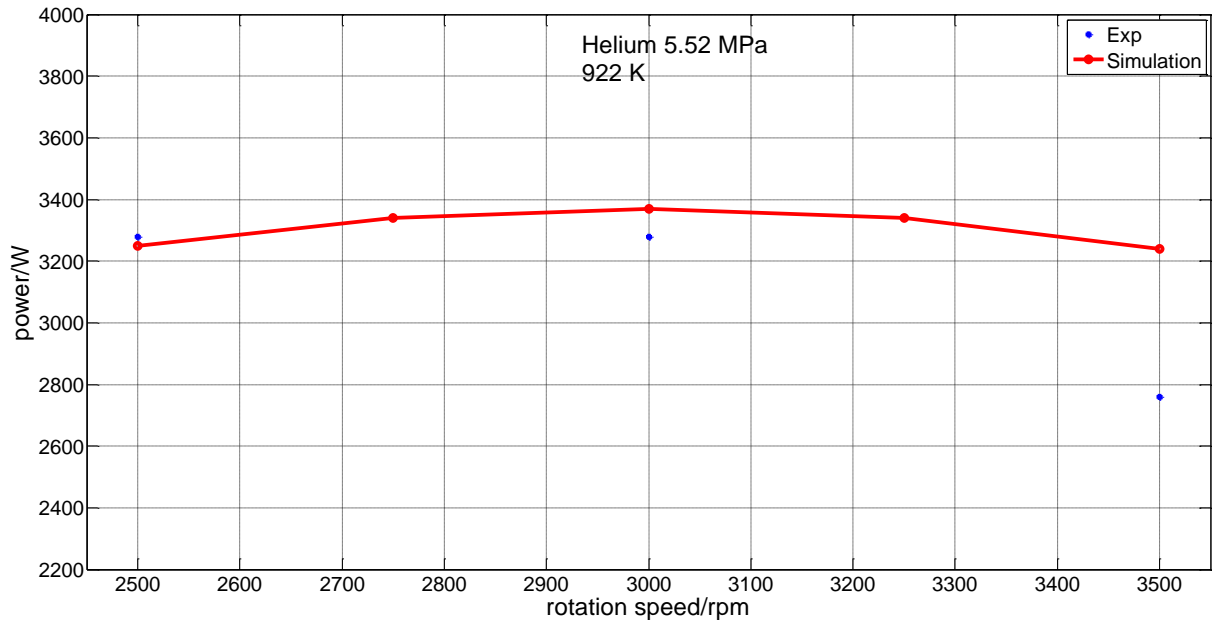


Figure 5.13 Output power variation with rotation speed for Helium at 5.52 MPa 922 K

Figure 5.14 shows thermal efficiency variation versus rotation speed for Helium as working gas, with an average compression volume pressure about 5.52 MPa, heater wall average temperature at 922 K, and cooler wall average temperature at 286 K. It can be seen that when the rotation speed increase, the relative error of the simulation results is nearly constant.

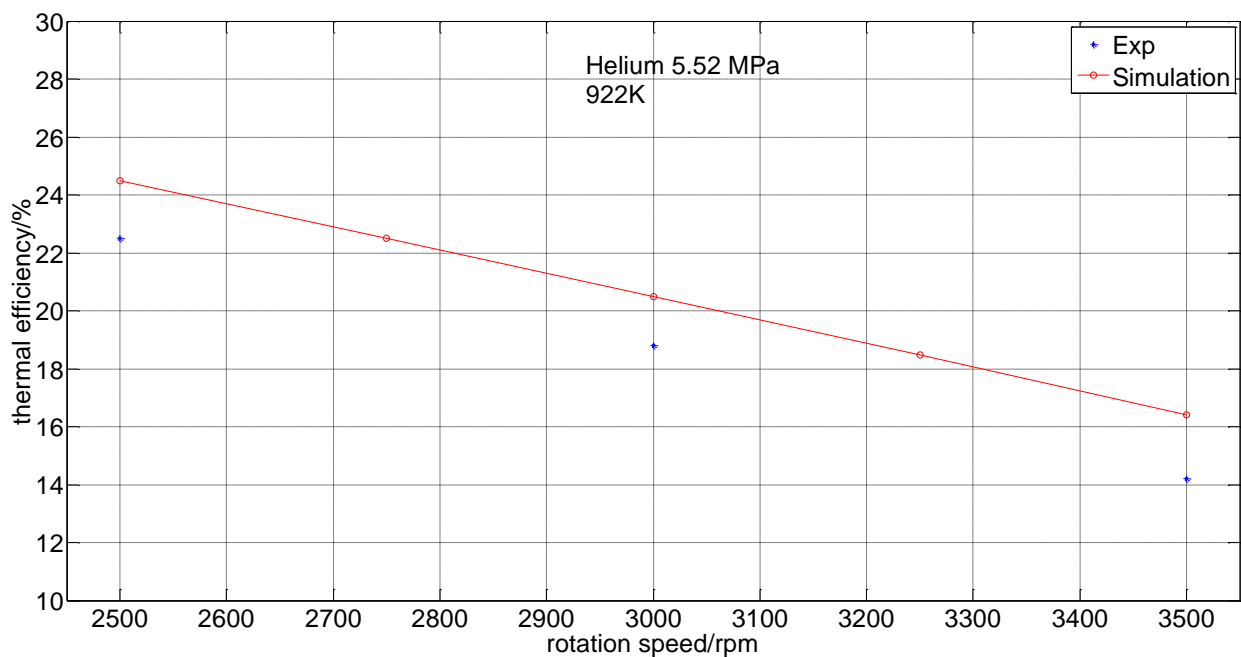


Figure 5.14 Thermal efficiency variation with rotation speed for Helium at 5.52 MPa 922 K

Figure 5.15 shows the output power variation versus rotation speed with an average compression pressure at 2.76 MPa, for Helium working gas, with heater wall temperature at 977K and cooler wall temperature at 288K. It can be seen that with the rotation speed increasing,

the relative error of the simulation model increase also. The model used in this paper is nearly parallel with the PSVL model, but the former one is closer to the experimental results.

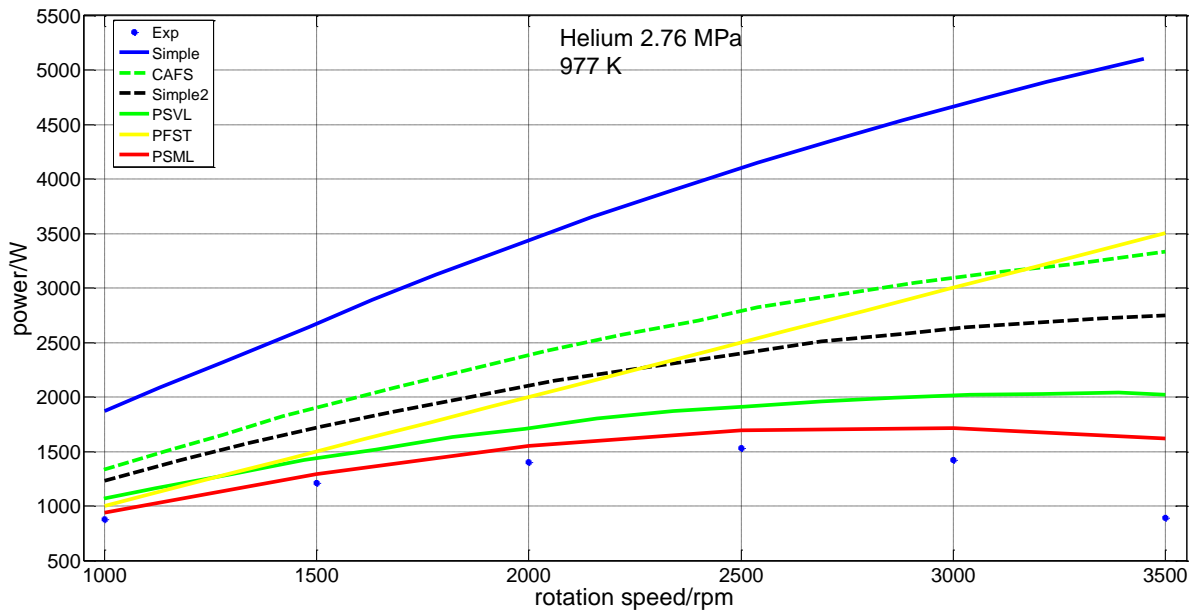


Figure 5.15 Output power variation versus rotation speed for Helium at 2.76 MPa 977K

Figure 5.16 shows the power variation with rotation speed with an average compression pressure at 2.76 MPa, for Helium working gas, with heater wall temperature at 977K and cooler wall temperature at 288K. It can be seen that with the rotation speed increase, the relative error of the simulation model increase also.

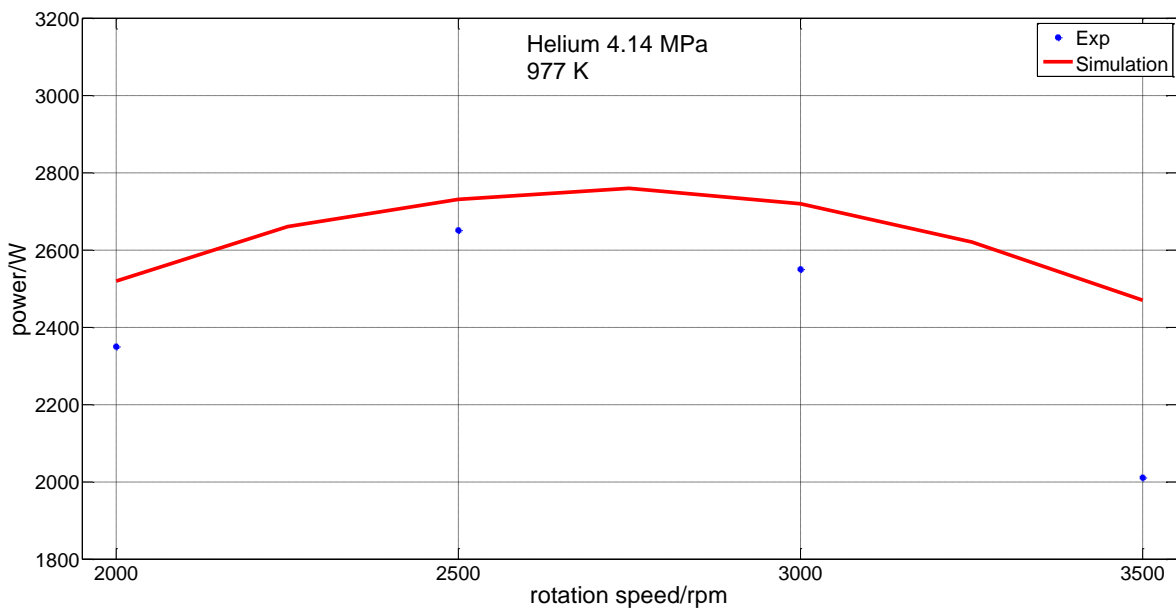


Figure 5.16 Thermal efficiency variation versus rotation speed for Helium at 2.76 MPa 977K

Figure 5.17 and Figure 5.18 show the output power variation and the thermal efficiency variation versus rotation speed with an average compression at 2.76 MPa, using Hydrogen as

working gas, with heater wall temperature about 977 K and cooler wall temperature about 288 K. It can be seen that with the rotation speed increasing, the relative error of the simulation model increase too.

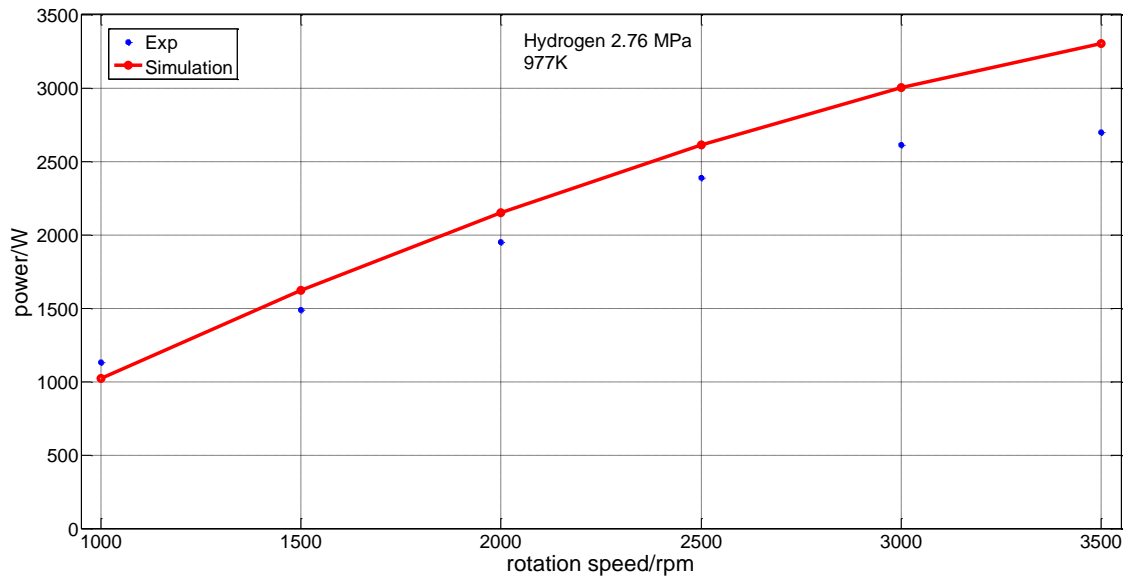


Figure 5.17 Output power variation with rotation speed for Hydrogen at 2.76 MPa 977 K

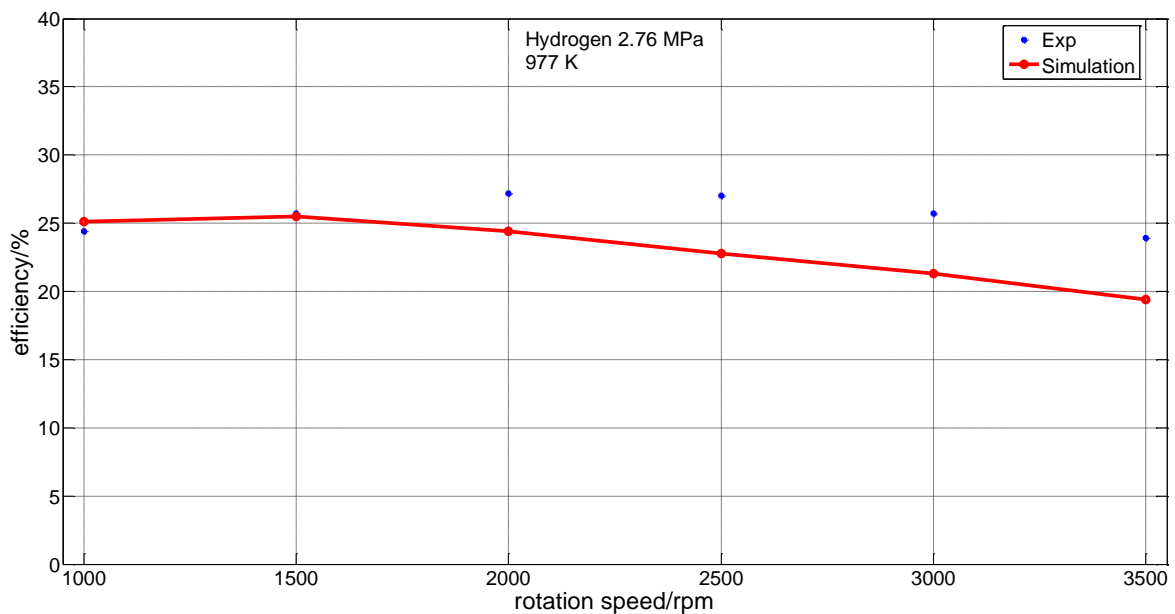
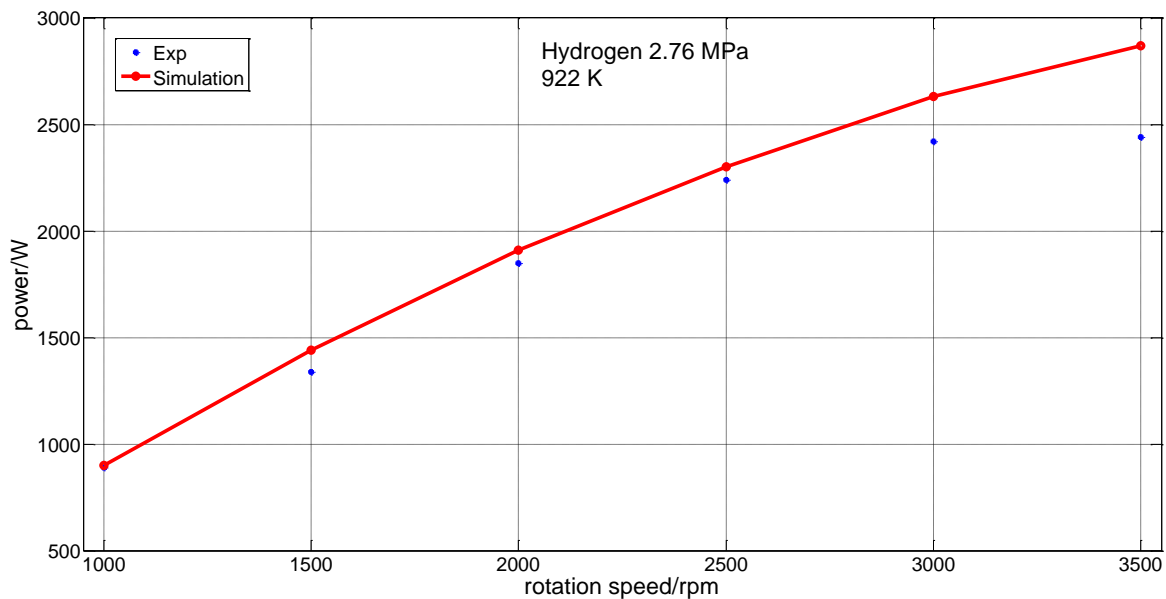


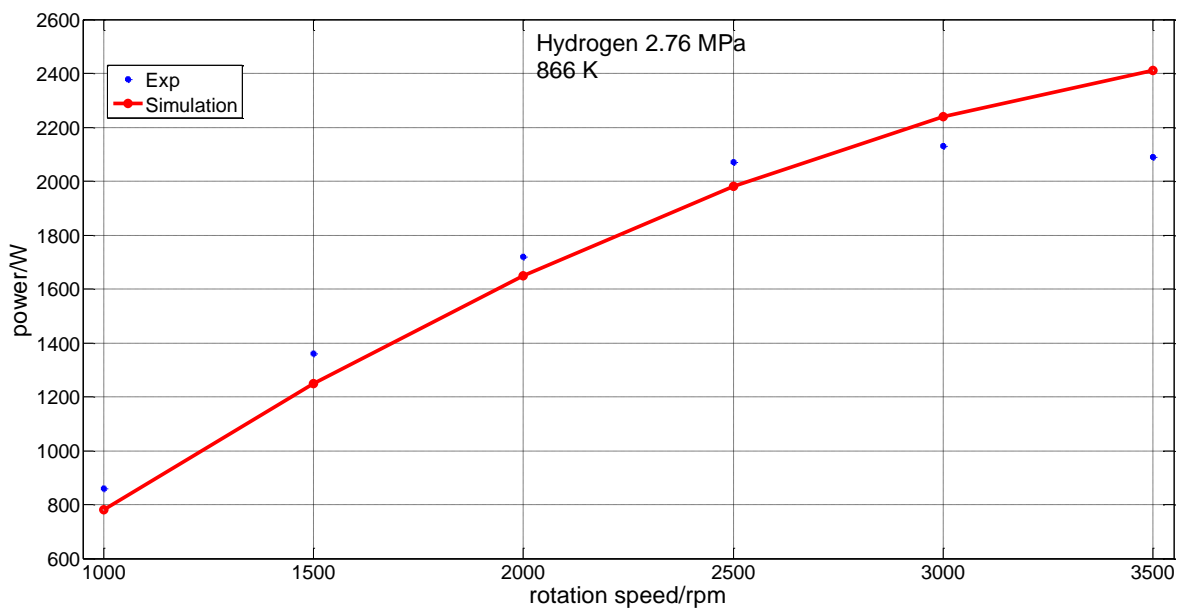
Figure 5.18 Thermal efficiency variation with rotation speed for Hydrogen at 2.76 MPa 977 K

Figure 5.19 shows the output power variation versus rotation speed, with heater wall temperature at 922K and 866K respectively. It shows that the simulation model is accurate if

the rotation speed is less than 2500 rpm, while it has a big relative error if the rotation speed exceeds 2500 rpm.



(a) Heater wall temperature at 922 K and cooler temperature at 288 K

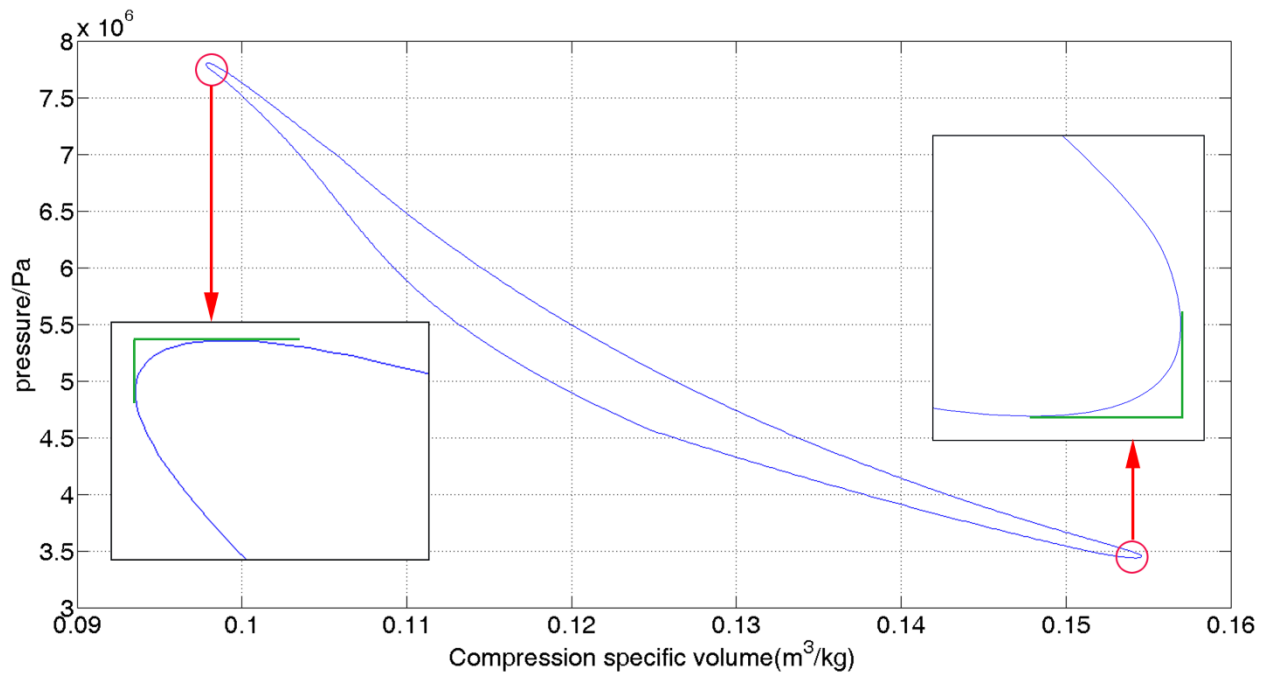


(b) Heater wall temperature at 866 K and cooler temperature at 288 K

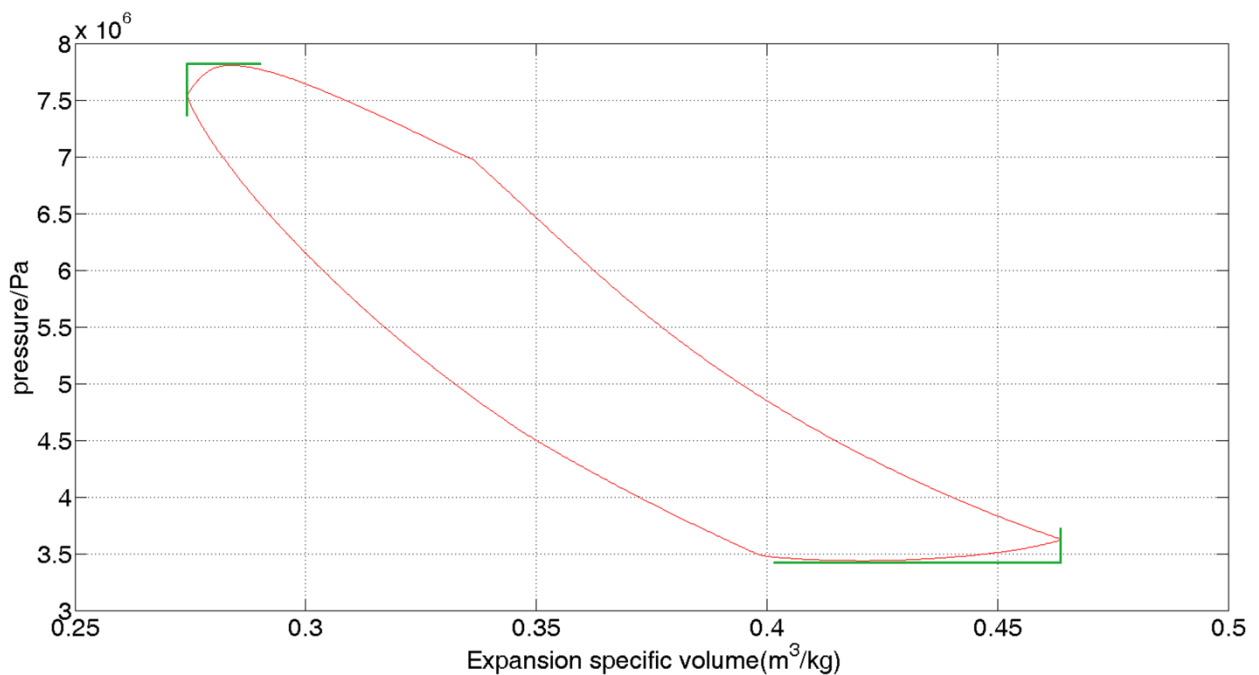
Figure 5.19 Output power variation with rotation speed for Hydrogen at 2.76 MPa

Thermodynamic cycle pressure variation versus specific volume in the compression and expansion spaces is plotted in Figure 5.20. It can be seen that at the upper left corner of the cycle there is a region between the maximal pressure point and the minimal compression (and expansion) specific volume point, where both the pressure and the specific volume increase, which leads the polytropic number being negative. Similarly, at the bottom right corner of the

cycle there is a region between the minimal pressure point and maximal specific volume point, where the polytropic number is negative too.



(a) Pressure versus specific volume in compression volume



(b) Pressure versus specific volume in expansion volume

Figure 5.20 Pressure versus specific volume in the compression (a) and expansion (b) spaces

Figure 5.21 shows the polytropic number value versus crank angle in compression ( $n_c$ ) and expansion ( $n_e$ ) volumes for Helium as working gas with an average compression pressure at 5.52 MPa, 41.67 Hz, heater wall average temperature at 922 K, and cooler wall average temperature at 286 K. Figure 5.22 shows the phase outline of the pressure, and specific volumes in compression and expansion spaces. In order to show them in similar range the pressure, compression specific volume and expansion specific volume are multiplied by a ratio as  $10^{-7}$ , 4.5 and 1.5 respectively. It can be seen that from  $0^\circ$  to  $6.48^\circ$  and from  $339.48^\circ$  to  $346.32^\circ$ , as both the pressure and the compression specific volume increase, the polytropic number tends to infinitive (seen in Figure 5.21 too). From  $8^\circ$  to  $90^\circ$  the polytropic numbers in the compression and expansion volumes are nearly to adiabatic exponent, indicating that these processes are close to adiabatic process. From  $131.04^\circ$  to  $135.72^\circ$ , both the pressure and the compression specific volume decrease and this lead to the infinitive compression polytropic number (seen in Figure 5.21). Similarly, from  $131.04^\circ$  to  $156.6^\circ$  and from  $339.48^\circ$  to  $360^\circ$  the expansion polytropic number is also infinitive (seen in Figure 5.21). From about  $145^\circ$  to  $254^\circ$  the compression polytropic number is bigger than the adiabatic value, then it decreases until about  $270^\circ$ , and maintain nearly constant until  $325^\circ$  (seen in Figure 5.21). Similarly, the expansion polytropic number decreases from  $160^\circ$  to about  $275^\circ$ , and then keep nearly constant (adiabatic value) until about  $325^\circ$ . Therefore, it can be seen that, during the compression process (from  $8^\circ$  to  $100^\circ$ ) and expansion process (from  $200^\circ$  to  $300^\circ$ ) the polytropic numbers are nearly to adiabatic value.

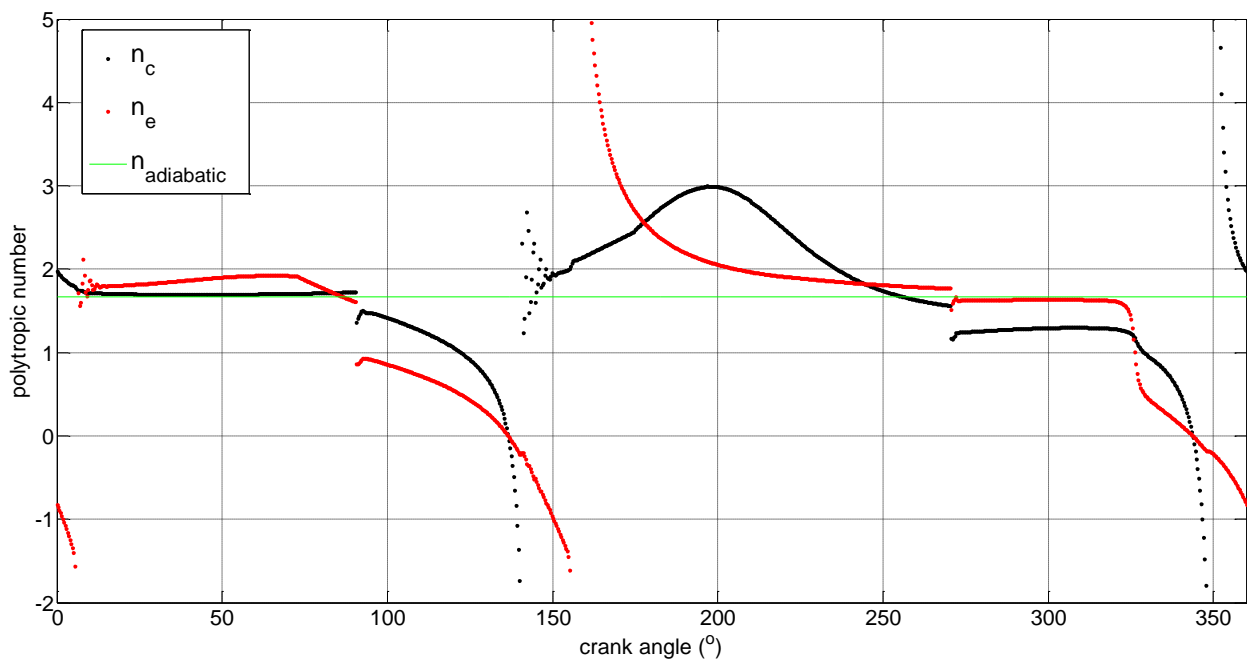


Figure 5.21 Polytropic number versus crank angle

Based on a general evolution of a polytropic number for gas fixed mass in a pressure-volume diagram, shown in Figure 5.23 (a), and using Figure 5.21 the polytropic numbers evolution in the  $PV$  diagram of compression and expansion volumes can be seen in Figure 5.23 (b).

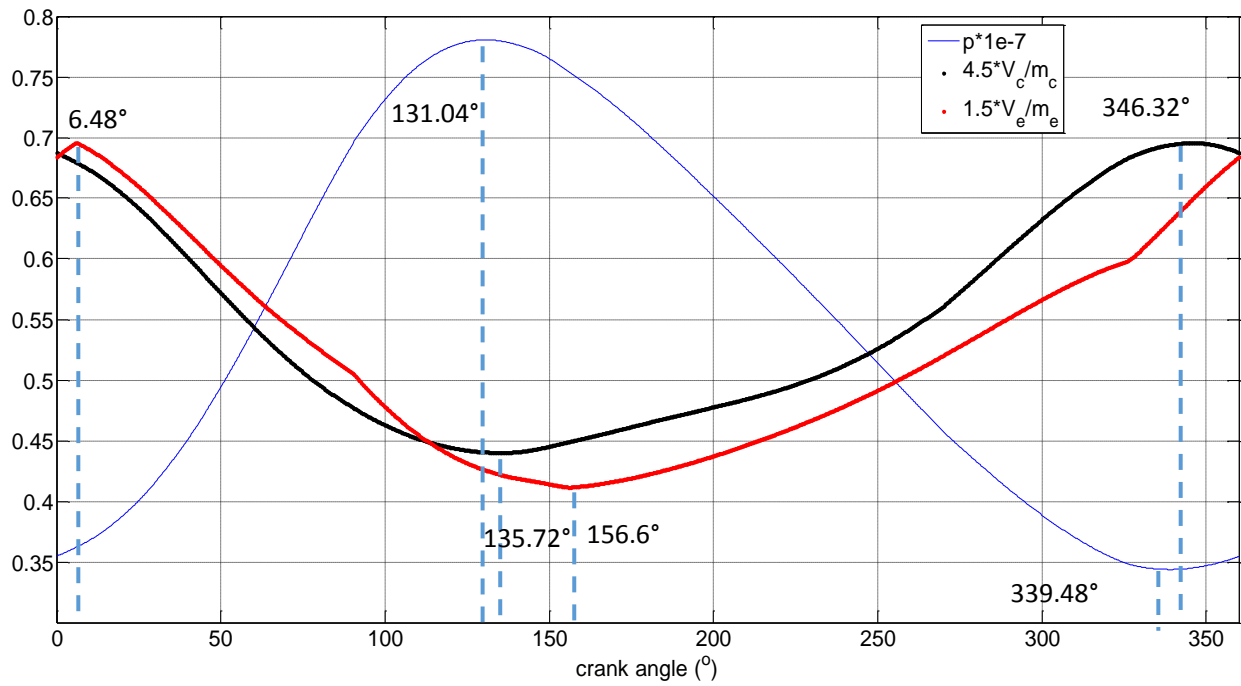
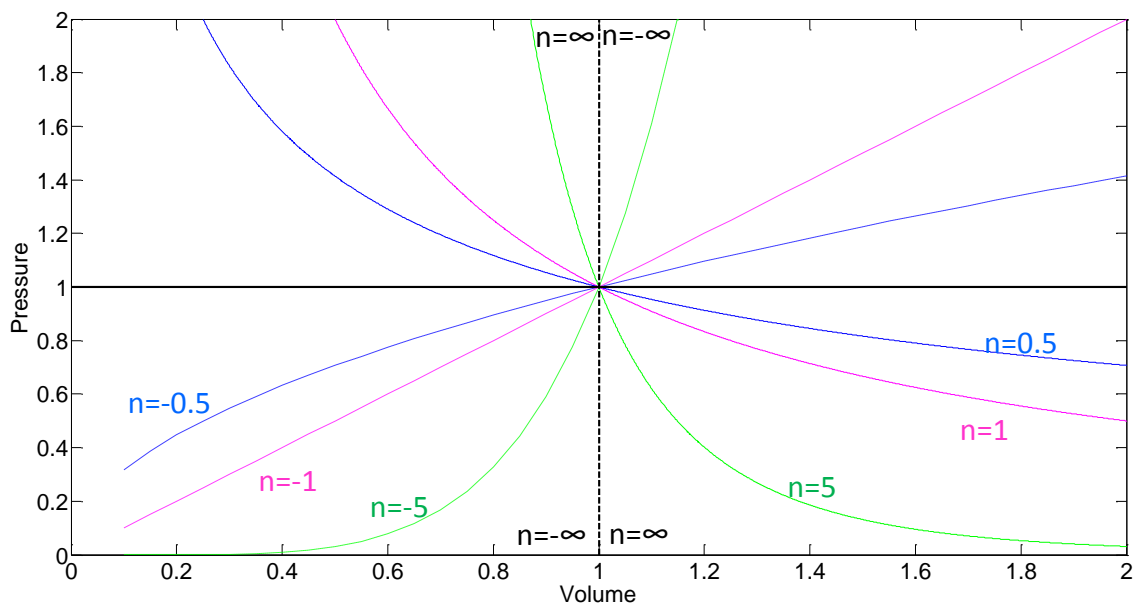
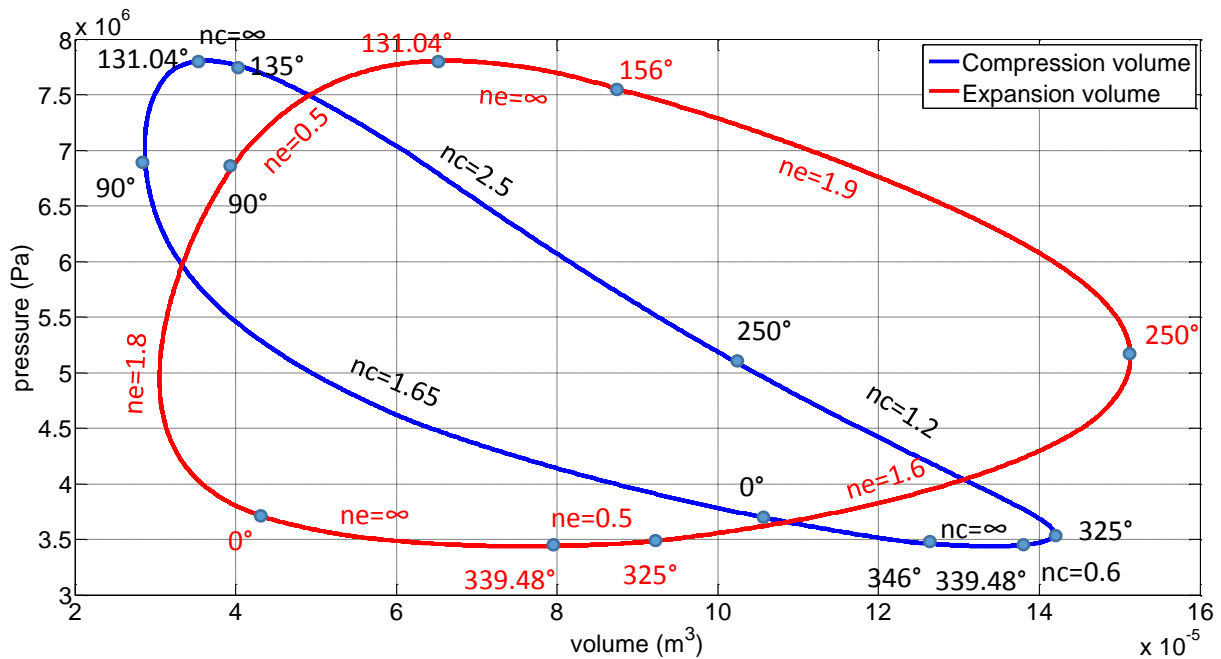


Figure 5.22 Phase outline of pressure and compression/expansion specific volumes



(a) General polytropic number evolution in PV diagram



(b) Polytypic number in the compression and expansion volumes

Figure 5.23 Polytypic number variation in PV diagram

Output power and efficiency variation was also studied versus rotation speed for different heater wall temperatures, respectively, using helium or hydrogen as working gas, an average compression pressure of 2.76 MPa, and a cooler wall temperature about 286K (Figure 5.24 and 5.25). It can be seen that the output power difference between different temperatures becomes bigger with the rotation speed increasing. The output power of the engine using hydrogen as working gas is bigger than that using helium at the same rotation speed and the difference between them becomes bigger with the rotation speed increasing. In opposition with that, the thermal efficiency of the engine using helium is higher than that using hydrogen for low rotation speeds (less than 2000 rpm). However, the engine using hydrogen has a bigger thermal efficiency when the rotation speed exceeds 2500 rpm. For helium, the engine reaches the maximum output power for a rotation speed about 2500 rpm, and then decreases rapidly with the rotation speed increasing. Therefore, the hydrogen working gas can bring a higher output power and thermal efficiency when the rotation speed exceeds 2500 rpm.

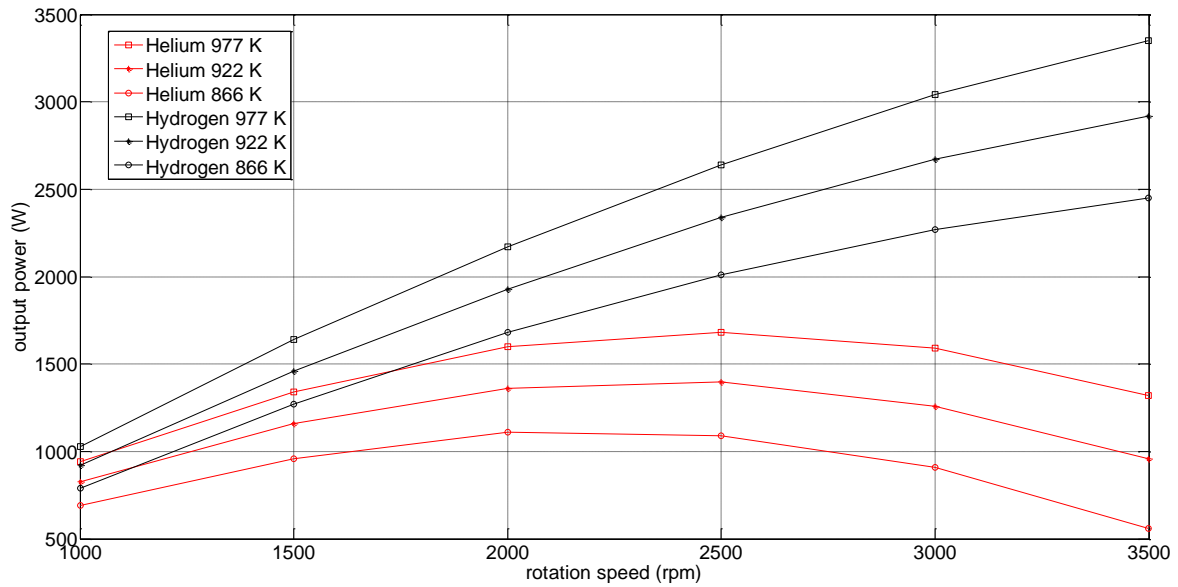


Figure 5.24 Output power versus rotation speed for helium and hydrogen and several hot temperatures

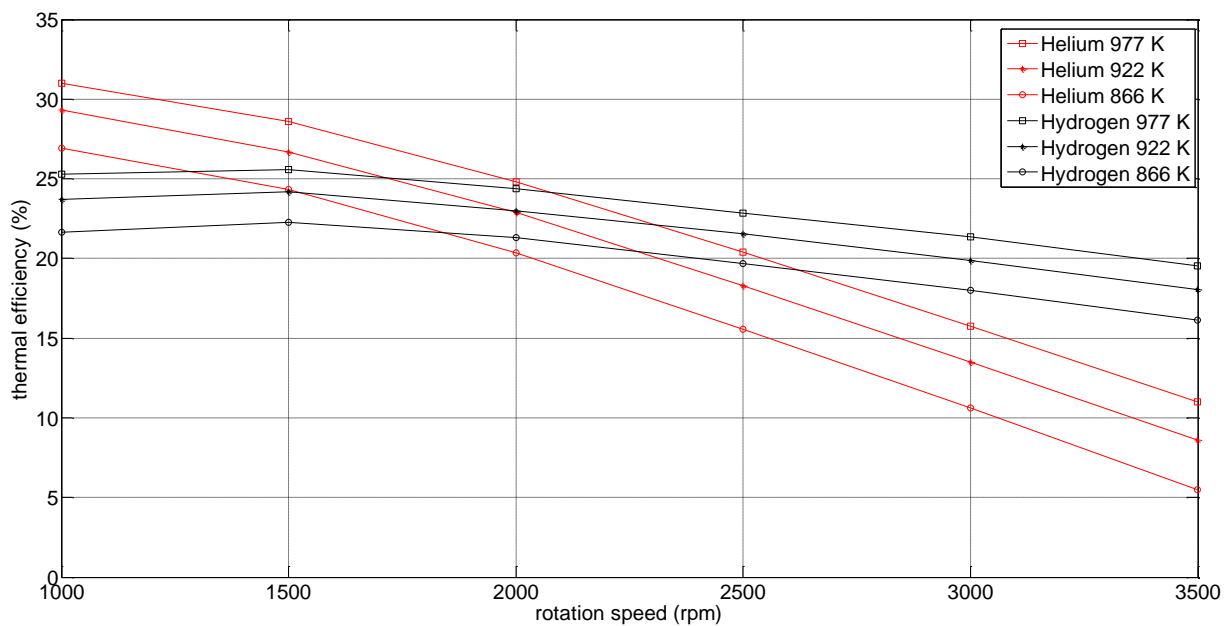


Figure 5.25 Thermal efficiency versus rotation speed for helium and hydrogen and several hot temperatures

Figure 5.26 and Figure 5.27 shows the output power and thermal efficiency versus rotation speed for different average compression pressures, with heater wall temperature about 922K and cooler wall temperature about 286K. From Figure 5.26, it can be seen that using helium as working gas, the output power reaches a maximum value, at about 1500 rpm and a pressure of 1.38 MPa, at about 2300 rpm and a pressure of 2.76 MPa and at 2600 rpm and a pressure of 4.14 MPa, respectively. It indicates that increasing average pressure of the engine can increase the optimum rotation speed for the maximum output power. In addition to this, the output power

difference among different average pressures becomes bigger for high rotation speed, for both helium and hydrogen as working gas. Figure 5.27 shows that increasing the average pressure in the engine can increase the thermal efficiency, but the increased amplitude decrease with the pressure increasing.

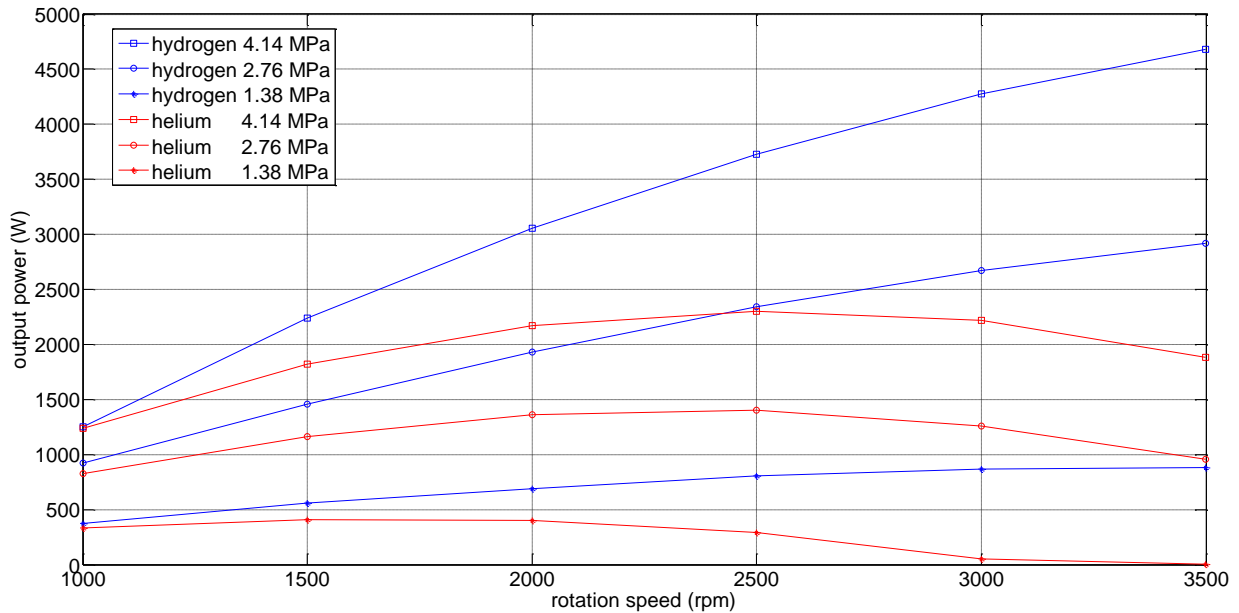


Figure 5.26 Output power versus rotation speed at different average compression pressures

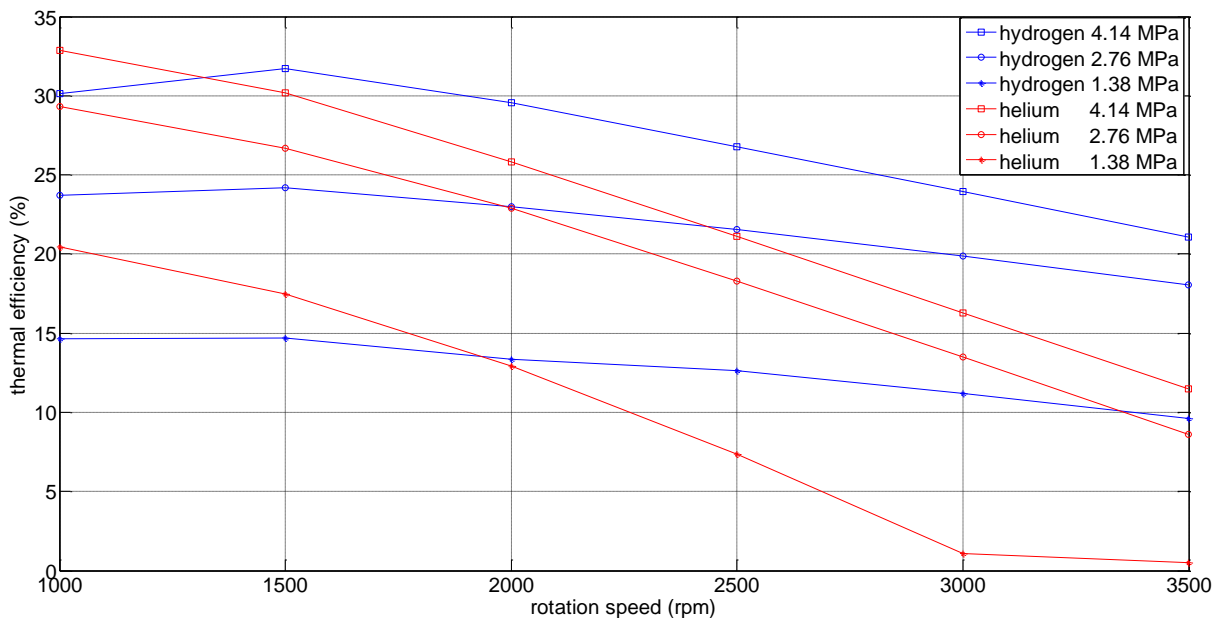
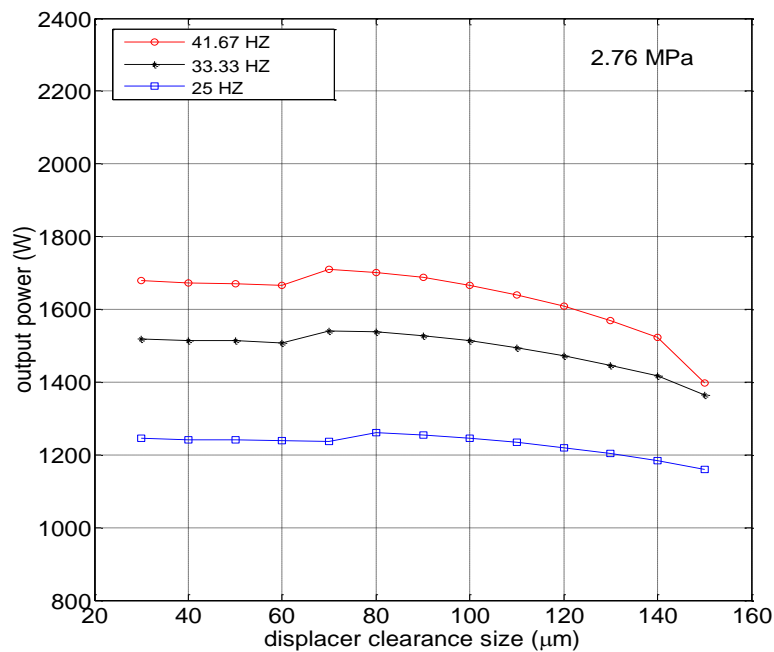


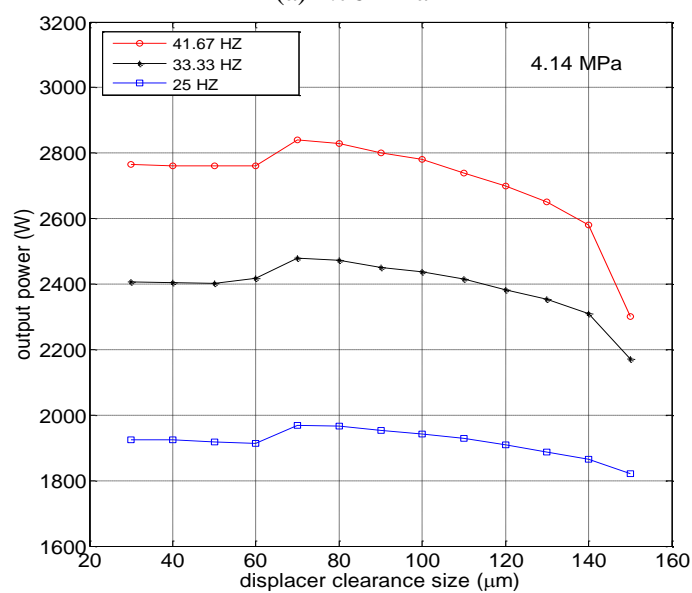
Figure 5.27 Thermal efficiency versus rotation speed for different average compression pressures

Figure 5.28 indicates the output power variation with the displacer clearance size, using helium as working gas, for heater wall temperature of 922K, cooler wall temperature of 286K, and an

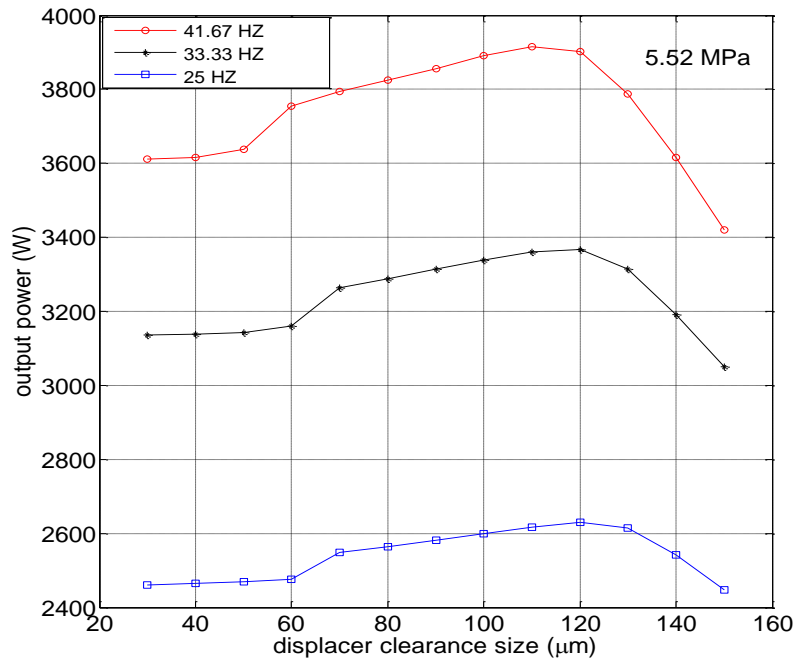
average compression pressure of 2.76 MPa, 4.14 MPa and 5.52 MPa respectively. Thus, an optimum displacer clearance size was found for a maximum output power for different rotation frequencies and different average pressures. The optimum displacer clearance size is about  $70\mu\text{m}$ ,  $75\mu\text{m}$  and  $120\mu\text{m}$  when the average compression pressure is 2.76 MPa, 4.14 MPa, and 5.52 MPa, respectively. There are two effects of the displacer clearance which contribute to the variation of the output power: shuttle heat transfer loss by the displacer's movement and gas mass leakage through the clearance. When the clearance size increases, the shuttle heat transfer loss decreases while the mass leakage increases. These two opposite effects lead to an optimum value for the clearance size. This optimum value increases with the engine's average pressure increasing.



(a) 2.76 MPa



(b) 4.14 MPa



(c) 5.52 MPa

Figure 5.28 Output power versus displacer clearance size

Figure 5.29 indicates the thermal efficiency versus the displacer clearance size, using Helium as working gas, for an average compression pressure of 4.14 MPa, a heater wall temperature of 922K and a cooler wall temperature of 286K. We can see that the thermal efficiency is nearly constant (reduce slightly) for a low displacer clearance until 80 $\mu\text{m}$  and rapidly decreases when the displacer clearance size exceeds 80 $\mu\text{m}$ .

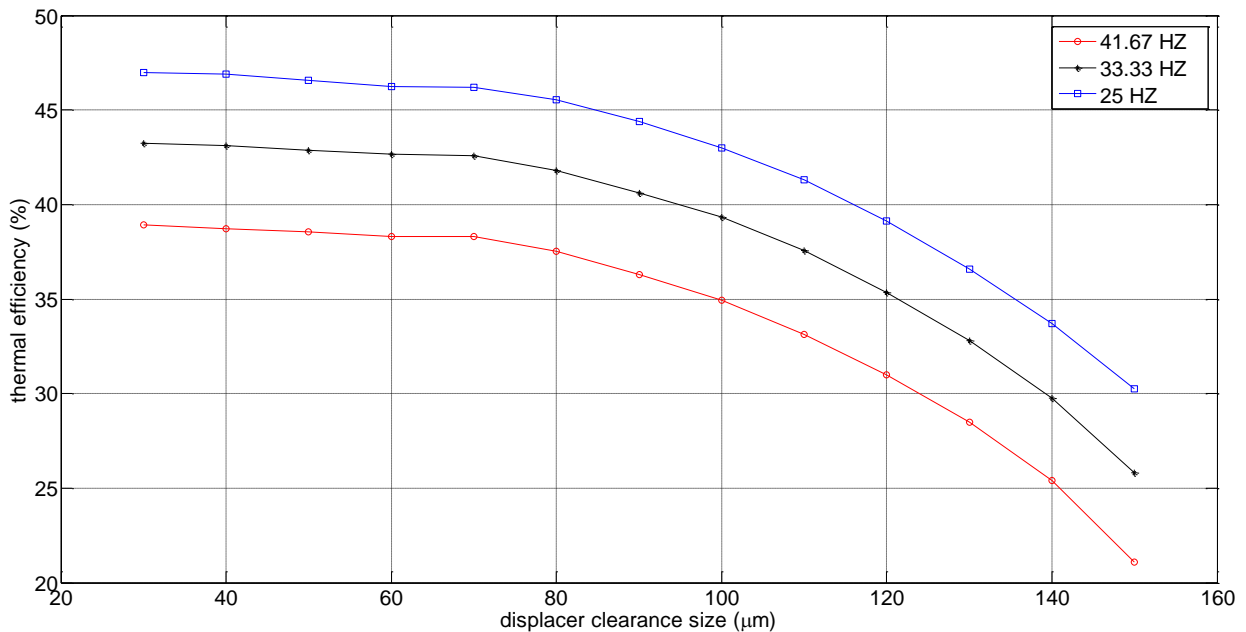


Figure 5.29 Thermal efficiency versus displacer clearance size, for a pressure of 4.14 MPa and using Helium

### 5.3 Summary

In this chapter, a new model named Polyotropic Stirling Model with Losses (PSML) has been proposed for predicting performance of Beta or Gamma type of Stirling engine. A bypass linking compression volume and expansion volume has been added in the classic adiabatic model of Stirling engine. Thus, polytropic processes have been considered in the compression and expansion volumes of the Stirling engine. Various kinds of losses have been considered in the model, including regenerator imperfection loss, heat conduction loss, fluid viscosity loss in heat exchangers (heater, cooler and regenerator), mass leakage loss from working space to buffer space, mechanical friction loss, piston finite speed loss, hysteresis spring loss, and temperature difference for heat exchange between gas and wall in heater/cooler. Shuttle heat exchange and mass leakage in the gap between the displacer and the cylinder have been also considered and all these losses are calculated in the same time step, as they interact each other. The GPU-3 Stirling engine has been used to validate the new model. It was shown that the new model (PSML) predict very accurately the output power and the thermal efficiency of the Stirling engine.

Polytropic number's evolutions in the compression and expansion volumes have also been studied. It was shown that during the compression and expansion processes, the polytropic number is nevertheless near to the adiabatic number during the most part of the cycle. Output power and thermal efficiency's evolution versus the rotation speed have been also studied. It was shown that there is an optimum rotation speed for a maximum output power, while the thermal efficiency decreases with the rotation speed increasing. The output power difference among different average pressures becomes bigger with the rotation speed increasing for both helium and hydrogen as working gas. In addition, an increase in the average pressure in the engine can increase the thermal efficiency, but the increased amplitude decreases with the pressure increasing. The comparison between helium and hydrogen as working gas leads to stating that hydrogen is more suitable for high rotation speed engine (more than 2500 rpm) as it has a bigger output power and a higher thermal efficiency.

The output power and thermal efficiency's variation with the displacer clearance size has also been studied. An optimum displacer clearance size was determined for a maximum output power which depends on the average pressure in the engine. This optimum displacer clearance size increases with the engine pressure increasing, which indicates that increasing average pressure in the engine is a good method to reduce the displacer clearance's effect on the engine performance.

### References

- [1] Urieli I. and Berchowitz D.M., Stirling cycle engine analysis. 1984: Taylor & Francis.
- [2] Tlili I., Timoumi Y., and Nasrallah S.B., Analysis and design consideration of mean

- temperature differential Stirling engine for solar application. *Renewable Energy*, 2008. **33**(8): p. 1911-1921.
- [3] Li R., Grosu L., and Queiros-Conde D., Multi-objective optimization of Stirling engine using Finite Physical Dimensions Thermodynamics (FPDT) method. *Energy Conversion and Management*, 2016. **124**: p. 517-527.
- [4] Homutescu V.M., Dumitraşcu G., and Horbaniuc B., Evaluation of the work lost due to leaks through cylinder-displacer gap. 2008.
- [5] Babaelahi M. and Sayyaadi H., A new thermal model based on polytropic numerical simulation of Stirling engines. *Applied Energy*, 2015. **141**: p. 143-159.
- [6] Wu C., *Recent advances in finite-time thermodynamics*. 1999: Nova Publishers.
- [7] Minassians A.D., *Stirling Engines for Low-Temperature Solar-Thermal-Electric Power Generation*, in U Berkeley. 2007, UC Berkeley.
- [8] Tanaka M., Yamashita I., and Chisaka F., Flow and heat transfer characteristics of the Stirling engine regenerator in an oscillating flow. *JSME international journal. Ser. 2, Fluids engineering, heat transfer, power, combustion, thermophysical properties*, 1990. **33**(2): p. 283-289.
- [9] Rohsenow W.M., Hartnett J., and Ganic E., *Handbook of heat transfer fundamentals*. 1985.
- [10] Petrescu S., et al., Application of the Direct Method to irreversible Stirling cycles with finite speed. *International Journal of Energy Research*, 2002. **26**(7): p. 589-609.
- [11] Babaelahi M. and Sayyaadi H., Modified PSVL: A second order model for thermal simulation of Stirling engines based on convective–polytropic heat transfer of working spaces. *Applied Thermal Engineering*, 2015. **85**: p. 340-355.
- [12] Thieme L.G. and Tew Jr R.C., *Baseline performance of the GPU 3 Stirling engine*. 1978.
- [13] Hosseinzade H. and Sayyaadi H., CAFS: The Combined Adiabatic–Finite Speed thermal model for simulation and optimization of Stirling engines. *Energy Conversion and Management*, 2015. **91**: p. 32-53.
- [14] Babaelahi M. and Sayyaadi H., Simple-II: A new numerical thermal model for predicting thermal performance of Stirling engines. *Energy*, 2014. **69**: p. 873-890.
- [15] Hosseinzade H., Sayyaadi H., and Babaelahi M., A new closed-form analytical thermal model for simulating Stirling engines based on polytropic-finite speed thermodynamics. *Energy Conversion and Management*, 2015. **90**: p. 395-408.



## Chapter 6 Multi-objective optimization of the experimental Gamma Stirling engine

For a Stirling engine, maximum output work and thermal efficiency are the two goals for engineering application. Minimum entropy generation should also be desired if ecological effect is considered. Acikkalp E. has used the thermo-ecological criteria to optimize the actual thermal cycles [1]. Ecological criteria has been used as the optimization criteria of heat engine by lots of authors such as: Ding Z. et al [2], Chen L. et al [3]. However, as those three goals usually cannot be obtained at the same time, a single objective is difficult to obtain an ideal optimization. Multi-objectives optimization method can optimize those goals at the same time based on which optimum point can be determined. Hosseinzade H. and Sayyaadi H. have optimized the output power and thermal efficiency of GPU-3 Stirling engine at the same time using multi-objective method and CAFS (Combined Adiabatic-Finite Speed) thermal model [4]. Ahmadi M. H. et al [5] have optimized the power and thermal efficiency of a solar powered Stirling engine by multi-objective evolutionary algorithms (MOEAs) based on the *NSGA-II* algorithm. Sayyaadi H. and Aminian H. R. [6] have optimized two objectives (the exergetic efficiency and the purchased equipment cost) of tubular recuperative heat exchanger which was used as a regenerator of a gas turbine cycle by programming in MATLAB (*NSGA-II*) based on the Genetic Algorithm. Later, Sayyaadi H. and Mehrabipour R. have multi-optimized (exergetic efficiency and the payback time for the capital investment) a recuperative heat exchanger used in a gas turbine using the *NSGA-II* algorithm and decision-making approaches (the fuzzy *Bellman-Zadeh*, *LINMAP* and *TOPSIS* methods).

In the previous studies, researchers who studied multi-objective optimizations, usually focused on output power and thermal efficiency. Ecological criteria optimization considers the ecological effect, however it's difficult to balance the output power, thermal efficiency, and ecological effect at the same time using one criteria.

Considering the above background, in this chapter, the Finite Physical Dimensions Thermodynamics method is used to optimize the power, thermal efficiency and entropy generation rate of the experimental Gamma type Stirling engine in the former chapter at the same time. Multi-objective genetic algorithm has been used, due to the complexity of the objective functions. Firstly, the Pareto frontier is gotten using the multi-objective genetic algorithm method. Secondly, two decision-making methods (*LINMAP* and *TOPSIS*) are used to get the optimum point.

### 6.1 Method for multi-objective optimization

In the multi-objective optimization problem, Pareto optimality is usually desired to get the corresponding Pareto Frontier. Pareto optimality is a state of allocation of resources from which it is impossible to reallocate so as to make any one individual or preference criterion better off without making at least one individual or preference criterion worse off. The concept is named after Vilfredo Pareto (1848–1923), Italian engineer and economist, who used the concept in his

studies of economic efficiency and income distribution [7]. The Pareto frontier is the set of all Pareto efficient allocations. Figure 6.1 is an example to explain the Pareto frontier.  $f_1$  and  $f_2$  are the two objective functions which are expected to obtain a minimum value, simultaneously. The boxes represent the individuals who have different kinds of combinations of the independent variables' value. The red line which connects the blue boxes, green box (A point), and yellow box (B point), is the Pareto frontier. The blue boxes, green box, and yellow box are the Pareto optimal individuals. Point A and Point B are on the frontier, as  $f_1(A) > f_1(B)$  while  $f_2(A) < f_2(B)$ , therefore it can't be concluded which point is better. However, point C is not on the Pareto frontier, as it can be seen that  $f_1(C) > f_1(A)$  and  $f_2(C) > f_2(A)$  ( $f_1(C) > f_1(B)$  and  $f_2(C) > f_2(B)$ ), therefore we can conclude that point C is worse than point A or B. In other word, point C is not on the Pareto frontier because it is dominated by both point A and point B. Points A and B are not strictly dominated by any other, and hence they are on the Pareto frontier.

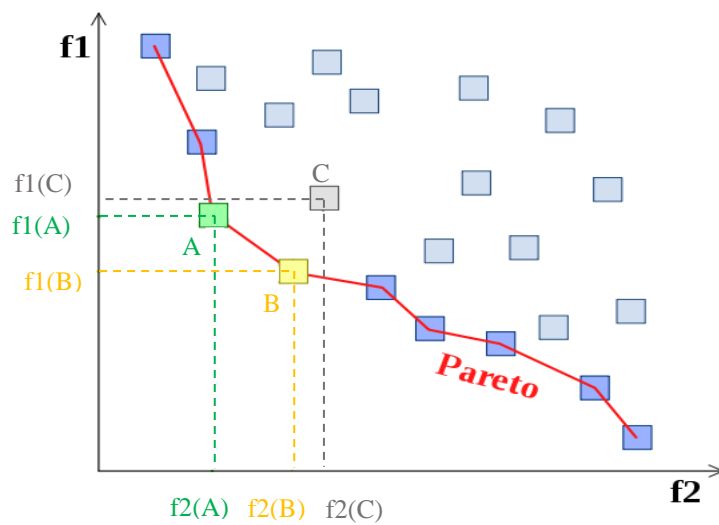


Figure 6.1 Sketch of Pareto frontier

For multi-objective problems, classical optimization methods (such as Gradient descent etc.) are not efficient to seek the Pareto frontier. The class of search algorithms that implement the Pareto approach for multi-objective optimization in the most straightforward way is the class of multi-objective evolutionary algorithms (MOEAs) [8]. MOEAs have been developed over the past decade; severe tests on complex mathematical problems and on real engineering problems have shown that they can eliminate the difficulties of classical methods [6, 8, 9]. Genetic Algorithm is a branch of evolutionary algorithm developed by John Holland in 1960s as a mean to import the mechanisms of natural adaptation into computer algorithms and numerical optimization [10]. Therefore, multi-objective genetic algorithm [11] has been used in this work and corresponding algorithm is shown in Figure 6.2.

Firstly, we gained the initial population which contains many combinations of the random variables' value. If there are equality constraints, the freedom of the optimization problem is the number of the variables minus the number of the equality constraints. We can suppose firstly initial values of part of the variables, number of which equals to the freedom. Then, the value of the others variables were gotten by solving the root of the equality constraints. Secondly, the

objective function value is evaluated for every individuals  $X_i$  ( $i=1,2,\dots,N$ ) in the population space. All the individuals are then ordered based on the Pareto dominance criteria [12]. Thirdly, based on the order of the individuals, offsprings are generated using cross over and mutation method [13]. The union set of the individuals and the offsprings are reordered again using the Pareto dominance criteria. New generation is gotten by choosing the top  $N$  best individuals among the union set. The above process repeats until stopping criteria is satisfied. Stopping criteria can be such as: maximum generations or number of generations which falls into stagnating status. Finally, Pareto frontier can be obtained.

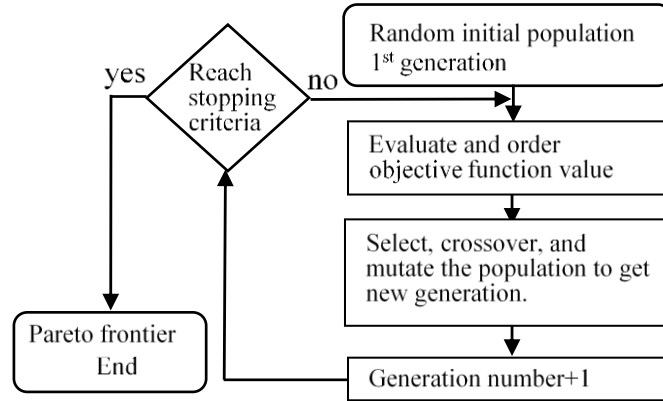


Figure 6.2 Sketch of multi-objective genetic algorithm

## 6.2 Non-dimensionalization method

After Pareto frontier is obtained, there are many possible solutions lying on the Pareto frontier. Among these solutions, an appropriate decision making method is required, to determine which solution is the best one. For multi-objective optimization problems, the dimensions of different objective functions are different. Therefore, the values of objective functions should be non-dimensionalized.

### 6.2.1 Linear non-dimensionalization

The matrix of objective values at different points in the Pareto frontier can be written as  $F_{ij}$  ( $i$  is the index of each point on the Pareto frontier  $i=1,2,3,\dots,k,\dots,m$ ,  $j$  is the index of each objective in the objectives space  $j=1,2,3,\dots,n$ ).

The Linear non-dimensionalization method gets the dimensionless matrix of objective values as [14]:

$$\bar{F}_{ij} = \frac{F_{ij}}{\max(F_{ij})} \text{ for maximizing objectives} \quad (1-1)$$

$$\bar{F}_{ij} = \frac{1/F_{ij}}{\max(1/F_{ij})} \text{ for minimizing objectives} \quad (1-2)$$

## 6.2.2 Euclidian non-dimensionalization

For Euclidian non-dimensionalization method [14], the  $i$ th point in the Pareto frontier of the  $j$ th objective values can be calculated as the quotient between the original value in this point and the 2-norm of the vector which contains the values of the  $j$ th objective at the Pareto frontier [14]:

$$\bar{F}_{ij} = \frac{F_{ij}}{\sqrt{\sum_{i=1}^m (F_{ij})^2}} \text{ for maximizing and minimizing objectives} \quad (2)$$

## 6.2.3 Fuzzy non-dimensionalization

In this method, the non-dimensionalized objective value  $\bar{F}_{ij}$  is defined as [14]:

$$\bar{F}_{ij} = \frac{F_{ij} - \min(F_{ij})}{\max(F_{ij}) - \min(F_{ij})} \text{ for maximizing objectives} \quad (3-1)$$

$$\bar{F}_{ij} = \frac{\max(F_{ij}) - F_{ij}}{\max(F_{ij}) - \min(F_{ij})} \text{ for minimizing objective} \quad (3-2)$$

After the objective values being non-dimensionalized, there are many methods to choose the optimum point among the Pareto frontier such as: *Bellman-Zadeh* decision-making technique, *LINMAP* decision-making technique, and *TOPSIS* decision-making technique [5, 14, 15].

## 6.3 Decision-making method

### 6.3.1 LINMAP decision-making technique

The dimensionless values of objective functions are expressed by  $\bar{F}_{ij}$ , then  $\bar{F}_{i1}$  is a vector of the 1<sup>st</sup> objective function value, among which the best value can be found (for example  $\bar{F}_{k_11}$ ).

Similarly, among the vectors  $\bar{F}_{i2}, \bar{F}_{i3} \dots \bar{F}_{in}$ , we also can find the best combination of parameters to get the optimum objective function values ( $\bar{F}_{k_22}, \bar{F}_{k_33} \dots \bar{F}_{k_nn}$ ) of the 2<sup>nd</sup>, 3<sup>rd</sup>...

objective respectively. Then, the point ( $\bar{F}_{k_11}, \bar{F}_{k_22}, \bar{F}_{k_33} \dots \bar{F}_{k_nn}$ ) is called ideal point.

Generally, in a multi-objective optimizations problem, the ideal point does not exist in the Pareto frontier, as all the objectives cannot attain their optimum value at the same time. The Euclidean distance between the point with the subscript  $i$  in Pareto frontier and the ideal point can be expressed as [14]:

$$d_{i+} = \sqrt{\sum_{j=1}^n (\bar{F}_{ij} - \bar{F}_{k_{jj}})^2}$$

Among the Euclidean distance vector,  $d_{i+}$  ( $i=1,2,\dots,m$ ), the minimum value  $d_{i+}$  represents the final optimum position ( $i'$ ) and the optimum combination of the parameter variable values.

### 6.3.2 TOPSIS decision-making technique

Among the dimensionless objective function values,  $\bar{F}_{ij}$ , the non-ideal point can also be found  $(\bar{F}_{\exists_1 1}, \bar{F}_{\exists_2 2}, \bar{F}_{\exists_3 3}, \dots, \bar{F}_{\exists_n n})$ , where  $\bar{F}_{\exists_1 1}, \bar{F}_{\exists_2 2}, \bar{F}_{\exists_3 3}, \dots, \bar{F}_{\exists_n n}$  are the worst values of the vectors  $\bar{F}_{i1}, \bar{F}_{i2}, \bar{F}_{i3}, \dots, \bar{F}_{in}$  respectively. The Euclidean distance between the point with the subscript  $i$  in the Pareto frontier and the non-ideal point can be expressed as:

$$d_{i-} = \sqrt{\sum_{j=1}^n (\bar{F}_{ij} - \bar{F}_{\exists_j j})^2}$$

A parameter  $Cl_i$  is defined as:

$$Cl_i = \frac{d_{i-}}{d_{i+} + d_{i-}}$$

Among  $Cl_i$  ( $i=1,2,\dots,m$ ), the biggest value  $Cl_{i'}$  represents the final optimum position ( $i'$ ) and the optimum combination of the parameter variable values.

Bellman-Zadeh decision-making method is not used in this chapter, its detailed mechanism can be seen in [14].

## 6.4 Case study: Gamma type Stirling engine

The T-s diagram of the SE system is presented in Figure 6.3 with its corresponding four processes: isothermal compression (1-2), isochoric heating (2-3), isothermal expansion (3-4), and isochoric cooling (4-1). As the regenerator is imperfect, the working gas can only be respectively heated to point 3' and cooled to point 1'. As it is shown in Figure 6.3, a temperature difference between the working gas and the heat reservoir/sink is considered.

As the piston and displacer of the Gamma type SE studied here are linked by crank connecting rod they move under sinusoidal displacement versus time. Consequently, the isochoric processes in Figure 6.3 are replaced by sinusoidal displacements in the model hereinafter. In addition to the regenerator imperfection and piston/displacer sinusoidal displacement, other losses including fluid dissipation, shuttle heat exchanger of displacer, piston finite speed,

hysteresis loss, and mechanical friction loss are also considered. Other main assumptions including uniform pressure in the engine, isothermal process in the compression and expansion volumes, no mass leakage from the working space to environment, ideal working gas in the engine are considered.

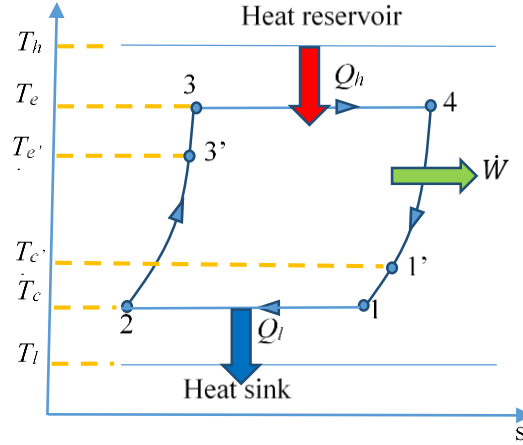


Figure 6.3 T-s representation of the SE cycle

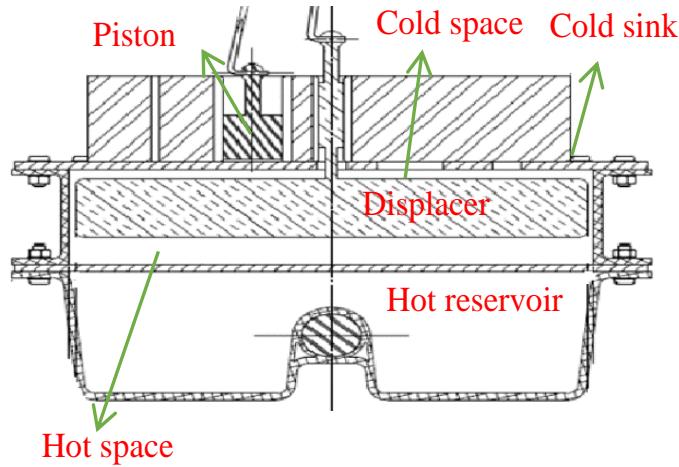


Figure 6.4 Gamma type Stirling engine

Considering the Gamma type Stirling engine presented in the previous chapter (Figure 6.4), the volumes can be written as:

$$V_e = \frac{V_{e0}}{2} [1 - \cos(\omega t)] \quad (4)$$

$$\begin{aligned} V_c &= \frac{V_{e0}}{2} [1 + \cos(\omega t)] + \frac{V_{c0}}{2} [1 - \cos(\omega t - \Phi_0)] \\ &= \frac{V_{e0}}{2} [1 + k + \cos(\omega t) - k \cos(\omega t - \Phi_0)] \end{aligned} \quad (5)$$

Where,  $k = V_{c0}/V_{e0}$ .

The total volume can be calculated as:

$$V_t = V_e + V_c + V_r = \frac{V_{e0}}{2} [2 + k - k\cos(\omega t - \Phi_0) + 2\chi] \quad (6)$$

Where,  $\chi = \frac{V_r}{V_{e0}}$

Supposing that the working gas is an ideal gas, the instantaneous pressure can be calculated as:

$$p = \frac{mr_g}{\frac{V_e}{T_e} + \frac{V_c}{T_c} + \frac{V_r}{T_r}} \quad (7)$$

Supposing a linear evolution of the regenerator temperature and a corresponding average temperature as  $T_r = \frac{T_e + T_c}{2}$ , using equation (1), (2) and (4), the engine pressure can be expressed as follow:

$$p = \frac{mr_g T_e}{V_{e0}} \left[ \frac{2\chi}{1+\tau} + \frac{1+\tau+k}{2\tau} + \frac{(1-\tau)\cos(\omega t)}{2\tau} - \frac{k\cos(\omega t - \Phi_0)}{2\tau} \right]^{-1} \quad (8)$$

where,  $\tau = T_c/T_e$

Thus, the indicated mechanical power provided by the engine is calculated as:

$$\dot{W} = \frac{1}{2\pi/\omega} \oint p dV_t \quad (9)$$

and after integration, the indicated power can be expressed as a function of  $T_e$ ,  $T_c$ ,  $n$ ,  $\Phi_0$ , and other dimensional parameters:

$$\dot{W}_i(T_e, T_c, n, \Phi_0) = \omega mr_g T_e \frac{\tau(1-\tau)k\sin(\Phi_0)}{a^2+b^2} \left[ \frac{\beta}{\sqrt{\beta^2-(a^2+b^2)}} - 1 \right] \quad (10)$$

Where,  $a = 1 - \tau - k\cos(\Phi_0)$ ,  $b = k\sin(\Phi_0)$ ,  $\beta = \frac{4\tau\chi}{1+\tau} + 1 + \tau + k$ , and  $\omega$ ,  $a$ ,  $b$ ,  $\beta$  depending on  $T_e$ ,  $T_c$ ,  $n$ ,  $\Phi_0$ .

For an open system (Figure 6.5), the energy balance can be written as:

$$dE = \delta Q + \delta W + dm_{in} \left( gz_{in} + \frac{u_{in}^2}{2} \right) + dH_{in} - dm_{out} \left( gz_{out} + \frac{u_{out}^2}{2} \right) - dH_{out}$$

Applying this equation balance compression and expansion space, the heat transfer flow from the heat reservoir and to the cold sink can be expressed as:

$$\dot{Q}_h(T_e, T_c, n, \Phi_0) = \omega mr_g T_e \frac{\tau k \sin(\Phi_0)}{a^2+b^2} \left[ \frac{\beta}{\sqrt{\beta^2-(a^2+b^2)}} - 1 \right] \quad (11)$$

$$\dot{Q}_l(T_e, T_c, n, \Phi_0) = -\omega mr_g T_e \frac{\tau^2 k \sin(\Phi_0)}{a^2+b^2} \left[ \frac{\beta}{\sqrt{\beta^2-(a^2+b^2)}} - 1 \right] \quad (12)$$



$$\dot{Q}_{h\ real}(T_e, T_c, n, \Phi_0) = \dot{Q}_h + \dot{Q}_r + \dot{Q}_{shuttle} \quad (18)$$

$$\dot{Q}_{l\ real}(T_e, T_c, n, \Phi_0) = \dot{Q}_l - \dot{Q}_r - \dot{Q}_{shuttle} \quad (19)$$

One of the particularities of a Stirling engine is the oscillated flow of the working fluid in the regenerator. Pressure loss due to the working fluid viscosity can be expressed as in the reference [16]:

$$\Delta p_r(t) = \Delta p_{max} \cos(\omega t) \quad (20)$$

where  $\Delta p_{max}$  can be calculated using Tanaka's experimental results:

$$\Delta p_{max} = \frac{\rho}{2} f_{max} \frac{L_r}{D_r} u_{max}^2 \quad (21)$$

with  $f_{max} = \frac{C_{sf}}{Re_{max}} + C_{fd}$ ,  $Re_{max} = \frac{1}{\nu} D_r u_{max}$ ,  $C_{sf}$  and  $C_{fd}$  are empirical factors (suggested to be  $C_{sf} = 175$  and  $C_{fd} = 1.6$  for stacks of screens).

Using equation (17) and (18), the average fluid friction dissipation in terms of power is calculated as:

$$\dot{W}_r(T_e, T_c, n, \Phi_0) = \frac{1}{t_{cycle}} \int_0^{t_{cycle}} \Delta p(t) dV(t) = \frac{\rho L_r}{4 D_r} u_{max}^3 A_0 \left( \frac{175 \mu}{\rho D_r u_{max}} + 1.6 \right) \quad (22)$$

The internal gas pressure in the engine is different from that acting on the piston surface, due to the finite speed of piston. An average pressure loss can be expressed as [19]:

$$\Delta p_{fin\ spe} = \frac{p_{mean} \sqrt{3 c_p / c_v} u_{ave\ p}}{\sqrt{3 r_g T_c}} \quad (23)$$

where  $u_{ave\ p} = 2nZ_p$ ,  $p_{mean}$  is the average pressure in the engine.

Thus, the average power loss due to piston finite speed is:

$$\dot{W}_{fin\ spe}(T_e, T_c, n, \Phi_0) = 2nV_{c0} \Delta p_{fin\ spe} \quad (24)$$

The working gas undergoes closed cycles in the engine, hysteresis loss must to taken into account, as the gas acts as an imperfect spring, which can be calculated as [20]:

$$\dot{W}_{hys}(T_e, T_c, n, \Phi_0) = \sqrt{\frac{1}{32} \omega \left( \frac{c_p}{c_v} \right)^3 (\gamma - 1) T_c p_{mean} k_g} \left( \frac{V_{t\ max}}{V_{t\ mean}} \right)^2 A_p \quad (25)$$

The mechanical friction loss of SE can be estimated using the following equation [21]:

$$\dot{W}_{friction}(T_e, T_c, n, \Phi_0) = 2nV_{c0} \frac{(0.4 + 0.0045 Z_p n) \times 10^5}{3 \left[ 1 - \frac{1}{3 V_{t\ max} / V_{t\ min}} \right]} \left( 1 - \frac{1}{V_{t\ max} / V_{t\ min}} \right) \quad (26)$$

Therefore, the shaft power and thermal efficiency can be expressed as:

$$P = \dot{W}_{shaft}(T_e, T_c, n, \Phi_0) = \dot{W}_i - \dot{W}_r - \dot{W}_{fin\ spe} - \dot{W}_{hys} - \dot{W}_{friction} \quad (27)$$

$$\eta(T_e, T_c, n, \Phi_0) = \frac{\dot{W}_{shaft}(T_e, T_c, n, \Phi_0)}{\dot{Q}_{h\ real}(T_e, T_c, n, \Phi_0)} \quad (28)$$

Supposing that the work losses are converted into heat and dissipated by the heat sink, the total heat rejected on the cold sink can be expressed as:

$$\dot{Q}_{l\ real}(T_e, T_c, n, \Phi_0) = \dot{Q}_l - \dot{Q}_r - \dot{Q}_{shuttle} - \dot{W}_r - \dot{W}_{fin\ spe} - \dot{W}_{hys} - \dot{W}_{friction} \quad (29)$$

Thus the entropy generation among this system can be calculated by the difference between the two entropy flows on the heat exchangers:

$$\dot{S}_g(T_e, T_c, n, \Phi_0) = -\frac{\dot{Q}_{l\ real}(T_e, T_c, n, \Phi_0)}{T_l} - \frac{\dot{Q}_{h\ real}(T_e, T_c, n, \Phi_0)}{T_h} \quad (30)$$

So, using Finite Physical Dimensions Thermodynamics and considering several losses, expressions of mechanical power, heat flow rate, efficiency and entropy generation can be obtained as functions of some main parameters from an engineer point of view (rotation speed, gas temperatures and out-of-phase). This mathematical model has been validated in the chapter 3. Comparing with the previous chapter, only the heat conduction loss and the leakage loss between the clearance of the piston and the cylinder are not considered in this optimization process, as they have not optimum point: the less heat conduction and leakage are, the better performance of the engine is.

For a Stirling engine, the maximum output work and thermal efficiency are the two goals for engineering application. Minimum entropy generation should also be required if ecological effect is considered. In our previous work, it was shown that the studied Gamma type Stirling engine provides small output power and thermal efficiency [22]. Therefore, Therefore in order to improve its performance, an optimum geometry is researched for three objective functions considered in this work:  $P(T_e, T_c, n, \Phi_0)$  equ. (27),  $\eta(T_e, T_c, n, \Phi_0)$  equ. (28), and  $\dot{S}_g(T_e, T_c, n, \Phi_0)$  equ. (30). The less differences between  $T_e$  and  $T_h$  and between  $T_c$  and  $T_l$  are, the bigger power and efficiency are, and the smaller entropy generation is. Using Finite Physical Dimensions Thermodynamics method, the temperature differences between the internal working fluid and the heat reservoir or sink are determined.

As in the SE, the thermal conductance (and the total area) of the heater and cooler can influence the investment cost, the total thermal conductance can be supposed fixed in this model (by an engineer constraint) ( $C_t$ ). Thermal conductance of the heater and cooler are respectively:  $C_h = \lambda C_t$ ,  $C_l = (1 - \lambda)C_t$ , where  $0 < \lambda < 1$ .

Based on the Newton's law, the relationship among temperature difference, thermal conductance, and heat flow can be expressed as:

$$\frac{\dot{Q}_{h\ real}(T_e, T_c, n, \Phi_0)}{T_h - T_e} = C_h = \lambda C_t \quad (31)$$

$$\frac{\dot{Q}_{l\ real}(T_e, T_c, n, \Phi_0)}{T_l - T_c} = C_l = (1 - \lambda)C_t \quad (32)$$

Due to the irreversibility of the SE, the internal temperature should be ruled by the inequality:

$$T_l < T_c < T_e < T_h \quad (33)$$

Therefore, using the multi-objective genetic algorithm mentioned above, the Pareto frontier is gotten firstly, the dimensionless matrix of the objectives' value is obtained using Euclidian non-dimensionlization method secondly, and two decision-making methods (*LINMAP* and *TOPSIS*) are used to get the optimum point finally.

## 6.5 Results and analysis

In the Table 6.1, here bellow are shown the parameters used to optimize the engine.

Table 6.1 Parameters of the mathematical model

$T_h$	75 °C	$D_p$	22 mm
$T_l$	30 °C	$L_d$	24.9 mm
$C_t$	0.1795 W/K	$L_p$	21.3 mm
$m_t$	0.9163 g	$D_{cy}$	176 mm
$Z_d$	9 mm	$V_{dead h}$	241.46 cm <sup>3</sup>
$Z_p$	21 mm	$V_{dead l}$	245.42 cm <sup>3</sup>
$D_d$	172 mm	$\Phi_0$	90°

Figure 6.6 shows the Pareto frontier of the multi-objective results. The curves with legend ' $n$ ', ' $T_c n$ ', ' $T_e T_c$ ', ' $T_e T_c \Phi_0$ ', ' $T_e T_c \Phi_0 \lambda_D$ ', ' $T_e T_c \Phi_0 \lambda_D \lambda_S$ ' and ' $T_e T_c \Phi_0 \lambda_D \lambda_S g_d$ ' represent the Pareto frontier when the optimized free variables are ' $n$ ', ' $T_c n$ ', ' $T_e T_c$ ', ' $T_e T_c \Phi_0$ ', ' $T_e T_c \Phi_0 \lambda_D$ ', ' $T_e T_c \Phi_0 \lambda_D \lambda_S$ ' and ' $T_e T_c \Phi_0 \lambda_D \lambda_S g_d$ ' respectively (the symbols can be seen in Table 6.2). For the curve with legend ' $n$ ', the thermal conductance distribution on heater and cooler are:  $C_h=0.169$  and  $C_l=0.0105$ , respectively; as long as the rotation speed ' $n$ ' is defined, the temperatures in hot and cold volumes,  $T_e$  and  $T_c$ , are defined; therefore, only ' $n$ ' is optimized. For curve with legend ' $T_c n$ ', as long as ' $T_c n$ ' are defined, the thermal conductance distribution and hot volume temperature  $T_e$  can be defined. For the curve with legend ' $T_e T_c \Phi_0$ ',  $\Phi_0$  is added as a variable (not the fixed value in Table 6.1). The curves with legends ' $T_e T_c \Phi_0 \lambda_D$ ', ' $T_e T_c \Phi_0 \lambda_D \lambda_S$ ', and ' $T_e T_c \Phi_0 \lambda_D \lambda_S g_d$ ' add  $\lambda_D$ ,  $\lambda_S$  and  $g_d$  as variables.

Table 6.2 Symbols of the parameters

$T_e$ , °C	Expansion space temperature	$\lambda_D$ , -	Dimeter ratio between piston and displacer
$T_c$ , °C	Compression space temperature	$\lambda_S$ , -	Stroke ratio between piston and displacer
$\Phi_0$ , °	Phase shift	$g_d$ , mm	Clearance size

The same results (seen on Figure 6.7) are more clearly represented in two dimensions graphics,  $(P, \eta)$  and  $(P, \dot{S}_g)$  shown in Figure 6.7 and Figure 6.8, respectively. We can see that the Pareto frontier in legend ' $T_e, T_c$ ' is very near that with legend ' $T_e, T_c, \Phi_0$ '. It means that the optimum  $\Phi_0$  is about  $90^\circ$  as initially considered in the Table 1. In addition, it can be seen that Pareto frontier is better when the number of free variables increases. From Figure 6.6 we can also see that optimizing the stroke ratio, implies about 2 times bigger thermal efficiency of the engine while the output power is the same.

From Figure 6.8 we can see that, after optimizing the stroke ratio, the engine can attain a smaller entropy generation rate when the output power is the same. Therefore, after optimizing the stroke ratio, the performance of the engine is much better than that before optimization, which indicates also that the present stroke ratio between piston and displacer is far from the optimum conditions. Similarly, after the clearance size was optimized, the engine can attain a bigger thermal efficiency and output power, which indicates that actual clearance size between displacer and cylinder wall is also different from the optimum point.

Therefore, after optimizing the different parameters (temperature in hot/cold volume, out-of-phase, diameter ratio, stroke ratio and clearance size), the engine could provide a higher mechanical output power (about 9 times) and a better thermal efficiency (about 3 times). Even if keeping the same entropy generation rate as before, the engine could still supply a higher output power (about 3 times) and thermal efficiency (about 3 times).

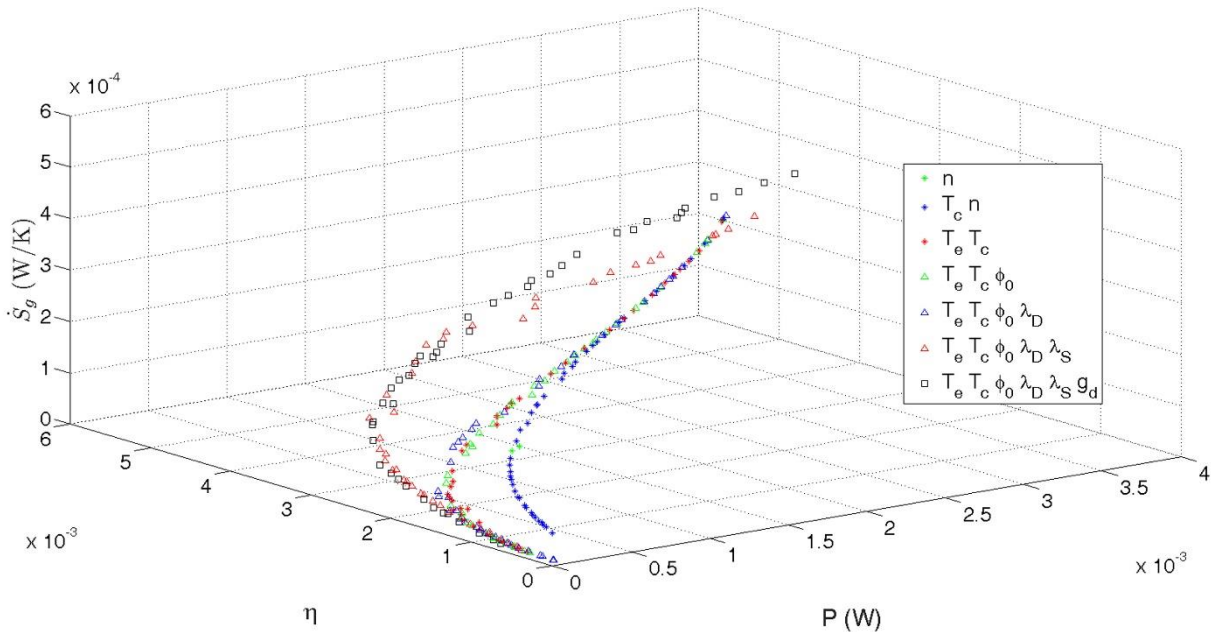


Figure 6.6 Pareto frontier for different freedoms

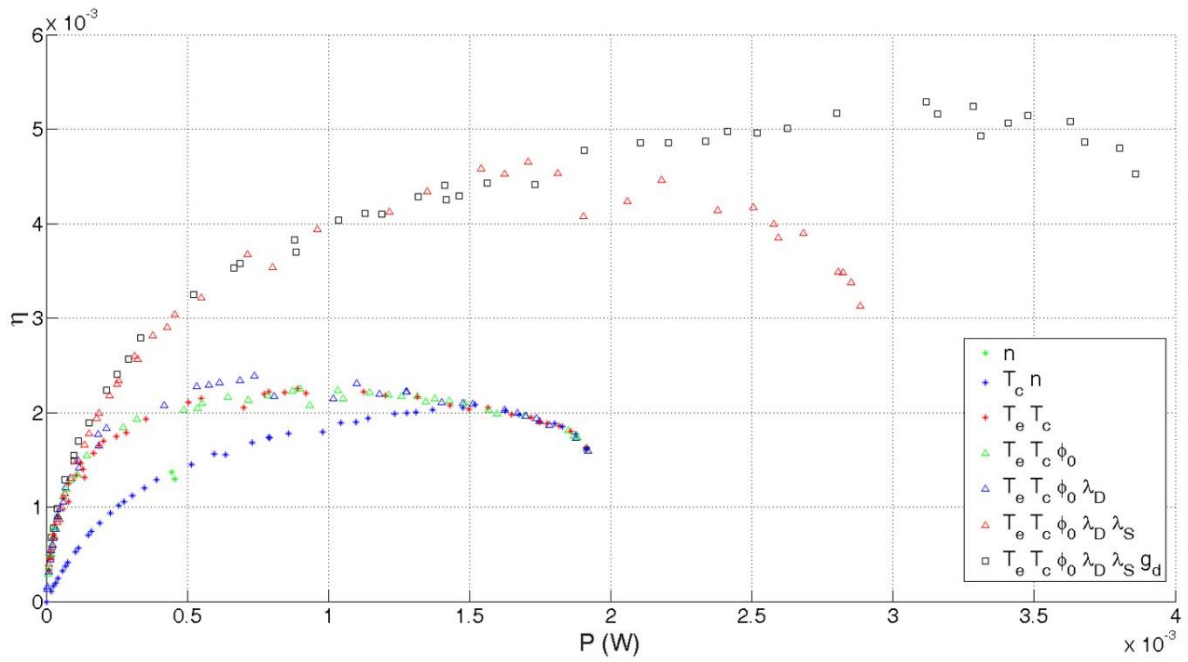


Figure 6.7  $P$  versus  $\eta$  for different freedoms

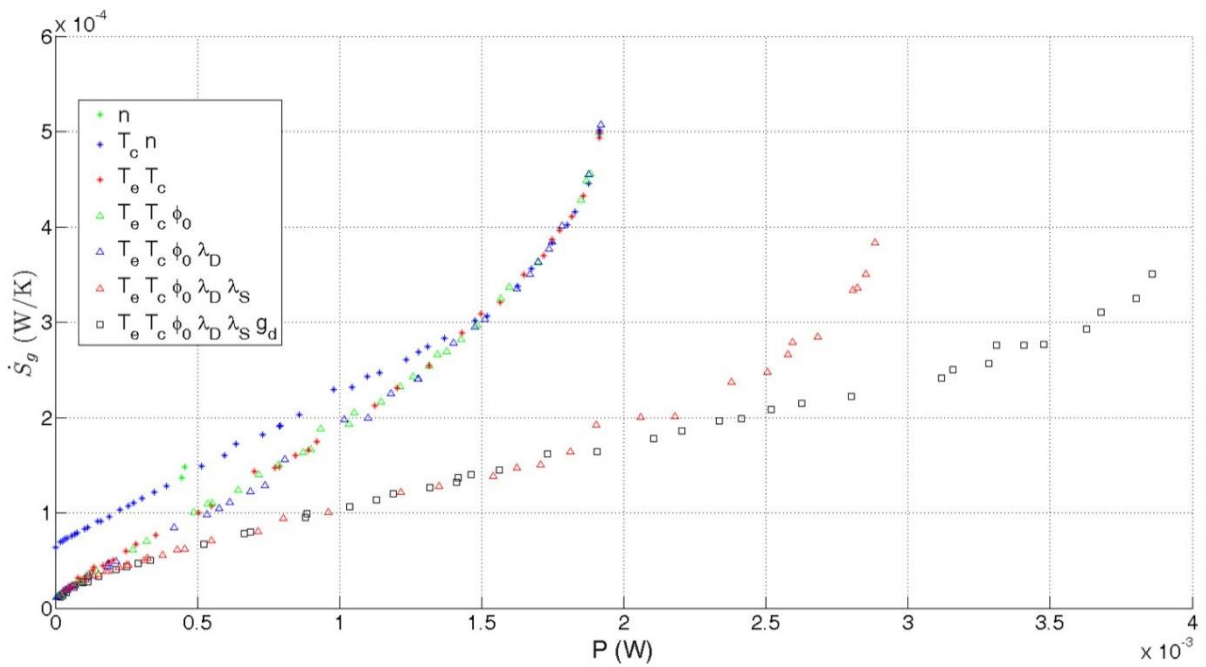
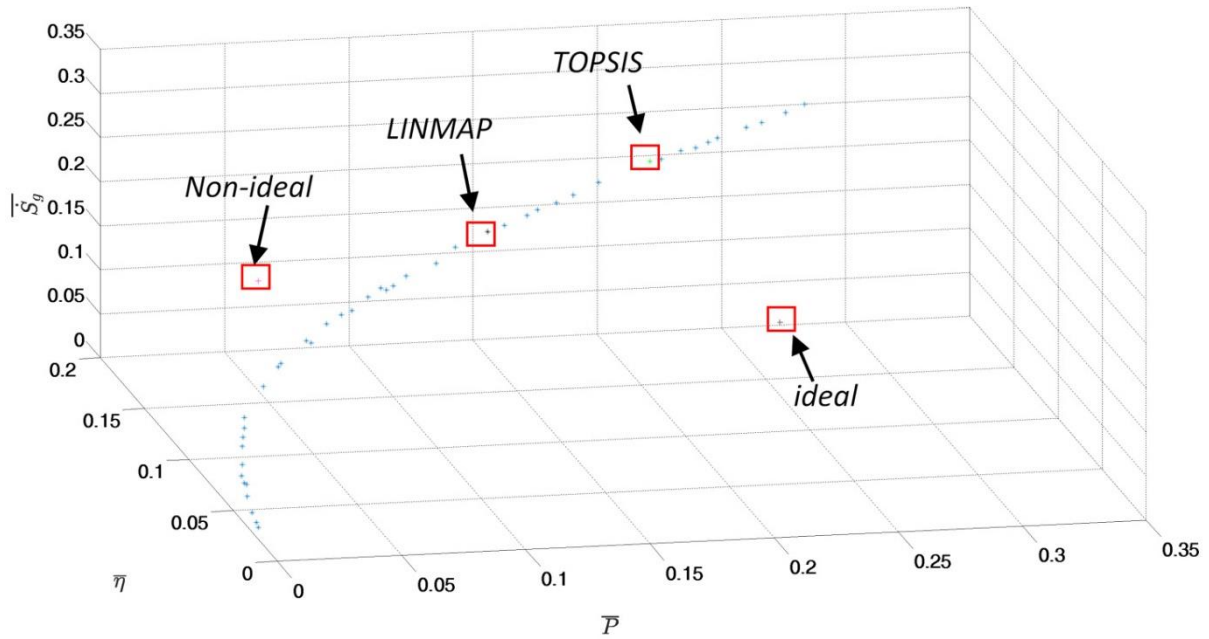
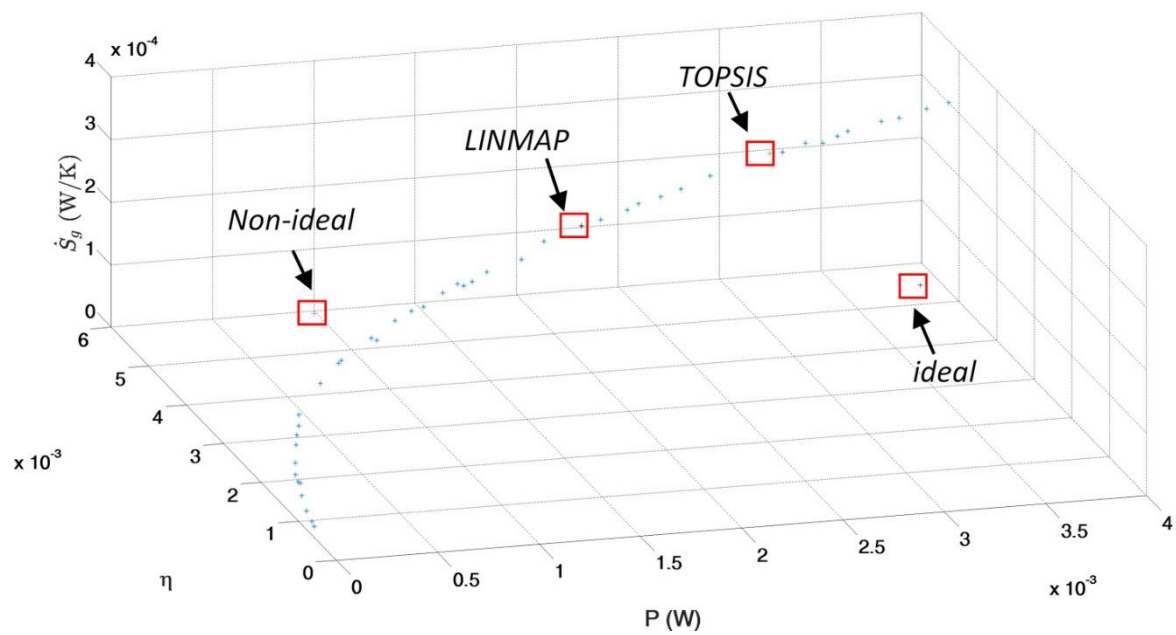


Figure 6.8 Mechanical power versus entropy generation rate for different freedoms

Figure 6.9 shows the optimum points in the Pareto frontier (curve with legend ' $T_e T_c \Phi_0 \lambda_D \lambda_S g_d$ '), using the *LINMAP* and *TOPSIS* decision-making techniques. The graphics (a) and (b) show the optimum points of dimensionless and dimensional objective functions, respectively.



(a) Optimum points of dimensionless objective functions



(b) Optimum points of the objective functions

Figure 6.9 Optimum point using two different making-decision methods

These results are compared with those obtained using ecological method [1-3], which we have adapted on our engine. An ecological function is defined as below to be the objective function for the optimization problem:

$$E = P - T_0 \dot{S}_g \quad (33)$$

where  $T_0$  is the ambient temperature.

We can see on Table 6.3, after optimization using ecological method, the entropy generation speed is reduced by twelve times; however, the output power and thermal efficiency decrease to about respectively 4% and 50% of those before optimization. By the *LINMAP* decision method, the entropy generation rate is about 30% higher than that before optimization; however, the output power and thermal efficiency increase to about respectively 475% and 354% of that before optimization. By the *TOPSIS* decision method, the entropy generation rate is about 75.9% higher than that before optimization, however, the output power and thermal efficiency increase to about 703% and 386% of those before optimization, respectively. Therefore, we can improve the performance of the engine using the optimum values indicated by the multi-objective method.

Compared with ecological method results, the *LINMAP* results increases the entropy generation rate to about 18 times, however the output power and thermal efficiency increase to about 115 and 7.1 times. Thus, even if operation increasing the cost (increasing entropy generation up to 18 times higher), we get a big return: output power is much bigger (115 times), and thermal efficiency increases also (7.1 times). Similarly, the *TOPSIS* method in this optimization also gets a big return: output power is much bigger (170 times), thermal efficiency is also bigger (7.8 times), with the cost of entropy generation rate increasing (21 times). Therefore, comparing with the ecological optimization method, the multi-objective method can better balance the three objective goals: output power, thermal efficiency and entropy generation rate. Comparing with *LINMAP* decision making method, the *TOPSIS* decision making method obtains bigger both output power and efficiency in this case. However, this phenomenon is not universal; it depends on the line type of the Pareto frontier, and sometimes they may coincide each other as reference [23] in the multi-objective optimization to GPU-3.

Table 6.3 Optimum variables and objective functions values

	$T_e$ (K)	$T_c$ (K)	$\Phi_0$ (°)	$D_d$ (mm)	$Z_p$ (mm)	$g_d$ (mm)	$P$ (mW)	$\eta$ (%)	$\dot{S}_g$ (mWK <sup>-1</sup> )
Before optimization	346.2	333.9	90	172.0	21.0	2.00	0.44	0.14	0.14
Ecological method	348.0	336.1	86	122.4	12.5	3.52	0.02	0.07	0.01
<i>LINMAP</i>	344.6	307.9	89	211.0	74.3	0.82	2.11	0.48	0.18
<i>TOPSIS</i>	342.2	310.1	90	216.3	80.1	1.25	3.12	0.53	0.24

The Pareto frontier variation with the heat source temperature variation is shown in Figure 6.10 and Figure 6.11 (2D for a better view). We can see that an increase in the hot volume temperature implies a huge increase of the output power and thermal efficiency of the engine. The output power corresponding to the maximum thermal efficiency increases also. For a LDT Stirling engine using solar energy, the pollution and ecological effect is small already; therefore, it's very useful to increase the hot volume temperature in our case. This can be possible by a good choice of the solar panel.

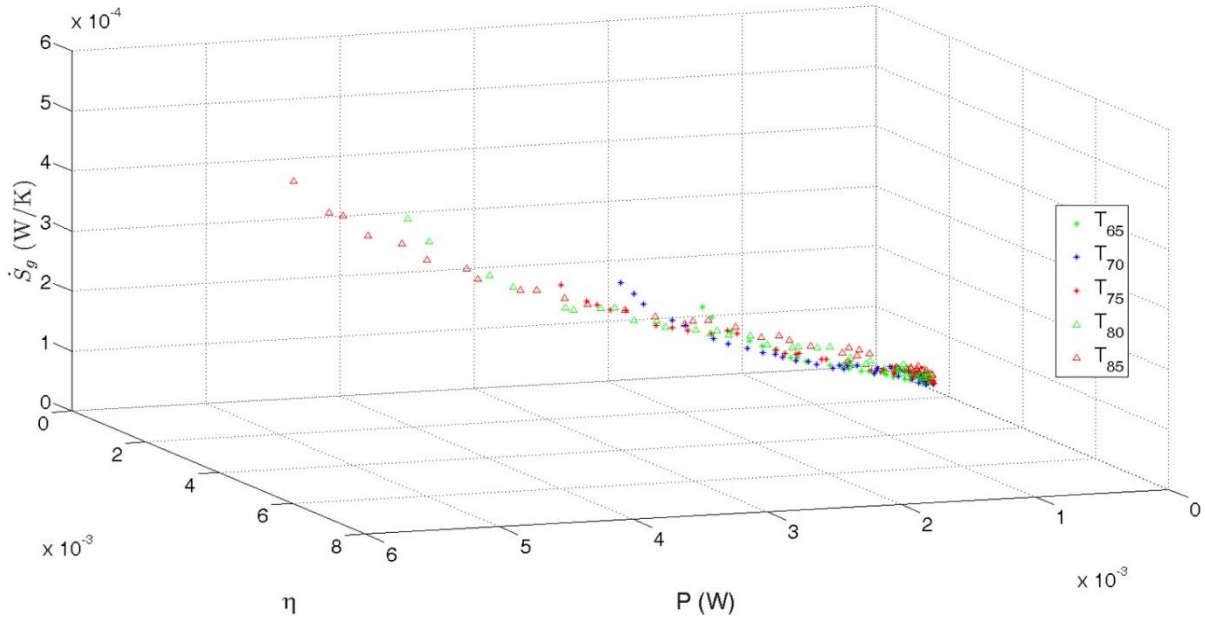
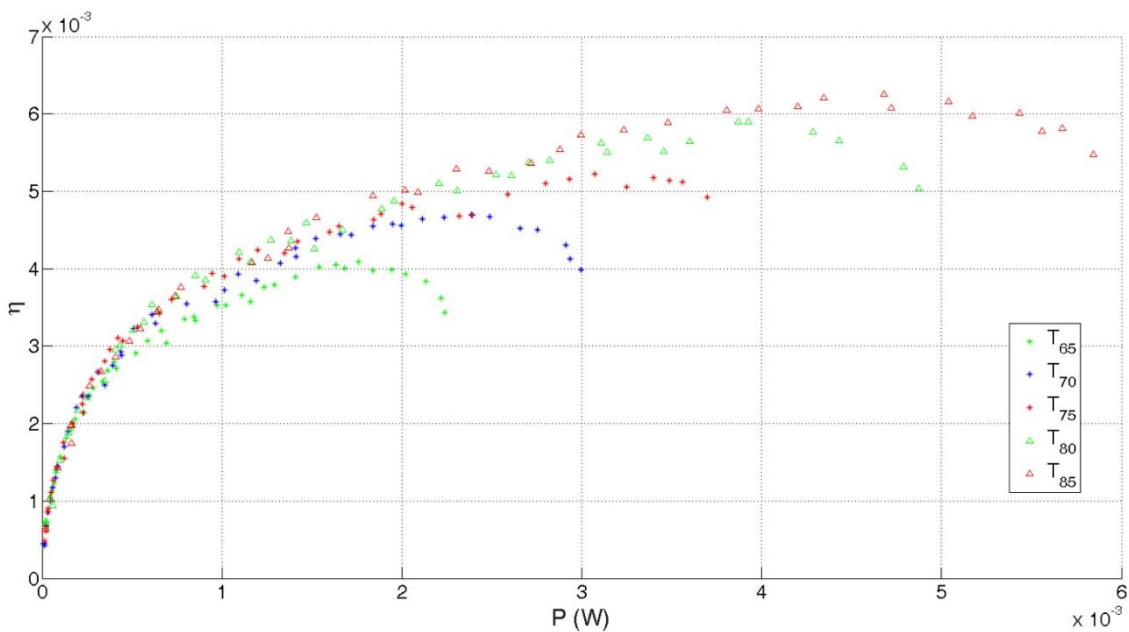
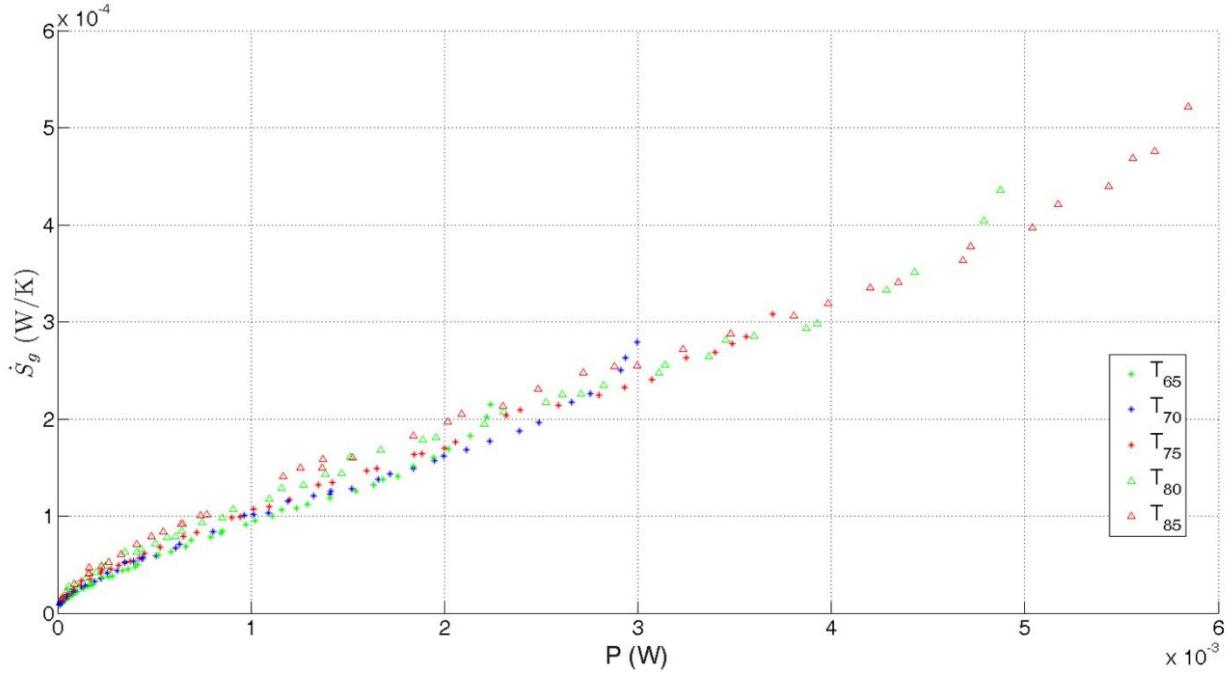


Figure 6.10. Pareto frontier for different heat source temperature



(a) P versus  $\eta$



(b) P versus  $\dot{S}_g$

Figure 6.11 2-D representation of the Pareto frontier of Figure 6.10

The Pareto frontier variation versus the thermal conductance is plotted in Figure 6.12 and Figure 6.13. A total thermal conductance increase indicates an increase in the output power and thermal efficiency. From Figure 6.13 (b), we can see that the entropy generation rate can be reduced by increasing the total thermal conductance and keeping the output power fixed. And the more the output power is, the more apparent this phenomenon is. This result indicates that the thermal conductance should be improved also for our engine in order to improve its performance.

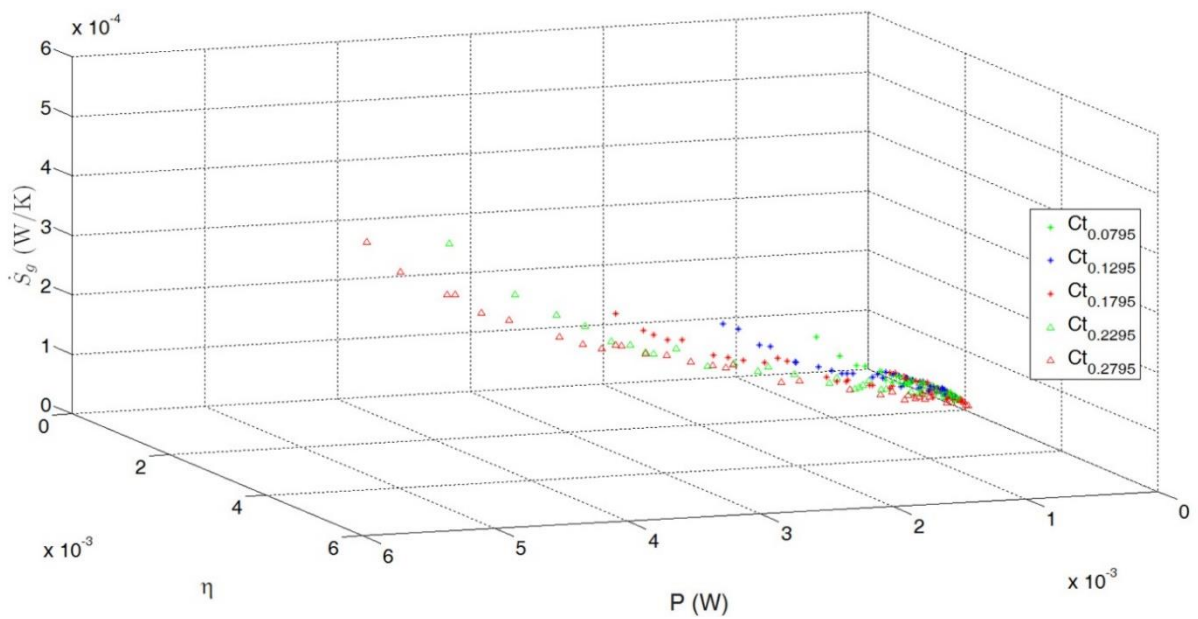


Figure 6.12 Pareto frontier for different thermal conductance

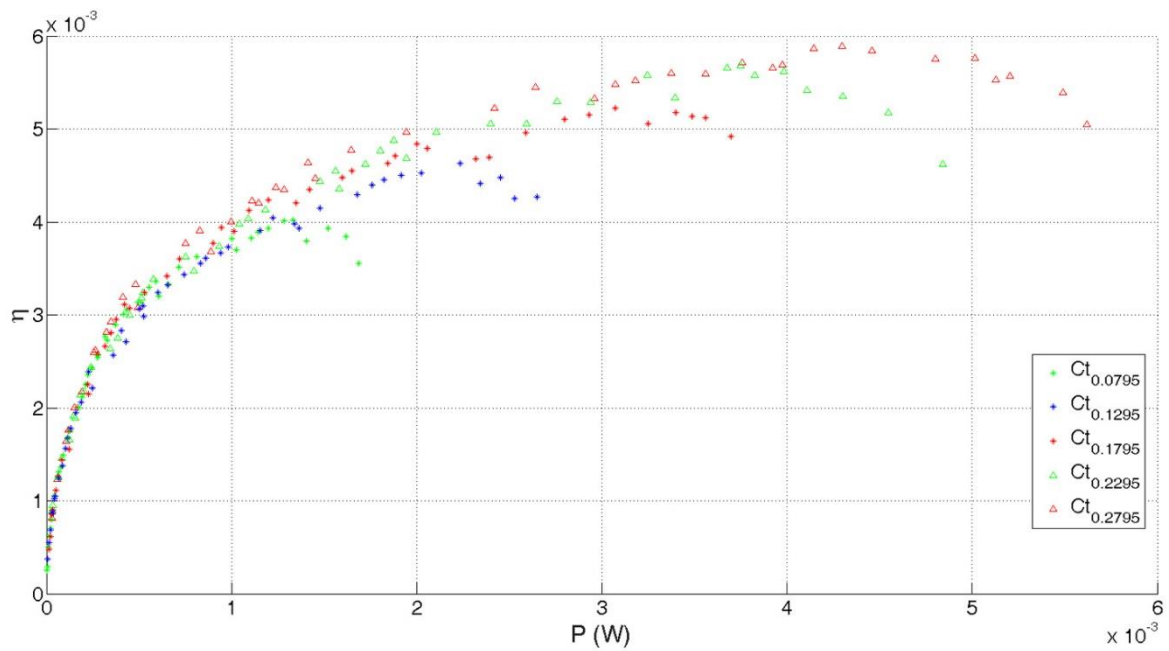
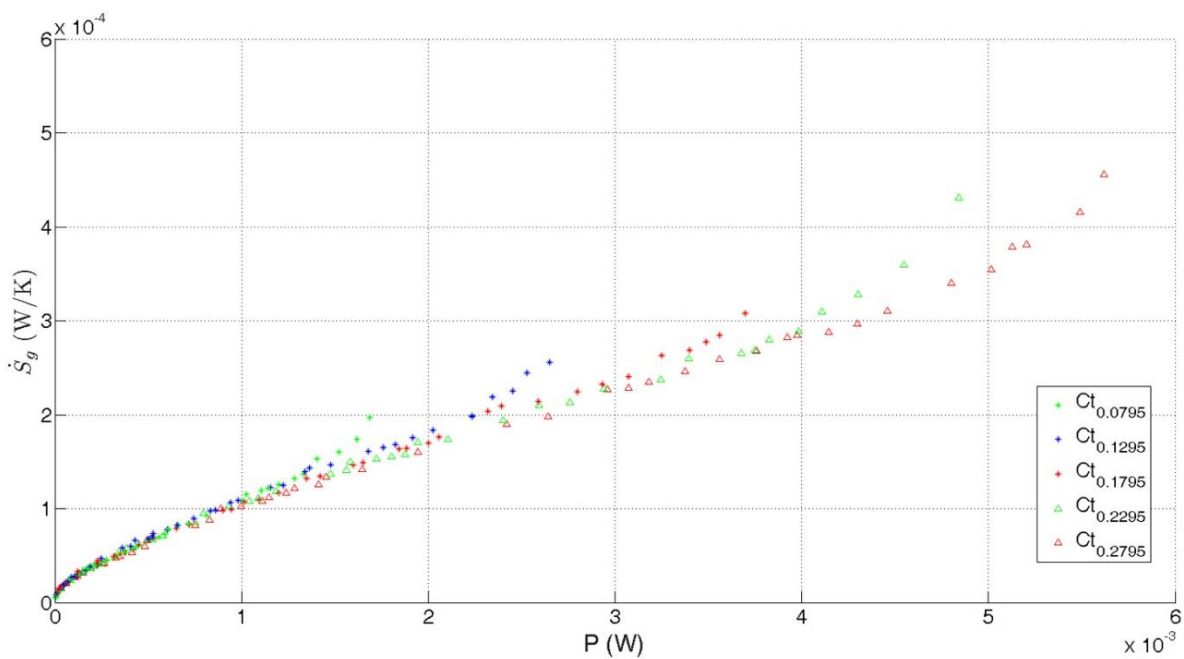
(a) P versus  $\eta$ (b) P versus  $\hat{S}_g$ 

Figure 6.13 2-D representation of the Pareto frontier of Figure 6.12

Figure 6.14 shows the typical average distance between individuals and typical average spread variation with the generations' calculation during the optimization process. We can see that from the beginning to the 50<sup>th</sup> generation, the average distance between individuals decreases slightly; and then after the 50<sup>th</sup> generation, the average distance is stable until the end of the calculation. The average spread decreases quickly from the beginning to the 50<sup>th</sup> generation, and keep nearly zero after the 100<sup>th</sup> generation, which indicates that after about 100<sup>th</sup> generation,

the optimization process is nearly stable.

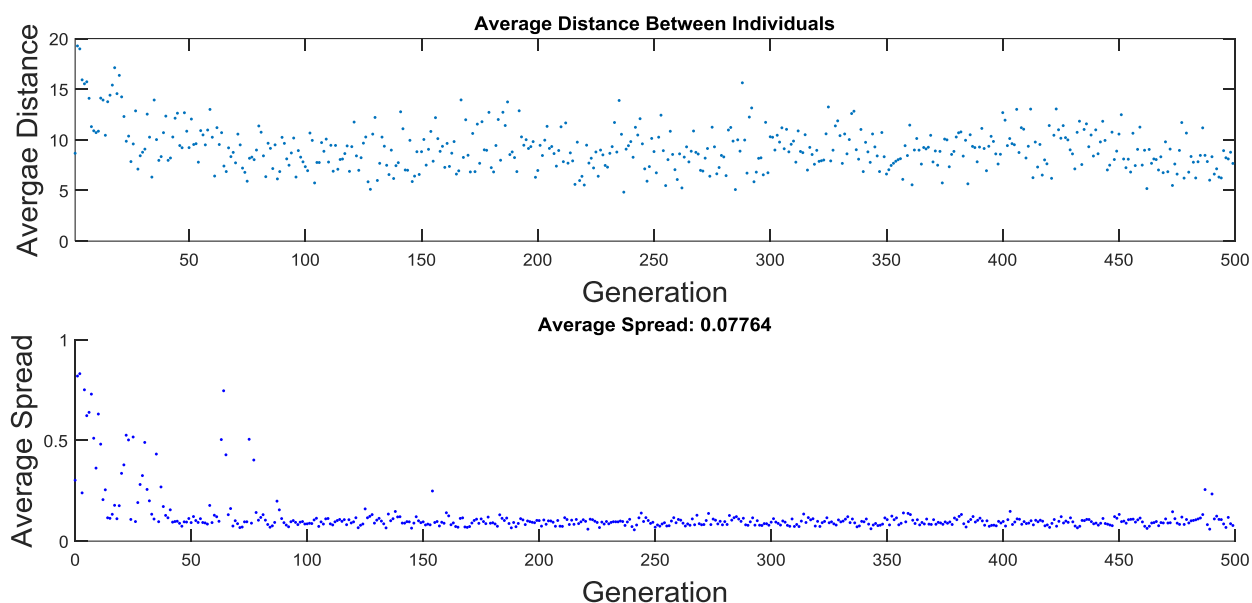


Figure 6.14 Average distance between individuals and average spread variation with generation

## 6.6 Summary

In this chapter, the gamma type Stirling engine has been optimized using Finite Physical Dimension Thermodynamics method with a multi-objective genetic method considering output power, thermal efficiency and entropy generating rate as objective functions simultaneously. Various losses due to the piston finite speed, the regenerator viscosity, the hysteresis spring of the working gas, the mechanical friction, the heat transfer imperfection on the regenerator and the shuttle of the displacer have been considered during the optimization process. Firstly, genetic algorithm was used to get the Pareto frontier. Then the matrix of the objective values was non-dimensionalized by the Euclian non-dimensionalization method. Finally, two decision-making methods (*LINMAP* and *TOPSIS*) were used to get the optimum point.

The entropy generation flow can be reduced by about twelve times using only ecological method optimization; however, the output power and the thermal efficiency decrease to about 4% and 50% respectively. Using *LINMAP* decision method, the entropy generation rate is about 30% higher than that before optimization but the power and the thermal efficiency increase to about respectively 5 times and 4 times. Using the *TOPSIS* decision method, the entropy generation rate is about 75.9% higher than that before optimization, while the power and thermal efficiency increase to about 7 times and 4 times of those before optimization, respectively. Therefore, the performance of the engine could be improved using the optimum values indicated by the multi-objective method. Comparing with the ecological optimization method, the multi-objective method can better balance the three objective goals: output power, thermal efficiency and entropy generation rate. Comparing with *LINMAP* decision making method, the *TOPSIS* decision making method obtains bigger both output power and efficiency in this case.

The effects of the hot volume temperature and the total thermal conductance on the Pareto frontier have also been studied: an increase in the hot volume temperature can increase both the output power and thermal efficiency of the engine, but also the entropy generation rate. In addition, an increase in the total thermal conductance implies a strong increase in the output power and the thermal efficiency, and only a slight increase in the entropy generation rate. These results indicate some improvements (increasing hot temperature and thermal conductance) to make on the studied experimental Gamma type Stirling engine, in order to improve its performance.

## References

- [1] Açıkkalp E., Models for optimum thermo-ecological criteria of actual thermal cycles. *Thermal Science*, 2013. **17**(3): p. 915-930.
- [2] Ding Z., Chen L., and Sun F., Ecological optimization of energy selective electron (ESE) heat engine. *Applied Mathematical Modelling*, 2011. **35**(1): p. 276-284.
- [3] Chen L., Zhang W., and Sun F., Power, efficiency, entropy-generation rate and ecological optimization for a class of generalized irreversible universal heat-engine cycles. *Applied Energy*, 2007. **84**(5): p. 512-525.
- [4] Hosseinzade H. and Sayyaadi H., CAFS: The Combined Adiabatic–Finite Speed thermal model for simulation and optimization of Stirling engines. *Energy Conversion and Management*, 2015. **91**: p. 32-53.
- [5] Ahmadi M.H., et al., Designing a solar powered Stirling heat engine based on multiple criteria: Maximized thermal efficiency and power. *Energy Conversion and Management*, 2013. **75**: p. 282-291.
- [6] Sayyaadi H. and Aminian H.R., Design and optimization of a non-TEMA type tubular recuperative heat exchanger used in a regenerative gas turbine cycle. *Energy*, 2010. **35**(4): p. 1647-1657.
- [7] Pareto efficiency. Available from: [https://en.wikipedia.org/wiki/Pareto\\_efficiency](https://en.wikipedia.org/wiki/Pareto_efficiency).
- [8] Fonseca C. and Fleming P., Multiobjective Optimization. In, Back T., Fogel DB, Michalewicz Z.(Eds.), *Handbook of Evolutionary Computation*. 1997, Oxford University Press.
- [9] Van Veldhuizen D.A. and Lamont G.B., Multiobjective evolutionary algorithms: Analyzing the state-of-the-art. *Evolutionary computation*, 2000. **8**(2): p. 125-147.
- [10] Fogel L., Owens A., and Walsh M., *Adaptation in natural and artificial systems*. 1975, University of Michigan Press, Ann Arbor, MI, USA.
- [11] Deb K., et al., A fast and elitist multiobjective genetic algorithm: NSGA-II. *Evolutionary Computation, IEEE Transactions on*, 2002. **6**(2): p. 182-197.
- [12] Veldhuizen D. and Lamont G.B., Multiobjective evolutionary algorithms: Analyzing the state-of-the-art. *Evolutionary computation*, 2000. **8**(2): p. 125-147.
- [13] Goldberg D.E., *Genetic algorithms in search, optimization, and machine learning*. Addison wesley, 1989. **1989**.
- [14] Sayyaadi H. and Mehrabipour R., Efficiency enhancement of a gas turbine cycle using an optimized tubular recuperative heat exchanger. *Energy*, 2012. **38**(1): p. 362-375.
- [15] Ahmadi M.H., et al., Multi-objective optimization of an irreversible Stirling cryogenic

- refrigerator cycle. *Energy Conversion and Management*, 2014. **82**: p. 351-360.
- [16] Minassians A.D., *Stirling Engines for Low-Temperature Solar-Thermal-Electric Power Generation*, in U Berkeley. 2007, UC Berkeley.
- [17] Tanaka M., Yamashita I., and Chisaka F., Flow and heat transfer characteristics of the Stirling engine regenerator in an oscillating flow. *JSME international journal. Ser. 2, Fluids engineering, heat transfer, power, combustion, thermophysical properties*, 1990. **33**(2): p. 283-289.
- [18] Araoz J.A., et al., Non-ideal Stirling engine thermodynamic model suitable for the integration into overall energy systems. *Applied Thermal Engineering*, 2014. **73**(1): p. 205-221.
- [19] Petrescu S., et al., Application of the Direct Method to irreversible Stirling cycles with finite speed. *International Journal of Energy Research*, 2002. **26**(7): p. 589-609.
- [20] Urieli I. and Berchowitz D.M., *Stirling cycle engine analysis*. 1984: Taylor & Francis.
- [21] Hosseinzade H., Sayyaadi H., and Babaelahi M., A new closed-form analytical thermal model for simulating Stirling engines based on polytropic-finite speed thermodynamics. *Energy Conversion and Management*, 2015. **90**: p. 395-408.
- [22] Li R., Grosu L., and Queiros-Condé D., Losses effect on the performance of a Gamma type Stirling engine. *Energy Conversion and Management*, 2016. **114**: p. 28-37.
- [23] Toghyani S., et al., Multi-objective optimization of GPU3 Stirling engine using third order analysis. *Energy Conversion and Management*, 2014. **87**: p. 521-529.



# Chapter 7 Isothermal model with losses applied to an Alpha type Stirling cryocooler

## 7.1. Introduction

With the development of High Temperature Superconductor (HTS) materials [1] and infrared detector technology [2, 3], the cryogenic technology is more and more widely used in energy, medical, and aerospace areas [4-9]. Stirling cryocooler is an excellent tool to supply cooling power in the various applications [5, 10, 11].

The Stirling cycle coolers were firstly introduced by the Philips company in the 1950s for liquid air production [12]. In 1960s, Philips company reported a two-stage Stirling cryocooler which attained a lowest temperature of 12 K and a cooling power of 100 W at 20 K with a relative Carnot efficiency of 17% [13, 14]. The pneumatically-driven split Stirling-cycle cryocooler was invented by Horn et al. in the 1970s [15, 16] which has low cold-tip vibration, low mass and high efficiency [17]. In 1970s, Oxford split-Stirling cryocoolers have been developed in Oxford University [18], which extended the life span of Stirling cryocooler greatly. Over the past decade years, various kinds of Stirling cryocoolers driven through crank-shaft, free displacer, and free piston free displacer, have been developed by scientists and researchers. Within the developing process, the mechanism and characteristics of the cryocoolers have also been studied by those researchers.

Walker et al. have developed a microcomputer simulation for Stirling cryocoolers [19] using isothermal assumption in compression and expansion volumes. Atrey et al. have used adiabatic model in compression and expansion volumes to analyze several Stirling cryocoolers [20]. Bauwens has divided the cryocooler into several spaces, some of which are isothermal and others are adiabatic [21]. Rijpma et al. have designed and constructed a small Stirling cryocooler used for the superconducting sensors for the heart scanner [22]. Zhang et al. have proposed a mathematical model of a one-stage Oxford split-Stirling cryocooler to simulate its dynamic performance solved by numerical method [23]. They studied the operating characteristics of the connecting pipe and its effect on the cooling performance of an 80 K Oxford split-Stirling-cycle cryocooler [24]. The effect of the connecting pipe can be seen in Figure 7.1 and Figure 7.2. Figure 7.1 shows that with the connecting pipe's diameter increasing the cooling power increase and the compressor input power decrease quickly initially and then gently after the diameter exceeding 2.5mm. Figure 7.2 shows that with the connecting pipe's diameter increasing both of the pressure wave phase lag and the pressure wave amplitude attenuation decrease quickly initially and then slightly after the diameter exceeding 2.5mm.

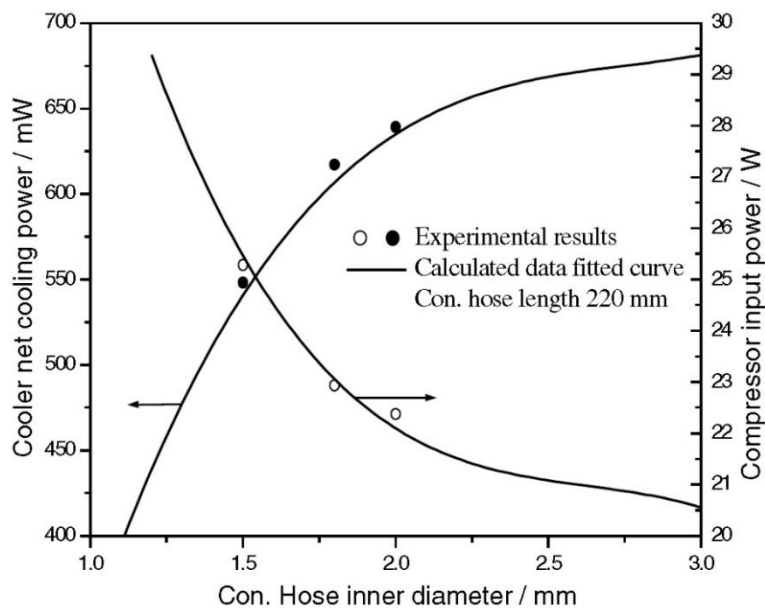


Figure 7.1 Connecting hose inner diameter VS cooler performance for one-stage Oxford split-Stirling cryocooler [24]

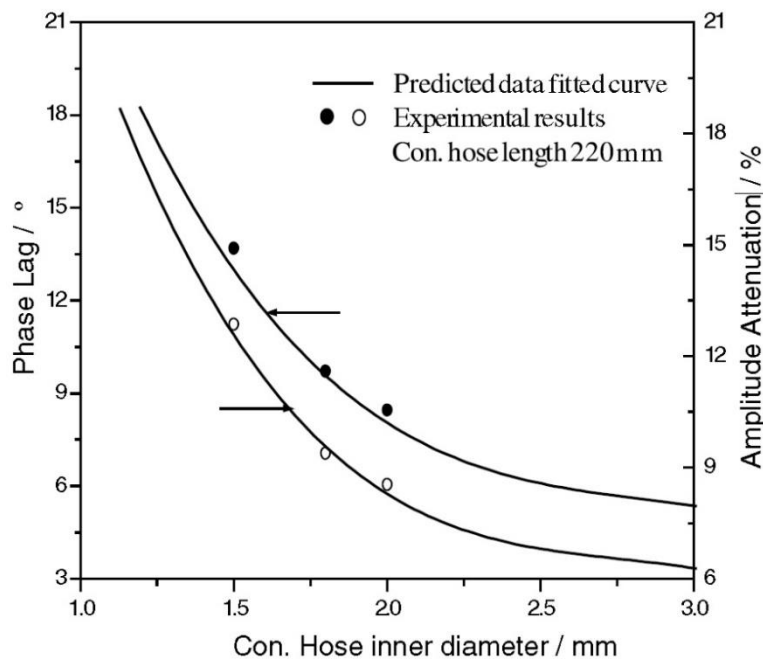


Figure 7.2 Connecting hose inner diameter vs. pressure phase lag and amplitude for one-stage Oxford split-Stirling cryocooler [24]

Bailey et al. have studied the gas spring losses in the linear clearance seal compressors used in cryocoolers experimentally [25]. Clearman et al. have used the CFD model to simulate the regenerator (which included 325 and 400 mesh stainless steel screens, stainless steel metal foam, sintered 400 mesh stainless steel screens, and a stack of micromachined perforated plates) and compared with experimental results which showed that the regenerator fillers are anisotropic [26]. Ahmadi et al. have multi-objective optimized an irreversible Stirling cryogenic

refrigerator cycle [27] and Stirling heat pump [28]. Three objective functions including input power, coefficient of performance (COP) and cooling load have been involved in the optimization process. Genetic algorithm is used to get the Pareto frontier firstly, and different decision making approaches including TOPSIS, LINMAP and fuzzy Bellman–Zadeh are used to determine the optimum operating parameters.

Park S. J. et al. have tested the performance of the split type free piston/free displacer type Stirling cryocooler and have studied the effect of operating parameters [12] and of the phase shift between the piston and displacer [29]. Figure 7.3 shows the phase shift between displacement of the displacer and the pressure of the compression space under different operating frequencies.

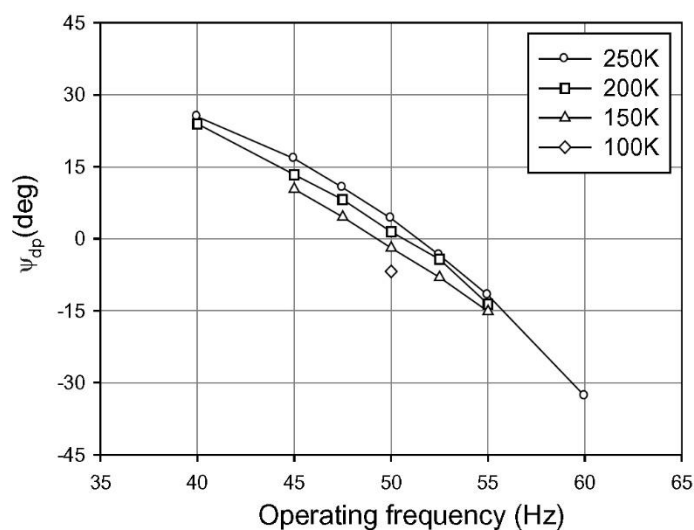


Figure 7.3 Phase shifts between displacements of the displacer and the pressure of the compression space under different operating frequencies.

Vladimir Dubrovsky has developed and tested an adaptive control system for the linear compressor used for Stirling cryocooler [30]. Narasaki et al. have developed a two-stage small Stirling cryocooler for the infrared astronomical satellite ASTRO-F [8] whose typical power is 200 mW at 20 K and total input power to the compressor and the cold head is below 90 W without driver electronics. Veprik et al. have done the theoretical study and practical implementation of an ultra-low vibration split Stirling linear cryogenic cooler with a dynamically counterbalanced pneumatically driven expander [31]. Yang and Chung have studied the size effects on miniature Stirling cycle cryocoolers, and found that there exists an optimum ratio between the hydraulic diameter and the length of the regenerator to get the maximum net refrigeration [32]. Cha et al. have studied the oscillatory flow in the regenerator for Stirling cryocooler or Pulse-tube cryocooler, numerically and experimentally [33]. Chen et al. have studied the phase shift characteristic of the pneumatic Stirling cryocooler with free piston and free displacer by means of experimental and theoretical method, of which parameters include charging pressure, natural frequency of displacer, damping coefficient of displacer, and working frequency on the pressure [34]. Riabzev et al. have developed a vibration-free Stirling cryocooler for high definition microscopy, using passive mechanical counterbalancing of the

main portion of the low frequency vibration export in combination with an active feed-forward multi-axes suppression of the residual wideband vibration, thermo-conductive vibration isolation struts and soft vibration mounts [35]. Razani et al. have developed a thermodynamic model for a Stirling Refrigerator including irreversibilities such as external heat transfer with the reservoirs, heat leak, flow and heat transfer in regenerator [36]. Xia and Chen have analyzed resonant frequency of moving magnet linear compressor for a Stirling cryocooler [37]. Dai et al. have studied the impedance match in Stirling type cryocoolers generalizing the basic principles concerning the efficiency and acoustic power output of the linear compressor [38]. He et al. have proposed a mathematical model based on thermodynamic theory of variable mass for the split Stirling refrigerator, in which, the whole machine was considered by one-dimensional approach while the processes in the regenerator were simulated by two-dimensional approach [39]. Yu et al. have developed a Free Piston Stirling Cryocooler with a high cooling capacity optimized with thermo-acoustic theory and Computational Fluid Dynamics (*CFD*) method [10]. They have obtained a cooling power of 56 W at 80 K with a charge pressure of 3 MPa of helium and operating frequency of 50 Hz, and the relative Carnot efficiency of input acoustic power was 16.4%. Kenta Yumoto et al. have developed a split Stirling cryocooler for HTS devices with a cooling capacity of 120 W at 70 K and a compressor input power of 2.15 kW with corresponding *COP* of 0.056 [1]. Wang et al. have designed and studied a high capacity two-stage free piston Stirling cryocooler working around 30 K, which reached a lowest cold-head temperature of 27.6 K and achieved a cooling power of 78 W at 40 K with an electric power input of 3.2 kW [13, 40]. The influences of different parameters such as mean pressure, electric power input and cold-head temperature have also been investigated. Figure 7.4 shows the cooling power and relative Carnot efficiency variation with the cold end temperature.

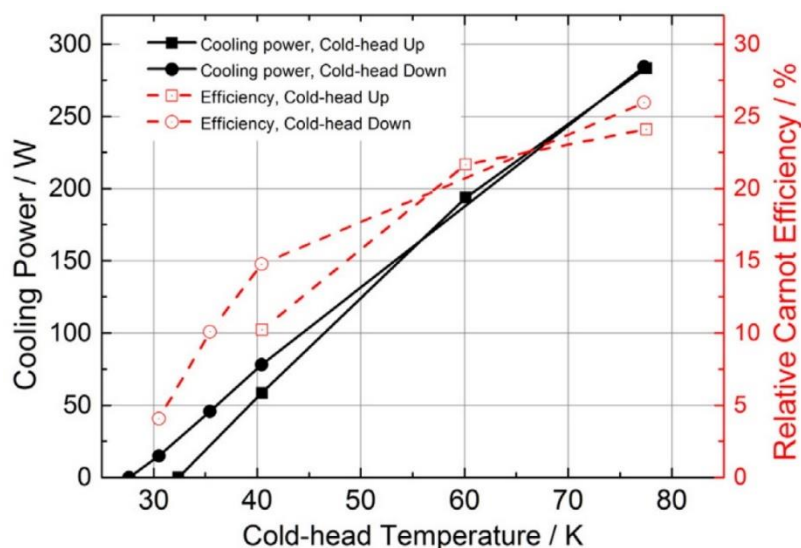


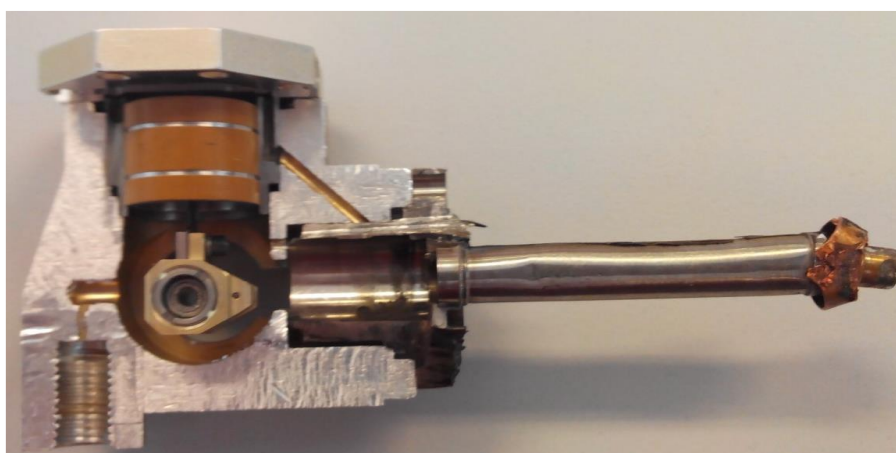
Figure 7.4 System performance at two different cold-head orientations, experiment

Caughley A. et al. have constructed and studied a diaphragm free-piston Stirling cryocooler by *CFD* and experimental method [41, 42]. Zhang and Zhong have proposed a theoretical model of a gas clearance phase regulation mechanism for a pneumatically-driven split-Stirling-cycle

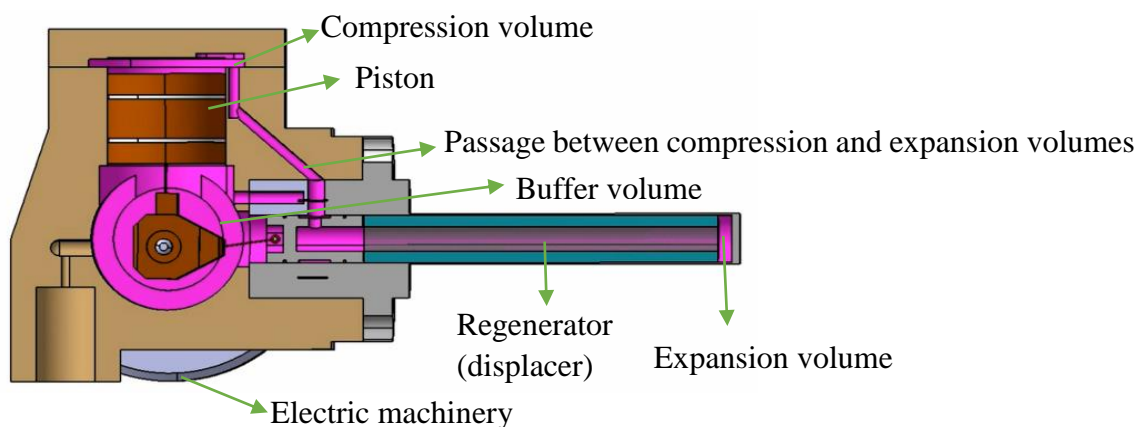
cryocooler, where the working characteristics of the compressor motor and the principal losses of cooling, including regenerator inefficiency loss, solid conduction loss, shuttle loss, pump loss and radiation loss, are taken into account [17].

## 7.2. Presentation of the studied cryocooler

The studied Stirling cryocooler in this thesis is used in the OMEGA instrument (Infrared mineralogical mapping spectrometer) in the frame of the Mars Express project by the European Space Agency (ESA). The geometry of the Stirling cryocooler can be seen in Figure 7.5. It consists of a working piston, a regenerator inserted in a displacer, a rotary electric machinery connected with the piston and the displacer rods, a compression volume, an expansion volume, and a buffer volume around the crankshaft. Table 7.1 shows the geometrical and physical parameters of the studied Stirling cryocooler.



(a) Main components



(b) Sketch of gas flow sections

Figure 7.5 Geometry of the Stirling cryocooler used in the Mars Express project

Table 7.1 Geometrical and physical parameters of the studied Stirling cryocooler

Piston stroke, mm	2	Internal regenerator diameter, mm	3.1
Displacer stroke, mm	2	Regenerator length, mm	41.8
Piston diameter, mm	14	Regenerator dead volume, mm <sup>3</sup>	210.76
Displacer diameter, mm	6	External cylinder diameter, mm	6.4
Piston swept volume, mm <sup>3</sup>	307.8	Internal cylinder diameter, mm	6
Displacer swept volume, mm <sup>3</sup>	56.5	Working gas	helium
Buffer space volume, mm <sup>3</sup>	4823.9	Rotate speed, RPM	1800
Piston length, mm	11.4	Compression volume temperature, K	290
Displacer length, mm	47.6	Expansion volume temperature, K	77
Expansion dead volume, mm <sup>3</sup>	11.3	Phase shift, degree	90
Compression dead volume, mm <sup>3</sup>	64.1	Average compression volume pressure, bar	6

Ideal reversed Stirling cycle can be seen in Figure 7.6, which consists of two isothermal processes ( $b-c$  and  $d-a$ ) and two isochoric processes ( $a-b$  and  $c-d$ ). Due to the sinusoidal oscillating movement of the piston and displacer, the Stirling cryocooler usually has the  $pV$  diagram like the ellipse inside of the ideal curve  $a-b-c-d$ . Because of the imperfection of the regenerator, during the regenerative processes  $a-b$  and  $c-d$ , the working gas can only reach state points  $a'$  and  $c'$ . There are also other imperfections and irreversibilities which need to be taken into account as presented here below.

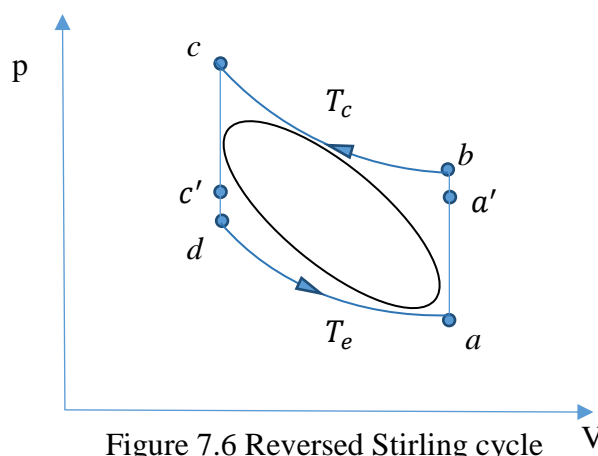


Figure 7.6 Reversed Stirling cycle

From Table 7.1, it can be seen that the buffer volume is much bigger than the working space,

and the buffer volume compression ratio (about 1.2) is much less than the working volume compression ratio (about 2.3). The average pressure in the buffer volume and working volume is 6 bar, therefore the pressure value oscillation in the buffer volume and working volume can be in the range of 5.5~6.5 bar and 3.6~8.4 bar respectively, if we don't consider the temperature oscillation in the working volume. Actually, due to the displacer's oscillating moving, the working volume is compressed when the working gas is displaced from cold space to hot space; and expanded when the working gas is displaced from hot space to cold space. Consequently, in reality, the pressure oscillation in the working volume is higher than 3.6~8.4. Therefore, during the cycle process, the pressure variation in the buffer volume is less than  $(6.5-5.5)/(8.4-3.6)=0.2$  times of pressure variation in the working volume. In addition, in the buffer volume, the temperature is assumed to be constant, and the phase lag between pressure and volumetric oscillation is assumed to be close to zero, as a result, the parasitic  $pV$  power of the buffer volume can be neglected.

Based on the reciprocating movement of the piston and the displacer, and the phase shift between them, the variation of compression and expansion volumes can be expressed as:

$$V_e = \frac{V_{e0}}{2} [1 - \cos(\omega t)] + V_{de} \quad (1)$$

$$V_c = \frac{V_{c0}}{2} [1 - \cos(\omega t - \varphi_0)] + V_{dc} \quad (2)$$

For the regenerator, linear temperature variation is assumed and the average temperature can be expressed according to [43] as below:

$$T_r = \frac{T_c - T_e}{\ln\left(\frac{T_c}{T_e}\right)} \quad (3)$$

Supposing that the working gas is an ideal gas, the pressure can be calculated as:

$$p = m_t r_g / \left( \frac{V_e}{T_e} + \frac{V_c}{T_c} + \frac{V_r}{T_r} \right) \quad (4)$$

$$dp = - \frac{p \left( \frac{dV_e}{T_e} + \frac{dV_c}{T_c} \right)}{\frac{V_e}{T_e} + \frac{V_r}{T_r} + \frac{V_c}{T_c}} \quad (5)$$

For an open system, the energy balance can be written as:

$$dE = \delta Q + \delta W + dm_{in} \left( gz_{in} + \frac{u_{in}^2}{2} \right) + H_{in} - dm_{out} \left( gz_{out} + \frac{u_{out}^2}{2} \right) - H_{out} \quad (6)$$

Considering the small dimensions of the studied Stirling cryocooler, the kinematic and potential energy variation can be neglected. Then, applying the energy balance on expansion and compression volumes, the heat transfer in these volumes can be obtained as:

$$\delta Q_e = \frac{c_v}{r_g} V_e dp + \frac{c_p}{r_g} p dV_e - c_p T_{re} dm_{re} \quad (7)$$

$$\delta Q_c = \frac{c_v}{r_g} V_c dp + \frac{c_p}{r_g} p dV_c + c_p T_{cr} dm_{cr} \quad (8)$$

The indicated theoretical work  $W_i$  can be expressed as:

$$\delta W_i = -pdV_e - pdV_c \quad (9)$$

However, there are some losses in Stirling cryocoolers to be taken into account such as: heat conduction loss, pump losses, flow viscosity, mechanical friction etc. Therefore, the real power required by the engine and the net cooling power can be expressed as:

$$\dot{W}_{motor} = \dot{W}_i + \sum \dot{W}_{loss} \quad (10)$$

$$\dot{Q}_{e\ net} = \dot{Q}_e - \sum \dot{Q}_{loss} \quad (11)$$

Different heat and power losses are analyzed in the following paragraphs.

### 7.2.1 Regenerator loss

According to reference [44] the pressure loss in the oscillating flow in the regenerator can be expressed as:

$$\Delta p_r(t) = \Delta p_{max} \cos(\omega t) \quad (12)$$

Where  $\Delta p_{max} = \frac{\rho}{2} f_{max} \frac{L_r}{D_r} u_{max}^2$ , and  $f_{max}$  is defined by Tanaka [45] as  $f_{max} = \frac{175}{Re_{max}} + 1.6$

Where  $\rho$  is the average density of the working gas in the engine,  $L_r$  is the length of the regenerator,  $f_{max}$  is the maximum friction factor,  $D_r$  is the hydraulic diameter in the regenerator,  $u_{max}$  is the maximum fluid velocity in the regenerator estimated as  $\frac{u_{re,max} + u_{cr,max}}{2\phi}$  where  $\phi$  is the porosity of the regenerator, and  $Re$  is the Reynolds number.

The average fluid friction dissipation in terms of power is calculated as:

$$\overline{\dot{W}_r} = \frac{1}{t_{cycle}} \int_0^{t_{cycle}} \Delta p(t) dV(t) = \frac{\rho L_r}{4D_r} u_{max}^3 A_0 \left( \frac{175\mu}{\rho D_r u_{max}} + 1.6 \right) \quad (13)$$

Where  $A_0$  is the fluid cross section area of the regenerator.

Due to the imperfection of the regenerator, the thermal efficiency of the regenerator can be calculated according to the reference [44] as:

$$\varepsilon_r = \frac{NTU}{NTU+2} \quad (14)$$

where  $NTU$  is the number of transfer units in the regenerator,  $NTU = \frac{A_{wetted} h}{\dot{m}_{ave} c_p}$ , where  $\dot{m}_{ave}$  is the gas average mass flow rate in the regenerator and  $h$  is the heat transfer coefficient which can be calculated by the follow equation proposed by Tanaka [45]:

$$h = \frac{Nu.K_g}{D_r} = \frac{K_g}{D_r} \cdot C_1 (Re_{ave} Pr)^{C_2} \quad (15)$$

Where  $K_g$  is the heat conductivity of the working gas,  $C_1$  and  $C_2$  are empirical coefficients ( $C_1 = 0.42, C_2 = 0.67$ ),  $Re_{ave} = \frac{\rho}{\mu} D_r u_{ave}$ ,  $u_{ave} = \frac{2}{\pi} D_r u_{max}$ ,  $Pr = \frac{\nu}{\alpha}$ .

$$\dot{Q}_r = \dot{m} c_p (1 - \varepsilon_r) (T_c - T_e) \quad (16)$$

### 7.2.2 Flow loss in heat exchangers and passage

In a Stirling cryocooler, especially those used in air liquefaction industry, in addition to the freezer there is usually a cooler to help discharge heat from the compression volume to the environment. The working gas flows through the tubes of cooler and freezer causing pressure loss due to the flow viscosity. In the Figure 8.1, it can be seen that there is a passage connecting the compression volume and the regenerator. The diameter of the passage is 1.2 mm, whose scale is similar with those of cooler and freezers. Therefore, the correlation of the flow loss in this passage is the same as that used in the cooler and freezer.

The pressure loss due to the working gas flowing through the tubes of cooler, freezer, and passage can be calculated as [46]:

$$\Delta p = f \frac{L \rho u^2}{2D} \quad (17)$$

where the friction factor  $f$  can be calculated as:

$$f = \frac{64}{Re}, \text{ if } Re < 2300 \quad (18\text{-a})$$

$$f = (0.79 \ln(Re) - 1.64)^{-2}, \text{ if } Re > 2300 \quad (18\text{-b})$$

The work loss in the passage during one cycle can be expressed as:

$$\delta W_{passge} = 2 \Delta p_{passge} \cdot V_{c0} \quad (19)$$

### 7.2.3 Loss due to piston finite speed

In the Stirling cryocooler, the working space is periodically compressed and expanded by the piston. On the surface of the piston there is an acting force between the working fluid and the piston which leads to an instantaneous pressure over the piston surface different from the cylinders mean pressure. This effect leads to that, during the compression process, the piston needs to provide more work to compress the gas and in the opposite, during the expansion process, a smaller pressure than that in the cylinder acts on the piston [47]. Therefore, the pressure loss due to piston finite speed can be calculated as:

$$\Delta p_{fin\ spe} = \frac{1}{2} \left( p \frac{a u_{p,c}}{c_c} + p \frac{a u_{p,e}}{c_e} \right) \quad (20)$$

The work loss due to piston finite speed in one cycle can be calculated as twice the product of pressure loss and the piston swept volume.

$$\delta W_{fin spe} = 2\Delta p_{fin spe} \cdot V_{c0} \quad (21)$$

where  $p$  represents the instantaneous pressure,  $u_p$  is the piston speed,  $c$  is the average molecular speed  $c = \sqrt{3r_g T}$  and  $a$  is a constant defined as  $a = \sqrt{3\gamma}$ , where  $\gamma$  is specific heat ratio and  $r_g$  is the gas constant.

#### 7.2.4 Hysteresis loss

As the working space is a closed space which is compressed or expanded by the piston periodically, the working gas acts actually as a gas spring which stores energy when it's compressed and releases energy when it's expanded. Dissipation due to the non-ideal character of the working gas, usually called hysteresis loss can be calculated according to studies of Kornhauser [48] and Bailey [25] as:

$$W_{hys} = \frac{\pi}{2} p_0 V_0 \left(\frac{p_a}{p_0}\right)^2 \frac{\gamma-1}{\gamma} \frac{1}{y} \frac{\cosh(y)\sinh(y) - \sin(y)\cos(y)}{\cosh^2(y) - \sin^2(y)} \quad (22)$$

$$y = 0.49 Pe_\omega^{0.43} \quad (23)$$

where  $p_0$  and  $V_0$  are respectively the average pressure and volume of the working space,  $p_a$  is the amplitude of the pressure wave,  $\gamma$  is the heat capacity ratio,  $Pe_\omega$  is the Peclet number based on the angular frequency and a conventional hydraulic diameter  $Pe_\omega = \frac{\omega D_p^2}{4\alpha}$ , and  $\alpha$  is the thermal diffusivity of the working gas.

#### 7.2.5 Mechanical friction loss

There are mechanical frictions in the joints of the studied Stirling cryocooler, because of the relative motion between two parts connected by the joints as between the displacer and the crank, between the piston and the crank, and between the crank and the axle of the electric motor. In addition, during the cycle, the direction of the force acted on the piston and on the displacer is not perfect concentric with their corresponding axial direction. As a result, the piston and displacer don't move in their axial direction perfectly. However, in order to seal the working gas to avoid leakage between working space and buffer space, the clearance between the piston/displacer and cylinder wall is reduced. Consequently, there is mechanical friction between the piston/displacer and the cylinder wall too.

In the studied cryocooler, the motor power loss due to mechanical friction is equivalent to a  $pV$  power loss in an engine where the mean pressure loss due to mechanical friction can be calculated according to Hosseinzade and Sayyaadi [49] as:

$$\Delta p_{mec fri} = \frac{(0.4+0.0045Z_p n) \times 10^5}{3\left(1-\frac{1}{3\tau}\right)} \left(1 - \frac{1}{\tau}\right) \quad (24)$$

And then, in the studied cryocooler, the work loss due to mechanical friction in one cycle can be calculated as:

$$W_{mec fri} = 2\Delta p_{mec fri} V_{c0} \quad (25)$$

### 7.2.6 Heat loss by displacer shuttle

The main displacer function is to move the working gas between the compression and expansion volumes but it acts also as an isolator to help maintain a big temperature difference between them. During its reciprocating movement, the displacer is in contact with different temperature layers of the gas which implies a shuttle heat loss. Sauer and Kuehl have used 1-dimensional differential model and divided the clearance gap between displacer and cylinder wall into several volume to calculate the clearance loss including shuttle loss and enthalpy loss [50]. Pfeiffer and Kuehl have used an one-dimensional differential model which consider the nonlinear temperature distribution along the axial direction, the conical design of the clearance, and the bottom gap width ratio, to optimize the clearance gap [51]. Considering the complexity in their one-dimensional differential model, method in reference [52] is used to calculate the shuttle loss for its concision and obviousness to observe parameter's effect on it:

$$\dot{Q}_{shuttle} = 0.4 \frac{Z_d^2 K_g D_d}{g_d L_d} (T_c - T_e) \quad (26)$$

where  $Z_d$  is the displacer stroke,  $K_g$  is the working gas thermal conductivity,  $D_d$  is the displacer diameter,  $g_d$  is the width of the gap between the displacer and the cylinder, and  $L_d$  is the length of the displacer.

### 7.2.7 Heat pump in the clearance

During the periodic variation of the pressure in the working space, the clearance between the displacer and the cylinder wall can absorb and discharge gas from or to the expansion volume. This effect can bring a cooling loss, named as pump loss, which can be calculated as [23, 53]:

$$\dot{Q}_{pump} = (1 - \eta) \dot{m} c_p (T_c - T_e) \quad (27)$$

Where  $\eta$  and  $\dot{m}$  are the efficiency of the clearance, and the mass flow rate through the clearance, respectively, which can be calculated as:  $\dot{m} = \frac{2\pi n D_d L_d g_d}{r_g (T_c + T_e)} p_a$ , and  $\eta = 1 -$

$$\frac{4}{3\pi} \frac{\dot{m}^{0.6} c_p^{0.6} g_d}{k_g^{0.6} L_d^{0.6} D_d}$$

where  $n$  is the frequency, and  $p_a$  is the pressure wave amplitude.

### 7.2.8 Heat conduction loss

Due to the big temperature gap between the compression and expansion volumes, which are separated by the displacer, heat conduction through the displacer and the cylinder wall can't be avoided. According to Fourier conduction law, the heat loss by conduction is written as:

$$\dot{Q}_{cond} = K \frac{A}{L} \Delta T \quad (28)$$

where  $K$  is the heat conductivity of the displacer or the cylinder wall,  $A$  is the corresponding

cross section area,  $L$  is the length of the displacer piston or the cylinder wall,  $\Delta T$  is the temperature difference between the hot volume and the cold volume.

### 7.3 Case study

Using the 0-D model presented above, which is a second order analysis, as parameters are calculated at each time step and all losses are estimated linked to each other, some interesting results are obtained and presented in this section. Dimension and physical parameters of the studied cryocooler are presented in Table 7.1. Results are presented on Figure 7.7 and Figure 7.8. The exergy of the heat at cold temperature bellowing the environmental temperature ( $T_0 = 290\text{ K}$ ) can be calculated as:

$$\dot{E}x_Q = \left(1 - \frac{T_0}{T_L}\right)\dot{Q} \quad (29)$$

From Figure 7.7, it can be seen that mechanical friction loss is the biggest mechanical power loss, but the gas spring hysteresis loss is also considerable. From equation (24) and (25) it can be seen that the mechanical friction loss increases linearly with rotation speed increasing. In the studied case, the rotation speed is up to 1800 RPM which leads the mechanical friction loss to be the biggest power loss. The pressure loss in the passage between compression volume and expansion volume,  $W_{\text{passage}}$ , is the smallest mechanical power loss. Heat conduction loss is the biggest heat loss, followed by the displacer shuttle heat loss.

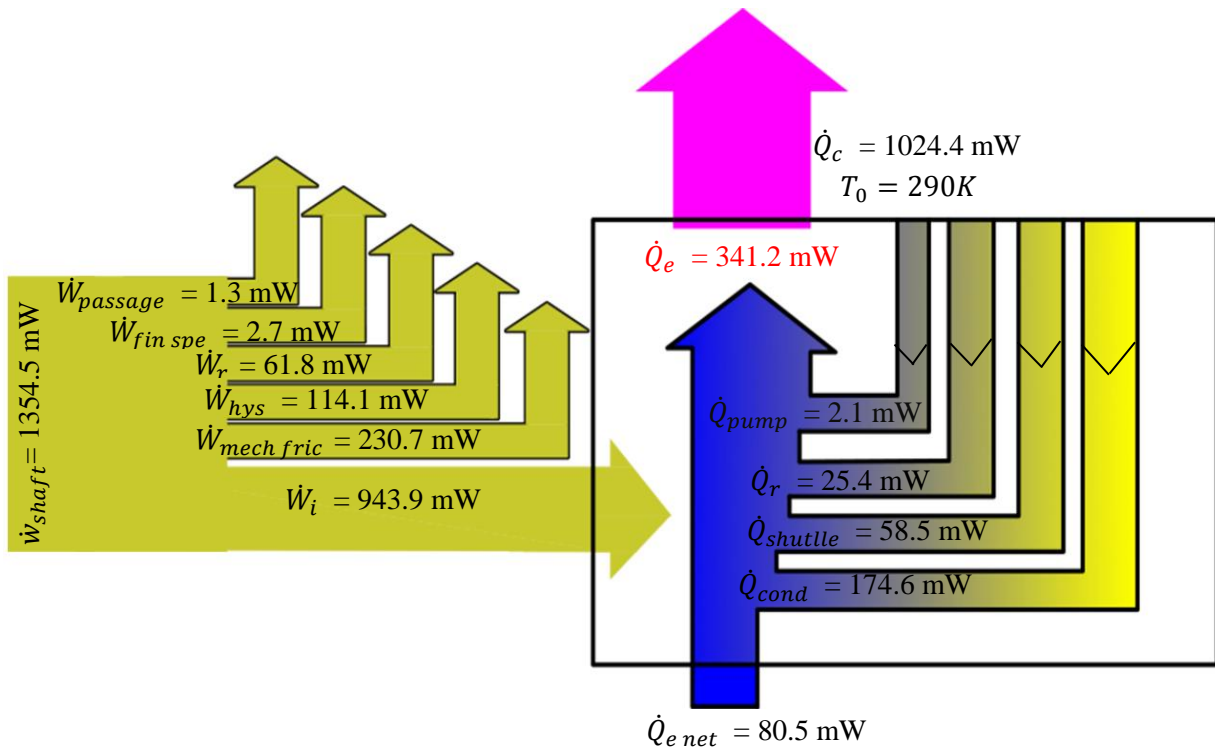


Figure 7.7 Energy balance of the cryocooler

Considering different temperature levels, exergy flows can be determined, associated on each energy flow. Therefore, in terms of exergy, the aim of the cryocooler is to supply an exergy flow to the cold end of the system. The mechanical energy (input exergy) consumed by the engine is

used to provide this exergy flow but also to balance different irreversibilities (exergy losses). From Figure 7.8, it can be seen that the exergy loss due to heat conduction accounts for 35.7% of the total input exergy, which make it the biggest exergy loss; the exergy loss due to mechanical friction accounts for 17.0% and is the second biggest exergy loss. Other exergy losses including shuttle heat loss, regenerator imperfection loss, heat pump loss, gas spring hysteresis loss, regenerator flow viscosity loss, piston finite speed loss, and passage flow viscosity loss, account a sum of 30.8% of the total input exergy.

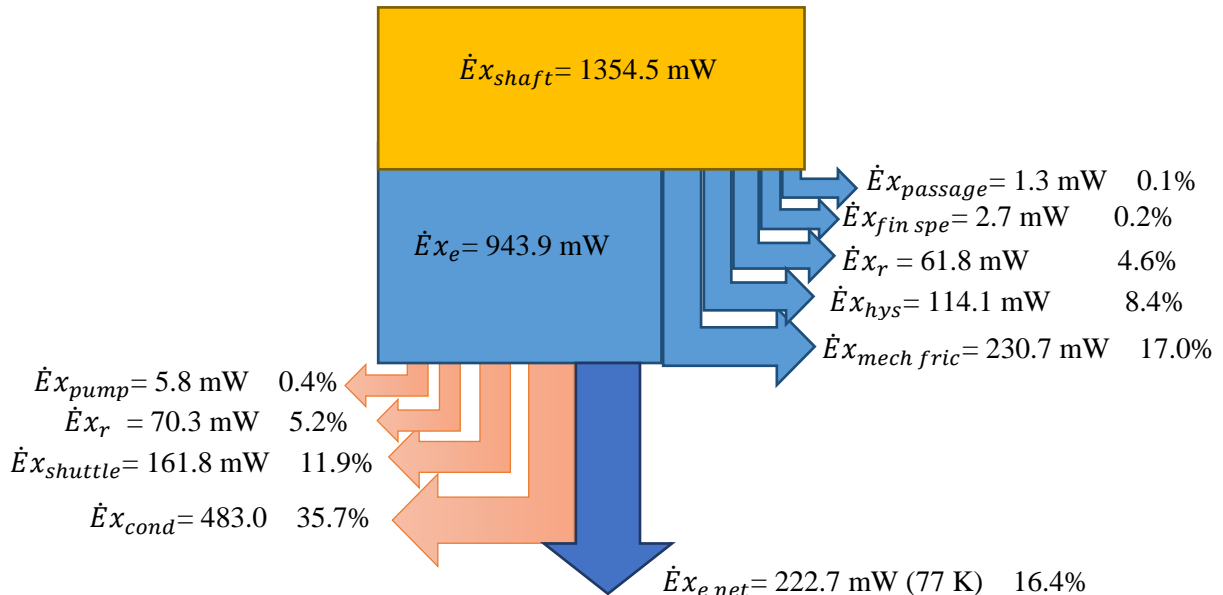


Figure 7.8 Exergy distribution of the input power

Figure 7.9 and Figure 7.10 show the input power and cooling power variation with the cold and hot end temperatures, respectively while other parameters are the same as those in Table 7.1. It can be seen that with a cold end temperature increasing the input power decreases nearly linearly, while the cooling power increases nearly linearly. When the hot end temperature increases, the input power increases nearly linearly and the cooling power decrease nearly linearly.

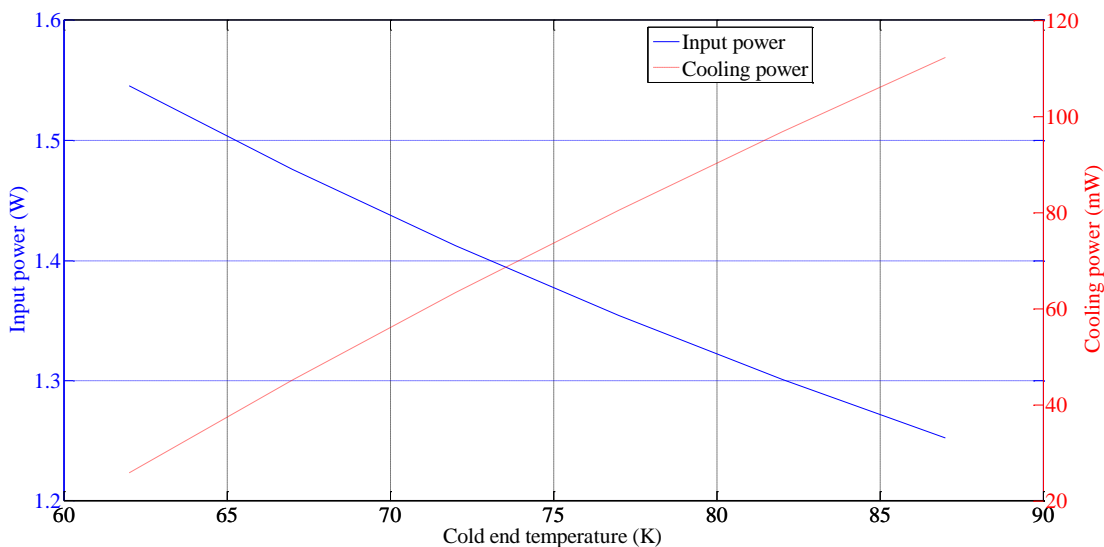


Figure 7.9 Input power and cooling power variation with cold end temperature

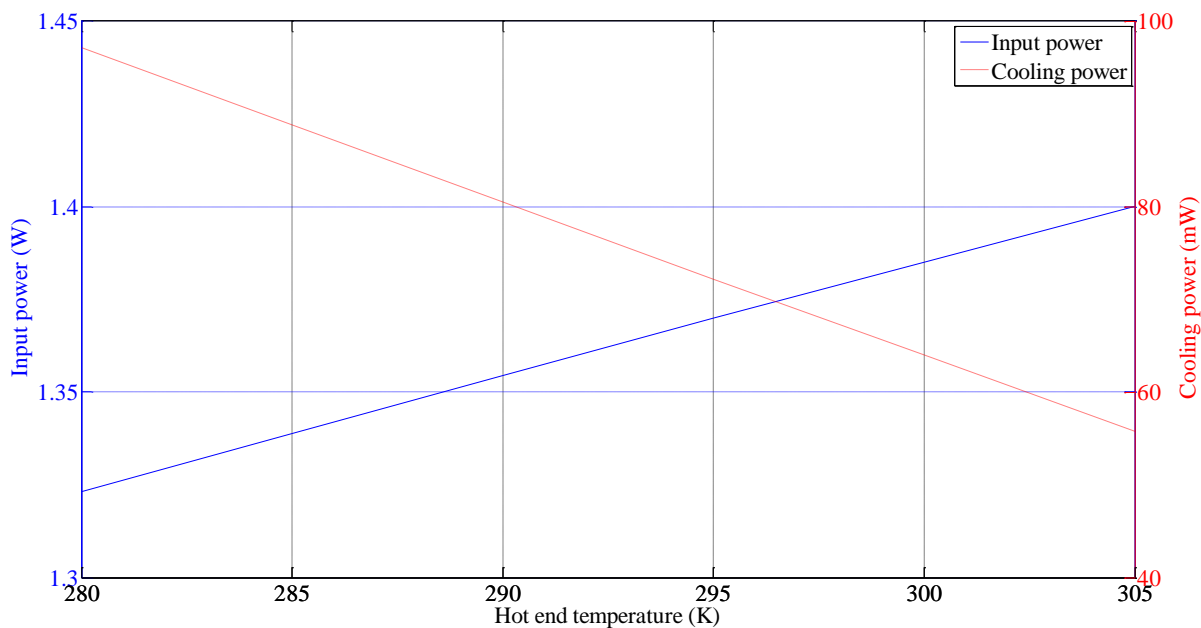


Figure 7.10 Input power and cooling power variation with hot end temperature

Figure 7.11 shows the input power and cooling capacity with the average pressure while other parameters are the same as those in Table 8.1. It can be seen that when the average pressure increases both input power and cooling capacity increase. The cooling capacity could be negative in the low average pressure condition, which implies the indicated cooling power cannot offset the heat losses, and, therefore, the cold end temperature cannot be achieved in this operating condition. And when the average pressure increases, the  $COP$  increases also, which offers a method to increase the  $COP$ .

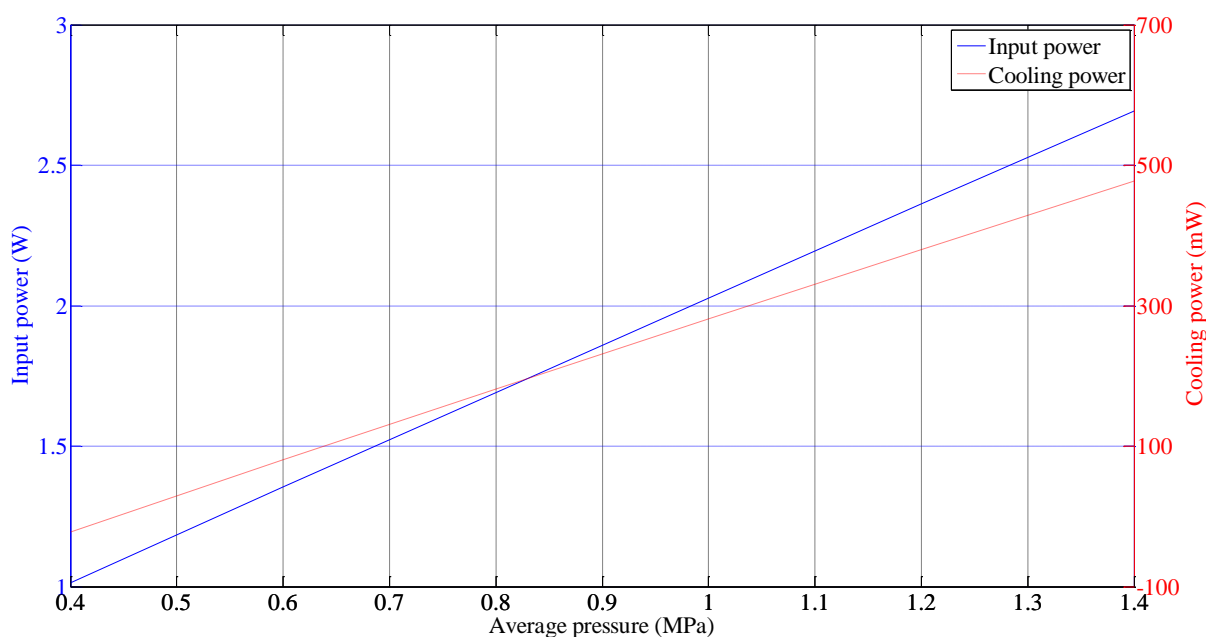


Figure 7.11 Input power and cooling power variation with average pressure

Figure 8.12 shows the input power and cooling power variation versus rotation speed corresponding to the same parameters in Table 8.1. The cooling power increases nearly linearly. The input power increases nearly linearly only from 500 to 2500 rpm, but the gradient increases slowly after 2500 rpm which indicates that the power losses increases quickly at high rotation speed.

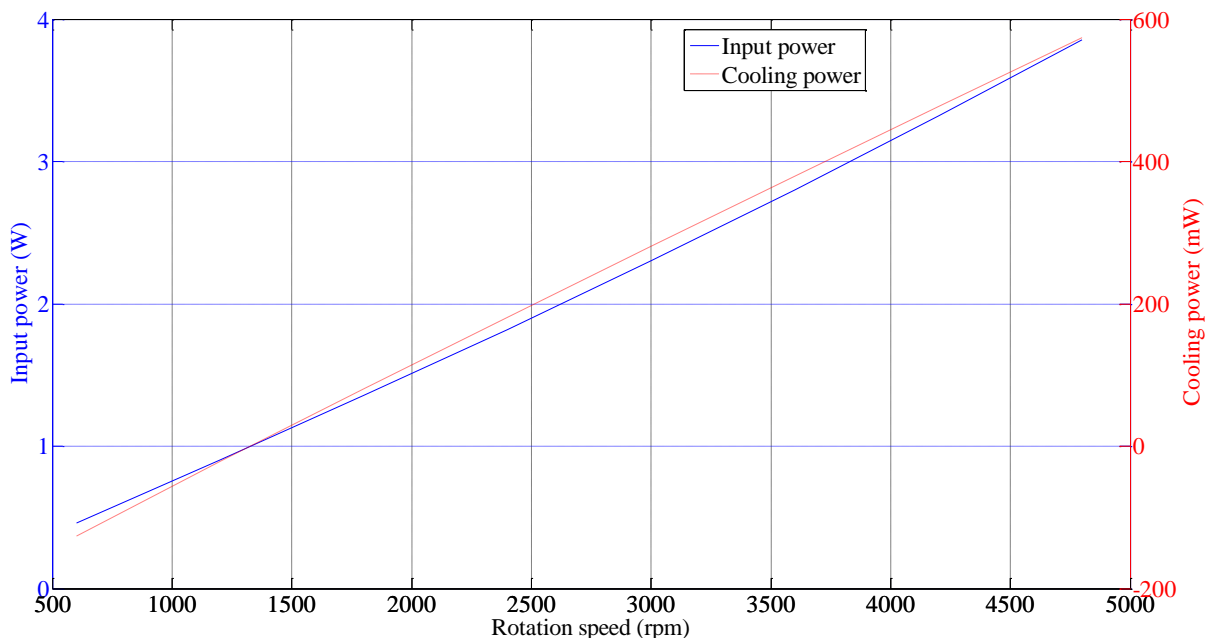


Figure 7.12 Input power and cooling power variation versus rotation speed

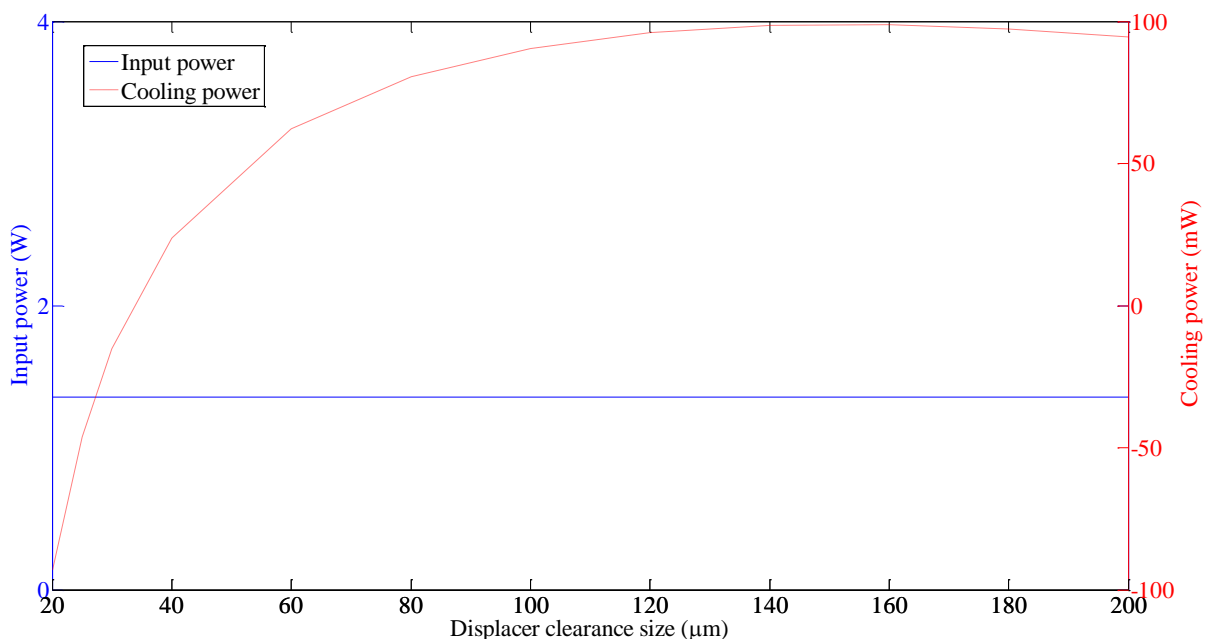


Figure 7.13 Input power and cooling power variation versus clearance size between displacer and cylinder

Figure 7.13 shows the input power and cooling power variation versus clearance size between

the displacer and the cylinder within the conditions of Table 7.1. It can be seen that the input power is fixed, while the cooling power attains a maximum value when the clearance size is about  $160\mu\text{m}$ . This phenomenon is due to the displacer's shuttle heat loss and pump heat loss which can be seen in Figure 7.14. It can be seen that the shuttle heat loss decreases quickly for clearance size increasing from  $0\mu\text{m}$  to  $160\mu\text{m}$ ; and then it decreases slowly when the clearance size exceeds  $160\mu\text{m}$ . For the pump heat loss, the phenomenon is opposite; it increases slowly for clearance size increasing from  $0\mu\text{m}$  to  $160\mu\text{m}$  and then increases quickly after that value. Consequently, the sum of the two heat losses attains a minimum value when the clearance size is about  $160\mu\text{m}$ .

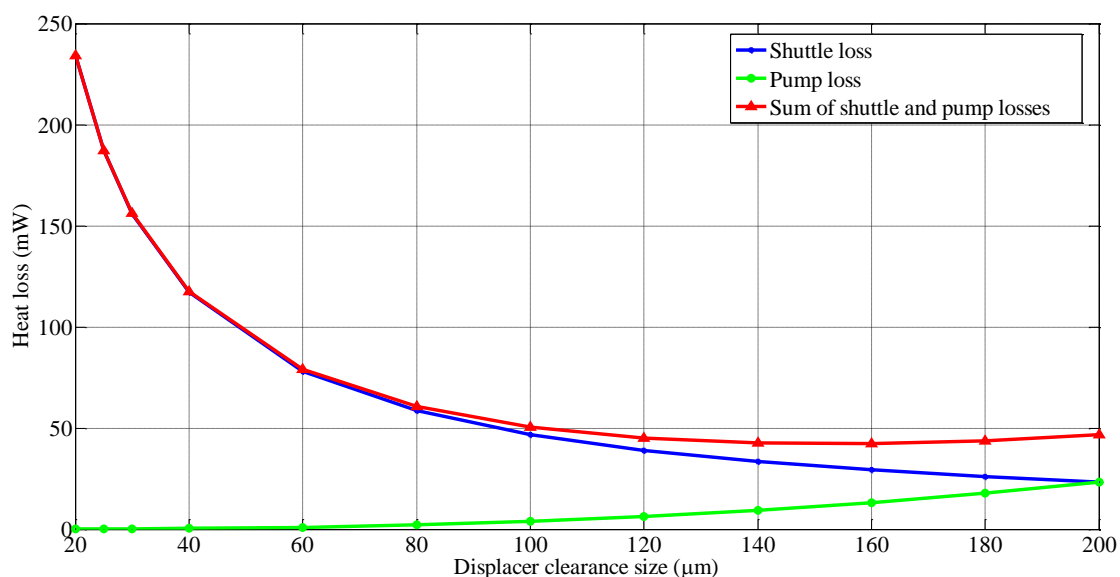


Figure 7.14 Displacer's shuttle heat loss and pump heat loss variation versus displacer clearance size

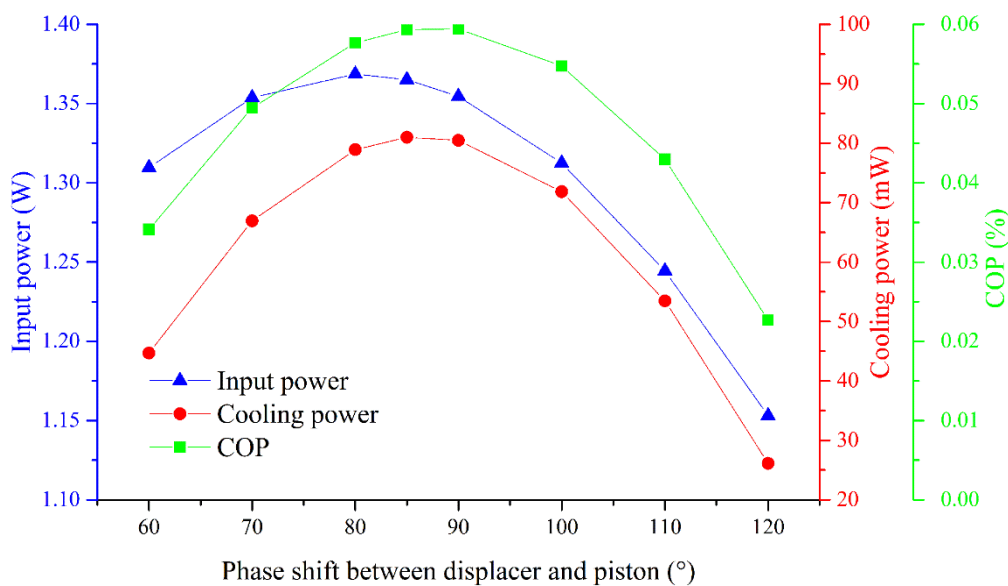


Figure 7.15 Input power, cooling power, and  $COP$  variation vs phase shift between displacer and piston

Figure 7.15 shows the input power, cooling power, and  $COP$  variation versus the phase shift between displacer and piston within the same conditions of Table 7.1. It can be seen that the input power and cooling power attain the highest value when the phase shift is about  $80^\circ$  and  $85^\circ$  respectively. The cooling power decreases slightly from  $85^\circ$  to  $90^\circ$ , and then decreases quickly when exceeding  $90^\circ$ . The input power decreases strongly after exceeding  $80^\circ$ . The  $COP$  attains its highest value at  $85^\circ$  and  $90^\circ$ , which implies that the optimum phase shift could be between  $85^\circ$  and  $90^\circ$ .

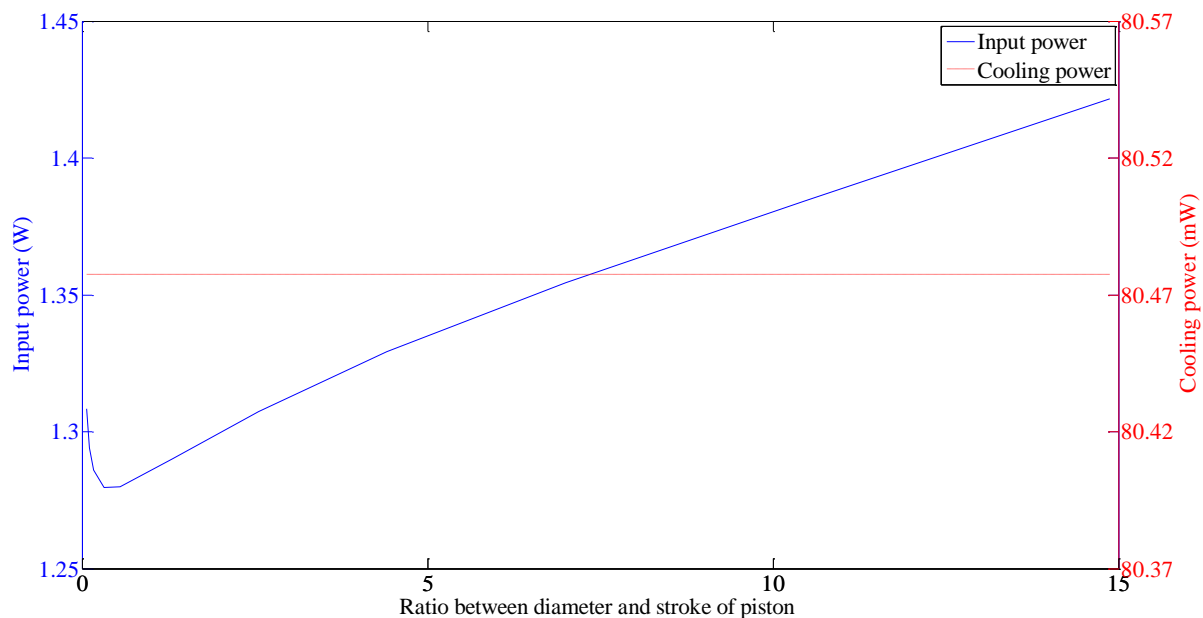


Figure 7.16 Input power and cooling power variation with ratio between diameter and stroke of piston

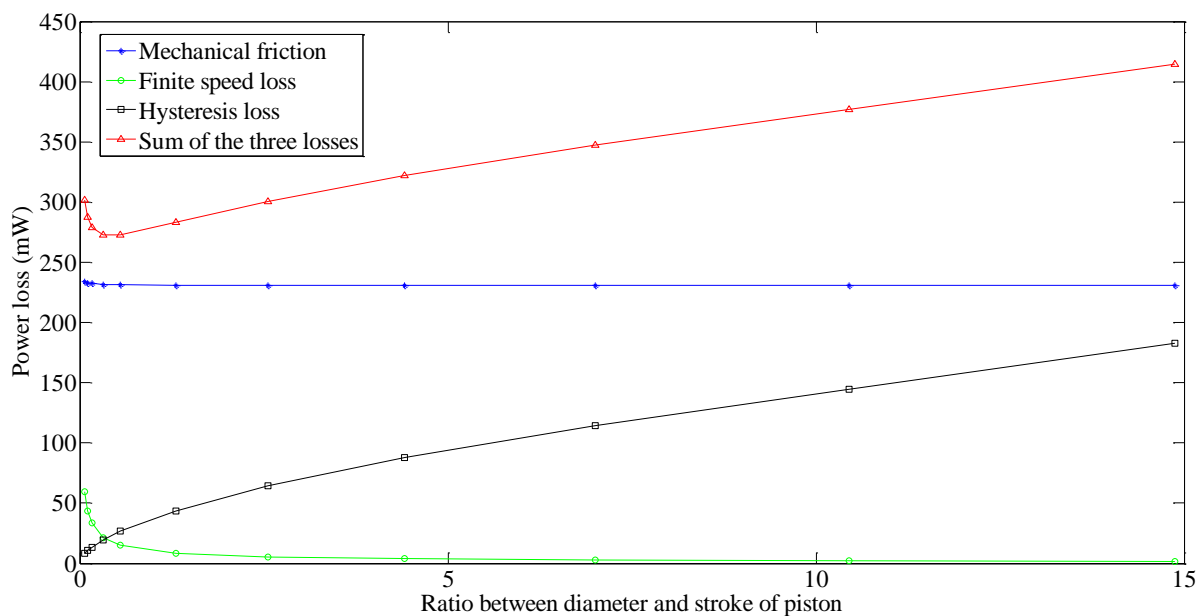


Figure 7.17 Power losses variation with the ratio between diameter and stroke of piston

Figure 7.16 shows the input power and cooling power variation versus the ratio between diameter and stroke of the piston keeping the piston swept volume constant (Table 7.1). It can be seen that the cooling power is constant while the input power decreases firstly, and then increases, which implies an optimum value of the ratio between diameter and stroke of piston about 1 (square engine). This phenomenon is due to the power losses variations with the ratio which can be seen in Figure 7.17. It can be seen that the mechanical friction loss is nearly constant while the piston finite speed loss decreases quickly with the ratio between diameter and stroke of piston increases from 0.07 to 1.5 and then keeps nearly constant after 1.5. On the contrary, the hysteresis loss increases with the ratio increasing, but the gradient becomes smaller and smaller. The sum effect of the three power losses is that there exists an optimum ratio between the diameter and stroke of piston for a minimum corresponding loss.

#### 7.4 Model validation

The model presented above has been applied to the PPG-102 Stirling cryocooler in reference [19], as both the studied cryocooler and PPG-2 cryocooler are single-acting integral Stirling cryocooler with similar mechanism of mechanical friction; therefore, the empiric coefficients for mechanical friction loss used in the two cases can be the same. The main parameters of the PPG-102 Stirling cryocooler are shown in the Table 7.2.

The simulation results of PPG-102 Stirling cryocooler were compared with the simulation results from Walker et al. [19], Atrey et al. [20], and with the experimental results (Table 7.3). It can be seen that the indicated power of current simulation is smaller than that of Walker and Atrey et al. while the freezer flow loss and cooler flow loss are similar with that of the two authors. The regenerator flow loss and mechanical friction loss of current simulation is higher than that of the two authors which causes our simulated total mechanical power is the biggest. The reason that our simulation value of regenerator flow loss is much bigger than those of Walker et al. and Atrey et al., is that we used oscillatory flow empirical correlation for regenerator flow loss according Tanaka's research [45], while Walker et al. and Atrey et al. used empirical correlation according Martini's study [54] who used unidirectional flow empirical correlation according to Kays and London's study [55]. In practice, due to the oscillating movement of the displacer, the flow in the regenerator is an oscillating flow, therefore, oscillating flow empirical correlation was used in our study. The indicated cooling power of current simulation is between that of Walker and Atrey, and the regenerator loss is bigger than that of the two authors. Both shuttle heat loss and pumping loss of current simulation are smaller than that of the two authors. Eventually, current simulated net cooling power is the closest to the experimental net cooling power. The relative error between simulated input power and cooling power and experimental results are 9.58% and 1.69%, respectively. Therefore, the model above can be used to accurately predict the input power and cooling power of the Stirling cryocoolers.

Table 7.2 Main parameters of the PPG-102 Stirling cryocooler [19]

Cylinder diameter, cm	7	Regenerator	
Displacer rod diameter, cm	0.5	Screen wire diameter, cm	0.008
Piston end clearance, cm	0.05	Porosity ratio of regenerator, -	60%
Displacer end clearance, cm	0.05	Surface area·Volume <sup>-1</sup> , cm <sup>2</sup> ·cm <sup>-3</sup>	179
Expansion gap, cm	0.04	Inner diameter of freezer tubes, cm	0.1
Expansion length, cm	10	Length of freezer tubes, cm	7.6
Expansion cylinder clearance volume, cc	1.924	Number of freezer tubes, -	180
Compression cylinder clearance volume, cc	1.924	Phase shift, °	72
Mechanical efficiency, -	70%	Expansion temperature, K	77.125
Number of cylinder, -	1	Compression temperature, K	293
Average pressure, MPa	2.5	Connecting rod length, cm	15
Engine speed, rpm	1450	Crank length, cm	2.65
Expansion cylinder wall thickness, cm	0.25	Stroke of piston, cm	5.3
Expansion cap wall thickness, cm	0.25	Stroke of displacer, cm	5.3
Regenerator housing wall thickness, cm	0.25	Swept volume, expansion cylinder, cc	203.968
Inner diameter of cooler tubes, cm	0.16	Swept volume, compression cylinder, cc	202.804
Length of cooler tubes, cm	10	Cooler dead volume, cc	42.127
Number of cooler tubes, -	200	Regenerator dead volume, cc	379.463
External diameter of regenerator, cm	12.7	Freezer dead volume, cc	12.668
Internal diameter of regenerator, cm			

Table 7.3 Comparison of simulation result of PPG-102 Stirling cryocooler with other authors and experimental results

	Results of Walker et al. (W) [19]	Results of Atrey et al. (W) [20]	Current simulation results (W)	Experimental results (W) [20]
Indicated power	4920.52	5541.04	4071.32	-
Freezer flow loss	371.02	287.73	394.66	-
Cooler flow loss	117.31	81.04	88.07	-
Regenerator flow loss	312.88	434.03	2212.82	-
Mechanical friction	2456.49	2718.78	2958.69	-
Finite speed loss	-	-	127.48	
Hysteresis loss	-	-	9.25	
<b>Total mechanical power</b>	<b>8188.29</b>	<b>9062.63</b>	<b>9862.29</b>	<b>9000</b>
Indicated cooling power	1379.23	1567.67	1450.90	-
Regenerator imperfection loss	282.38	277.2	380.68	-
Shuttle heat loss	57.07	66.44	18.38	-
Pumping loss	103.03	113.29	31.70	-
Conduction	3.20	3.20	3.2	-
<i>P-V</i> loss due to pressure drop	-	89.94	-	-
<b>Net cooling power</b>	<b>933.51</b>	<b>1017.74</b>	<b>1016.94</b>	<b>1000</b>

## 7.5 Summary

In this chapter, an isothermal model considering various losses was developed. The compression and expansion volumes are supposed to be isothermal, the variation of the regenerator temperature is supposed to be linear. The losses including regenerator imperfection thermal loss, piston finite speed loss, gas spring hysteresis loss, displacer shuttle heat loss, clearance heat pump loss, heat conduction loss, and flow viscosity loss are calculated at the same time step as they have interaction with each other. Energy and exergy balances of the cryocooler were developed. They show that the mechanical friction loss is the biggest mechanical loss, hysteresis loss of the gas spring being also considerable; the conduction loss

is the biggest heat loss, followed by the displacer shuttle heat loss. The exergy analysis highlights that the exergy loss of heat conduction accounts for 35.7% of the total input exergy, which makes it the biggest exergy loss; the exergy loss of mechanical friction accounts for 17.0% and is the second biggest exergy loss. Other exergy losses including shuttle heat loss, regenerator imperfection loss, heat pump loss, gas spring hysteresis loss, regenerator flow viscosity loss, piston finite speed loss, and passage flow viscosity loss, account for a sum of 30.8% of the total input exergy.

The effect of various parameters on the cryocooler performance (cooling power and input power) are investigated. The parametric study includes cold end temperature, hot end temperature, average pressure, rotation speed, displacer clearance size, phase shift between the piston and the displacer, and ratio between diameter and stroke of piston. It shows that a cold end temperature increasing implies an input power decreasing nearly linearly while the cooling power increases nearly linearly. With the hot end temperature increasing, the input power increases nearly linearly while the cooling power decreases nearly linearly. With the average pressure or rotation speed increasing, both the input power and the cooling power increases nearly linearly. With the displacer clearance size increasing, the input power is constant while the cooling power increases to an optimum value of  $160\mu m$  and then decreases, which is determined by two loss mechanisms (displacer shuttle loss and clearance pump loss). With the phase shift between piston and displacer increasing, both the input power and the cooling power increase firstly and then decrease. The optimum phase shift for cooling power is about  $85^\circ$ , while the input power is maximum at about  $80^\circ$ . The *COP* attains its highest value at  $85^\circ$  and  $90^\circ$ , which implies that the optimum phase shift could be between  $85^\circ$  and  $90^\circ$ . An increase of the ratio between the diameter and stroke of the piston keeps a cooling power constant but implies a decrease of the input power to an optimum (minimum) value corresponding to a square geometry (ratio equal to 1). This phenomenon is due to the increase of hysteresis loss and to the decrease of the piston finite speed loss, while the mechanical friction stands nearly constant, which results in a minimum sum of all these losses when the ratio is about 1. The simulation results for PPG-102 Stirling cryocooler were compared with two other simulation results of the literature and with experimental results which indicated that this model is convincing to predict the performance of the Stirling cryocooler.

## References:

- [1] Yumoto K., Nakano K., and Hiratsuka Y., Development of High Capacity Split Stirling Cryocooler for HTS. *Physics Procedia*, 2015. **67**: p. 462-467.
- [2] Breniere X., et al. Reliability optimization for IR detectors with compact cryo-coolers. in *Defense and Security*. 2005. International Society for Optics and Photonics.
- [3] Sugita H., et al., Development of mechanical cryocoolers for the Japanese IR space telescope SPICA. *Cryogenics*, 2008. **48**(5–6): p. 258-266.
- [4] Duband L., Space Cryocooler Developments. *Physics Procedia*, 2015. **67**: p. 1-10.
- [5] Radebaugh R., Cryocoolers: the state of the art and recent developments Contribution of NIST; not subject to copyright in the US. *Journal of Physics: Condensed Matter*, 2009. **21**(16): p. 164219.
- [6] Hirai H., et al., Development of a turbine cryocooler for high temperature

- superconductor applications. *Physica C: Superconductivity*, 2009. **469**(15–20): p. 1857-1861.
- [7] Ross R.G. and Boyle R., An overview of NASA space cryocooler programs—2006. 2006: Pasadena, CA: Jet Propulsion Laboratory, National Aeronautics and Space Administration.
- [8] Narasaki K., et al. Development of Two - Stage Stirling Cooler for ASTRO - F. in *Advances In Cryogenic Engineering: Transactions of the Cryogenic Engineering Conference-CEC*. 2004. AIP Publishing.
- [9] Ross Jr R.G., et al. NASA advanced cryocooler technology development program. in *Proceedings of SPIE*. 2003.
- [10] Yu G., et al., Initial Test of a Stirling Cryocooler with a High Cooling Capacity. *International Cryocooler Conference*, 2014. **18**: p. 169-175.
- [11] Penswick L., et al., High-Capacity and Efficiency Stirling Cycle Cryocooler. *International Cryocooler Conference*, 2014. **18**: p. 155-162.
- [12] Park S.J., et al., The effect of operating parameters in the Stirling cryocooler. *Cryogenics*, 2002. **42**(6–7): p. 419-425.
- [13] Wang X., et al., Study on a high capacity two-stage free piston Stirling cryocooler working around 30 K. *Cryogenics*, 2016.
- [14] Prast G., A Philips gas refrigerating machine for 20° K. *Cryogenics*, 1963. **3**(3): p. 156-160.
- [15] Horn S., et al., Miniature cryogenic coolers. *Advances in Cryogenic Engineering*, 1976. **21**: p. 428.
- [16] Horn.S.B., Lumpkin.M.E., and B.T. W., Pneumatically driven split-cycle cryogenic refrigerator. *Adv Cryog Eng*. Vol. 19. 1974. 216-233.
- [17] Zhang C.-q. and Zhong C., Theoretical modeling of a gas clearance phase regulation mechanism for a pneumatically-driven split-Stirling-cycle cryocooler. *Cryogenics*, 2015. **66**: p. 13-23.
- [18] Davey G., Review of the Oxford cryocooler, in *Advances in cryogenic engineering*. 1990, Springer. p. 1423-1430.
- [19] Walker G., et al., Microcomputer simulation of Stirling cryocoolers. *Cryogenics*, 1989. **29**(8): p. 846-849.
- [20] Atrey M.D., Bapat S.L., and Narayankhedkar K.G., Cyclic simulation of Stirling cryocoolers. *Cryogenics*, 1990. **30**(4): p. 341-347.
- [21] Bauwens L., Adiabatic losses in Stirling cryocoolers: a stratified flow model. *Cryogenics*, 1994. **34**(8): p. 627-633.
- [22] Rijpma A.P., et al., Construction and tests of a heart scanner based on superconducting sensors cooled by small stirling cryocoolers. *Cryogenics*, 2000. **40**(12): p. 821-828.
- [23] Zhang C.Q., et al., Dynamic simulation of one-stage Oxford split-Stirling cryocooler and comparison with experiment. *Cryogenics*, 2002. **42**(9): p. 577-585.
- [24] Zhang C.Q., et al., Connecting hose's operating characteristics and its effect on the cooling performance of an 80 K Oxford split-Stirling-cycle cryocooler. *Cryogenics*, 2003. **43**(6): p. 335-344.
- [25] Bailey P.B., et al. Gas spring losses in linear clearance seal compressors. in *International Cryocooler Conference*. 2007.

- [26] Clearman W.M., et al., Anisotropic steady-flow hydrodynamic parameters of microporous media applied to pulse tube and Stirling cryocooler regenerators. *Cryogenics*, 2008. **48**(3-4): p. 112-121.
- [27] Ahmadi M.H., et al., Multi-objective optimization of an irreversible Stirling cryogenic refrigerator cycle. *Energy Conversion and Management*, 2014. **82**: p. 351-360.
- [28] Ahmadi M.H., et al., Thermodynamic optimization of Stirling heat pump based on multiple criteria. *Energy Conversion and Management*, 2014. **80**: p. 319-328.
- [29] Park S.J., et al., An experimental study on the phase shift between piston and displacer in the Stirling cryocooler. *Current Applied Physics*, 2003. **3**(5): p. 449-455.
- [30] Dubrovsky V., Adaptive control of linear Stirling cryogenic coolers. 2003, Loughborough University.
- [31] Veprik A.M., et al., Ultra-low vibration split Stirling linear cryogenic cooler with a dynamically counterbalanced pneumatically driven expander. *Cryogenics*, 2005. **45**(2): p. 117-122.
- [32] Yang X. and Chung J.N., Size effects on miniature Stirling cycle cryocoolers. *Cryogenics*, 2005. **45**(8): p. 537-545.
- [33] Cha J.S., Ghiaasiaan S.M., and Kirkconnell C.S., Oscillatory flow in microporous media applied in pulse – tube and Stirling – cycle cryocooler regenerators. *Experimental Thermal and Fluid Science*, 2008. **32**(6): p. 1264-1278.
- [34] Chen X., et al., Study on the phase shift characteristic of the pneumatic Stirling cryocooler. *Cryogenics*, 2009. **49**(3–4): p. 120-132.
- [35] Riabzev S.V., et al., Vibration-free stirling cryocooler for high definition microscopy. *Cryogenics*, 2009. **49**(12): p. 707-713.
- [36] Razani A., Dodson C., and Roberts T., A model for exergy analysis and thermodynamic bounds of Stirling refrigerators. *Cryogenics*, 2010. **50**(4): p. 231-238.
- [37] Xia M. and Chen X., Analysis of resonant frequency of moving magnet linear compressor of stirling cryocooler. *International Journal of Refrigeration*, 2010. **33**(4): p. 739-744.
- [38] Dai W., et al., Impedance match for Stirling type cryocoolers. *Cryogenics*, 2011. **51**(4): p. 168-172.
- [39] He Y.-L., et al., Numerical analysis on performance and contaminated failures of the miniature split Stirling cryocooler. *Cryogenics*, 2014. **59**: p. 12-22.
- [40] Wang X., et al., Design of a Two-stage High-capacity Stirling Cryocooler Operating below 30K. *Physics Procedia*, 2015. **67**: p. 518-523.
- [41] Caughley A., et al., CFD analysis of a diaphragm free-piston Stirling cryocooler. *Cryogenics*, 2016. **79**: p. 7-16.
- [42] Caughley A., et al., A Free-piston Stirling cryocooler using metal diaphragms. *Cryogenics*, 2016.
- [43] Li R., Grosu L., and Queiros-Condé D., Losses effect on the performance of a Gamma type Stirling engine. *Energy Conversion and Management*, 2016. **114**: p. 28-37.
- [44] Minassians A.D., Stirling Engines for Low-Temperature Solar-Thermal-Electric Power Generation, in U Berkeley. 2007, UC Berkeley.
- [45] Tanaka M., Yamashita I., and Chisaka F., Flow and heat transfer characteristics of the Stirling engine regenerator in an oscillating flow. *JSME international journal. Ser. 2*,

- Fluids engineering, heat transfer, power, combustion, thermophysical properties, 1990. **33**(2): p. 283-289.
- [46] Rohsenow W.M., Hartnett J., and Ganic E., Handbook of heat transfer fundamentals. 1985.
- [47] Costea M., Petrescu S., and Harman C., The effect of irreversibilities on solar Stirling engine cycle performance. Energy conversion and management, 1999. **40**(15): p. 1723-1731.
- [48] Kornhauser A. and Smith J., The effects of heat transfer on gas spring performance. Journal of energy resources technology, 1993. **115**(1): p. 70-75.
- [49] Hosseinzade H. and Sayyaadi H., CAFS: The Combined Adiabatic–Finite Speed thermal model for simulation and optimization of Stirling engines. Energy Conversion and Management, 2015. **91**: p. 32-53.
- [50] Sauer J. and Kuehl H.-D., Numerical model for Stirling cycle machines including a differential simulation of the appendix gap. Applied Thermal Engineering, 2017. **111**: p. 819-833.
- [51] Pfeiffer J. and Kuehl H.-D., Optimization of the Appendix Gap Design in Stirling Engines. Journal of Thermophysics and Heat Transfer, 2016. **30**(4): p. 831-842.
- [52] Li R., Grosu L., and Queiros-Conde D., Multi-objective optimization of Stirling engine using Finite Physical Dimensions Thermodynamics (FPDT) method. Energy Conversion and Management, 2016. **124**: p. 517-527.
- [53] Bian S.X., Miniature Cryocoolers [in Chinese]. 1983: Chinese Mechanical Industry Press.
- [54] Martini W.R., Stirling engine design manual, Second edition. 1983: US Department of Energy, Office of Conservation and Solar Applications, Division of Transportation Energy Conservation.
- [55] Kays W.M. and London A.L., Compact heat exchangers. 1964.

## Chapter 8 Summary of thesis work and future research

### 8.1 Summary of thesis work

In this work three type of SE were studied using new thermodynamic models, developed in order to take into account several losses at each engine: a Gamma type solar powered low temperature difference Stirling engine tested in our laboratory, a Beta type single-cylinder rhombic-drive Stirling engine using geometrical dimensions published in the literature, and an Alpha type integral Stirling cryocooler whose geometry was studied in our laboratory.

- (1) In the solar powered gamma type Stirling engine part, isothermal model and finite speed method are coupled, including mass and energy balances through different spaces of the engine, to simulate the behavior of the Gamma type low temperature difference Stirling engine tested in our laboratory. Different kind of thermal and mechanical losses have been considered in the model, in order to analyze thermodynamic process and losses in the Stirling Engine. The considered losses are the effects of viscous friction, regenerator imperfection, hysteresis, clearance seal leakage, displacer shuttle, finite speed piston and heat conduction.

Results show that heat loss in the regenerator is the most important loss, and work dissipation due to the leakage through clearance between piston and cylinder wall is very important too. The total working gas mass in the engine is fluctuant considering leakage and the amplitude of the pressure wave is smaller than that without leakage.

The comparison between the experimental results and the simulation results at different phase shift between displacer and piston, and at different piston stroke shows that the model is convincing to predict the Stirling engine performance. It shows that the output work, frequency, work loss (including regenerator flow loss, mechanical friction loss, piston finite speed loss, and gas spring hysteresis loss), and heat loss (including conduction loss, regenerator imperfect heat exchanging loss, displacer shuttle loss, and seal leakage loss through the clearance between piston and cylinder wall) are nearly linearly to the hot space temperature. The optimal phase shift for maximal output power is about  $85^{\circ}$ ~ $115^{\circ}$  and is similar at different piston stroke. And if the distance between actually phase shift and optimal phase shift is the same, the output power is similar, whether it's higher or lower than that of the optimal phase shift.

After the isothermal was validated by experimental results, the Gamma type Stirling engine has been optimized using the Finite Physical Dimensional Thermodynamics model coupling with a multi-objective genetic method considering output power, thermal efficiency, and entropy generating rate as objective functions simultaneously. Firstly, genetic algorithm was used to get the Pareto frontier. Then the matrix of the objective values was non-dimensionalized by the Euclidian non-dimensionalization method. Finally, two decision-making methods (*LINMAP* and *TOPSIS*) were used to get the optimum point.

Therefore, the performance of the engine could be improved greatly using the optimum

values indicated by the multi-objective method. Comparing with the ecological optimization method, the multi-objective method can better balance the three objective goals: output power, thermal efficiency and entropy generation rate.

The effects of the hot volume temperature and the total thermal conductance on the Pareto frontier indicate some improvements too (increasing hot temperature and thermal conductance) to adapt on studied Stirling engine, in order to improve its performance.

- (2) In the beta type Stirling engine part, a new model named Polytropic Stirling Model with Losses (PSML) has been proposed for predicting performance of Beta or Gamma type of Stirling engine. A bypass linking compression volume and expansion volume has been added in the classic adiabatic model of Stirling engine. Thus, polytropic processes have been considered in the compression and expansion volumes of the Stirling engine. Various kinds of losses have been coupled in the model. The GPU-3 Stirling engine has been used to validate the new model. It was shown that the new model (PSML) predict very accurately the output power and the thermal efficiency of the Stirling engine.

It was shown that during the most part of the compression and expansion processes, the polytropic number is near to the adiabatic number. Also there is an optimum rotation speed for a maximum output power, while the thermal efficiency decreases with the rotation speed increasing. The output power difference among different average pressures becomes bigger with the rotation speed increasing for both helium and hydrogen as working gas. In addition, an increase in the average pressure in the engine can increase the thermal efficiency, but the increased amplitude decreases with the pressure increasing. The comparison between helium and hydrogen as working gas leads to state that hydrogen is more suitable for high rotation speed engine (more than 2500 rpm) as it has a bigger output power and a higher thermal efficiency. There exists an optimum displacer clearance size for a maximum output power which depends on the average pressure in the engine. This optimum displacer clearance size increases with the engine pressure increasing, which indicates that increasing average pressure in the engine is a method to reduce the displacer clearance's effect on the engine performance.

- (3) In the alpha type Stirling cryocooler part, an isothermal model considering various losses was developed to simulate the behavior of a Stirling cryocooler used on Mars Express project and whose geometry dimensions were measured in our laboratory. This model was validated by the PPG-102 Stirling cryocooler. The compression and expansion volumes are supposed to be isothermal, the variation of the regenerator temperature is supposed to be linear. Results show that the mechanical friction loss is the biggest mechanical loss, hysteresis loss of the gas spring being also considerable; the conduction loss is the biggest heat loss, followed by the displacer shuttle heat loss.

Parameters' effect study on the cryocooler performance shows that a cold end temperature increasing implies an input power decreasing nearly linearly while the cooling power increases nearly linearly and with the hot end temperature increasing, the input power increases nearly linearly while the cooling power decreases nearly linearly. With the average pressure or rotation speed increasing, both the input power and the cooling power increases nearly linearly. The optimum displacer clearance value for cooling power is about  $160\mu\text{m}$ , which is determined by two loss mechanisms (displacer shuttle loss and clearance pump loss). The optimum phase shift is between  $85^\circ$  and  $90^\circ$ . There exists an optimum ratio

between the diameter and stroke of the piston corresponding to a square geometry (ratio equal to 1).

## 8.2 Future research

There are some part of the research which need to be continued as following:

- (1) The Gamma type solar powered Stirling engine needs to add an regenerator to increase the current regenerator heat exchanger efficiency (actually it's the clearance between displacer and cylinder wall). The design of the regenerator such as the material and the size need to be studied in the future. The stroke of the displacer need to be adjusted in the future in order to increase the output power. In addition, the heat exchangers (heater and cooler) also need to be improved so as to increase the heat exchanger effect.
- (2) The Beta type Stirling engine model has estimated the polytropic number in the expansion and compression volumes during the cycle. Nodal method can be developed in the future to study the polytropic number evolution during the cycle more detailed.
- (3) The Stirling cryocooler model is an 0-D model. More accurate model such as 3-D model can be developed in the future to study the cryocooler more detailed.

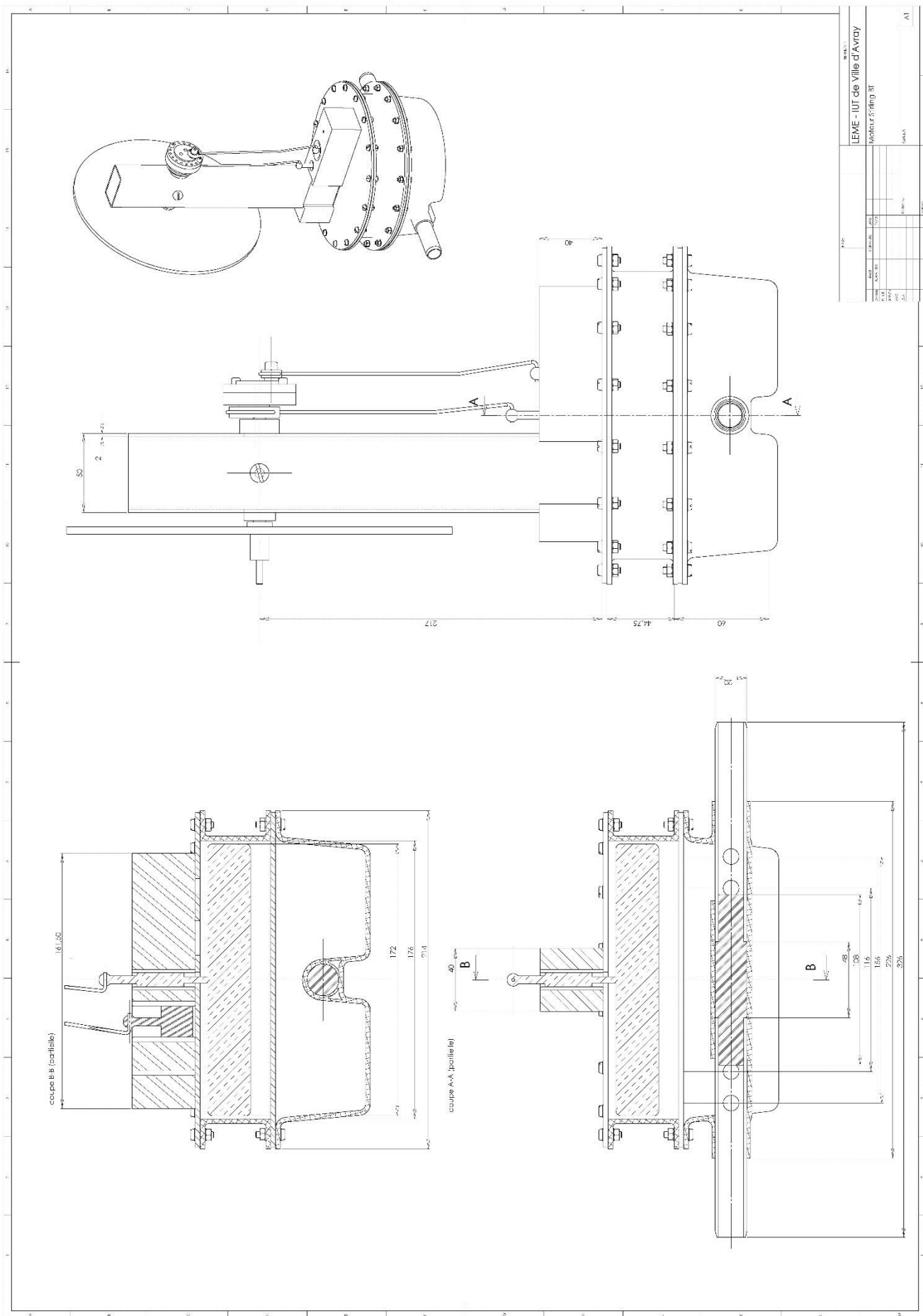


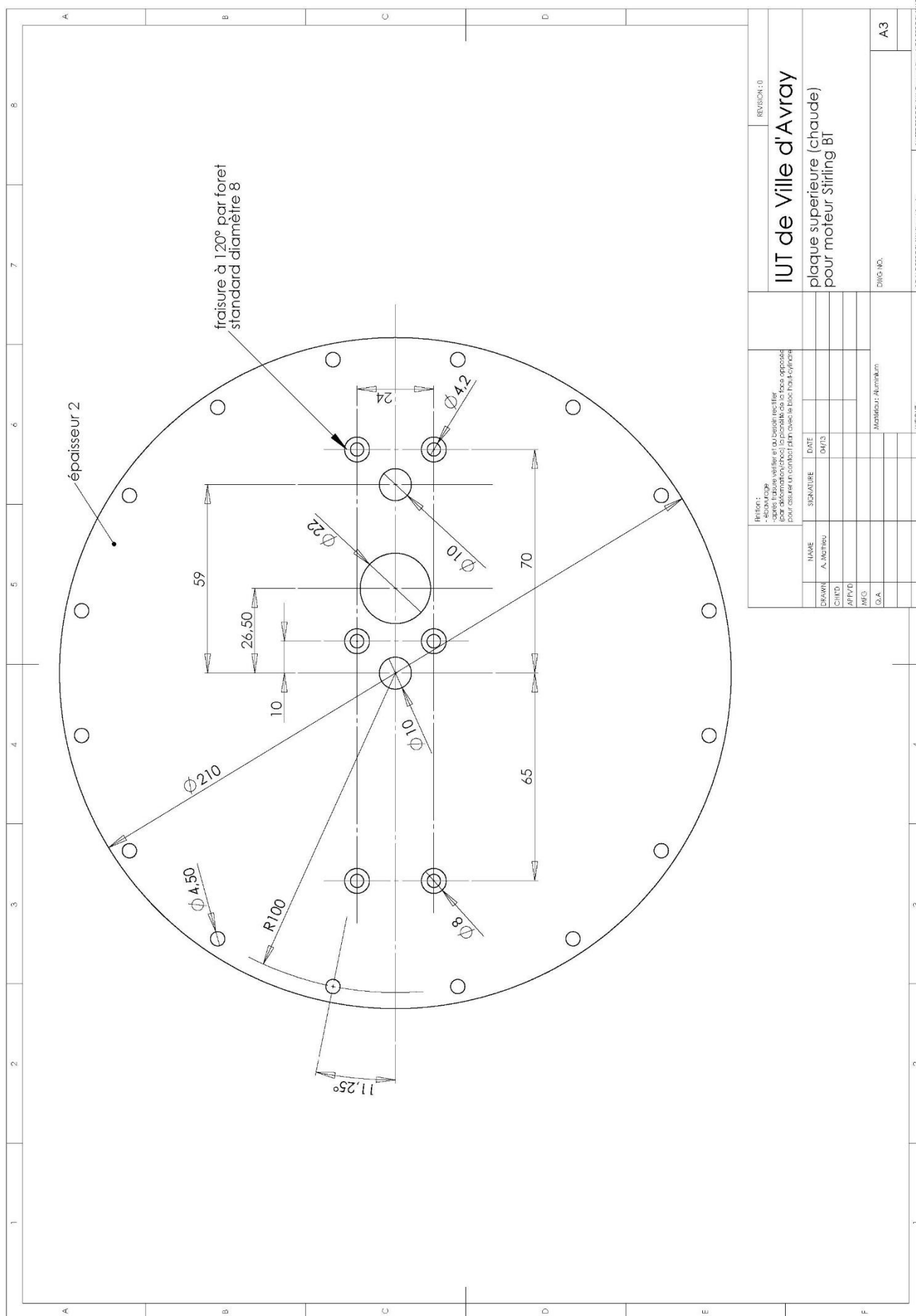
## **Appendix**

### **Technical drawing for the solar powered Gamma type low temperature difference Stirling engine prototype**

This appendix contains the engineering drawings to make the Gamma type Stirling engine prototype.

The first drawing is the dimensions and configuration of the entire engine, including the internal and external arrangement and the corresponding size. The second drawing is the panel of the hot space of the engine, which is also connected with the cold space. The third drawing is the panel of the hot space of the engine, which is next to the hot water tank of the engine. The fourth drawing shows the implantation of thermocouple in the panel of the hot space, which is next to the hot water tank of the engine. The fifth drawing shows the implantation of thermocouple in the panel of the hot space, which is connected with the cold space of the engine.

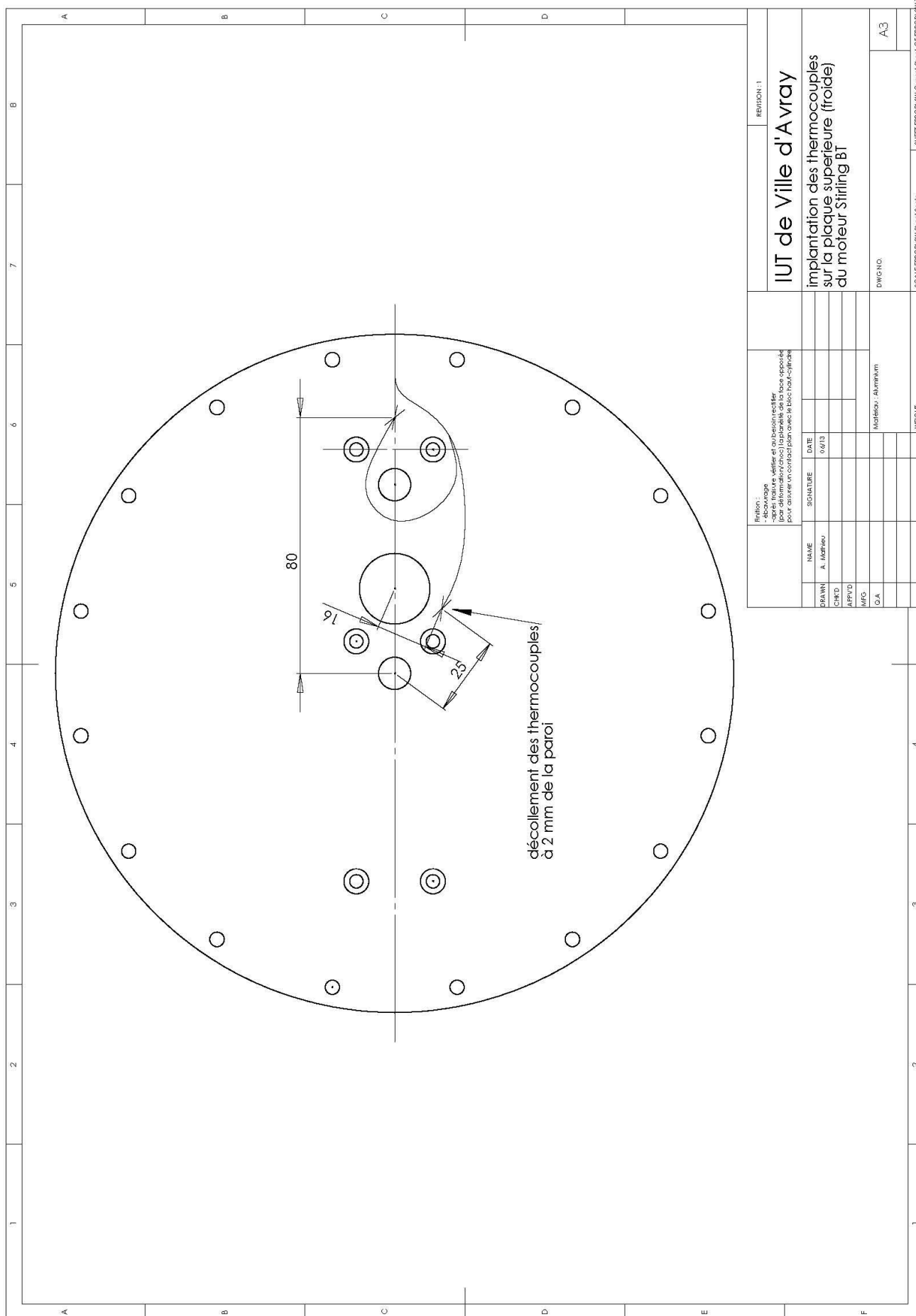




REVISION: 01	
<b>IUT de Ville d'Avray</b>	
plaque superieure (chaude) pour moteur Stirling BT	
Révisions: - REVISION 01 après fabrication et au besoin rectifier les surfaces usées, après pour assurer contact plan avec le bloc bas refroidisseur	
DRAWN	DATE
CHKD	04/13
APPYD	
MKS	
DWG. NO.	Modifié en Aluminium
A3	
SCALE: ENGLISH: Sheet Scale	
SHEET ENGLISH: Current Sheet Of ENGLISH: 1 of 1	







REVISION: 11 <b>IUT de Ville d'A vray</b> implantation des thermocouples sur la plaque supérieure (froide) du moteur Stirling BT		REVISION: 11 IUT de Ville d'A vray implantation des thermocouples sur la plaque supérieure (froide) du moteur Stirling BT	
Fonction : - dessin - après lecture, vérifie et valide le dessin - pour assurer un contact plan avec le bloc haut cylindre		DWG NO. A3 SCALE: B3: 3/4" = 1" Sheet Scale SHEET ERROR: 3/4" = 1" Sheet Scale DWG NO. A3	
DRAWN: A. MATHOU	NAME: A. MATHOU	SIGNATURE: [Signature]	DATE: 0/6/13
CHKD: [Blank]	NAME: [Blank]	SIGNATURE: [Blank]	DATE: [Blank]
APP'D: [Blank]	NAME: [Blank]	SIGNATURE: [Blank]	DATE: [Blank]
MFC: [Blank]	NAME: [Blank]	SIGNATURE: [Blank]	DATE: [Blank]
G.A. [Blank]	NAME: [Blank]	SIGNATURE: [Blank]	DATE: [Blank]
MATERIAL: Aluminum		WGT: [Blank]	

